Universiteit Gent
Faculteit Wetenschappen
Vakgroep Vastestofwetenschappen

Texture of thin silicide and germanide films

Koen De Keyser

Proefschrift tot het bekomen van de graad van
Doctor in de Wetenschappen:
Natuurkunde
Academiejaar 2010-2011

Universiteit Gent
Faculteit Wetenschappen
Vakgroep Vastestofwetenschappen

Promotoren: Prof. Dr. Christophe Detavernier
Prof. Dr. Roland Van Meirhaeghe

Universiteit Gent
Faculteit Wetenschappen

Vakgroep Vastestofwetenschappen
Krijgslaan 281 - S1, B-9000 Gent, België

Proefschrift tot het behalen van de graad van
Doctor in de Wetenschappen:
Natuurkunde
Academiejaar 2010-2011

Table of Contents

III Impact of texture on technological properties

References

1

Introduction

In this thesis, a study of the texture of thin films of silicides or germanides, that are formed on single crystal silicon or germanium wafers, with a specific orientation (i.e. (100), (111) or (110)) is presented. This research was started in September 2005, and results obtained up to September 2010 are included. As relatively little literature concerning this topic was available at the start of the research, the choice was made not to focus this thesis on one particular metal/semiconductor system, but to try and study texture in a variety of different systems, in the hope of getting a better understanding of the importance of the naturally occurring (i.e. non-epitaxialy grown) texture of thin films on single crystal substrates. Of course, as is the case for many research projects, the direction of this research has been heavily influenced by the successes or failures that where obtained in the different metal/semiconductor systems, and by observations in specific systems that were both surprising and intriguing. As a result of this, an important fraction of the work described here will concern the Ni/Si system, for which several unexpected results have been obtained in our research group during the last years. In addition, nickel silicides are important from a technological point of view.

The work described in this thesis was only possibly thanks to the collaboration with the researchers at the IKS KULeuven, IBM Research, École Polytechnique de Montréal, the TEM characterization group at Imec and ASM Europe.

1.1 Outline

This thesis is divided into three parts. The first part consists of an introduction to texture, an overview of the state-of-the-art of thin film texture research and describes measurement, visualization and analysis strategies. Relatively little new results will be presented in this part. The main goal however is to provide a self-contained overview of the practicalities of thin-film-texture research, as no one-stop reference books are currently available. In addition, literature on the texture measurement techniques often skip over the basics, making it difficult to follow the reasoning. In my experience, one really needs to understand these fundamentals to arrive at a correct interpretation of the data, and I believe that only by understanding all of the arguments, including all of the implicit assumptions, one can accomplish this. The goal of the first part is to resolve this. In this section, a description of the software developed to make the analysis possible of texture data of thin films on single crystal substrates is also provided.

The second part will focus on the identification of texture in different silicide and germanide systems. The technological relevance of these materials will be pointed out and the texture of 3 metal/semiconductor systems will be investigated and described. The goal here is to gain insight into what the important texture components are and whether one can rationalize their origin.

In the final third part, the impact of texture on the properties of the silicides and germanides will be investigated. In particular, the thermal stability of NiSi will be linked to the microstructure, and effects of downscaling and different methods of increasing this thermal stability will be discussed.

Part I

Texture: measurement and analysis techniques

2

Crystallographic texture in materials

The concept of texture is used in a variety of different fields, such as computer graphics, materials science or textile. In each of these fields, it is used to indicate properties with little or no relation to one another. In the context of this thesis, texture is used to indicate the *crystallographic* texture: it describes how, in a poly-crystalline material, the orientation of the grains is distributed, i.e. with what frequency a specific grain orientation occurs in the sample.

The goal of this chapter is to present a short overview of the concept of crystallographic texture in materials and establish the commonly used terminology. The focus will then move to thin films, and more specifically to thin films on single crystal substrates, where the texture originates from a solid state reaction. This is the type of material under investigation in this work. For this system, an overview of the state-of-the-art concerning the determining factors in texture selection and the most commonly used theories in explaining and/or predicting texture will be given.

2.1 Texture and anisotropy

A poly-crystalline material consists of a large number of small crystallites, called grains, which can be considered as being perfect single crystals. Each of these grains can have a different orientation in the material, which is displayed in figure

2.1, where the grains were given a color, corresponding to one of the unit cells that show the orientation of the crystal in the grain. Because many materials have anisotropic properties on the crystal lattice level, this anisotropy might be manifested on the macroscopic scale as well, depending on how the individual grains are oriented and interact. In one extreme case, the sample might consist of only one grain, and will thus exhibit the same anisotropy as the crystal lattice, while in the other extreme case, a sample might consist of a large number of grains with a completely random orientation distribution. This will average out the different anisotropic properties of the crystal lattice, resulting in macroscopic isotropic behavior. Where the grains touch one another, grain boundaries are formed, which are crystal defects that separate the regions of perfect crystals. Depending on the relative orientation of two grains, and the orientation of the contact plane, these grain boundary will have different properties, and will influence the macroscopic properties of the material as well.

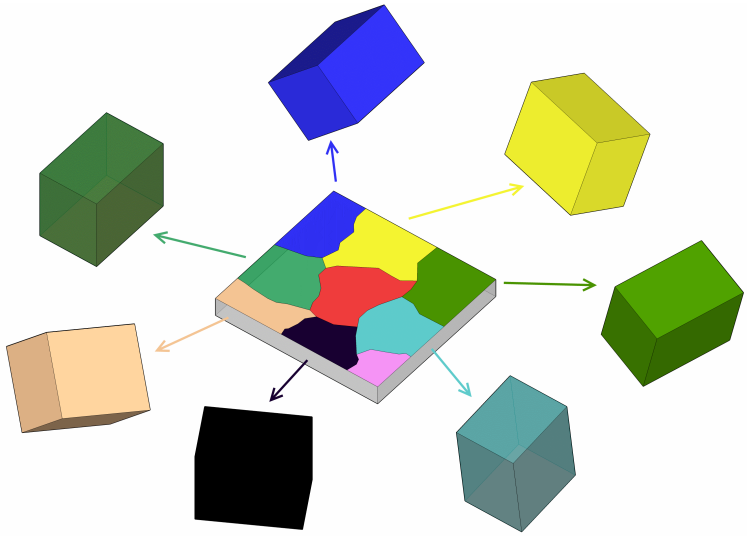

Figure 2.1: A top view of a sample with the grain in a different color. The corresponding orientation of the unit cell is displayed, showing the different grain orientations.

A good understanding of the structure of a poly-crystalline material is essential to understand and/or predict its properties. One aspect of this structure is the texture, which describes the grain orientations and their frequency of occurring within the sample. Typically, no spatial information (the location where the specific orientations of the grains occur within the sample) is provided when the term “texture” is used. If this spatial information is provided, the most common designation is the “micro-structure” instead of texture.

The concept of texture is well studied within the field of metallurgy, as various deformation treatments, such as rolling and drawing, or heat treatments give rise to a variety of textures in metals. In these materials, texture often originates from processing that is done on an initially textureless (i.e. random textured) sample: the existence of a preferential direction, for example the rolling direction, results in the destruction of the isotropy of the sample, as a preferentially oriented force is applied to the grains, which will cause the formation of a preferential orientation of the grains in the material and thus texture. In general, texture always originates from a source of anisotropy, either during the formation of the material itself (e.g. anisotropy in surface or interface energies, in thermal expansion and elasticity), or from an anisotropy in a processing step carried out on the material. In geology, crystallographic texture is studied as well, as it can provide information on the origin or history of a rock.

2.2 Mathematical description

Texture describes the statistics with which a specific grain orientation occurs, and the mathematical tools used to represent it are borrowed from the mathematical representation of rotations. Every orientation of a grain can be specified by defining a reference orientation and an additional rotation to go from the reference orientation to the observed one (figure 2.2a). The problem of describing texture thus reduces to describing the probability of a specific rotation occurring, and defining the reference orientation in a meaningful way.

For the reference orientation, one can in principle make any choice one wishes. In practice, a natural reference orientation often arises from the geometry of the sample or from the geometry of the process that induced the texture in the sample. For example, in a rolled metal, it makes sense to give the rolling direction a special significance, and to incorporate it into the reference orientation.

For the choice of the representation of the rotation itself, one can choose any representation of the special orthogonal group in 3 dimensions, SO(3), which consists of the proper rotations, but in practice the Euler angles are used most often. Here, the rotation is specified by three angles. These angles define the angles of rotation of three consecutive rotations about a predefined choice of axes, and one can end up in any orientation by doing this. This can be seen in figure 2.2b, where one gets from the reference orientation to the observed orientation by a rotation about Z, then about X and finally again about Z.

Alternatively, one can use an axis/angle representation, where the desired orientation is reached by rotating from the reference orientation about a specified axis, for

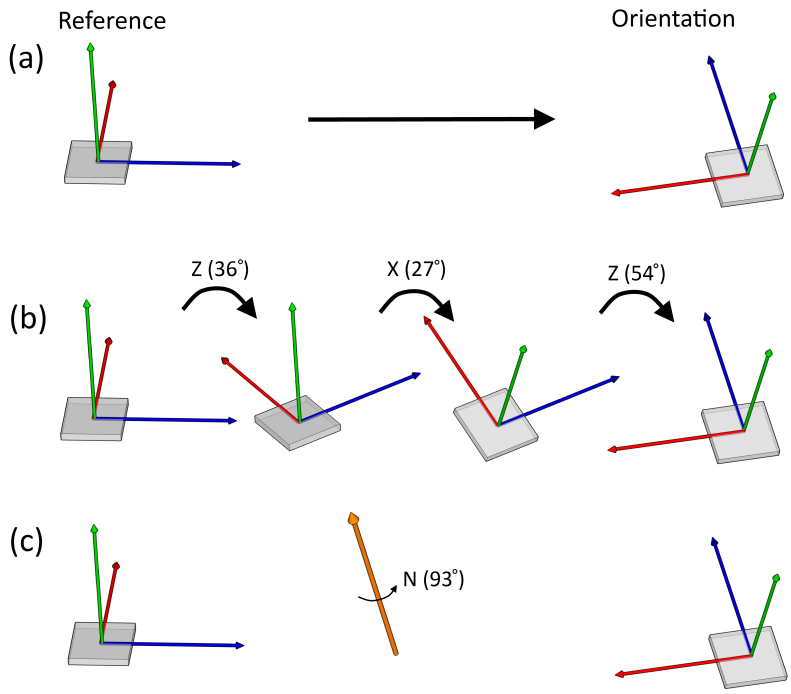

Figure 2.2: A unit cell with attached X (blue), Y (red) and Z (green) axes. Subfigure (a) shows the reference orientation on the left, and an observed orientation on the right. In subfigure (b), the Euler angle description of the rotation to go from the reference to the observed rotation is shown, as a series of 3 rotations, about the Z, X and Z axes. Subfigure (c) show how to go from the reference orientation to the observed one using one rotation about a specific rotation axis (drawn in orange).

a specified angle. This is displayed in figure 2.2c, where the rotation axis is indicated in orange. In some cases, quaternions, 4-dimensional extensions of complex numbers, are used, as any rotation in 3D can be represented by a unit quaternion. In computer based calculations, the orthogonal matrix (with positive determinant) representation is most often used. All of these representations have in common that they have three degrees of freedom, which all need to be specified to uniquely define the rotation.

2.3 Thin films

The occurrence of texture is of course not restricted to bulk materials: any crystalline material can exhibit it. In this thesis, the materials under investigation will

be thin films on single crystal substrates. For this reason, the remaining discussion in this chapter will be focused on texture in thin films.

Most thin films originate from a deposition of a thin layer of one material, on top of a substrate of another material, and one ends up with a heterophase system, as more than one phase exists in the sample. Common deposition techniques are thermal evaporation, sputter deposition or molecular beam epitaxy. Tuning of the deposition parameters, in addition to the properties of the substrate, will influence the properties of the resulting thin film, including its texture. After deposition, the sample can be given a heat treatment, which might change the texture, and cause solid-state reactions to occur, leading to the creation of new phases. As these phases can have radically different crystallographic properties, this will have its effect on the texture in the sample.

The texture in thin films can be classified into different types. A first case is simply the absence of any preferential orientation: all of the grains have a completely random orientation, and this is designated as **random texture**. This is shown in figure 2.3a. There are no constraints on the possible orientations of a grain.

In a second case, the orientation of the grains in the film is uniquely defined with respect to the substrate: only one single orientation (and the symmetrical equivalent orientations) of the grains occur. When the substrate is a single crystal, one uses the term **epitaxy**. It typically occurs when the crystal lattice of the film material has a special relation to that of the substrate, such as being very similar in size, or the ratios of the lattice constants being rational, so that a "natural" orientation exists for the film grains to be oriented with respect to the substrate. Figure 2.3d displays this. In this case, the grain boundaries no longer correspond to a change in orientation, but defects can still exist, such as steps, that separate different areas.

A typical example of an epitaxial film is the chemical vapor deposition growth of $Si_{1-x}Ge_x$ on silicon substrates, where the $Si_{1-x}Ge_x$ has almost identical lattice constants as pure Si, and the thin layer of $Si_{1-x}Ge_x$ is grown in a way as if it continues the silicon substrate structure. Another example is the growth of $NiSi_2$ on Si(111) substrates, where the epitaxy is not achieved during deposition, but where a nickel layer reacts with the substrate during a heat treatment, to form $NiSi_2$ which is epitaxially oriented on the Si(111) substrate [1]. When the substrate is not a single crystal, but poly-crystalline or amorphous, the term "biaxial texture" is more commonly used to indicate a well defined orientation of the film grains. In practice, the designation biaxial texture is used in a more relaxed way, as it often includes a larger spread around an average orientation, when compared to epitaxy.

In a third case, the orientation of the grains is no longer uniquely constrained to one orientation, but a series of related orientations is observed. In this case, all of the grains have the alignment of one crystal plane in common, but no additional

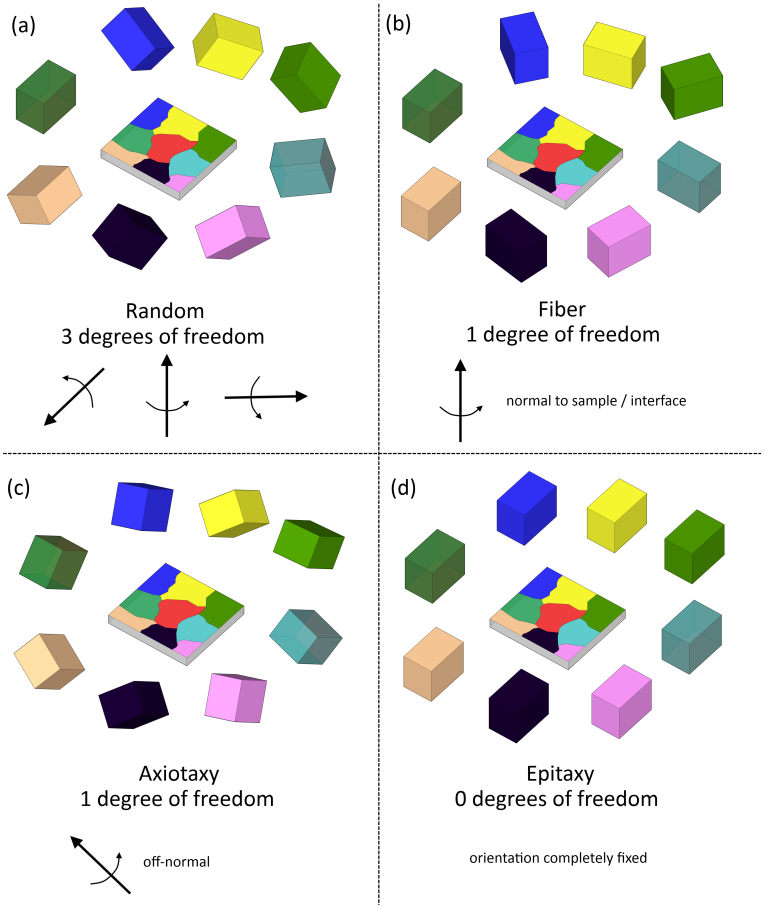

Figure 2.3: The 4 types of texture in thin films: (a) random texture, (b) fiber texture, (c) axiotaxy, (d) epitaxy

constraints on the orientation exist. Rotations which have the rotation axis perpendicular to this crystal plane will leave the alignment of this special plane invariant, so that all of the grains can have an additional random rotation about this axis, and no single unique, well defined orientation is observed. In many cases, this occurs when a plane in the film material has special properties related to the surface energy (e.g. a closest packed plane). Energetic constraints will then force the grains to have a specific crystal plane parallel to the interface of the substrate or the surface of the sample. The resulting texture is called a **fiber texture** and is designated with the index of the plane which has the preferential orientation. The rotation axis perpendicular to the aligned planes is then called the fiber axis, and is typically perpendicular to the interface or surface, as can be seen in figure 2.3b.

Depending on deposition parameters, such as the direction of the incoming flux, a small tilt of the fiber axis can be caused. An example of fiber texture is observed after the deposition of copper on glass, where the closest-packed copper planes are preferentially parallel to the surface plane, which is claimed to minimize the surface energy. On single crystal substrates, one can observe this when depositing Ni on Si(100), where a Ni (111) fiber texture is typically formed.

In some cases, the crystal plane that is aligned is not (nearly) parallel to the interface or surface, but has a large tilting which causes this plane to be (almost) parallel to a specific plane of the substrate. This is an off-normal fiber texture, which is called **axiotaxy**. It was first observed in NiSi on Si(100) [2], where it was found that a number of NiSi planes are aligned to the Si $\{101\}$ planes of the substrate. Even though there is a similarity between a traditional fiber texture and axiotaxy, the origin is clearly different. While a fiber texture is typically the results of a stacking or plane-on-plane matching at the interface, axiotaxy is caused by a matching of planes across the interface. For this reason, axiotaxy can be best considered as a separate, fourth type of texture in thin films. Figure 2.3c shows what the orientation of the grains can be in such a case: all of the grains are related to one another by a rotation about the same off-normal axis.

If we go back to the mathematical representation of texture, the difference of these types of texture becomes very clear. For a random texture, for every possible rotation, one can find some grains that have this orientation, so all three parameters (e.g. the Euler angles) can have a random value. This means that the random texture is described by 3 degrees of freedom. For the case of a fiber texture or axiotaxy texture, the direction of one plane is fixed for all of the grains, but each can have a variable rotation about the plane normal, resulting in 1 degree of freedom (i.e. the rotation angle about this normal) in the texture. Finally, for epitaxy, the orientation of the grains is completely fixed, so no degrees of freedom exist anymore: in the epitaxial texture, all 3 parameters of the orientation are completely fixed, and 0 degrees of freedom exist.

2.4 Thin films on single crystal substrates with solid-state reactions

In the description of the texture of thin films, little regards was given to the type of substrate used, which could be amorphous (e.g. glass), poly-crystalline (e.g. a steel sheet), or single crystal (e.g. Si (100)). In this thesis, the focus lies on the texture of thin films on single crystal substrates, where both the film and substrate can be complex materials containing covalent bindings. There are two main reasons for using single crystal substrates. A first one is due to choice of inves-

tigating silicides and germanides. Without going into details (which will be done in chapter 6), one of the main technological applications of these materials is as electrical contacts in CMOS technology, where a single crystal substrate is used. Secondly, the use of a single crystal substrate has the fundamental advantage of making one part of the problem, i.e. the substrate, reproducible, making thin films on single crystal substrates ideal model systems to study the mechanisms behind texture selection. Because texture originates from the peculiarities of the interface between two phases or grains, in general one needs to characterize both the film and the substrate on a local scale, resulting in the difficulty of acquiring large datasets and making reliable conclusions. In the case of a single crystal substrate, one part of the problem (the substrate) is identical for all of the grains in the film, and can be easily characterized, making it much easier to get to statistically sound conclusions, as all attention can be focused on the film.

The samples under investigation in this thesis not only have a single crystal substrate, but the method by wich the film itself is fabricated is not random either. The films are not simply produced during the deposition process, but only part of the material to form the desired phase in the film is deposited. A subsequent thermal annealing induces a solid state reaction between the deposited material and the single crystal substrate to form a layer of a new phase. This phase originates from a reaction between two components, and the typical processes of nucleation of a new phase and growth will be observed and will influence the texture. In this way, an important difference exists with traditional as-deposited coatings, where the texture often results from directionality of the deposition process or is dependent on the mobility of the deposited atoms at the time of deposition.

Fundamentally, the texture selection during the formation of a new phase is similar to the generation of precipitates in a matrix, and for the reasons mentioned before, thin films on single crystal substrates can thus make an ideal model system to try and understand precipitation reactions. Another reason for the study of solid state reactions is again the technological relevance of the technique for the microelectronics industry in the fabrication of electrical contacts.

2.5 The physical origin of texture

In section 2.3, an overview of the 4 types of textures in thin films was presented, and one can wonder why a specific type of texture will occur in one sample, and not in another. Fundamentally, one can split this question into two parts.

First of all, one can wonder how a specific grain orientation is initially formed. In our case, where a new phase is formed on a single crystal substrate, this means that the nucleus of the new phase must be allowed to nucleate with the specified

orientation. Essentially, this is a thermodynamical argument, as this considers a trade-off between interface, strain and bulk energy.

Secondly, even when a specific orientation can be formed, we have to wonder if the grain will grow, and how fast? There can be competition between the different texture components, and one or more of these can become dominant by growing much faster than the others. The growth of the new phase in a solid state reaction is indeed often a competition between different nuclei with a variable speed of growth. This is a kinetic argument, as it is linked to the speed or kinetics of the different reactions that are occurring.

In principle, if one could calculate the thermodynamics and kinetics of the system, one could ab-initio calculate which phases would form and predict their texture. In practice, this is not possible, as this depends both on local parameters (i.e. bonding between the atoms), and global parameters such as stress and strain, diffusion through grain boundaries and bulk. A simulation that is both accurate on a atom-level scale, as well as on a macroscopic scale of thousands of grains is currently not feasible.

Most models focus on the thermodynamical aspect, as the effect of anisotropy on the interface energy is generally much more outspoken than its effect on the kinetics through the diffusion. Methods of trying to understand or predict texture components then reduce to the rationalization of observed interface structures, or their prediction. However, the problem of merging the local atom interactions with the long range strain effects largely remains unsolved, and the ab-initio calculation of interface structures remains a problem for non-trivial materials. Simplifying the problem even more, one can focus on just the crystallography of the problem, and consider the matching of the crystallographic lattices as a qualitative measure of the interface energy. While one has to admit that this is a long way from describing the original problem, it is the basis of most theories on texture. Ultimately, the only measure of the validity of these theories, is applying them to real cases and testing their power of predicting or explaining observations.

In the following sections, a short overview of some common crystallographic theories used to explain texture selection will be presented.

2.5.1 Coincidence site lattice

If one first considers a substrate and a film material with an identical crystal structure, then an obvious way to align a grain of the film material to the substrate, is to orient the film grain in a way that it continues the crystal structure of the substrate. If we take one unit cell of both materials and put them together in this way, we will get a good matching at their interface, as chemical bonds between the film

and substrate will be saturated, and the interface energy will be low, much lower than when we would put the film grain on the substrate in a way that two non-similar crystal planes would make contact. When both film and substrate material have the same lattice constants, this matching will be repeated in every direction, and more importantly, within the interface plane as well. This extends the good, local matching of the unit cells to an arbitrarily large area at the interface, and the total interface energy will thus be low. In this case, only one orientation is expected in the film, and we get an epitaxial texture.

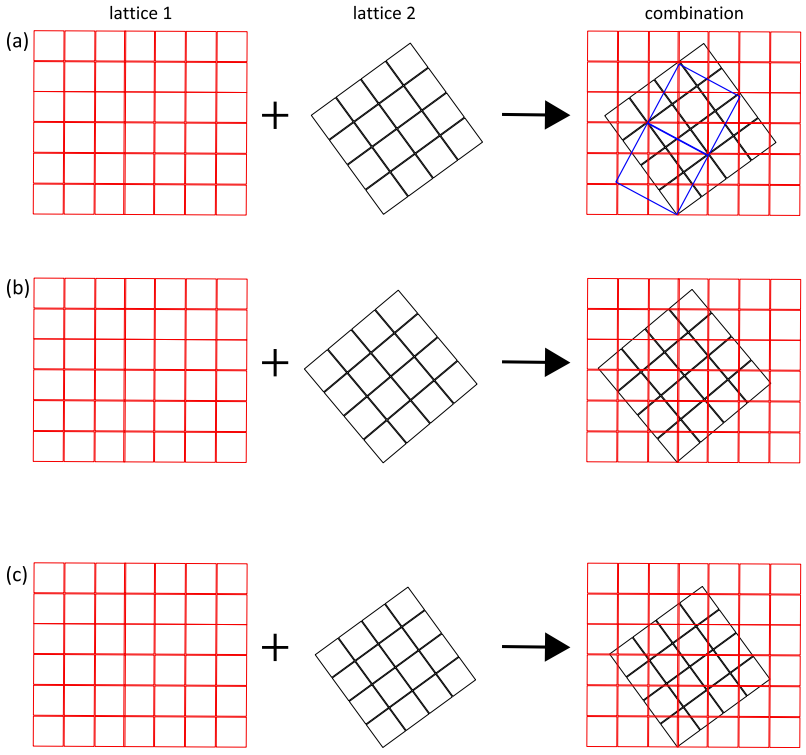

Figure 2.4: Two lattices with a different orientation, and the resulting coincidence site lattice. In (a), the combination of the red and black lattices generate a coincidence site lattice in blue. In (b), the orientation of the black lattice is slightly changed from (a), resulting in the lack of a coincidence site lattice, while in (c), the black lattice has a slightly smaller lattice constant compared to (a) and (b), also resulting in the lack of a coincidence site lattice.

In addition to putting the film grain on the substrate so that it continues the substrate structure, one can wonder what the results would be if it had a different orientation. In general, a random orientation between the two grains will not lead to a good matching, but there might be special orientations which do exhibit some

repeating structure. This idea is the basis of the coincidence site lattice theory, which aims to investigate the interface structure between two similar materials with a specific orientation, by determining the periodicity of the combination of the two lattices. In practice, a new lattice is defined, that is called the coincidence site lattice (CSL), which is the smallest lattice that can reproduce the combination of the two lattices. If both film and substrate lattices are the same, and have an identical orientation, the CSL is identical to the lattice of the film and the substrate. In other cases, e.g. when the film and substrate lattice have some arbitrary tilt to one another, the coincidence site lattice quickly becomes very large. For some special orientations, one obtains a CSL which is of reasonable size, typically a few times the size of the lattice of one of the phases, indicating a reasonably low interface energy and thus a possibly occurring orientation. An example of this is shown in figure 2.4a. The lattices (red and black) are identical, but rotated with respect to one another. For the specific rotation angle used in figure 2.4a one can define a CSL (in blue) . The ratio of the volume of the CSL to the lattice of the crystallographic phase itself, is called the Σ number. In the 2D example of figure 2.4a, we find a $\Sigma 5$ grain boundary. The CSL theory is most often used for the case of homophase interfaces, e.g. for grain boundaries within one phase. Specific Σ numbers correspond to specific types of grain boundaries (such as twin boundaries). While in principle the extension can be done to heterophase systems like thin films, it has proven to be difficult to make meaningful conclusions in those cases. A more detailed overview of the CSL theory can be found in [3].

While the CSL theory has proven useful in the analysis of homophase grain boundaries, there is a fundamental problem with the theory. We go back to the example where we started with a substrate and film with identical lattice and had oriented the film grain in a way that we get a reasonably small coincidence site lattice. We can now depart from this situation in two ways. First, let us introduce a small additional rotation to one of the grains. We would expect to go in a smooth way from the good matching to a situation of a little worse matching. However, a very small rotation completely changes the CSL lattice, and it becomes extremely big, which seem to indicate a discontinuous change in interface energy. This is shown in figure 2.4b, where no CSL points can be found anymore. Secondly, if we keep the orientation of film and substrate the same, but take a film material with a crystal lattice that is slightly larger, we once again see that the CSL expands from very small to extremely large, as shown in figure 2.4c. This second situation is even worse than the first case, since it is well know that slight differences in lattice size can be tolerated and still lead to epitaxial textures. The reason for this discrepancy between the CSL theory and these observations, is that the CSL theory assumes a completely rigid lattice and does not allow for any strain or dislocations. Attempts to resolve this issue have been made, resulting in the near-CSL theory [4], which extends the matching of the lattice points to include near-coincidence sites as well,

and the 0-lattice theory [5], which takes a fundamentally different approach to the same problem, eliminating the aforementioned problems.

2.5.2 The 0-lattice

The 0-lattice theory was developed by Bollmann and starts from the observation that matching between unit cells does not necessarily need to be limited to the matching of lattice points, as was the case in the CSL theory. The 0-lattice theory postulates that, if there is a repeated matching between points within the lattices of the two grains, we still get a low-energy interface.

The method of determining the 0-lattice works in 2 steps. First, an equivalence relation between the two lattices, taking into account their orientation, is established:

$$x^{(2)} = A.x^{(1)}$$

where $x^{(1)}$ is the vector in the first lattice, $x^{(2)}$ the vector in the second lattice, and A the matrix that describes the linear, non-singular transformation between the two lattices. In case both lattices are identical, A reduces to the rotation matrix which rotates lattice 1 to the same orientation of lattice 2. If the lattices are not identical, A will contain a scaling and/or shearing component. It is important to note that A is not unique: any transformation A that relates the two lattices in a one-to-one way, can be used from a mathematical point of view.

Secondly, we consider one point in the first lattice: the grain, which consists of a large number of these lattices, stacked one next to another, will contain a series of equivalent points, originating from the chosen point and found by adding a translation vector of the lattice. Any such point can be described as:

$$x'^{(1)} = x^{(1)} + t^{(1)}$$

where $t^{(1)}$ is any translation vector of the first lattice. To fulfil the 0-lattice criterion, a vector $x^{(2)}$ thus needs to fulfil:

$$\begin{aligned} x^{(2)} &= x^{(1)} + t^{(1)} \\ &\Updownarrow \\ x^{(2)} &= A^{-1}.x^{(2)} + t^{(1)} \end{aligned}$$

If we give the points that match this equation the index 0, we can write this as:

$$\begin{aligned} x^{(0)} &= A^{-1}.x^{(0)} + t^{(1)} \\ &\Updownarrow \\ (I - A^{-1}).x^{(0)} &= t^{(1)} \\ &\Updownarrow \\ x^{(0)} &= (I - A^{-1})^{-1}.t^{(1)} \end{aligned}$$

As the translation vectors form a lattice, the $x^{(0)}$ vectors will form a lattice as well. This lattice is called the 0-lattice.

The interpretation of this 0-lattice is not straightforward, and presenting all of the details would cover a book by itself. Bollmann's magnus opus, "Crystal Defects and Crystalline Interfaces" [5] provides an excellent and detailed description of the theory. The most important conclusion is that the 0-lattice points can be described as points of best matching, and that the 0-lattice is in fact closely related to the dislocation distribution in the material. One can show that it is an extension of Frank's formula which describes the dislocation content of subgrain boundaries. Indeed, the minimum-strain points, obtained using Frank's formula can be shown to be special 0-lattice points.

While no fundamental proof is given by Bollmann for the special importance of the 0-lattice points, it is *reasonable* to accept its interpretation in so far that it allows the explanation or prediction of observed orientation relations. This is indeed the case, as the 0-lattice theory has been used to explain the type and shape of multiple phase boundaries. In addition, the 0-lattice theory does not exhibit the same problems as the CSL theory: a slight change in misorientation between two grains, will lead to a continuous change in the 0-lattice itself, indicating a smooth change in interface energy. The same is true when considering very similar, but non-identical lattices: the 0-lattice has the expected behavior of being only slightly different from the one obtained for truly identical lattices.

Even though the 0-lattice theory has its clear merits, the application of the theory to the systems under investigation in this thesis is problematic at best. The main problem is the choice of the transformation matrix A. While Bollmann provides a set of rules in choosing the right transformation, they ultimately rely on an intrinsic similarity of the two crystal structures, as the transformation should relate those atoms that will bind. If one investigates the interaction of two completely dissimilar phases, e.g. NiSi and Si, there simply is no physical foundation to base the choice of the transformation on. As a different transformation leads to a different 0-lattice and thus different predictions, it has proven to be difficult to get

meaningful results from it for our film/substrate systems.

2.5.3 Alternative theories - recent advances

In addition to the CSL and 0-lattice theories, a variety of rules-of-thumb, observations and guidelines where established in different fields of material science to explain different observed orientation relationships.

From the study of precipitations, the invariant-line criterion [6] was put forward, which proposes that there should exist a line of atoms in the matrix and the precipitate which is invariant during the precipitation, and is located in the interface between the matrix and the precipitate. The difficulty with this is, just as in the case of the 0-lattice, that this assumes that there is a special, known relation between the precipitate lattice and the matrix lattice, which is not the case if we study the interface between two randomly chosen materials.

When studying TEM electron diffraction images, it was observed that specific reciprocal space vectors $\mathbf{g}$ of the two phases were often aligned in a way that the difference, $\mathbf{\Delta g} = \mathbf{g_1} - \mathbf{g_2}$ is perpendicular to the interface plane. If two independent $\mathbf{\Delta g}$'s could be found, one can combine the respective $\mathbf{g}$ vectors, resulting in even more $\mathbf{\Delta g}$'s being perpendicular to the interface plane. If we look at the full reciprocal space, the fact that $\mathbf{\Delta g}$ is perpendicular to the interface plane actually means that the planes corresponding to $\mathbf{g_1}$ and $\mathbf{g_2}$ will have the same *projected* d-spacing on the interface plane. The $\mathbf{\Delta g}$ criterion thus means that an orientation will occur if we have a repeated matching of planes at the interface in two independent directions. In practice, this theory is mostly used to explain observed orientation relations, by identifying $\mathbf{\Delta g}$'s in TEM diffraction images.

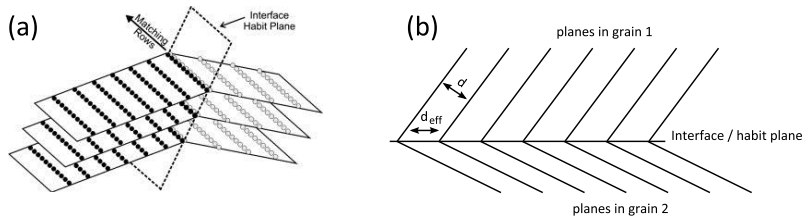

Figure 2.5: (a) Matching of atom rows in the edge-to-edge model (taken from [7]). (b) Cross section view of the matching planes. Notice that, while the d-spacing of the 2 sets of planes is not identical, the effective d-spacing at the interface is.

The edge-to-edge matching theory [8] postulates that a matching of rows of closest-packed atoms between the two materials is the determining factor for the interface energy, and thus the occurrence of a specific orientation relationship. This matching can be accomplished by tilting the planes, which contain the closest-packed

atom rows, so that the effective d-spacing of the plane in the first grain, at the interface with the second grain, matches the effective d-spacing of the plane from the second grain. The advantage of this theory, compared to the invariant-line or $\mathbf{\Delta g}$ theory which are more explanatory than predictive, is that it was formulated in a way that provides a formal method, based on the structure of the two materials, to predict orientation relations. It has had moderate success, e.g. in explaining the texture of $TiSi_2$ on Si (100) [9], but fails to explain the observed axiotaxy, e.g. in NiSi on Si (100) [10].

As pointed out by Kelly and Zhang [11], the edge-to-edge matching, the $\mathbf{\Delta g}$ criteria and the invariant line method are fundamentally equivalent. They ultimately revolve around the matching of atom lines or planes *at* the interface.

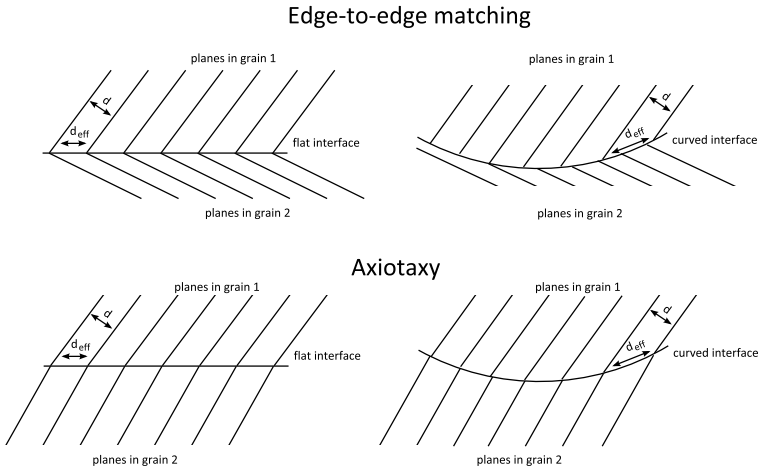

Figure 2.6: Effect of a curved interface on the edge-to-edge matching and axiotaxy model. The effective d-spacing is dependent on the curvature of the interface. If the sets of planes are not nearly parallel, this will cause the matching at the interface to be lost.

In the original report on the observation of axiotaxy [2], a rationalization of the occurrence of axiotaxy was made based on a plane-to-plane matching at the interface between film and substrate, which is similar to the concept of edge-to-edge matching and $\mathbf{\Delta g}$. The main difference is that in [2], a limit is imposed on the tilting angle to reach the edge-to-edge matching, based on the argument that this matching needs to be preserved even when the interface is not completely flat. This is reasonable, as it is likely that an initially forming nucleus will not have a perfectly flat interface with the substrate, and it shifts the main idea from matching *at* the interface, to matching *across* the interface. The effect of a curved interface for the axiotaxy and edge-to-edge matching model is shown in figure 2.6.

In addition, the observation of axiotaxy clearly showed that the $\mathbf{\Delta g}$ criterion is

too strict. Even when matching only occurs along one direction, the orientation relation seems to be preferred to a completely random orientation. The fact that this was missed in the $\mathbf{\Delta g}$ theory is most likely caused by its TEM origin, where only limited statistics can be collected.

While all of the theories discussed in this section have been used to get important insights in the origin of specific orientation relationships, it is clear that none of them provides a complete, ab initio technique for the prediction of the observed orientations. What all of the theories have in common, is the fact that a local matching is not sufficient for a low energy interface: the matching needs to be repeated within a sufficiently large area. This can only be accomplished if there is some shared periodicity between the structure of the film and the substrate within the interface, and it is this idea that will be the rule-of-thumb when interpreting the measurements described in this thesis.

3

Measurement techniques for texture

A whole range of measurement techniques that can provide information concerning the texture of a sample is nowadays available. They all make use of fact that the crystal structure of the material will interact with an incoming beam and create an orientation dependent diffraction pattern. The interpretation of this diffraction pattern will then result in information concerning the local or global texture, depending on the interaction volume of the beam within the sample.

In this chapter, an overview of a selection of these techniques will be given. Electron Backscattered Diffraction (EBSD) and X-ray diffraction (XRD) will be discussed in detail, as these are the techniques that were used to characterize the samples in this thesis. The use of a linear detector for X-ray diffraction will be described, as a way to speed up data acquisition and gather more information. Commonly used alternative techniques such as neutron diffraction and transmission electron microscopy diffraction will be briefly discussed, including their advantages or disadvantages for the study of thin films on single crystal substrates.

3.1 Electron Backscattered Diffraction

In the last decade, EBSD, short for Electron Backscattered Diffraction, has become a popular technique for the analysis of the grain size and crystallographic texture of many materials. It allows for the identification of the local crystal orientation

in a material, and by carrying out this technique on a rectangular or hexagonal measurement grid, one can identify areas with the same orientation (i.e. grains). From this data, one can deduce or calculate a large number of properties of the material, for example grain size, types of grain boundaries, the statistical texture or precipitation orientation relationships.

3.1.1 Principles

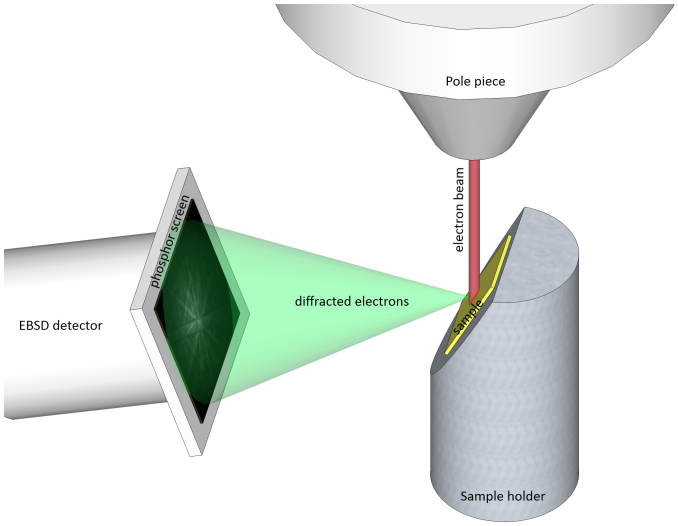

Figure 3.1: Schematic view of the generation of an EBSP in an SEM.

A typical EBSD setup consists of a focused electron beam in a scanning electron microscope (SEM) and a CCD camera with a phosphor screen in front of it (see figure 3.1). The SEM is used to focus an electron beam which then hits a sample. The interaction of the incoming electrons with the nuclei of the sample will result in the generation of backscattered electrons in the irradiated area. These backscattered electrons, which have an energy very close to the energy of the incoming electrons, are generated within the sample, in a small volume, resulting in the creation of what can be best described as a point source of backscattered electrons. After being backscattered, they continue to interact with the surrounding atoms, and part of the electrons will eventually leave the sample again, after several of these interactions. It is this fraction of the backscattered electrons that will generate the Electron Backscattered Diffraction Pattern (EBSP). One can view its generation in two ways: the source of backscattered electrons can be described as a source of Bloch waves, which interact with the crystal lattice, and the resulting diffraction of these waves with the crystal lattice results in a variable amount of backscattered

electrons leaving the sample at different positions and angles. An alternative, simplified view on this process is to view the surrounding crystal lattice as a medium with "channels", through which the backscattered electrons move preferentially, thus generating a non-uniform spatial distribution of the outgoing backscattered electrons. From either view, it is clear that this distribution will be closely related to the local crystal structure and orientation of the crystal. The full mechanism of the generation of this backscattered electron distribution is quite complicated, and to be able to predict all of the intensity variations (such as the occurrence of higher order Laue zones), one needs to use the dynamical diffraction theory. However, based on the simpler kinematical theory, one can already qualitatively explain the location and width of the maxima and minima in this distribution. A full discussion of the generation of EBSP's can be found in [12].

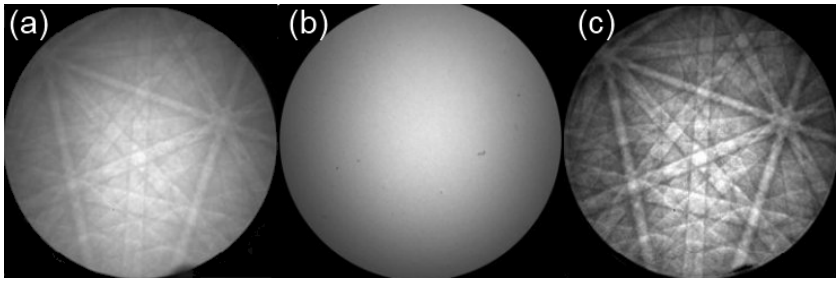

Figure 3.2: (a) Raw EBSP. (b) Background. (c) Processed EBSP. (Images by Oxford Instruments)

From a practical point of view, the EBSP first needs to be acquired, which is accomplished by using a CCD camera and a phosphor screen which converts the incoming electrons into light. This photographic image of the electron distribution is then collected by the CCD. An example of such a pattern can be seen in figure 3.2. It shows a circular shaped gray area, in which bands of different intensity can be seen. The image can be decomposed into two parts. Firstly, there is the circular shaped area, with a high intensity in the middle, which slowly diminishes towards the edges. Secondly, there is a series of bands superimposed. These bands have a relation to the crystallographic planes of the sample: their location, width and orientation are used in the EBSD technique to gather information on the crystal structure and orientation. The total amount of backscattered electrons contained in the whole circular area, is related to the mass of the elements that exist in the sample. This information is in general not used in the EBSD technique, and this radial non-uniform intensity distribution of the EBSP is actually filtered out of the EBSP by subtracting either a calculated, physical model of the non-uniformity, or an experimentally measured "background" image, which is the average of a series of EBSP's. This background image no longer shows any bands, but only the shape

and intensity distribution of the circular area.

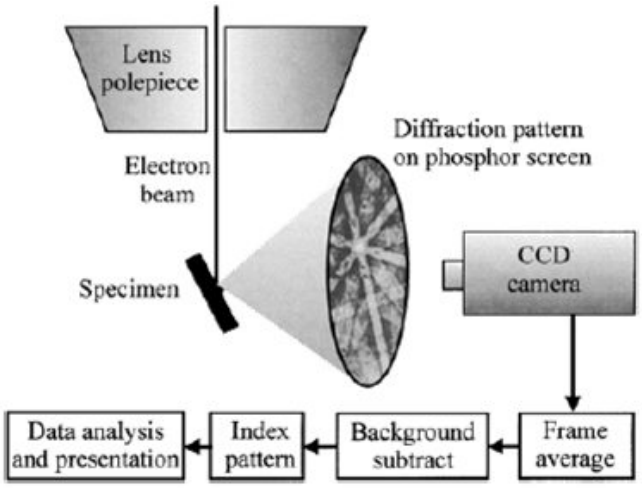

Figure 3.3: An overview of the different steps during an EBSD measurement. (taken from [12])

In practice, the process of carrying out an EBSD measurement consists of a series of steps, which are summarized in figure 3.3. Firstly, the electron beam is focused on a specific area, and an EBSP is generated on the camera. This EBSP is digitized and collected by a computer, which carries out the correction for the non-uniform intensity distribution by subtracting the background signal or the model. Next, the location and width of a number of bands is identified using a software algorithm, most commonly the Hough transform, closely related to the Radon transform, which is an image analysis technique to identify lines in an image by doing a polar transformation, converting lines into spots which are straightforward to detect by computer. The width of the bands is related to the d-spacing of a crystal plane, and the angles at which the bands intersect provide information on crystal plane angles. This information can be used to select the corresponding crystal phase from a list of potential candidates. The exact location and orientation of the bands, relative to the microscope reference frame, allows to deduce how the crystal that generated the EBSP, is oriented. A simulation of the EBSP is then made for this crystal phase and its orientation, which is shown and compared to the measured data. In the end, the crystal phase (ID), location of the beam on the sample (X,Y), and orientation of the crystal (Euler angles) are stored, together with some description of the goodness-of-fit, and the quality of the collected pattern. Until recently, it was not common to store the EBSP images themselves during automated EBSD, due to storage constraints.

3.1.2 Spatial resolution

State of the art field emission gun SEM's can focus the electron beam to a spot size in the nanometer range. This results in a very high spatial resolution for standard SEM imaging, since most secondary electrons are generated in an area roughly the same size as the electron spot, very close to the surface of the sample (depending on the energy of the incoming electrons). However, alternative measurement techniques carried out with the same electron beam can have an intrinsic lower resolution, when the signal of interest originates from a much larger area. A typical example of this is the spatial resolution of Energy-Dispersive X-ray spectroscopy (EDX): since the X-rays, which are characteristic for the elements that occur in the sample, are generated in an area much larger than the directly irradiated area of the sample, and originate from a significant depth below the sample surface, the resulting compositional information has a much lower spatial resolution, compared to SEM imaging. This also applies to the EBSD technique, since the backscattered electrons which make up the pattern, originate from an area which is significantly larger than the spot size of the incoming electron beam. This area, combined with a specific penetration depth of the beam, defines the interaction volume of the beam for the generation of the EBSP.

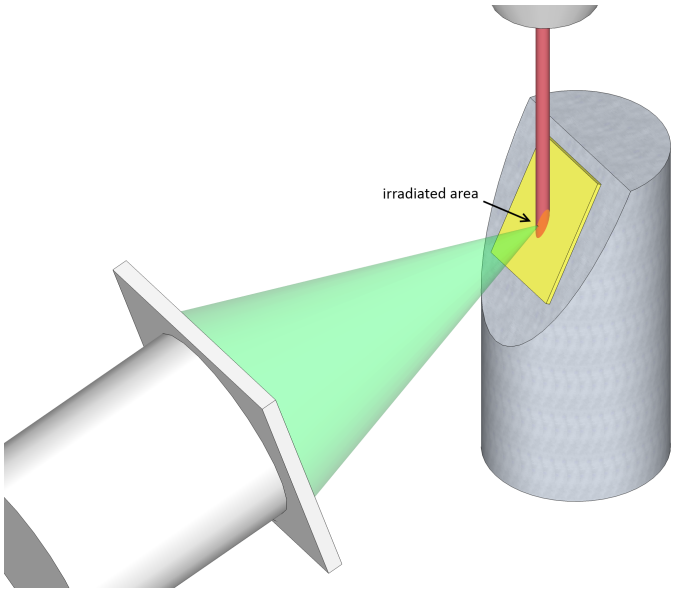

Figure 3.4: Close-up of the size of the electron beam on the sample. Due to the tilt of the sample, the irradiated area is much larger than the beam cross-section.

Several factors influence this interaction volume, and thus the resolution of EBSD.

First of all, since EBSD is carried out with the sample titled with respect to the beam, the effective spot size on the sample will be much larger than the width of the electron beam (see figure 3.4). This will automatically lead to a lower spatial resolution compared to traditional secondary electron imaging. Secondly, the EBSD pattern is generated from the diffraction of backscattered electrons, which are electrons of the incoming electron beam that are backscattered by atoms of the irradiated sample. The volume in which these are generated, is even larger than the spots size of the beam on the sample. In practice, three main factors govern the size of this interaction volume: the size of the electron beam, its energy and the composition of the sample.

The first factor, electron beam size, can be optimized by focusing the beam as small as possible. To reach this goal, a field-emission SEM is instrumental, as the spot sizes can be an order of magnitude smaller than in the cases of W or LaB_6 tips. In addition, one can opt for a lower beam current, but this also has the effect that less electrons hit the sample and thus less backscattered electrons are generated, lowering the intensity of the EBSP, whose features quickly get lost in the background noise. There is little use in focusing the beam smaller than a few nm, as the interaction volume is then no longer limited by the electron beam size.

Secondly, the beam energy also influences the interaction volume. Because the energy of the beam depends on the acceleration voltage used in the SEM, this can easily be tuned. In contrast to standard SEM imaging, where a higher resolution is obtained at higher acceleration voltages due to the better focussing of the beam when the acceleration voltage is increased, the spatial resolution of EBSD shows the inverse relation when using a FEGSEM: as the backscattered electrons have the same energy as the incoming electrons, a high acceleration voltage will lead to longer interaction lengths of the backscattered electrons within the sample. While lowering the energy therefore increases spatial resolution, decreasing the acceleration voltage below 10 kV has a severe impact on the electron-to-photon conversion efficiency of the phosphor screen, so that the measurement time needs to be increased significantly.

Finally, the composition of the sample, more precisely the mass of the atoms, heavily influences the generation of the backscattered electrons, as the backscattering coefficient for electrons increases with increasing atomic number. Of course, this is not something which is tunable in the measurement.

Taking these three factors into account, Humpreys [13] reported the interaction volume as having a minimum size of 50 nm in the direction of the tilt axis for an aluminum sample, and roughly 1/3 of that in the direction perpendicular to the tilt axis, when the SEM is tuned for a maximum spatial resolution and one still obtains usable EBSP's.

While the size of the interaction volume represents a fundamental limit for the EBSD technique, one cannot simply translate this into the effective spatial resolution. This becomes clear if one considers the impact of the interaction volume on the EBSP generation: as long as the interaction volume is contained within one grain, a clean EBSP will be produced, and in most cases the analysis of this pattern will result in the correct determination of the local grain orientation. If the interaction volume is spread out over 2 or more grains however, the EBSP will consist of the convolution of the separate patterns of each of the grains, each with a low intensity, resulting in an unclear EBSP. This can lead to an unindexed EBSP, or even worse, to an incorrectly indexed pattern. However, even when an EBSP is collected which contains convoluted patterns, the software can deconvolute the patterns and try to identify them. In practice, this only works when the convoluted EBSP contains one relatively strong component, and one or more much weaker ones, but it does show that measurements with a higher spatial resolution than determined by the interaction volume, can be carried out. Humpreys [14] determined an effective spatial resolution of 20 nm for aluminum, 10 nm for α-iron and 9 nm for brass, which is indeed significantly better than what would be expected from the interaction volume.

It is important to note that the determination of the effective spatial resolution relies on human intervention, as the currently available automatic EBSD systems will often fail when feeding it EBSP's of poor quality, where a human operator would otherwise succeed. In practice, it is of course not possible to manually intervene during an EBSD measurement on samples where tens of thousands of points are recorded. This means that the effective spatial resolution of run-of-the-mill measurements is currently limited by the analysis software, especially when working with materials that exhibit a low symmetry. The automatic indexation software will often introduce errors into the data when working on small grained materials, so one needs multiple data points to make sure that the determined grain and its orientation are in fact correct. This lowers the spatial resolution of automatic measurements to 2 or 3 times the values reported by Humpreys.

As a way to partially work around this problem, the EBSD measurements in this thesis which were carried out on small grained materials, where manually checked in those locations where the automatic indexation provided inconsistent results. This was made possible thanks to the use of the GUSTAV software (see chapter 5), which allows for an interactive re-analysis of selected data points by the user, something which was not possible with the currently commercially available EBSD software.

3.1.3 Angular resolution

The purpose of an EBSD measurement is to determine the crystal orientation of a number of grains. The precision with which this orientation can be determined is the angular resolution and signifies the minimum misorientation that must exist between two grain orientations to be able to distinguish between them. Because the determination of the orientation relies on the identification of the location and the orientation of the bands in the EBSP, it is clear that the image resolution and quality of the EBSP will be the main determining factors for the angular resolution. The use of high beam currents, long acquisition times and a high resolution CCD camera will thus improve the angular resolution, but at the expense of spatial resolution, measurement time and cost. The absolute angular resolution in commercially available systems is typically 1-2°. The relative angular resolution can be much higher (order of 0.1° [15]), if EBSP's from the same area would be compared, however this technique is not yet commercially available.

3.1.4 Practical limitations

The EBSD technique comes very close to being the ideal technique for texture determination. In most materials, the limits on spatial or angular resolution present no problem, so one can get a complete characterization of the microstructure of the material. For the thin films under investigation in this thesis, some problems did show up.

As the grain sizes in very thin films can be quite small, one ends up close to the spatial resolution limit. This makes it necessary to be careful when automatically analyzing the data, as pattern quality can be quite poor. One way to overcome this problem is by increasing the measurement time, but this is limited due to the surface contamination of the sample and SEM: as the electron beam is hitting the sample, the electron beam will start to decompose any residual hydrocarbon and leave a trail of deposited carbon behind. As the EBSD pattern is a diffraction pattern, any surface contamination will influence the quality of the pattern. This results in a trade-of between increasing measurement time to increase the amount of collected diffracted electrons, and decreasing it to lower surface contamination with carbon. In many cases, these two constraints cannot be fulfilled at the same time in an ordinary SEM and no reliably EBSD measurements are possible. This is especially the case when working with nickel containing samples, as the nickel will have an additional catalytic effect on the decomposition of hydrocarbons. A thorough cleaning of both the sample (e.g. with an oxygen-plasma treatment) and the SEM chamber can alleviate this problem, but ultimately, only the switch to ultra-high-vacuum systems will allow the use of EBSD on very small grained

materials.

3.1.5 Determining volume fractions of texture components

EBSD is ideally suited for quantitative texture analysis, as one readily obtains a number of data points, each with a specific orientation. By assigning a fraction of the data points to a specific texture component and comparing it to the total number of points, one finds the volume fraction of this specific texture component. Most commonly, a data point is assigned to a texture component if its misorientation to this component is less than a predefined value. This leaves the question however, what a reasonable value is for this maximum misorientation. It makes little sense to choose it below the spatial resolution of the measurement technique, i.e. 1-2° for EBSD, as the noise within this range will then start to influence the volume fraction. Also, a lot of commonly occurring textures do not consist of exactly defined orientation, but are intrinsically quite broad (e.g. deformation textures). This results in the use of arbitraty cut-off values, like 5 or 10° of misorientation, where there is often no physical reason behind this choice.

While the focus in this thesis will not lie on quantitative texture analysis, in some cases volume fractions will be determined. As a way to eliminate the need to choose an arbitrary cut-off angle of misorientation, we will present volume fractions as a function of misorientation degree. This has the added advantage that one can immediately see whether a specific texture component consists of a very sharply defined orientation or is in fact rather broad. Based on this information, one can then make a reasonable choice for the maximum misorientation that defines a particular texture component.

3.2 Kossel Lines

When a sample is hit by an electron beam, not only backscattered electrons are generated, but characteristic X-rays are emitted as well. These will form a diffraction pattern due to their interaction with the surrounding crystal lattice. If one collects the resulting spatial distribution of the characteristic X-rays coming out of the sample, one obtains a Kossel line pattern. An example of this is shown in figure 3.5. The image consists of a mostly uniform background, on which curves of different intensity are superimposed. These curves are the equivalent of the EBSD bands, and again, information concerning crystal structure, symmetry and orientation can be extracted from this.

An important problem of the Kossel lines technique is the low intensity of the lines

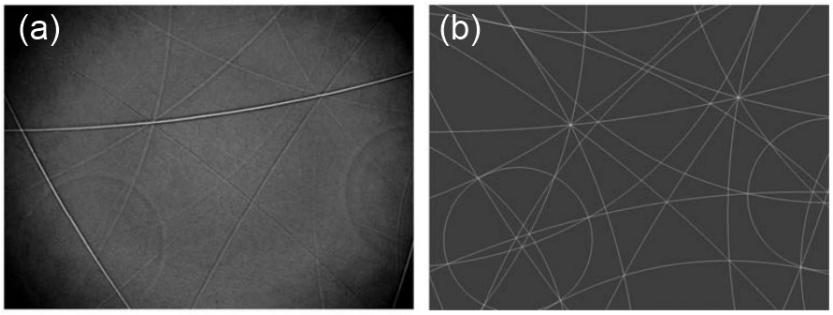

Figure 3.5: (a) Kossel line pattern generated by a CuAlBe sample and (b) the simulation of the Kossel lines. Images taken from [16].

with respect to the background. This makes a sensitive detection mechanism necessary. In addition, as the X-rays are generated by the atoms in the sample, the X-ray wavelength is determined by the composition of the sample. Characteristic X-rays are generated in a volume of about 1 cubic micron around the beam position, making the spatial resolution of the technique much lower than EBSD. The main interest in Kossel lines originates from the fact that the technique has a very high angular resolution of about 5.10^{-5} ° [16]. This makes it perfectly suited for the study of epitaxial growth and the determination of local strain.

3.3 X-ray diffraction

The discovery of X-ray rays by Röntgen in 1895 and the observation that a crystal lattice can act as a diffraction grid for these waves by Knipping and von Laue in 1912, opened the possibility of studying the atomic structure of crystals. A change in orientation of a grain corresponds to a rotation of the crystal lattice, and this will influence the interaction with the X-ray and the resulting diffraction pattern, making it possible to study crystallographic texture.

3.3.1 Principles

X-ray diffraction techniques use the interaction of X-rays with a the crystal lattice as a way to extract information about this crystal. The most commonly used technique is the θ-2θ scan in Bragg-Brentano geometry, where a sample is titled towards an X-ray beam over an angle θ and a detector is rotated over the angle 2θ so that the Bragg diffraction criterion is fulfilled for planes that are parallel to the sample stage, if they have the correct d-spacing determined by the wavelength of

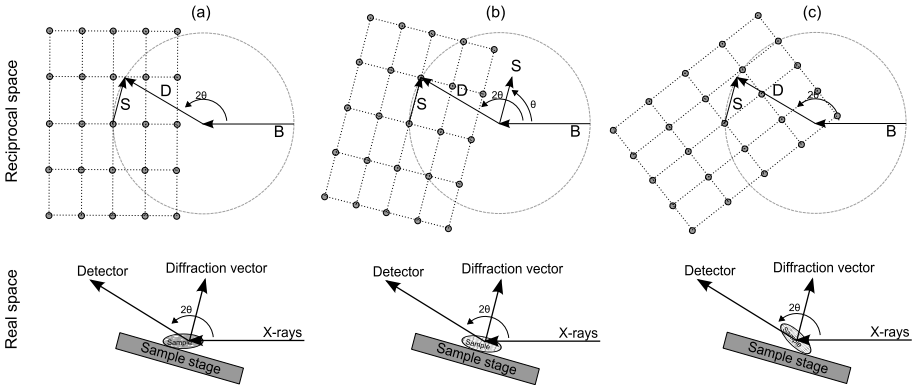

Figure 3.6: 2D construction of the Ewald sphere for a θ-2θ setup where the crystallite has 3 different orientations. Only in the (b) orientation will diffracted intensity be measured by the detector, as a reciprocal lattice point lies on the detector vector.

the X-rays and the 2θ angle of the detector through the Bragg rule $2d\sin\theta = n\lambda$. While θ-2θ scans have become a run-of-the-mill technique, it is important to be aware of the limitations, as the used geometry will result in a signal which *only* depends on the crystal planes *parallel* to the sample stage surface, and thus any information on the occurrence or orientation of other planes is lost. For the study of materials which can be provided as a powder, this raises no problems, as the statistical distribution of the plane orientations will be uniform (resulting in random orientation of the crystal planes), but for textured samples a lot of information will be missed.

If one carries out a θ-2θ measurement on a textured thin film, the results will not necessarily apply to the whole film, since only grains with the "right" orientation contribute to the measured diffracted intensity. The construction of the Ewald sphere for the case of a single crystal or epitaxial film in figure 3.6 makes this clear. The vector B is the beam vector, indicating the direction of the incoming beam and the wavelength (by its length of $1/\lambda$). The detector vector indicates the location of the detector with respect to the beam: one can see the 2θ angle it makes with the beam. If one chooses the origin of the reciprocal space opposite of the origin of the beam vector, it follows from the Bragg diffraction criterion that one will only measure diffracted intensity if a reciprocal lattice vector exists that connects the origin of the reciprocal space with the end point of the detector vector. This vector will be called the diffraction vector S, and bisects the beam vector B and the detector vector D, if we move it to the center of the Ewald sphere. Figure 3.6 shows 3 cases with identical crystal phases (and thus identical reciprocal lattices as well). One can notice that only for the second case (figure 3.6b), the orientation of the crystal results in a reciprocal space point coinciding with the detector vector

end point on the Ewald sphere, so that diffracted intensity will be measured. In the other cases, the θ-2θ measurement will fail to provide any information.

In the θ-2θ measurement, a series of points in the reciprocal space is sampled, as θ and 2θ are moved through their respective ranges. The result is a measurement of the reciprocal space along one line, which corresponds to the sample holder normal, and going through the origin of the reciprocal space. In reciprocal space, distance from the origin is inversely related to d-spacing, so a range of d-spacings will be sampled this way. However, this is limited to only one point per d-spacing, and this point corresponds to planes that are parallel to the sample holder surface.

As the standard θ-2θ scan only depends on planes of one orientation, it is clearly not suited to study texture, and different techniques have to be used. The X-ray texture data presented in this thesis was collected using two different methods. Initially, the Schultz method for pole figure measurements was used, using a photon counting point detector. During the work on this thesis, a linear detector became available and part of the goal of this research was to use this detector for texture measurements by developing the required measurement strategies and analysis software. Both of these techniques will be be discussed in the following sections.

3.3.2 The Schulz method

The most common way to study texture in thin films using X-ray diffraction is based on the methods described by Schultz [17, 18]. Here, a sample is placed on a four-circle diffractometer, which allows to tilt and rotate the sample, and choose the inclination of the sample with respect to the incoming X-ray beam. Also, the angle between the incoming X-ray beam and an X-ray point detector can be chosen. For the choice of the name for the angle of tilting and the rotation of the sample about its normal, a variety of conventions are used. In this thesis, χ will be used to indicate the tilting of the sample and ϕ to indicate the rotation about its normal. The inclination of the sample with respect to the incoming beam corresponds to the θ angle, and the angle between beam and detector will always be chosen as twice this value, so 2θ, to fulfill the Bragg diffraction condition. A schematic of this setup is shown in figure 3.7. By choosing the 2θ angle, one selects one or more crystallographic planes from which the diffracted intensity will be recorded. Because both the beam and the detector remain in a fixed position during the measurement, the diffraction vector has a fixed orientation, regardless of the choice of the χ and ϕ rotation angles. We define $\chi = 0$ as the tilt angle which brings the normal of the sample surface onto the diffraction vector. $\phi = 0$ is typically defined with respect to a specific feature of the sample, in our case it will be related to the orientation of a crystal plane of the single crystal substrate.

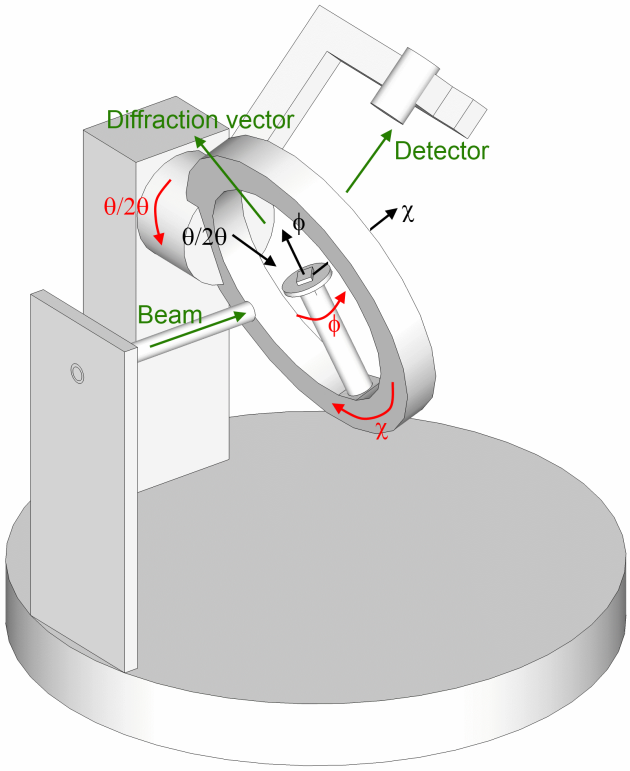

Figure 3.7: A four-circle diffractometer. The beam vector, detector vector and the diffraction vector which bisects them, are indicated in green. The four different axes of rotation ($\chi, \phi, \theta, 2\theta$) are indicated in black, with the θ and 2θ axis coinciding. The resulting rotation is indicated in red.

The purpose of the χ and ϕ rotation is to bring all reciprocal space points corresponding to the selected d-spacing onto the diffraction vector. If we consider the reciprocal space of the sample, we can define a coordinate system in spherical coordinates, using two angles α and β, and a distance from the origin r. The Z-axis is then chosen to coincide with the normal to the sample holder. Every point in the reciprocal space is characterized by its distance from the origin r, the angle it makes with the Z-axis α, and an angle within the plane of the sample holder β. Figure 3.8 shows this situation where we consider a randomly oriented plane (colored green) in the sample. The corresponding reciprocal lattice vector is indicated in green, and its coordinates r, α and β are indicated. In the initial situation, with $\chi = 0$ and $\phi = 0$, the ϕ rotation axis coincides with the sample holder normal as well as the diffraction vector. The χ rotation axis is perpendicular to it. From the

picture, it is clear that if we rotate the sample over an angle β about the χ axis, and about the angle α about the ϕ axis, the reciprocal lattice vector ends up on the diffraction vector S. Because χ and β, and ϕ and α are so closely related, one often does not distinguish between the rotation angles χ and ϕ of the diffractometer, and the orientation angles α and β in the reciprocal space.

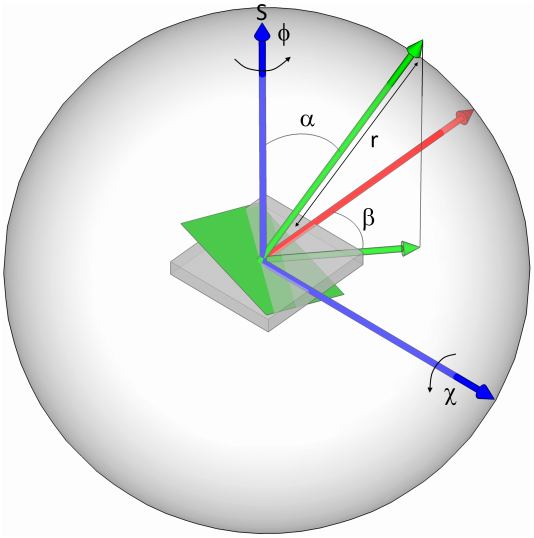

Figure 3.8

One can see an example of the effect of these rotations in figure 3.9, where a 3D view of the Ewald sphere is shown. On the left side, the initial situation is drawn ($\phi = 0, \chi = 0$) and one can see that none of the reciprocal space points lie on the detector vector, resulting in no diffracted intensity being recorded. By rotating the sample over the appropriate χ and ϕ angles, we end up in a new situation, displayed on the right. Here, a reciprocal space point does hit the detector vector and we will measure a specific intensity, depending on the structure factor of the crystallographic plane.

By scanning the whole χ (-90 to 90 °) and ϕ range (0 to 360 °) in small steps, one obtains the diffracted intensity for every possible orientation of the investigated crystallographic plane. The use of X-ray diffraction results in the introduction of centrosymmetry, even if the material under investigation does not exhibit it by itself (Friedel's law), making it sufficient to measure χ from 0 to 90°. Additional symmetry in the sample might exist, e.g. due to a symmetry of the substrate, which will of course be reflected in the reciprocal space. This will further reduce the range of χ and ϕ one needs to measure. Typically, the result of such a scan of χ and ϕ is then displayed on a pole figure, where the measured intensity is converted

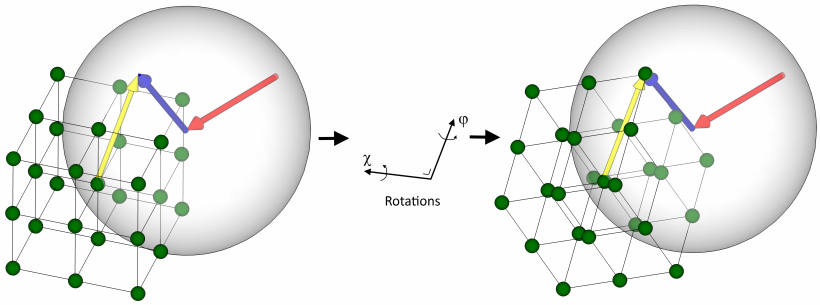

Figure 3.9: The 3D Ewald sphere construction, with the beam vector in red, the detector vector in blue, and the resulting diffraction vector in yellow. The rotation axes for χ and ϕ are shown in the same reference frame.

to a color scale. This is then marked on the disc using polar coordinates, where the angle corresponds to ϕ, and the radial distance is a function of χ. The result is called a pole figure and its properties will be discussed in detail in chapter 4.

Because the result of a measurement using the Schulz method only provides information about the orientation of one type (i.e. one d-spacing) of crystal plane, it does not provide complete texture information. First of all, the orientation of one plane does not fix the orientation of a grain, as one degree of freedom (an additional rotation about the plane's normal) remains. It therefore makes sense to use the Schulz method not for just one d-spacing, but to select a series of d-spacings corresponding to the phase under investigation and carry out the measurement for each of these. Secondly, there is not a one-to-one connection between the reciprocal space of a sample and its texture distribution. This means that one cannot readily get the texture distribution from the acquired pole figures. For textures which are not too sharp and materials which are relatively high in symmetry (e.g. cubic, hexagonal), the calculation of a texture distribution based on the pole figures can be carried out quite successfully using the spherical harmonics technique [19] or iterative techniques [20] which propose a discretized texture distribution, calculate the pole figures from this, and then compare it with the measured results. The difference between calculation and measurement can then be used to improve the proposed texture distribution until convergence is reached. One important note here is that the discretization of the texture distribution is arbitrary and bears no relation to any physical reasons for the occurrence of texture. In cases where one has a rather sharply defined texture, this necessitates the use of a very finely spaced discretization grid, resulting in a huge increase in calculation time and often convergence can no longer be reached.

An alternative way to analyze the pole figures is by considering the texture dis-

tribution as consisting of a series of texture components, where these components are parameterized descriptions of physically occurring texture components. One can then simulate what regions of the pole figures would have a high intensity if these texture components were real and compare to the measurements. In this case, one mainly focuses on a qualitative agreement with the pole figures, and this is especially useful when dealing with materials that exhibit a series of uniquely identifiable texture components. This is often the case for thin films, where one can break down the texture as a combination of epitaxy, fiber, axiotaxy and random. The samples investigated in this thesis are all thin films, so this technique was the analysis method of choice.

3.3.3 Pole figure measurements with a linear detector

As pointed out in the previous section, a measurement using the Schulz method and a point detector only provides information about one crystallographic plane. One can repeat the measurement for additional d-spacings, changing the θ and 2θ angles in the diffractometer, but the required measurement time quickly becomes prohibitive. In addition, the Schulz method is only practical if one knows in advance which phases to expect, and thus at which 2θ angles one will measure diffracted intensity. If this is not the case - and this is to be expected when investigating unknown samples - one can only make an educated guess for the d-spacings to measure. In practice, this can easily lead to an incomplete characterization of the sample, as the fraction of the grains that have an unexpected phase, will leave no trace in the measured pole figures.

These problems can be resolved when using a linear detector. The experimental setup is exactly the same as in the case of the Schulz method, but instead of a point detector located at an angle 2θ, we now use an array of detectors located in the plane perpendicular to the θ rotation axis. In effect, this means that all of the detectors are positioned at different 2θ angles. A schematic overview of such a setup can be seen in figure 3.10.

Each of the detectors has its own detector vector D_1 to D_n and since the diffraction vector bisects the beam vector and the detector vector, a whole array of diffraction vectors S_1 to S_n now exists. For a given orientation of the sample, this means that a line in the reciprocal space is sampled. When the detectors are placed in the plane perpendicular to the θ/2θ rotation axis, each of the detectors will collect intensity for a different 2θ value. For the sample however, one has to choose one specific θ angle. Only one of the detectors will thus make an angle with the beam direction that is twice this θ angle. In this discussion, it is assumed that this is the case for the center of the linear detector. For this central detector pixel, nothing has changed compared to the Schulz method. As we scan the χ and ϕ ranges,

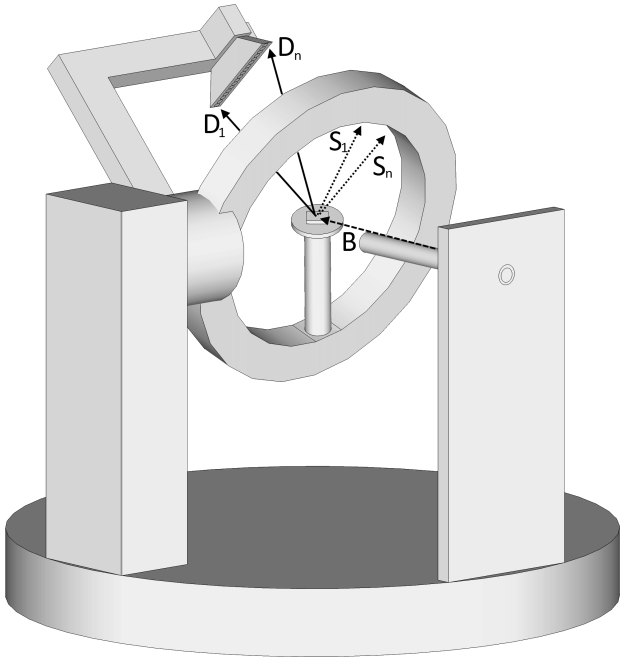

Figure 3.10: Linear detector mounted on a 4-circle diffractometer and the resulting detector, diffraction and beam vectors

we acquire all of the data to draw the pole figure for the plane corresponding to the 2θ angle of this detector pixel. While moving χ and ϕ, the intensity in the other detectors is recorded as well, but it is no longer straightforward to plot this information on a pole figure.

Figure 3.8 showed the location of the different rotation axes and the diffraction vector in the Schulz geometry. Due to the fact that the diffraction vector coincided with the ϕ rotation axis, the χ and ϕ motor angles were identical to the α and β orientation angles. In figure 3.11 the same situation is drawn for the case of a detector pixel which no longer has its diffraction vector coinciding with the ϕ rotation axis. A consequence of this is that it has become impossible to measure complete pole figures with the detector pixels that are off-center. Figure 3.11 makes this clear. A reciprocal lattice vector is rotated to coincide with the diffraction vector in two steps: first a ϕ rotation is applied, and then a χ rotation. The last part, the χ rotation, can only move a reciprocal lattice vector onto the diffraction vector if it is already located on the χ-rotation circle through the diffraction vector (visible as the large circle in the figure). This means that the purpose of the ϕ rotation is to rotate the reciprocal lattice vector onto this large circle. However, if one considers

a vector that has its end point within the region between the diffraction vector and the ϕ rotation axis (i.e. the red-colored disc), this is impossible to accomplish, and this reciprocal space vector will thus never be measured during the χ,ϕ scan. Using the linear detector setup, a small fraction of the sphere can therefore not be measured if one only rotates χ and ϕ, and a small hole in the pole figure will result from this. The size of this hole depends on the angle between the diffraction vector of the detector pixel and the ϕ rotation axis. The problem can be solved by adding an additional series of scans where one changes the θ angle, but this has the problem that it significantly affects the irradiated volume of the sample and the background signal. One could correct for this if one has a good model for this background and the change in interaction volume, however this was not considered in this work.

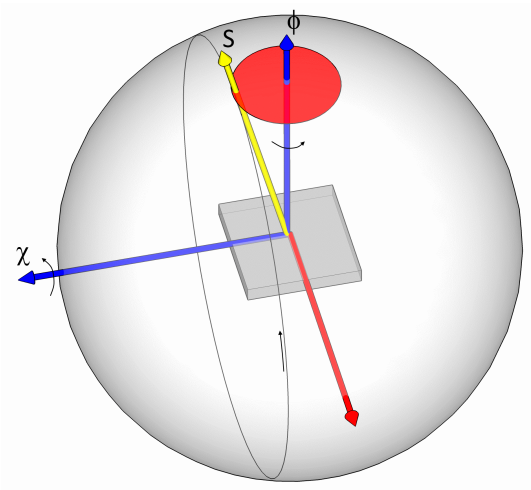

Figure 3.11: Origin of the "dead zone" for non-Bragg-Brentano detector pixels

Another problem is that in the case of an off-center detector pixel, there is no straightforward connection between χ, ϕ and α,β anymore. We can see that in figure 3.11, even though $\phi = 0$ and $\chi = 0$, the crystallographic plane with $\alpha = 0$ and $\beta = 0$ would not have its reciprocal lattice point on the diffraction vector. On the figure, we can estimate that a plane with $\alpha = 5°$ and $\beta = 90°$ would in fact have the right orientation to be detected by the detector pixel. It is clear that the relation between the motor angles χ and ϕ and the orientation angles α and β has become more complex and depends on the orientation of the detector vector.

The use of an array of X-ray detectors, either as line or area detectors, is not new, but the amount of information in literature is remarkably limited. Heizmann et al. [21] investigated the simultaneous measurement of several X-ray pole figures

using multiple detectors, as well as Wcislak and Bunge [22, 23], however, the proposed relations between χ, ϕ and α, β do not agree with one another, and only limited information is available in the papers on the method they used to get to those results. For this reason, a detailed calculation based on the representation of rotations with matrices will be made in the following paragraphs.

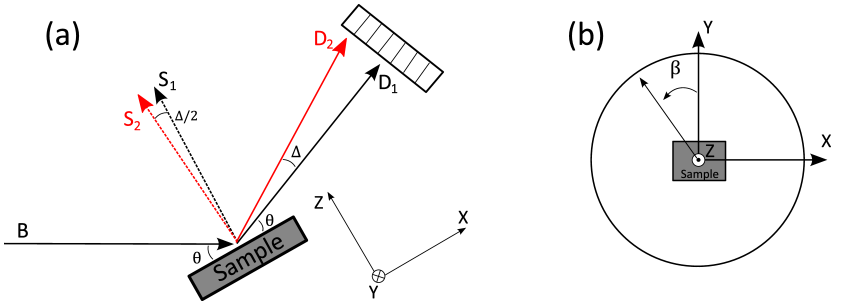

Figure 3.12: Schematic view of diffractometer, vectors and axes

Figure 3.12a shows a schematic cross section of the diffractometer setup perpendicular to the θ rotation axis and through the linear detector. One can see the sample, being hit by the beam B. The directions of two detectors D_1 and D_2 are indicated, and D_1 is assumed to be the center of the linear detector, corresponding to the traditional θ-2θ setup. The resulting diffraction vector for D_1 is called S_1 and is perpendicular to the sample holder.

A second detector pixel D_2 of the linear detector is also considered, and the angle between this detector pixel and the central detector pixel D_1 is Δ. As a result of this, the corresponding diffraction vector S_2 is titled back over an angle $\frac{\Delta}{2}$ with respect to S_1. An orthonormal basis (X,Y,Z) is introduced, where the Z-axis coincides with the S_1 diffraction vector, normal to the sample holder, and thus coinciding with the ϕ rotation axis. The X-axis is defined as lying within the plane of the drawing (i.e. going through the Z-axis and the linear detector) making it coincide with the χ rotation axis, and the Y-axis is then added as going within the paper, perpendicular to both X and Z, to result in a right-handed, orthonormal basis. This Y-axis then corresponds to the θ-2θ rotation axis as well.

In figure 3.12b, a view along the Z-axis towards the sample is shown. The (arbitrary) choice of the starting position of the β angle is defined as the angle with the Y-axis. The α angle is still defined as the angle with the Z-axis. A plane normal with direction specified by α and β will thus have cartesian coordinates:

$$N_1 \quad = \quad (-\sin\beta\sin\alpha, \cos\beta\sin\alpha, \cos\alpha)$$

We will only measure its diffracted intensity in detector D_1 if we can rotate this plane normal N so that it coincides with diffraction vector S_1. From figure 3.12b, one readily obtains that a ϕ-rotation (Z-axis) of $-\beta$, followed by a χ-rotation (X-axis) of α accomplishes this.

If we normalize all vectors to unit vectors, we get the following coordinates:

$$\begin{aligned} B &= (\cos\theta, 0, -\sin\theta) \\ D_1 &= ((\cos\theta, 0, \sin\theta) \\ D_2 &= ((\cos(\theta+\Delta), 0, \sin(\theta+\Delta)) \\ S_1 &= (0,0,1) \\ S_2 &= (-\sin\frac{\Delta}{2}, 0, \cos\frac{\Delta}{2}) \end{aligned}$$

The aforementioned rotation can then be expressed as:

$$\underbrace{\begin{bmatrix} 1 & 0 & 0 \\ 0 & \cos\alpha & -\sin\alpha \\ 0 & \sin\alpha & \cos\alpha \end{bmatrix}}_{\chi \text{ rotation}} . \underbrace{\begin{bmatrix} \cos\beta & \sin\beta & 0 \\ -\sin\beta & \cos\beta & 0 \\ 0 & 0 & 1 \end{bmatrix}}_{\phi \text{ rotation}} . \underbrace{\begin{bmatrix} -\sin\beta\sin\alpha \\ \cos\beta\sin\alpha \\ \cos\alpha \end{bmatrix}}_{\text{plane normal}} = \begin{bmatrix} 0 \\ 0 \\ 1 \end{bmatrix} = S_1$$

This indeed rotates the plane normal onto the diffraction vector S_1. When applying this rotation, a different plane normal N_2 will have been rotated onto S_2. If we consider a general ϕ and χ rotation, we can obtain the cartesian coordinates of N_2 using the orthogonality of the rotation matrices:

$$\begin{bmatrix} 1 & 0 & 0 \\ 0 & \cos\chi & -\sin\chi \\ 0 & \sin\chi & \cos\chi \end{bmatrix} . \begin{bmatrix} \cos\phi & -\sin\phi & 0 \\ \sin\phi & \cos\phi & 0 \\ 0 & 0 & 1 \end{bmatrix} .N_2 = S_2$$

$$\Updownarrow$$

$$N_2 = \begin{bmatrix} \cos\phi & \sin\phi & 0 \\ -\sin\phi & \cos\phi & 0 \\ 0 & 0 & 1 \end{bmatrix} . \begin{bmatrix} 1 & 0 & 0 \\ 0 & \cos\chi & \sin\chi \\ 0 & -\sin\chi & \cos\chi \end{bmatrix} .S_2$$

$$\Updownarrow$$

$$N_2 = \begin{bmatrix} -\cos\phi.\sin\frac{\Delta}{2} + \sin\phi.\sin\chi.\cos\frac{\Delta}{2} \\ \sin\phi.\sin\frac{\Delta}{2} + \cos\phi.\sin\chi.\cos\frac{\Delta}{2} \\ \cos\chi.\cos\frac{\Delta}{2} \end{bmatrix}$$

Going back to the representation in spherical coordinates, one then gets:

$$\alpha = \arccos(\cos\chi.\cos\tfrac{\Delta}{2})$$
$$\beta = \arctan 2\left[\cos\phi.\sin\tfrac{\Delta}{2} - \sin\chi.\sin\phi.\cos\tfrac{\Delta}{2}, \sin\phi.\sin\tfrac{\Delta}{2} + \sin\chi.\cos\phi.\cos\tfrac{\Delta}{2}\right]$$

which indeed reduces back to:

$$\alpha = \arccos(\cos\chi) = \chi$$
$$\beta = \arctan 2\left[-\sin\chi.\sin\phi, \sin\chi.\cos\phi\right] = -\phi$$

for the case $\Delta = 0$, i.e. the central pixel of the detector.

These equations show how to calculate the orientation of the plane normal that will cause the diffracted intensity in a detector of the linear array, when the diffractometer is in a specific χ and ϕ position. For the case $\Delta > 0$ they corresponds to those provided in [21], which where however found to be incorrect when $\Delta < 0$. In addition, the method using rotation matrices makes it easy to extend the reasoning to area detectors, as pointed out in [24].

3.3.4 Irradiated area

The area of the sample that gets irradiated by the X-ray beam depends on the beam size, but also on the orientation of the sample with respect to this beam. Because this area has an influence on the statistics (i.e. the larger the area, the more grains will be sampled), and can cause problems when the irradiated area becomes bigger than the sample, resulting in the irradiation of the sample holder which will introduce spurious diffraction in the recorded data, one needs to get an idea of the size of this area.

If one considers a beam of width w and height h, one can introduce the vectors $A_1 = (0, w, 0)$ and $A_2 = (h.\sin\theta, 0, h.\cos\theta)$, both perpendicular to the beam vector B. The sample initially has its normal N located at $(0, 0, 1)$, but a ϕ, χ rotation brings this to the $N = (0, -\sin\chi, \cos\chi)$ orientation. The irradiated area of the sample is now determined by the projection of the A_1 and A_2 vectors onto the sample, along the beam direction B, resulting in the $A_{1,p}$ and $A_{2,p}$ vectors:

$$A_{1,p} = A_1 + k_1.B \text{ with } A_{1,p} \circ N = 0 \Rightarrow k_1 = \frac{-A_1 \circ N}{B \circ N} = -\frac{w.\tan\chi}{\sin\theta}$$

$$A_{2,p} = A_2 + k_2.B \text{ with } A_{2,p} \circ N = 0 \Rightarrow k_2 = \frac{-A_2 \circ N}{B \circ N} = h.\cot\theta$$

One obtains in components:

$$A_{1,p} = w.(-\cot\theta.\tan\chi, 1, \tan\chi) \Rightarrow |A_{1,p}| = w.\sqrt{1+\tan^2\chi.(1+\cot^2\theta)}$$

$$A_{2,p} = h.(\frac{1}{\sin\theta}, 0, 0) \Rightarrow |A_{2,p}| = \frac{h}{\sin\theta}$$

The area of the irradiated sample is then:

$$S = |A_{1,p} \times A_{2,p}| = \frac{w.h}{\cos\chi.\sin\theta}$$

The obtained relation for the irradiated area is plotted in figure 3.13, and shows that for low θ and high χ angles, the irradiated area can become very large, making it important to work with a sufficiently large sample.

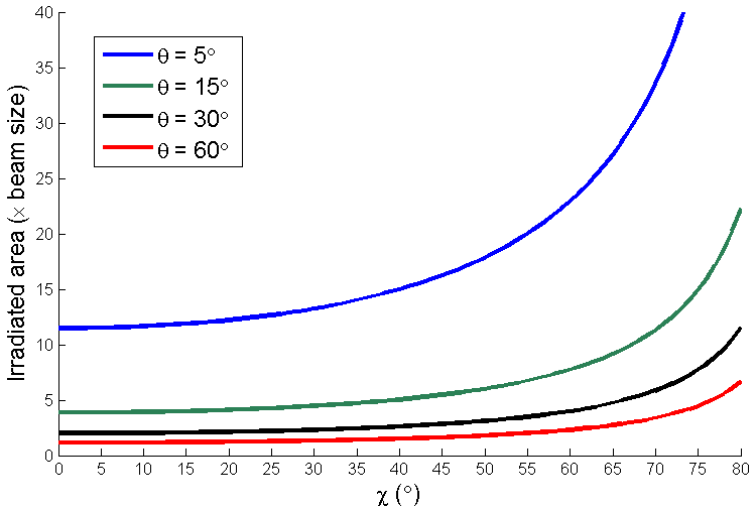

Figure 3.13: Size of the irradiated area of the samples as a function of χ, for different θ values.

3.3.5 Irradiated volume

The intensity of a diffraction peak is significantly influenced by the amount of material contributing to the diffraction, i.e. the irradiated volume. In a thin film, there is a significant influence of the film thickness and the direction of the incoming

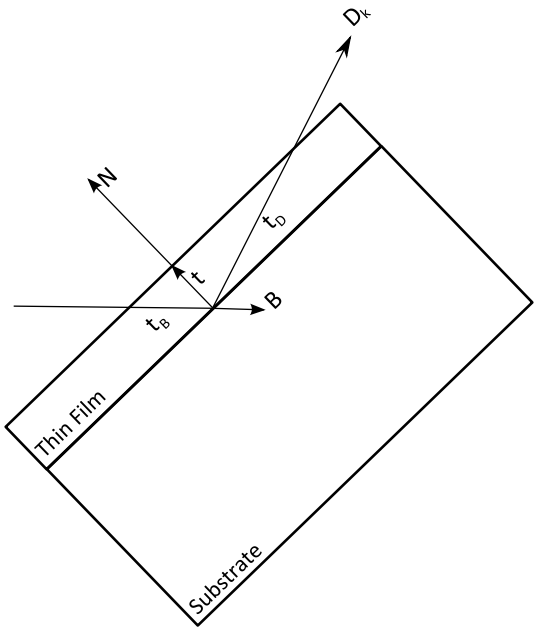

Figure 3.14: Effect of layer thickness (t) on the distance the incoming beam travels through the layer (t_B) as well as the diffracted beam going towards the detector pixel (t_D). For the sake of simplicity, t, t_B and t_S are drawn in the same plane, but in general this is not the case.

X-ray beam on this volume, which is for example exploited in the case of grazing incidence geometry to increase the contribution of the thin film to the signal.

In figure 3.14, a schematic cross section of a thin film with thickness t is shown, as well as the incoming and diffracted beam. The length of the path that the incoming or diffracted beam travels through the film (t_B and t_D) is clearly dependant on the orientation of the sample (defined by the sample normal N). One obtains for these lengths:

$$t_B = -\frac{t}{N \circ B} = \frac{t}{\sin\theta . \cos\chi}$$

$$t_D = \frac{t}{N \circ D_k} = \frac{t}{\sin\Delta + \theta . \cos\chi}$$

In the previous section, the projected beam vectors $A_{1,p}$ and $A_{2,p}$ where calculated and the total irradiated volume can then be calculated using the mixed product with gives the volume of the parallelepiped described by t_B, $A_{1,p}$ and $A_{2,p}$:

$$V = |t_B \circ (A_{1,p} \times A_{2,p})| = t.w.h$$

Rather surprisingly, there is no dependence on the geometry or orientation of the sample. However, even though the irradiated volume is always the same, the intensity that arrives at different parts of this volume is not constant, because the X-rays are also absorbed when passing through the film. In the same way, diffracted intensity will be partially absorbed on its way out of the sample towards the detector.

If we split up the total volume in small slabs of thickness ds (along the beam), then the intensity that arrives at such a slab (with volume $ds.w.h$) after the beam has travelled a distance s through the film is $I = I_0.\exp(-\mu.s)$. The produced diffracted intensity in this slab is then $I_D = F.I_0.\exp(-\mu.s)$ (with total structure factor F), which still needs to leave the sample and which will cause absorption. Since the slab is located at a distance s along the beam, beneath the surface, the relation between the layer thickness t, and the t_B / t_D distances can be used to calculate the absorption of the diffracted intensity. One obtains:

$$I_D = F.I_0.\exp(-\mu.s).\exp(-\mu.s.\frac{\sin\theta}{\sin(\Delta+\theta)})$$

The total diffracted intensity $I_{D,t}$ can be obtained by integrating over the whole layer, i.e. $s = 0...t_B$:

$$I_{D,t} = \int_0^{t_B} F.I_0.\exp(-\mu.s).\exp(-\mu.\frac{\sin\theta}{\sin(\Delta+\theta)}.s)\,\mathrm{d}s$$

$$= F.I_0.\frac{\sin(\theta+\Delta)}{\mu.(\sin(\theta+\Delta)+\sin\theta)}.\left(1-\exp\left[-\frac{\mu.t.(\sin(\theta+\Delta)+\sin\theta)}{\sin(\theta+\Delta).\sin\theta}.\frac{1}{\cos\chi}\right]\right)$$

For a point detector, $\Delta = 0$, one obtains the simplified expression:

$$I_{D,t} = F.I_0.\frac{1}{2\mu}.\left(1-\exp\left[-\frac{2.\mu.t}{\sin\theta}.\frac{1}{\cos\chi}\right]\right)$$

In figure 3.15, $\frac{I_{D,t}}{F.I_0}$ is plotted for a nickel film and Cu k-α radiation (μ= $401/mm$), showing the influence of the layer thickness and the effect for the non-central detector pixels ($\Delta \neq 0$). The color scale is logarithmic with base 2, so that an increase of 1 unit corresponds to a double X-ray intensity. Contour lines indicate this doubling of intensity. The absorption effect is most outspoken in the cases where θ is small and χ is large, i.e. in grazing incidence geometry. This can increase the intensity by 2^6. The dependence on the Δ angle is smaller, but as Δ is increasing, an increase in intensity is observed for small θ and large χ angles, while the reverse is true for large θ and small to medium χ angles.

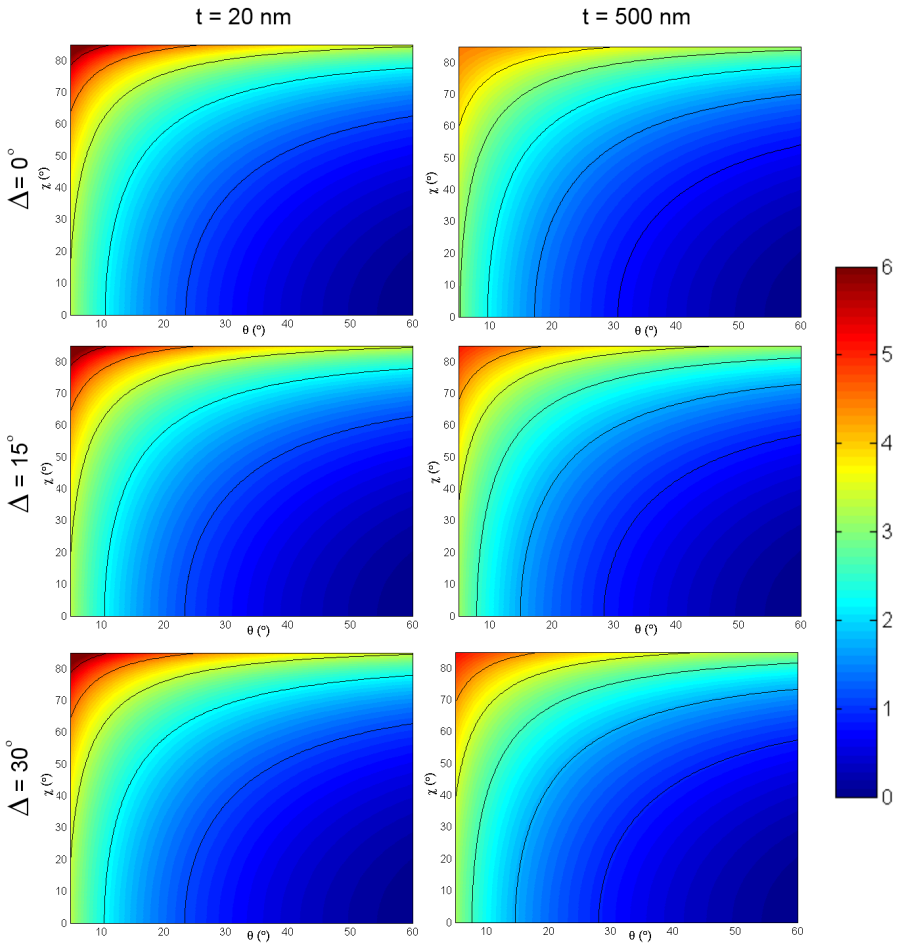

Figure 3.15: $\frac{I_{D,t}}{F.I_0}$ *for 20 nm and 500 nm nickel films and* $\Delta = 0, 15 or 30°$.

3.3.6 Defocusing

In a lab based setup, the X-rays originating from an X-ray tube do not consist of a perfectly parallel bundle, but have a slight divergence. In addition, the bundle often has a considerable spectral width and does not correspond to an ideal point source, but has a specific size. These factors contribute to the defocusing of the diffracted X-rays, which means that the diffracted intensity is spread out in a region around the 2θ value.

When using a synchrotron source, the defocusing is much lower because both the divergence of the beam and the spectral width can be orders of magnitude lower. There is still an effect of the finite X-ray source area, because the irradiated area depends on this, as was pointed out in the previous section. This also determines the width of the diffracted X-ray beam.

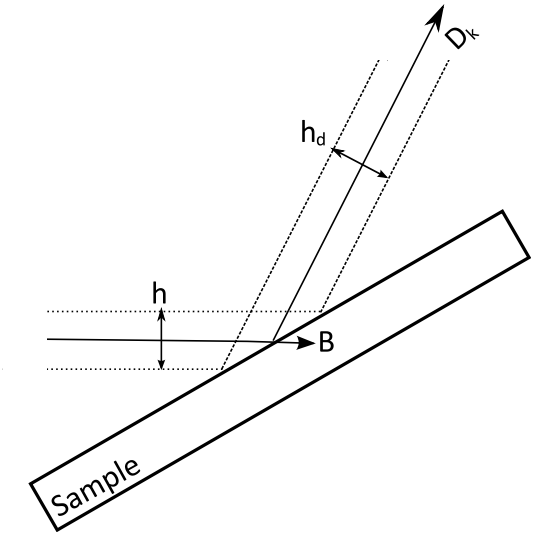

Figure 3.16: Defocusing effect due to finite beam size

In figure 3.16, a schematic side view of the beam interacting with the sample and producing the diffracted beam is shown. Here, only the "height" h of the beam is considered, i.e. the size of the beam along the A_2 vector. Projected onto the sample, one obtained the $A_{2,p}$ vector. If one considers diffracted intensity produced in the D_k detector direction, the "height" h_d of this beam can be calculated as:

$$h_d = |A_{2,p} \times D_k| = \frac{h.\sin(\theta + \Delta)}{\sin\theta}$$

For the case $\Delta = 0$, one observes $h = h_d$. This corresponds to the Bragg-Brentano geometry where no peak broadening from the setup is expected. On the other hand, for $\Delta > 0$, the beam gets wider, resulting in a reduction of the 2θ resolution. For $\Delta < 0$, the beam gets more focussed. This is presented in figure 3.17 for various θ values.

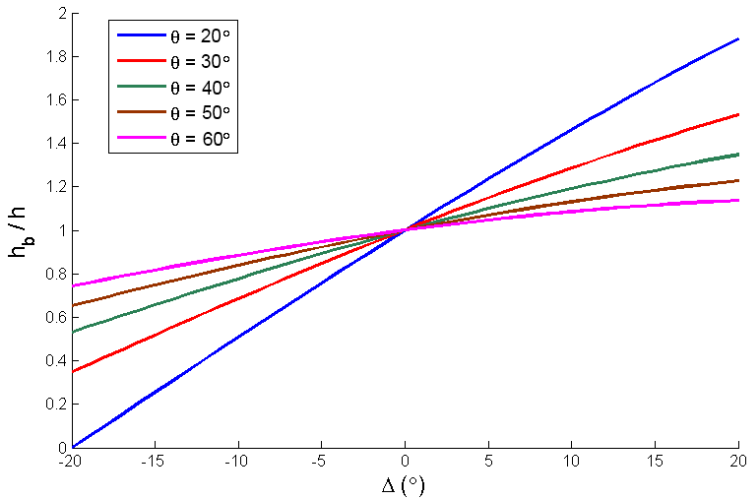

Figure 3.17: Defocusing effect in a linear detector.

3.4 Peak broadening due to size effects in thin films

In thick samples with large grains, X-ray diffraction can be described as Bragg reflection on crystal planes, because the corresponding reciprocal space image of the crystal planes in these samples contains only very well defined spots, due to the large number of these crystal planes and their lateral extension, resulting in periodicity over a large volume. However, in the case of thin films, both the limited thickness of the films, as well as the small grain sizes, make this view inappropriate. In figure 3.18, the combinations of large/small grain sizes and think/thick films on the reciprocal space image is represented. For the case of a thick film with large grains, one observes a spots in reciprocal space. The distance of this spot to the origin determines the 1/d value and its location corresponds to the orientation of the plane normal. One can observe that for a thick film with large grains, diffracted intensity will be observed for only one 2θ, χ,ϕ combination.

When the layer gets thinner, i.e. the dimension along the periodicity of the plane stacking gets smaller, one obtains a line shaped peak, going through the origin of

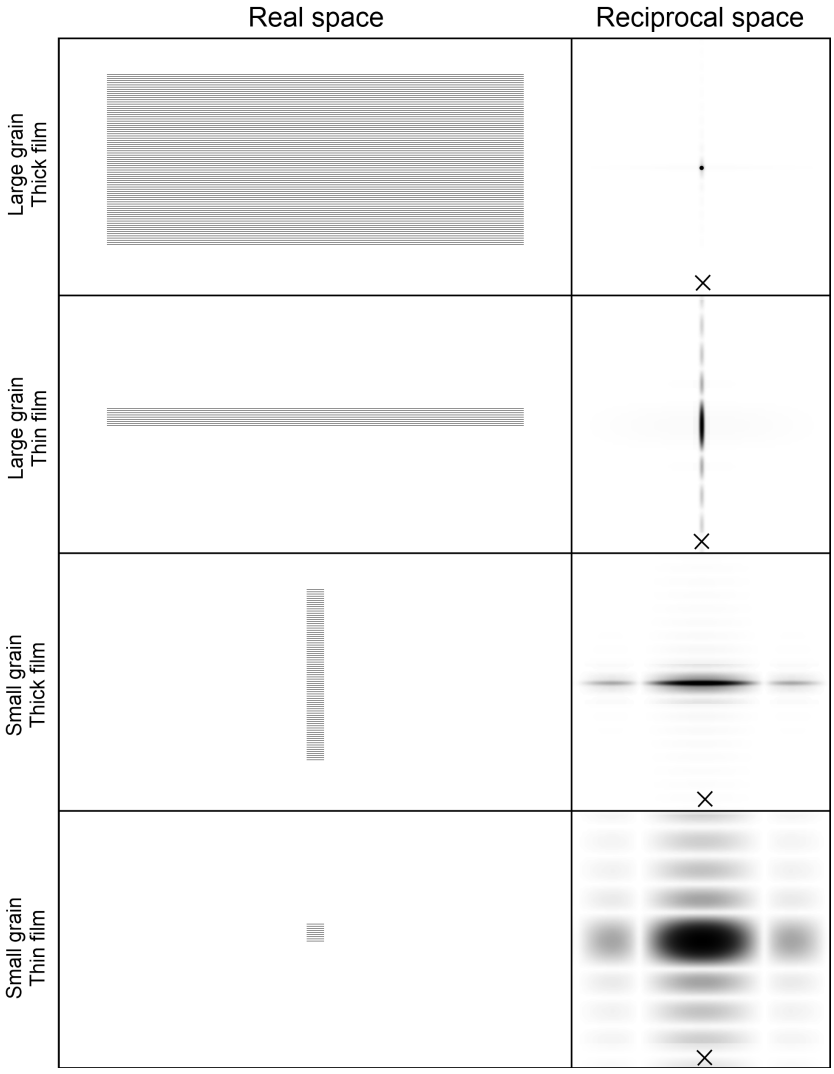

Figure 3.18: Effect of layer thickness and grain size on the peak shape (of 1 selected peak) in reciprocal space, calculated for 1 step of planes. X marks the origin of the reciprocal space.

the reciprocal peak. This corresponds to the peak broadening in 2θ typical for thin films. However, the peak is still located at one χ,ϕ locations.

One the other hands, if the dimension perpendicular to the periodicity get smaller, as in the case of very small, columnar grains in a thick films, one observes a line shaped feature in reciprocal space, perpendicular to the plane normal. This results in a more complicated diffraction image when collecting pole figures, as each point on this line corresponds to a different 2θ, χ,ϕ triplet.

If both the film thickness and the grain size are small, the reciprocal space image becomes a broad blob and one observes a high intensity region in the pole figures in a large 2θ interval.

It is important to remark that the examples of thin/thick films and small/large grains are just examples, and that it would be better to describe the length scales along or perpendicular to the periodicity of the planes. This is very clear when one considers a thin, but large grain: if one is investigating diffraction by crystal planes that are aligned parallel to the interface, only a limited number of these planes will be stacked due to the limited film thickness, but their lateral extension will be large. On the other hand, in the same grain, planes that are perpendicular to the interface can also exist, but in this case, the lateral extension of the planes is limited by the layer thickness, while the number of stacked planes will be very high, and one obtains the reciprocal space image of the small grain/thick film example. As the planes parallel to the interface are measured at $\chi = 0°$, and those perpendicular at $\chi = 90°$, diffraction spots of the same grain can have a dependence on χ in the pole figure.

3.4.1 Practical aspects of pole figure collection using a linear detector

We have established that the data coming out of the linear detector needs some processing before it can be interpreted. If, for every detector pixel, we know the angle it makes with the central pixel, we can use the correction equations from the previous sections. In practice, this angle is determined by sweeping a narrowly focused beam through the detector pixels. For example, one can use a diffraction peak of a well aligned single crystal, and move all of the detector pixels through this diffraction peak by changing the 2θ motor position, resulting in a *calibration* scan.

Based on this calibration scan, and a log file providing the read-out of the linear detector for every χ,ϕ motor position, one can then calculate the pole figures. In the context of this thesis, a Python program was developed for this goal, which outputs the pole figures either as individual pole figure files, or as pole figure *movies*,

where the displayed d-spacing is changing as a function of the running time. This provides a quick overview of the data. Based on the data, the program can also calculate a simulated powder diffraction scan: by discarding the orientation information and summing all of the collected intensity for one detector pixel, one ends up with a signal as function of the 2θ values of the detectors, which is no longer influenced by the texture of the sample. This is an easy way to do phase identification based on powder diffraction reference data. However, a phase that occurs as a relatively small volume fraction might not be visible in this calculated powder diffraction spectrum as the statistical noise ($\sqrt{n}$) might be higher than the signal coming from this phase. This is especially true if the phase occurs in a small amount and is epitaxial. This results in a small number of sharp peaks, with low intensity due to the limited amount of material in the phase, but still distinguishable from the *local* statistical noise in the pole figure. However, by adding all of the intensity in the pole figure to get the corresponding simulated powder diffraction intensity, the total number of count increases proportionally to the number of data points in the pole figure, while the signal from the epitaxial phase only increases by the amount of peaks it has in the pole figure. The signal-to-noise ratio thus changes by a factor $\frac{M}{\sqrt{N}}$, with M the multiplicity of the epitaxial peak in the pole figure, and N the number of data points. In general, N is much larger than M^2, resulting in a significantly lower signal-to-noise level.

The resulting pole figure data can then be analyzed using the same techniques used for pole figures recorded with a point detector, e.g. the GUSTAV software, which will be described in chapter 5.

3.4.2 Mapping of the reciprocal space

In the previous sections, the technique of recording pole figures as a way to study texture has been described. It was shown how the use of an array of detectors, i.c. a linear detector, can significantly speed up the acquisition and even provide much more information. Still, the approach was to use the linear detector to collect more pole figures and analyze them separately.

However, as the linear detector setup samples whole lines in reciprocal space, we can skip the conversion of the data to pole figures and analyze the results directly in reciprocal space. This has the advantage that effects which are typically not visible or difficult to analyze on pole figures, become much more clear. For example, the effect of small grain sizes and the thickness of the layer is clear, as it has a direct correlation to the size and shape of the corresponding reciprocal space features. Additionally, defects in the crystalline structure often also have a very specific signature in the reciprocal space, extending the scope of the measurement technique beyond just phase and texture identification.

The main problem with this technique is the availability of data-analysis techniques. Recently, a collection of Matlab routines has been developed by S. Gaudet [25, 24] which provides a series of tools to help with this. In this thesis, the data is still analyzed using the traditional pole figure analysis techniques.

3.5 Transmission Electron Microscopy

Transmission Electron Microscopy (TEM) uses a well focused electron beam to probe a thin sample. The interaction of the electron beam with the local crystal lattice will result in diffraction. Techniques such as selected area diffraction (SED) or convergent beam electron diffraction (CBED) allow both local phase and orientation determination. In addition, Kikuchi lines can be generated in a TEM as well, which, similarly to EBSD, allow for the determination of the local orientation.

While the unique high spatial resolution of TEM sets it apart from the other techniques for nano-scale materials, this advantage also has a drawback: the statistical reliability of claims regarding texture, based on *only* TEM measurements is low: because only a handful of grains can be measured in reasonable time, a material with a complex texture will only be partially characterized. To make reliable claims concerning the global texture of a sample, a complementary technique such as EBSD or X-ray diffraction should be used.

3.6 Neutron Diffraction

In neutron diffraction, a high intensity source of neutrons is used and is allowed to interact with the crystal lattice of a sample. Just as was the case with X-rays, the resulting diffracted intensity will provide phase and texture information. The main advantage of neutrons is their high penetration depth. For large bulk samples, this makes it possible to get reliable information on the whole volume of the sample. In addition, neutron diffraction has, compared to X-rays, different interaction cross sections for most elements. Especially for light elements, it can provide information which cannot be obtained with X-rays. For thin films, it is seldom used, because the interaction with the limited amount of material in the film is far too low. In addition, the need for a high intensity neutron source makes access to this technique much more difficult than lab-based X-ray sources or even synchrotron facilities.

3.7 Summary

In this chapter, an overview of the most common techniques to measure texture was presented. It is clear that two of these techniques, EBSD and X-ray diffraction, are especially suited for the measurement of texture in thin films, which is why these techniques were given special attention in this chapter. The method of using multiple X-ray detectors (i.c. a linear detector) for the simultaneous recording of multiple pole figures, or for a full reciprocal space mapping, was discussed, and the relation between the diffractometer reference frame (χ and ϕ angles) and the sample reference frame (α and β) was established.

4

Visualization of texture data

The texture or microstructure of a material concerns the grain orientations that occur in this material. A measurement of the texture typically results in a large data set containing a numerical description of these orientations. To be able to interpret the data, it is necessary to get a clear and concise representation of this data. In this chapter, a number of these representations will be discussed, with the focus of orientation maps and pole figures, as these are the most common ways to display respectively EBSD and X-ray diffraction data. The Rodrigues-Frank visualization will be discussed in detail, showing its advantages and particularities when used to display the texture of thin films on single crystal substrates.

4.1 Orientation maps

An orientation map, which displays the texture information as a function of the location where it was measured, provides the most straight forward and complete representation of the microstructure of a material. It is a function $f(x, y, ...) \rightarrow (R, G, B)$ which depends on the position of the measurement within the sample and which associates with every orientation a unique color. Because the orientation of a crystal is defined by three degrees a freedom, a unique relation between orientation and color can be defined. Typically, the three degrees of freedom for the orientation are chosen to be the Euler angles, and these three angles are con-

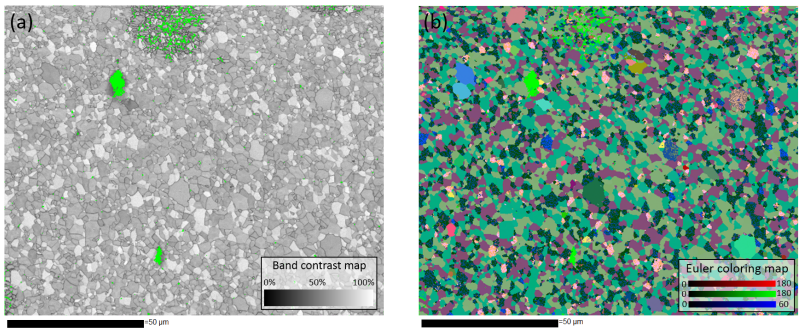

Figure 4.1: Orientation map of θ-nickel-silicide on Si (100). Figure (a) shows a band contrast map, clearly showing the individual grains. Figure (b) is using Euler coloring, showing that the largest part of the film consists of grains with only 4 different orientations.

verted to red, green and blue intensities, which combined make up a unique color. Evidently, alternative mappings between texture information and color can be defined as information in addition to, or replacing the Euler angles can be used, e.g. local crystallinity or the chemical composition.

In the case of data obtained from an EBSD measurement, all of the information needed to produce an orientation map is readily available, since for each EBSP, the location of the electron beam was recorded, and the analysis of the EBSP resulted in the determination of the local crystal orientation, which was stored as the three Euler angles. In addition to this, information such as goodness-of-fit or band contrast of the EBSP is typically stored as well. In particular, the band contrast, which quantifies the contrast in the EBSP and which is high for a good quality EBSP, is a fast and reliable way to get a first estimate of grain size. Because the contrast is high when the electron beam is hitting only one grain - all of the backscattered electrons then contribute to one single diffraction pattern - and this contrast becomes much lower when hitting a grain boundary, due to the lower local crystallinity and the convolution of EBSP's from neighbouring grains, there is a clear difference in signal between grain and grain boundary. Two examples of orientation maps, obtained on a thin film of θ-nickel-silicide, are displayed in figure 4.1. The first one shows an orientation map, showing band contrast, while the second one is using Euler coloring.

Data obtained from X-ray diffraction does not lend itself to being displayed as orientation maps. The spot size of the X-ray beam is typically much larger than the grain size in thin films, which results in a loss of spatial information. As spot sizes of X-ray beams become smaller and smaller in the new generation synchrotrons, it might become feasible to do microdiffraction on thin films with grain sizes in the order of tens of nanometers. However, during the time the research described in

this thesis was carried out, no such setups were available.

4.2 Pole figure

A pole figure is a statistical representation of the orientation distribution of one specific family of crystal planes. An easy way to visualize this, is shown in figure 4.2a, where a sample is positioned in the center of a sphere and its grains have been given individual colors. One specific family of crystal planes is chosen, e.g. $\{100\}$, and for every grain in the sample, the orientation of these crystal planes is identified. The plane normals of these crystal planes are then determined and the intersections of the plane normals with the sphere are marked. After this has been carried out for all of the grains, the density of markings on the sphere is converted to a color or gray scale. This sphere is projected onto a flat surface. This projected image, which has the shape of a disc, is the pole figure.

An example of these different steps is shown in figure 4.2, where for the sake of simplicity, no symmetry (i.e. space group 1) is assumed, so that the $\{100\}$ family of planes consists only of the (100) planes, and each grain only has one plane normal associated with $\{100\}$. If the symmetry is higher, every grain will cause multiple spots to appear on the pole figure, e.g. one for each plane of the list (100), (010), (001).

As there are multiple ways to project a sphere onto a disc, one needs to specify the choice one makes. In practice, the stereographic and the equal area projection are most often used. In the stereographic projection, one uses a projection plane through the center of the sphere. A point on the sphere is then projected onto this plane, by connecting the point on the sphere with the south pole of the sphere. The intersection of this line with the projection plane gives the location of the projected point. If one defines the location on the sphere using spherical coordinates, with α the angle with respect to the Z-axis through the pole, and β the angle in the XY-plane, one can define the relation between the spherical coordinates of a point on the sphere, and the polar coordinates ρ, θ of the projected point on the disc as:

$$\begin{aligned} \rho &= tan\frac{\alpha}{2} \\ \theta &= \beta \end{aligned}$$

While the stereographic projection is angle preserving, its disadvantage is that, in case the distribution of poles on the sphere is uniform, the projected distribution does not reflect this and the pole figure will have a non-uniform intensity. This

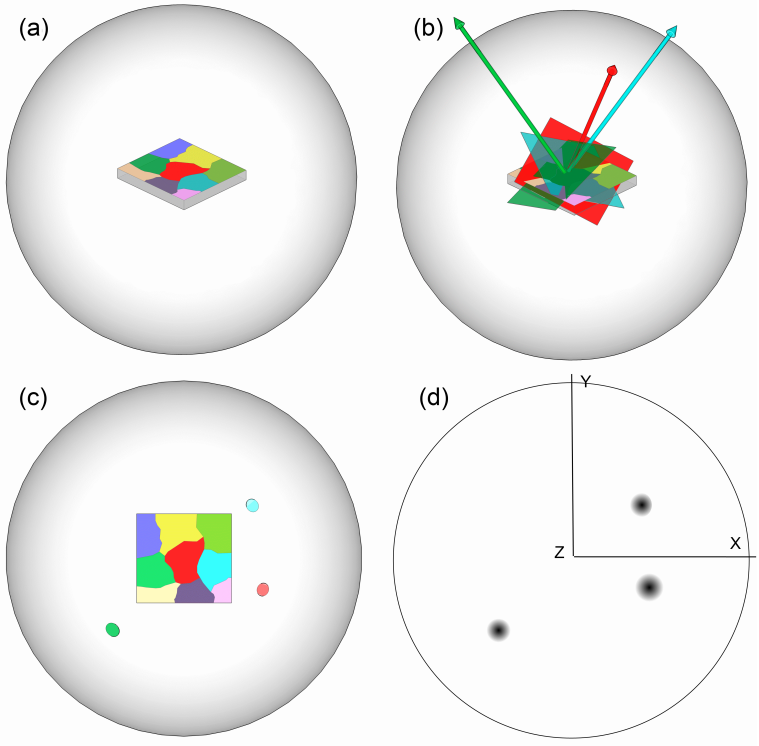

Figure 4.2: Construction of a pole figure, showing (a) the sample in a sphere, (b) the orientation of the plane normals, (c) the intersection of these normals with the sphere and (d) the resulting pole figure.

can give the impression of the occurrence of a non-random texture, even though in reality, the sample has a random texture distribution. Another commonly used projection is the equal area projection, which does not have this problem. Here, the distance from a point on the sphere to the north pole of the sphere is used as the value for ρ on the pole figure, so one gets:

$$\begin{aligned} \rho &= sin\frac{\alpha}{2} \\ \theta &= \beta \end{aligned}$$

This equal area projection will result in a uniform intensity on the pole figure, if there is a uniform distribution on the sphere, and is therefore preferred if one wants to make statistically relevant conclusions. It lack of angle preservation is in most cases of less importance.

The description of the projections in the previous paragraphs is only valid if one is projecting the upper half sphere onto the projection plane, however, nothing was said about the lower half sphere. The most commonly used techniques to measure pole figure data are X-ray and neutron diffraction and will automatically result in the appearance of centrosymmetry in the data, so both the upper and lower half sphere will be identical. If one would use a technique that does not destroy the non-centrosymmetry of a material, one could project both halves on two different pole figures, and display this pair of pole figures.

The orientation of a grain is always defined in respect to a reference frame, so the choice of the reference frame will influence the visual appearance of the pole figure. A different choice of the reference frame will lead to a rotation of the sphere, or alternatively, will lead to the choice of a different projection plane to project the colored sphere onto.

Pole figures are often used to display X-ray diffraction data collected using the Schulz method, as this method measures the diffracted intensity caused by one family of crystal planes, as a function of the orientation of the plane. This corresponds exactly with the definition of a pole figure. In practice, there are some additional aspects that can influence the diffracted intensity, such as a change in irradiated volume, absorption of X-rays in the sample and changes in the background signal due to a change in geometry or fluorescence of the sample. In some cases, these influences can be corrected for, however in many publications, one will find the raw diffraction data plotted. If the analysis is limited to a qualitative analysis, this presents no problems. For a reliable quantitative determination of the texture, these aspects need to be taken into account.

From an EBSD measurement, one can construct the orientation matrix for every

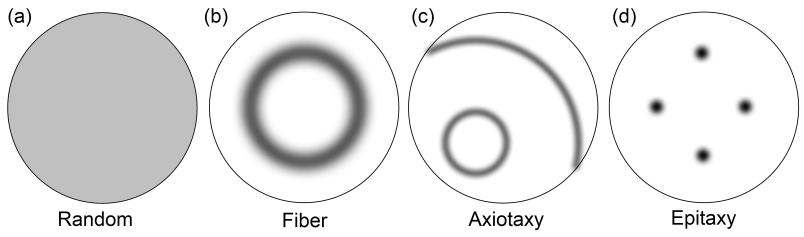

Figure 4.3: Pole figures for typical thin film textures: (a) random texture, (b) fiber texture, (c) axiotaxy, (d) epitaxy

data point, and based on the unit cell of the phase, the orientation of the plane normals can easily be calculated. Using the technique described in the previous paragraphs, one can thus calculate a pole figure from the EBSD data.

4.2.1 Pole figures for thin film textures

As pointed out in chapter 2, texture in thin films typically consists of a combination of 4 fundamental types: random, fiber, axiotaxy and epitaxy. As many of the samples investigated for this thesis exhibit a complex combination of these types, it is useful to first establish the signature of these basic components in the pole figures.

A random texture corresponds to a uniform distribution of the grain orientations. This means that, when looking at a specific plane normal orientation, every possible orientation in space will have the same probability. The pole figure sphere will thus have a uniform density distribution, which is translated into a pole figure of one single uniform color if one used the equal area projection. An example of such a pole figure can be seen in figure 4.3a.

When looking at a sample which exhibits a fiber texture, we have to distinguish between 2 possibilities. A fiber texture is defined by the constraint that one plane normal in all of the grains is perpendicular to the interface, so this specific plane normal has only one possible orientation and we get one single spot of high intensity on the pole figure sphere, which translates to one single spot on the projected pole figure. In general, the reference frame of the pole figure is chosen so that the normal to the interface corresponds to the center of the pole figure, and the spot will thus end up here.

For the other plane normals, which do not coincide with the fiber axis, their orientation is not constrained to one single possibility. As the grains in a fiber texture have one rotational degree of freedom about the fiber axis, a specific plane normal

will describe a circle around the fiber axis due to this rotation, resulting in a circular shaped pattern on the pole figure after projection, centered around the fiber axis, which is most commonly the center of the pole figure. This is shown in figure 4.3b.

In practice, most pole figures contain contributions from multiple symmetrically equivalent planes. Therefore, even when the pole figure was collected for the plane normal that coincides with the fiber axis and thus gives rise to a spot in the center of the pole figure, contributions from additional symmetrically equivalent planes will also show up as rings in the same pole figure.

When axiotaxy is present in the sample, the pole figures are similar to the case of fiber texture, as axiotaxy is an off-normal fiber texture. Since it is off-normal, the spot or circle changes location on the pole figure and will coincide or be centered around the off-normal fiber axis (figure 4.3c).

In the case of an epitaxial film, all of the grains have the same orientation, so for any choice of crystallographic plane, the plane normal will have a unique orientation. This leads to one or more spots on the pole figure, as can be seen in figure 4.3d.

4.3 Inverse pole figure

In a pole figure, the orientation of a direction or plane normal of the crystal is visualized in the reference frame of the sample, e.g. the single crystal reference frame in the case of thin films on single crystal substrates. An inverse pole figure reverses the role of the crystal lattice frame and the sample reference frame by giving a visual representation of the probability of finding a direction of the sample reference frame having a specific orientation with respect to the crystal lattice frame. This is particularly useful when one wants to determine a macroscopic property of the sample, e.g. the tensile strength along a specific direction of the sample. In the case of thin films, inverse pole figures are seldom used. While it is in principle possible to directly measure an inverse pole figure using X-ray diffraction, most of the inverse pole figures are calculated, either from EBSD data, or from regular pole figures (by first calculating the ODF, see next section).

As a regular pole figure and an inverse pole figure are so closely related and only differ in the choice of reference frames, the same remarks concerning symmetry and projections apply. In practice however, for a pole figure the whole pole figure is shown, while an inverse pole figure is typically reduced to its “fundamental” zone: only the unique part of the inverse pole figure is plotted (depending on the symmetry of the crystal this can be 1/2, 1/4, 1/8, ...). An example of an inverse

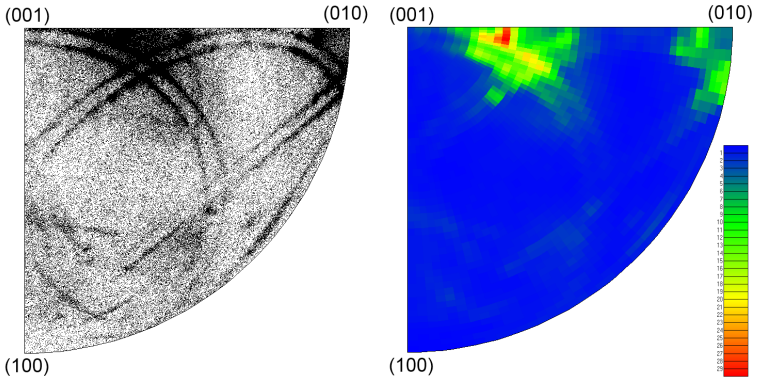

Figure 4.4: Inverse pole figure for 60 nm NiSi on Si(100), calculated from an EBSD measurement. The Si (100) direction (normal to the wafer) is shown in the reference frame of the NiSi crystal lattice. Individual EBSD measurement points are visible on the left, and total intensity is shown on the right.

pole figure calculated from an EBSD measurement on 60 nm NiSi on Si(100) is displayed in figure 4.4. Only the unique 1/4 part of the total inverse pole figure is plotted due to the NiSi symmetry.

4.4 Orientation Distribution Function

Texture is the statistical distribution of the occurrence of grain orientations. We can define a function that gives the probability of finding a grain in a specific orientation $f(G)$ where G is the three-parameter representation of the orientation. This function is called the Orientation Distribution Function (ODF).

While the choice of the parametrization of G is not strictly defined, one will find that in literature the term ODF is almost only used when the Euler angle representation is chosen. In practice, this means that the ODF is defined as a function $f(\phi_1, \Phi, \phi_2)$, depending only on the three Euler angles. If this distribution is properly normalized, so that $\int_\Sigma f(G)\,\mathrm{d}G = 1$, with Σ the whole Euler space and $G = (\phi_1, \Phi, \phi_2)$, then the chance to find a grain within an orientation range ΔG is $p = \int_{\Delta G} f(G)\,\mathrm{d}G$.

The ODF describes the complete texture in the sample. As it is a function that relates a density to a triplet of real numbers, it makes sense to try and visualize this function in 3D: the density is converted to transparency, with complete transparency meaning $f(G) = 0$ and the maximum value of $f(G)$ corresponding to opaque. An example of this can be seen in figure 4.5. In practice, one will often

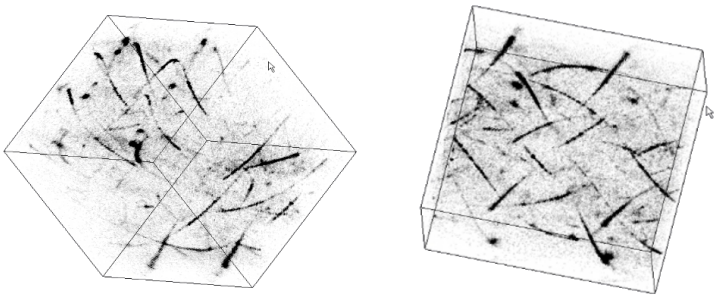

Figure 4.5: Two views of the orientation distribution function of NiSi on Si (100). A combination of higher intensity regions (black) corresponding to epitaxy and curves corresponding to axiotaxy can be observed.

construct planar cuts of the ODF and display these.

The ODF can provide a quick idea of the most important features of the ODF and makes it possible to compare samples, but it is difficult to interpret it on its own for two reasons. First of all, the texture components do not have a well defined shape in the Euler space. Fiber and axiotaxy texture components have 1 intrinsic degree of freedom, which is visible in their representation in the ODF as a line, but this line can have any shape and curvature, which even depends on the choice of the reference orientation. Epitaxy corresponds to a spot in the ODF.

Secondly, it is difficult to represent symmetry in the ODF. Due to the crystallographic symmetry of the film and substrate materials, different triplets of Euler angles can correspond to the same physical grain orientation, so that one texture component can be visible in the ODF multiple times. A symmetry operation that exists in the film or substrate material will thus generate spurious copies of texture components in the ODF. To make interpretation of the ODF straightforward, the reduction of the ODF to a region where the texture components occur only once is necessary. To accomplish this, one has to decide which one of the symmetrically equivalent Euler angle triplets one chooses to represent the physical orientation. The standard choice is choosing the representation which involves the smallest total rotation from the reference orientation. If one carries this out for every possible orientation, one ends up with a region of the ODF which represents all of the physically different orientations only once. While conceptually this sounds easy, in practice it is very difficult due to the definition of the Euler angles. Every symmetry operation will result in the rejecting of part of the ODF, but the 3D surfaces that defines the edges of these parts can have a very complex shape. For the study of thin films on single crystal substrates, where a large number of symmetry elements can occur, this makes the ODF visualization a poor choice.

4.5 Rodrigues-Frank space

The Rodrigues-Frank space [26] is an alternative to the Euler space and is based on the representation of rotations by the Rodrigues vector. Any rotation can be described by a unit rotation axis $N = (N_1, N_2, N_3)$ and the rotation angle θ about this axis. One can combine this into one, non-unit 3D vector:

$$R = (N_1, N_2, N_3).\tan\frac{\theta}{2}$$

This is the Rodrigues vector. All possible Rodrigues vectors describe a space, and when used to represent orientations in materials science, this space is given the name Rodrigues-Frank space, whose origin represents the chosen reference orientation. θ is limited to the range $0^\circ \ldots 180^\circ$ and the Rodrigues-Frank space thus covers the whole $\mathbb{R}^3$ space.

The definition of the Rodrigues vector, using $\tan\frac{\theta}{2}$ as a way to introduce the rotation-angle-dependence into the vector representation might seem arbitrary. Indeed, one can combine the rotation axis and the rotation angle into one vector using many functions of θ, but this specific choice results in some interesting properties of the Rodrigues-Frank space.

A first aspect is that the combination of two rotations can be calculated efficiently. In [27], it is shown that the total rotation R, resulting from a first rotation R_1 followed by a second rotation R_2, is given by:

$$R = \frac{R_A + R_B - R_A \times R_B}{1 - R_A \circ R_B} \tag{4.1}$$

It is immediatly clear that a series of orientations, all related to the reference orientation through a rotation about the same axis but with a different rotation angle, will be represented in the Rodrigues-Frank space as a straight line through the origin, as these orientations are described by the vectors $\lambda.R$. From the combination formula, it also follows that any group of orientations, not including the reference orientation, that can be connected to one another through rotations about the same axis, will also describe a straight line. If we consider a first orientation R_1 and apply the rotation λR_2 to it, with λ any real number, we find:

$$R = \frac{R_A + \lambda.R_B - R_A \times R_B}{1 - \lambda.R_A \circ R_B} \tag{4.2}$$

Reordering leads to:

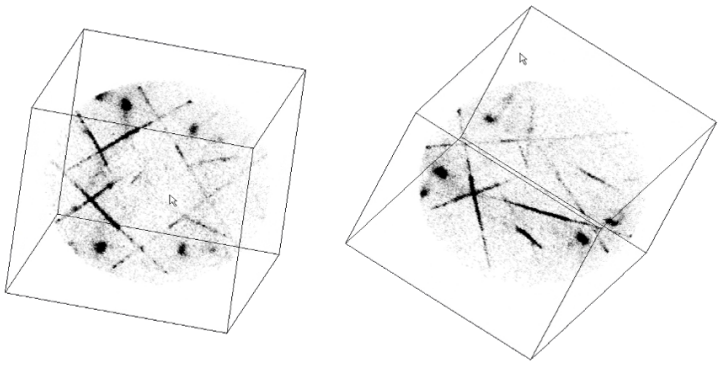

Figure 4.6: Example of the Rodrigues Frank space showing the texture of NiSi on Si (100). Straight lines in black corresponding to axiotaxy and spots corresponding to epitaxy can be observed.

$$R = R_A + \frac{\lambda}{1 - \lambda . R_A \circ R_B} . (R_A \circ R_B R_A + R_B - R_A \times R_B) \qquad (4.3)$$

This is the parametric equation of a straight line, through R_A, as the second part of the formula is just a real number times the direction vector of the line.

The consequence of this is that fiber and axiotaxy texture components will be immediatly recognizable as straight lines if one visualizes the Rodrigues-Frank space. Epitaxy will be visible as a small dot, just as was the case for the ODF.

The second advantage of the Rodrigues-Frank space becomes clear if we consider the effect of the symmetry operations that exist in the crystal lattice. Let us first consider a pure rotational symmetry operation, i.e. a proper rotation. A random orientation R will be converted into a new, symmetrically equivalent orientation R_S by applying the symmetry operation S. If we want to limit the Rodrigues-Frank space to the zone where only those orientations exist that have the smallest rotation angle of all of the symmetrically equivalent ones, then we either have to reject R or R_S depending on which one has the largest rotation angle. Since this angle is directly related to the length of the Rodrigues vector, $\tan \frac{\theta}{2}$, we reject the point in the Rodrigues-Frank space which is the farthest away from the origin and end up with the region where $|R| \leq |R_S|$. The edge of this region is defined by $|R| = |R_S|$, which can equivalently be expressed as $(R - R_S) \circ (R + R_S) = 0$. Using the expression 4.3 for combining rotations, with $\lambda = 1$, we can write this as:

$$[(R \circ S).R + S - R \times S] \circ [2(1 - R \circ S).R + (R \circ S).R + S - R \times S] = 0 \qquad (4.4)$$

Expanding this formula, using the Lagrange identity, one obtains:

$$(1 + R \circ R)[(2 - R \circ S)(R \circ S) + (S \circ S)] = 0 \tag{4.5}$$

As $(1 + R \circ R)$ is always strictly positive, the second part of the equations needs to be zero:

$$\begin{aligned}
(2 - R \circ S)(R \circ S) + (S \circ S) &= 0 && (4.6)\\
[(R \circ S) - 1]^2 &= (S \circ S + 1) && (4.7)\\
R \circ S &= 1 \pm \sqrt{S \circ S + 1} && (4.8)\\
R \circ u_S &= \frac{1}{|S|}.(1 \pm \sqrt{S \circ S + 1}) && (4.9)
\end{aligned}$$

This final equation gives the geometrical location of all Rodrigues vectors R that fulfil the initial criterion. It describes two planes, both perpendicular to the direction of the S vector, and with a distance from the origin given by the value of the right hand side of the equation. Considering that $|S| = \tan\frac{\theta}{2}$, with θ the rotation angle of the symmetry operation, we can simplify this expression and end up with two cases:

$$R \circ u_S = \left\{ \begin{array}{c} \cot\frac{\theta}{4} \\ -\tan\frac{\theta}{4} \end{array} \right.$$

Every symmetry operation that is a pure rotation will thus divide the Rodrigues-Frank space in 3 regions, due to the introduction of 2 cutting planes perpendicular to the rotation axis of the symmetry operation. Because the symmetry operations form a mathematical group, S and its inverse S^{-1} will occur in pairs, resulting in 4 planes: 2 at a distance $\tan\frac{\theta}{4}$ from the origin and 2 at $\cot\frac{\theta}{4}$. As θ is limited to $0...180°$, we can discard the planes at $\cot\frac{\theta}{4}$, since there will always be a plane at $\tan\frac{\theta}{4}$ nearer to the origin. Every proper symmetry operation thus gives rise to a cutting plane in the Rodrigues-Franks space at $\tan\frac{\theta}{4}$.

Until now, only the proper symmetry operations were considered. In many case, improper symmetry elements also exist, in which case there are 2 possibilities: either the crystal is centrosymmetric, or it is not.

If the crystal is centrosymmetric, the improper symmetry operations correspond to one of the proper symmetry operations followed by the inversion. This means that starting from the random orientation R, these symmetry operations still generate the same symmetrically equivalent orientations as the proper symmetry elements,

but followed by an inversion. Since the crystal in centrosymmetric, this inversion makes no physical difference, so no additional symmetrically equivalent orientations are generated, and the Rodrigues-Frank zone is not additionally divided up. All of the cutting planes are defined by the proper symmetry operations.

On the other hand, when no centrosymmetry is present, the improper symmetry elements are not related to the proper ones through an inversion, but can be decomposed as a proper rotation, not part of the symmetry group of the crystal, followed by an inversion, also not part of the symmetry group. Again starting from a random orientation R, the improper symmetry operations will generate symmetrically equivalent orientations or R, by applying the proper rotational part of the symmetry operation, followed by an inversion which changes the "handedness" of the crystal. If we associate with every point in the Rodrigues-Frank space two options, i.e. left- and right-handed, the improper symmetry S operations thus introduce additional cutting planes, again at a distance $\tan\frac{\theta}{4}$ of the origin, as if the corresponding proper symmetry $\bar{1}.S$ operation would exist in the crystal symmetry, at the expense of making it necessary to associate a handedness with every point in the Rodrigues-Frank space.

In summary, the symmetry operations that exist in the crystal lead to a division of the Rodrigues-Frank space. These cutting planes are generated by the proper rotations in the symmetry group of the crystal, as well as those additional proper rotations that correspond to the rotation part of the improper symmetry elements. In many cases, these cutting planes will identify a closed volume around the origin, which is called the fundamental zone. Any physically distinct orientation is represented by a point in this zone. It should be noted that translation symmetry elements have no impact on the orientation, and thus have no influence on the fundamental zone. It thus suffices to limit the symmetry operations to those of the point group.

For the case of the orientation or misorientation of grains in bulk, mono-phase samples, the fundamental zone is determined by enumerating the symmetry elements of the point group of the crystal. There are 6 distinct, bounded fundamental zones, displayed in figure 4.7, for the point groups 222, 32, 422, 622, 23 and 432. In four cases, the fundamental zone is bounded in only 1 direction, for 2, 3, 4 and 6, and in the case of the point group 1 with no symmetry elements, there is no subdivision of the Rodrigues-Frank space.

When using the Rodrigues-Frank space to visualize bulk phase transformations, 2 different crystal structures are involved, and the symmetry elements of both crystals need to be taken into account. The relevant fundamental zones were calculated and reported in [28], for one choice of the reference frame.

When working with thin films on single crystal substrates, the symmetry elements

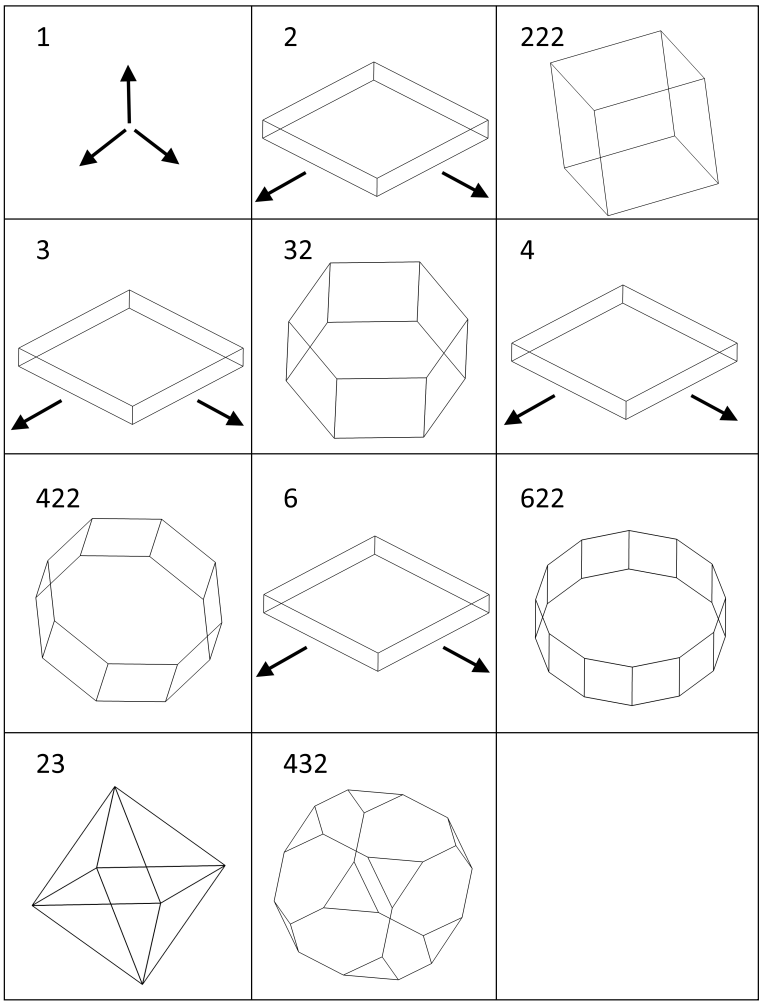

Figure 4.7: Fundamental zones in Rodrigues-Frank space for the different proper point groups, determined using GUSTAV. Arrows indicate directions in which the fundamental zone is unbounded.

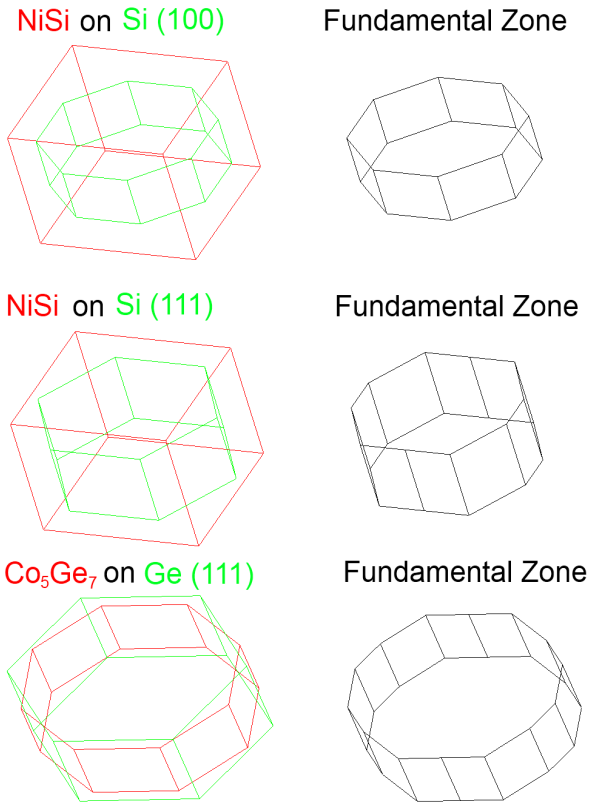

Figure 4.8: The fundamental zones for 3 thin film on single crystal substrates. In red, the fundamental zone of the film crystal is displayed. In green, the fundamental zone caused by the substrate and the choice of habit plane is shown. On the right side, the fundamental zone of the combination of film/substrate is presented.

originate from the symmetry of the film and substrate crystal lattice, but are reduced due to the introduction of a preferential direction, the normal to the substrate. This means that, for the substrate, only symmetry operations that leave the interface invariant, will contribute to the construction of the fundamental zone. In addition, the choices one makes for the reference frame will influence the shape of the fundamental zone, so to be able to use the Rodrigues-Frank space visualization as a routine technique, a fast method for the determination of the fundamental zone was devised and implemented in the GUSTAV program (see chapter 5). Some examples of fundamental zones of thin films on single crystals can be seen in figure 4.8, for the cases of Si or Ge substrates.

At the moment, the Rodrigues-Frank representation has been mainly used for

the represention of misorientations [29], as the construction of the fundamental zone makes an unambigious representation of the misorientation relation between the two crystal lattices possible. In other fields, e.g. thin films, bulk texture or phase transformations, this visualization has received relatively little attention, most likely due to a lack of commercially or freely available tools that calculate fundamental zones and plot texture distributions in them.

5 GUSTAV

GUSTAV, short for Ghent University Software for Texture Analysis and Visualization is a software package developed in the course of this thesis. During the initial stages of the research, it became clear that the available analysis tools (both commercially as well as free/open-source) were unable to handle the type and amount of data needed for the detailed analysis of texture in thin films on single crystal substrates. In addition, the particularities of texture on single crystal substrates made the use of traditional texture analysis tools impractical. This made it necessary to develop custom software.

This chapter provides a short overview of the workings of GUSTAV, its advantages compared to other software, and discusses the main design choices.

5.1 Goals

GUSTAV was developed to fulfil 3 tasks:

1. Processing

The data used in this thesis comes from two sources. Either EBSD data, recorded in the lab in Ghent, or X-ray diffraction data, recorded at the X20A beam line in Brookhaven, using a point or linear detector. As pointed out in chapter 3, when

using a linear X-ray detector, the raw data needs significant processing based on the geometry of the experimental setup. This is implemented in the GUSTAV software. In addition, a stand-alone tool was developed for a quick inspection of the data at the beam line.

2. Visualization

Multiple ways to visualize the data are implemented. For X-ray diffraction data, one can plot pole figures. In the case of EBSD data, orientation maps can be plotted, pole figures can be calculated, and the orientation distribution function, as well as Rodrigues-Frank space can be plotted in the fundamental zone appropriate for the specific combination of film/substrate/sample symmetry. All of the visualizations are fully interactive, and are displayed in 3D where this provides benefits (pole figures and ODF / Rodrigues Frank).

The main difference with already available software is the high resolution with which pole figures and ODF / Rodrigues Frank space are displayed. This allows for a more clear visualization of sharply defined texture components, such as axiotaxy. For the ODF / Rodrigues-Frank space visualization, this made it necessary to implement a recent volumetric visualization algorithm [30] that runs on the GPU of the graphics card.

3. Analysis

The final goal of the software is to make it possible to identify the different texture components in the sample. In GUSTAV, this works by building a texture model, which is a combination of parametric texture components. This allows the user to fit the experimental data by adjusting the texture component parameters in an interactive way: any change in the texture model is immediately reflected in the simulations, which are shown on top of the experimental data. In addition, the visualizations are interactive, letting the user select interesting features on them, which can then be used as the basis for the texture components.

5.2 Advantages for singly crystal substrates

GUSTAV is designed to make use of all the information the user provides about the film and the substrate. This means that, in case the substrate is a single crystal, GUSTAV will take this into account when texture components are defined, and the variants, caused by the symmetry of the substrate, will automatically be calculated. In addition, since the space groups of the film and substrate materials are known to the program, it can, based on the Hall symbols [31] calculate the symmetry matrices and take these into account when the user is trying to fit a texture component.

This reduces the amount of fitting work for the user, especially if high symmetry materials are used. For example, when analyzing a film of $CoSi_2$ (cubic, space group $Fm3m$) on Si(100) (cubic, space group $F\bar{4}3m$) and trying to fit an epitaxial texture component, just indicating the high intensity regions on the pole figures will allow GUSTAV to try every combination of all of the symmetrical equivalent planes of the film, and all of the symmetrical equivalent planes of the substrate, reduced by the decrease in symmetry originating from the sample symmetry. For example, when a $CoSi_2$ $\{112\}$ plane is found to be aligned with a Si $\{110\}$ plane, and a $CoSi_2$ $\{011\}$ plane is found to be aligned with a Si $\{102\}$ plane, on Si(100), one obtains 768 geometrically allowed combinations of all of the different symmetrically equivalent planes of $CoSi_2$ and Si(100). These are reduced to 16 unique $CoSi_2$ orientations, as the other 756 ones can be constructed from these 16 by symmetry operations of the $CoSi_2$ point group. In addition, the 16 can be further reduced to only 4 if one considers the symmetry of the substrate, as each of the 4 orientations has 3 additional variants due to the Si(100) 4-fold symmetry. From this example, it is clear that a manual determination of these orientations would be very impractical, as each of the 768 possible combinations would have to be constructed manually.

5.3 Technical background

The software was developed in a combination of technologies. It consists of a calculation back-end in C++, a user-interface in .NET (C# and Managed C++), and a package in Python (NumPy, SciPy) for data processing.

C++ was the language of choice for the calculation back-end due to the required speed. The central idea of the software was to make it possible to follow a "what-if" approach: let the user try different scenarios and give immediate feedback on what the simulations look like. This was only possible in C++, using optimized algorithms. As a example of this, the calculation of high resolution pole figures from EBSD data takes less than 0.5 s in GUSTAV, while in the standard commercial EBSD software, this takes more than 10 s. In addition, much larger data set can be processed with GUSTAV, and the resulting figures show more detail, which was instrumental for the correct analysis of the data.

The choice for a .NET GUI was based on the speed of development using C#, the good integration of accelerated 3D drawing through Direct3D, and the preference of the users for the Windows platform. The managed C++ layer provides a translation layer between the C++ backend and the C# interface.

A separate set of processing tools were also developed in Python (SciPy, NumPy), making it possible to run these tools at the synchrotron beam line (UNIX based),

and allowing for a first inspection of the data during measurements.

5.4 An overview of GUSTAV for the NiSi/Si(100) case.

GUSTAV works in a project-based fashion. Initially, all of the different crystallographic phases need to be defined, as well as their reference orientation. An example for Si(100) and NiSi is shown in figure 5.1.

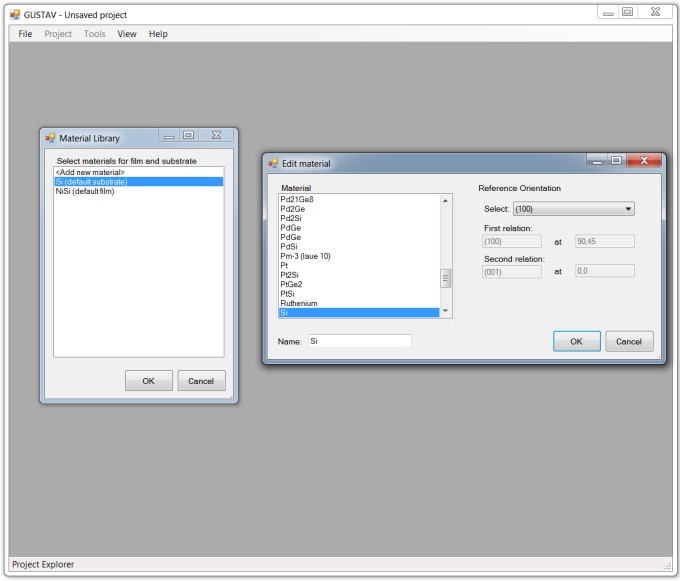

Figure 5.1: Material and reference orientation definition

Next, experimental data needs to be loaded. In figure 5.2, a NiSi {202}+{211} pole figure has been loaded and is shown.

By loading multiple pole figures and identifying region on interest (i.e. high intensity), one can then start to identify the different texture components. GUSTAV shows a simulation of the identified texture component as an overlay on the pole figures, making it easy to compare the texture model and the experimental data (figure 5.3),

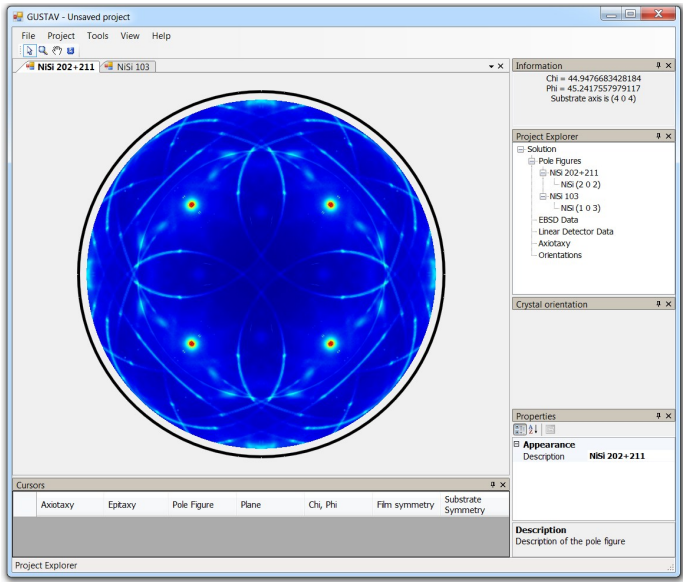

Figure 5.2: XRD pole figures.

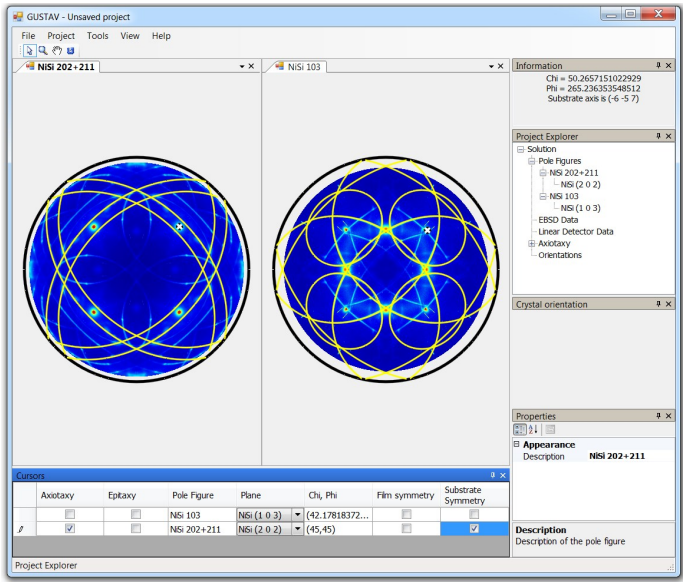

Figure 5.3: Interactive identification and simulation (yellow) of axiotaxy.

Alternatively, texture components can be created by specifying their crystallo-

graphic origin, e.g. the matching of different NiSi and Si planes. GUSTAV allows to take symmetry into account in both the construction of the texture component, as well as in reducing the texture components to those that are unique up to a symmetry operation. In figure 5.4, this is shown for an epitaxial NiSi texture component.

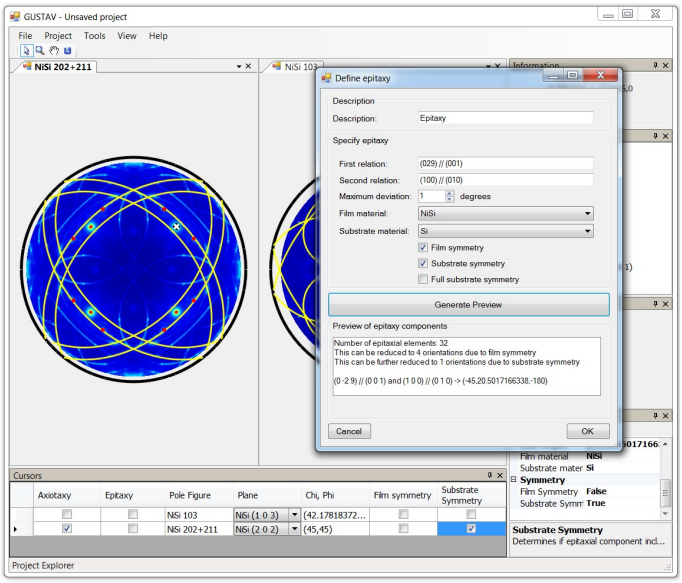

Figure 5.4: Identification and simulation (red) of an epitaxial texture component based on its crystallographic definition.

To help with the understanding of the origin of specific texture components, visualizations of the reciprocal space of the substrate and film orientation are provided. On the left hand side of figure 5.5, the stereographic projection of the reciprocal space is given. On the right hand side, the projection of the reciprocal space vectors onto the interface plane is shown. This makes the identification of matching planes across the interface possible as they will produce matching points in this projection.

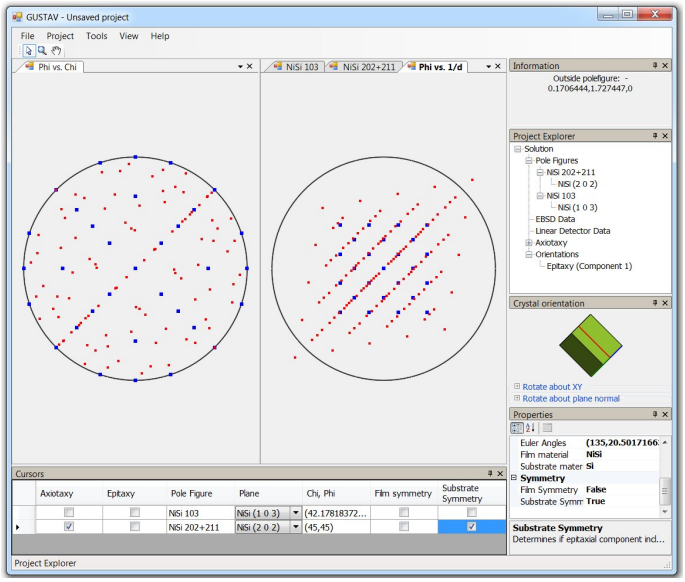

Figure 5.5: Reciprocal space visualization of identified texture components

Figures 5.6 and 5.7 show the different visualization options of GUSTAV: both 2D and 3D visualization, as well as zooming capabilities on the pole figures allow to get a quick idea of the relative importance of different texture components.

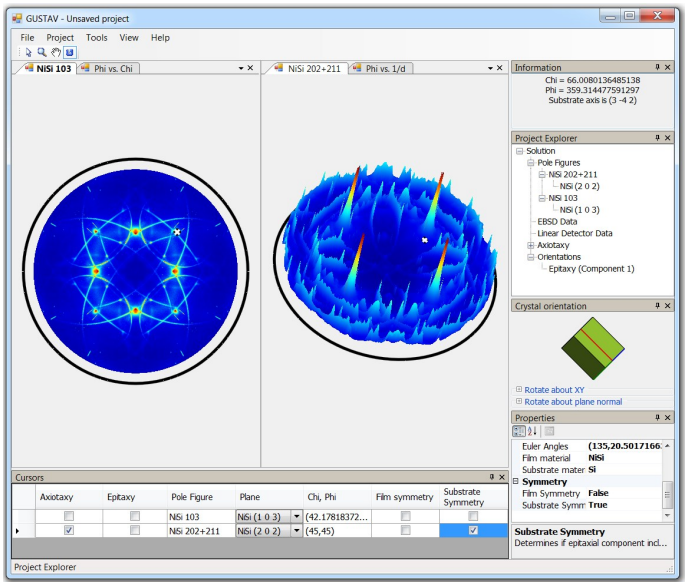

Figure 5.6: 2D and 3D visualization of pole figures

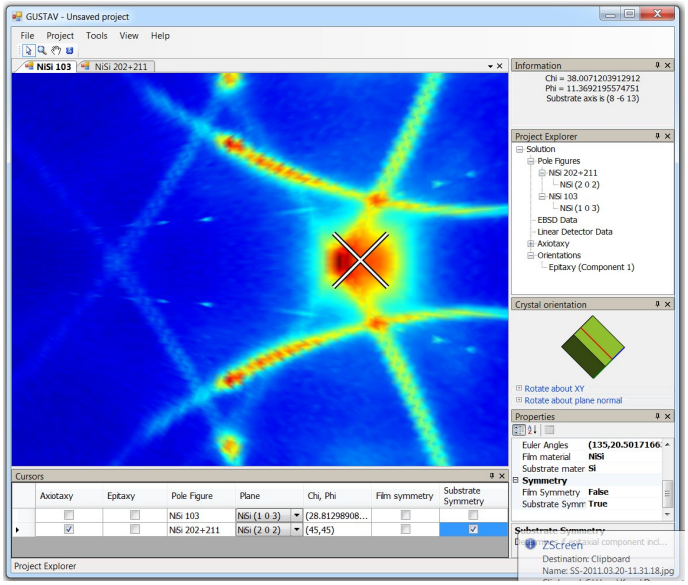

Figure 5.7: Zooming and the identification of features.

Large EBSD data set can also be loaded into GUSTAV, and maps (Euler coloring,

band contrast) can be shown. One can calculate high resolution pole figures from this data, as shown in figure 5.8.

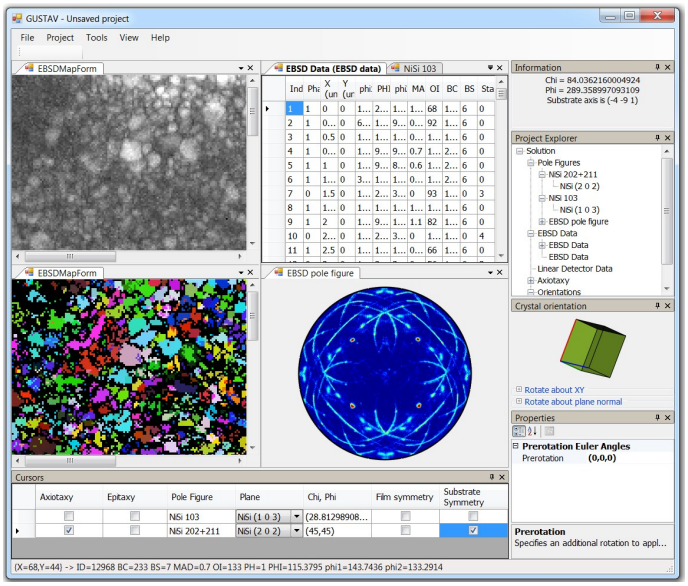

Figure 5.8: EBSD data and visualizations

For any substrate and film crystal symmetry and orientation, the fundamental zone of the Rodrigues-Frank space can be calculated and interactively visualized. Figure 5.9 demonstrates this.

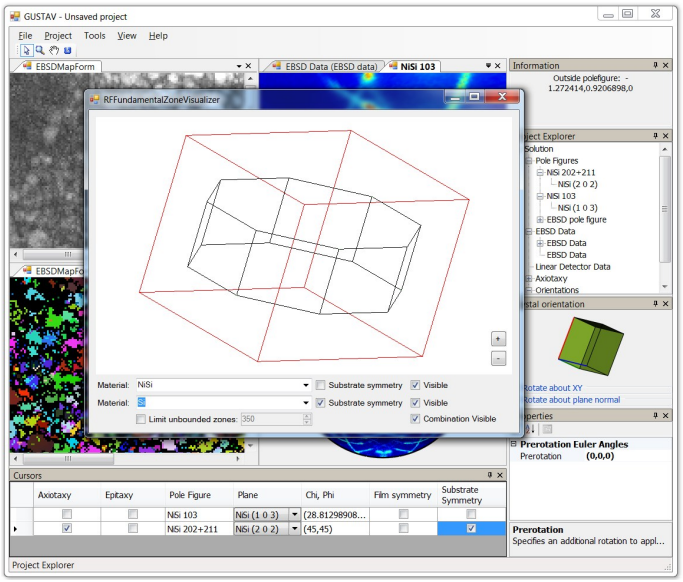

Figure 5.9: Fundamental zone of the Rodrigues-Frank space for NiSi / Si(100). In red, the fundamental zone of NiSi is shown, black represent the fundamental zone of the combination of NiSi on Si(100).

Part II

Texture of silicides and germanides

6

Silicides and germanides: formation and texture

Silicides and germanides are compounds consisting of a metal and silicon or germanium. As most metals will react and form one or more silicides or germanides, there is a huge collection of these materials and their study has shown that they can exhibit a wide range of different interesting properties.

Silicides have many different applications. For this thesis, the main interest is the use of silicides in micro-electronic devices, where their compatibility with the silicon semiconductor is a huge advantage. But silicides can also be used as coatings, e.g. to improve corrosion resistance [32, 33] and they are of special interest to very high temperature applications such as in jet turbines [34]. They can be used in sensor application, e.g. as thermoelectric materials [35] and even the nuclear industry has a keen interest in silicides, as the uranium-silicides can be used as nuclear fuel material with favorable properties [36].

In the case of germanides, the main interest is in their use as contacting materials for next-generation micro-electronics. As the silicon-based technology is getting closer to the fundamental limits regarding the speed of its devices, alternative semiconductors are considered. Germanium is one of the top-candidates and germanides are the natural candidates as contacting materials. There is also considerable interest in germanides as contacting materials on GaAs based devices, due to

the similarity between the crystallography of Ge and GaAs.

In this chapter, an overview of the state-of-the-art of silicide and germanide research for micro-electronic applications will be presented and the importance of texture for silicides and germanides will be established.

6.1 Silicides and germanides in micro-electronics

6.1.1 Silicides

Constant miniaturization is a driving force for the success of the micro-electronics industry. Through downscaling, the speed and complexity of VLSI devices has increased orders of magnitude in a couple of decades. As silicon has been - and still is - the semiconductor of choice for the production of most integrated circuits, a huge amount of research has been carried out on silicon-based devices and the reduction of their size.

A modern chip consists of up to a few billions of individual transistors, which need to be connected to one another in a specific way to end up with an IC that carries out the required function. Interconnecting of silicon-based devices started with pure metals i.e. aluminum in direct contact with the silicon. Due to electromigration and pit formation problems, Al/Si and Al/Si/Cu alloys replaced pure Al. As feature sizes became smaller and speeds increased, the contact resistance could only be kept low enough by introducing silicides in the areas where the interconnections make contact with the devices. While initially a variety of silicides, such as PtSi, Pd_2Si, $MoSi_2$, WSi_2, $TaSi_2$ or $TiSi_2$ were studied and used, the continued downscaling forced a change from $TiSi_2$, which was used when feature sizes were in the range of 250 nm, to $CoSi_2$, and for deep-submicron (65 nm or less) devices, NiSi is now typically used. More details about the history of silicides can be found in [37] and [38].

The replacement of pure metals by silicides has also made it possible to use a self-aligned approach to form electrical contacts. In this way, the electrical contact area no longer needs to be defined using photolithography, the so called *polycide* technique, but instead metal is deposited everywhere and will only react with the regions where the silicon has been exposed, forming the required phase to make a good electrical contact. The unreacted metal is then etched away while the silicide is resistant to the etching process and remains. This is the *salicide*-process, short for self-aligned silicide, and in this process the silicide contact is generated on source, drain and gate regions in one process step. The resulting contacts can be seen in figure 6.1. It is this salicide process that forms the backbone of the current contacting process in silicon CMOS technology.

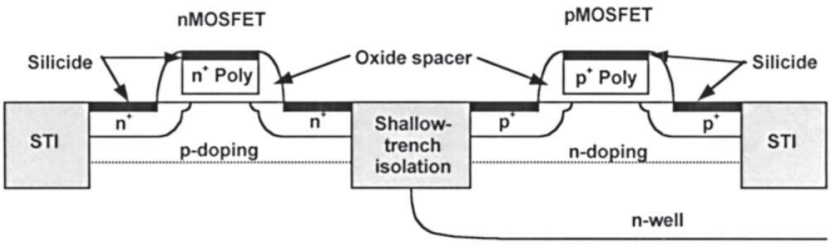

Figure 6.1: A cross section of n- and p-MOSFETS. The silicide layers on source, drain and gate region are clearly visible. Figure taken from [38].

The silicide contacts are formed in the salicide process through the reaction of a metal with the exposed silicide. As most metals react with silicon and will form one or more silicide phases, the list of candidate materials is huge. Even though this results in hundreds of potential contacting materials, the requirements that a contacting material has to fulfill are huge and diverse. In [37], these requirements were listed:

1. low electrical resistivity
2. good adhesion to silicon
3. low contact resistance
4. appropriate barrier height
5. high thermal stability
6. good morphology
7. corrosion resistance
8. adhesion to and minimal reaction with SiO_2
9. low stress
10. compatibility with processing steps
11. low metal penetration
12. low electromigration
13. low formation temperature

Not many silicides meet these criteria. Even when the fundamental bulk material properties of the silicide are acceptable, it is often a big challenge to form the required phase in the small contacts. Three silicides have found extensive use in production.

6.1.1.1 $TiSi_2$

When dealing with - to modern standards - large feature sizes of 250 nm or more, $TiSi_2$ meets the criteria. It was the first silicide to be used on a large scale with the salicide process. As feature sizes became smaller, the so called "fine-line effect" became insurmountable: in very fine lines, it was no longer possible to keep the resistivity of the $TiSi_2$ contacts low. This is caused by the polymorphism of $TiSi_2$: it exists in two crystal structures, the C49 and C54 phases, of which only the C54 phase has the required low electrical resistivity. However, during the reaction of the thin film of Ti with the Si of the contact area, C49-$TiSi_2$ will initially be formed and will only be converted to C54 through a nucleation-controlled process at elevated temperatures. As the nucleation will start at triple points of C49-$TiSi_2$ grain boundaries, the reduction in the amount of grains one obtains when the line widths get small, will prevent the conversion to the required C54 phase. This made a shift to new materials necessary as feature sizes dropped below 250 nm.

6.1.1.2 $CoSi_2$

In the range of feature sizes between 180nm and 65nm, $CoSi_2$ can be used as it does not suffer from the C49 to C54 conversion problem of $TiSi_2$, since only one crystal structure of $CoSi_2$ exists and the nucleation of $CoSi_2$ from CoSi poses no problems. When the line widths reach 50nm or less however, the formation of low resistivity $CoSi_2$ becomes problematic, most likely due to void formation. Additionally, the high silicon consumption for the formation of a $CoSi_2$ contact become problematic on silicon-on-insulator (SOI) substrates, where the active Si layer is very thin. The increased use of Ge, e.g. to stress the channel of the transistor, also limits the use of $CoSi_2$, as no $CoSi_{2-x}Ge_x$ phases can be formed, hindering the formation of low resistance contacts, which made the success of $CoSi_2$ relatively short-lived.

6.1.1.3 NiSi

Starting with the 65nm node, NiSi has become the contacting material of choice in the salicide process. The low formation temperature of NiSi, its low resistivity, compatibility with SiGe, low silicon consumption and the lack of fine-line effect make it the currently preferred contacting material for deep submicron silicon technology.

However, in contrast to $TiSi_2$ and $CoSi_2$, NiSi is not the most silicon-rich silicide phase of the corresponding metal/silicon system. This means the NiSi contact can react further with the Si substrate, resulting in the formation of $NiSi_2$. This

would both consume much more silicon and result in a higher sheet resistance, resulting in a poor contact. In addition, as the NiSi contacts get thinner and thinner, the morphological stability of the contact becomes an important problem: the NiSi layer will start to break up into small island, destroying the low resistivity in the process. It was shown [39] that this presents a more important problem for very thin ($<$ 30 nm) NiSi contacts than the conversion to $NiSi_2$, as it occurs before the thermodynamically driven transformation to $NiSi_2$ can take place. A lot of research was carried out on ways to stabilize NiSi, both with respect to the thermodynamical instability ($NiSi_2$ formation), as well as the morphological instability. It was shown that Pt addition (10-15%) to the as-deposited Ni can alleviate these problems [40, 41], resulting in the use of $Ni_{1-x}Pt_xSi$ contacts.

6.1.2 Germanides

The use of self-aligned silicides has been one of the enabling technologies in the production of current deep-submicron silicon based electronic devices. However, for applications where even higher switching frequencies are required than are possible with silicon, other semiconductor such as germanium (Ge), silicon-germanium (SiGe) or gallium-arsenide (GaAs) have an intrinsic advantage due to their higher carrier mobility. On Ge, germanides are a natural choice for the production of self-aligned contacts.

In comparison to the huge amount of literature on silicides, germanides have received relatively little attention. Recently, an extensive review of the phase formation of metals with Ge (100) and amorphous germanium was published [42], which provides an excellent starting point in the search for germanides that can be used as contacts. The main candidates were identified as NiGe, PdGe and $CoGe_2$, based on their formation temperature, stability and low electrical resistivity.

6.2 Formation of silicide and germanide contacts

The use of the salicide process for the formation of contacts results in the occurrence of a solid-state reaction between the deposited metal film and the semiconductor substrate. Since the metal thickness layer is much smaller than the wafer thickness, the amount of metal is tiny when compared to the amount of semiconductor material. The phases expected to have formed when thermodynamic equilibruim has been reached, can be found in the metal/semiconductor phase diagram on the semiconductor-rich side. For example, for the Co/Si case, this would be $CoSi_2$ in contact with Si, and for the Ni/Si system, it would be $NiSi_2$ and Si.

6.2.1 Diffusion and nucleation

As the initial situation of pure metal on semiconductor is not a thermodynamically stable situation, the system will move towards the equilibrium. However, the speed at, and path through which this equilibrium can be reached depends on the exact properties of the system and the environment. There are 2 main phenomena that will occur.

Firstly, there is the diffusion of metal and semiconductor atoms, due to the chemical potential gradient which is initially very high. This diffusion can be described by the Nernst-Einstein relation and relates material transport to the diffusion coefficient D, the concentration and the chemical potential gradient.

Secondly, there is the driving force for phase changes to occur through the nucleation of a new phase. The driving force for this process is the gain in free energy that can be accomplished by the phase change, if at a specific temperature, a new phase has a lower free energy per unit of volume than the existing phase. However, this gain in free energy can be offset by the generation of the new interface area, with its associated interface or surface energy, the introduction of elastic strain energy due to a crystallographic misfit between the different phases or the energy associated with defect generation (e.g. dislocations) for the relaxation of this strain. In the classical nucleation theory, the trade-off between these different contributions is translated into a critical nucleus size R^*, which is the minimal size a nucleus has to have to be able to grow instead of being consumed and disappear.

These two different phenomena, diffusion and nucleation, are of course not isolated from one another. For a new phase to nucleate, the local composition must meet that of the new phase, which means that material transport has to occur. The introduction of a grain of the new phase through nucleation will change the diffusion coefficient, as this is dependent on the phase. Additionally, microstructural evolution, such as grain growth will influence the environment in which the diffusion and nucleation takes place, resulting in a generally extremely complicated situation. In some cases, one of the two processes will occur at a significantly higher rate than the other, resulting in the net effect that the solid state reaction is controlled by the speed of the slowest process, i.e. a diffusion or nucleation controlled reaction.

This thesis does not aim to study the complete phase formation through its kinetics and thermodynamics, but focuses on how anisotropy, through the microstructure or texture, will influence certain aspects of this phase formation and the properties of the resulting phases. For this purpose, it is interesting to investigate how texture and microstructure will influence nucleation and diffusion.

6.2.2 The role of texture and microstructure

In most discussions on solid state reactions, the influence of the texture or microstructure is hardly discussed, even though both diffusion, through the orientation of the grains, the grain size, the type of grain boundaries and the orientation of the grain boundaries, as well as nucleation through the interface energy and the strain energy, will depend on it.

Diffusion is related to the material properties through the diffusion coefficient. However, the diffusion can occur in multiple ways: either atoms move through the bulk material, but they can also move through grain boundaries, along the free surface or the interface. For the case of material transport in thin films, towards the interface, the surface and interface diffusion contributions are of less importance. Therefore, the effective diffusion coefficient depends mainly on the crystallographic phase the atoms are diffusing through, whose bulk diffusion properties are described by the lattice diffusion coefficient and on the microstructure through the grain boundary diffusion coefficient which describes transport of material through the grain boundaries.

Grain boundary diffusion is most often described using the Fisher model [43], which assumes that the grain boundary can be modelled as a slab of certain thickness, i.e. the grain boundary thickness, which makes up a volume in the material with a local high diffusion coefficient, i.e. the grain boundary diffusion coefficient. Based on this model, an approximate relation between the effective, the lattice and the grain boundary diffusion coefficients can be written as:

$$D = D_l + \frac{\delta}{2.a}.D_{GB}$$

where D is the effective diffusion coefficient, D_l the lattice diffusion coefficient, δ the grain boundary thickness, a the grain size and D_{GB} the grain boundary diffusion coefficient. D, D_l and D_{GB} are in general tensors and describe the diffusion anisotropy in the material. In addition, D_{GB} can depend on the type of grain boundary as well and can thus depend on the specific location within the sample.

This immediately makes the effect of the microstructure and texture clear. A different phase and/or orientation of the grains will lead to different diffusion coefficients and grain boundaries. Changes in microstructure, e.g. grain size, will also shift the relative contributions of lattice and grain boundary diffusion. An additional complication arises from the fact that diffusion coefficients are temperature dependent through $D = D_0 exp(-Q/kT)$, with an activation energy Q that can be significantly higher for lattice than for grain boundary diffusion. In practice, this generally results in a dominance of grain boundary diffusion at low temperatures and a mixture of both lattice and grain boundary diffusion at higher temperatures. An example for FCC metals is shown in figure 6.2.

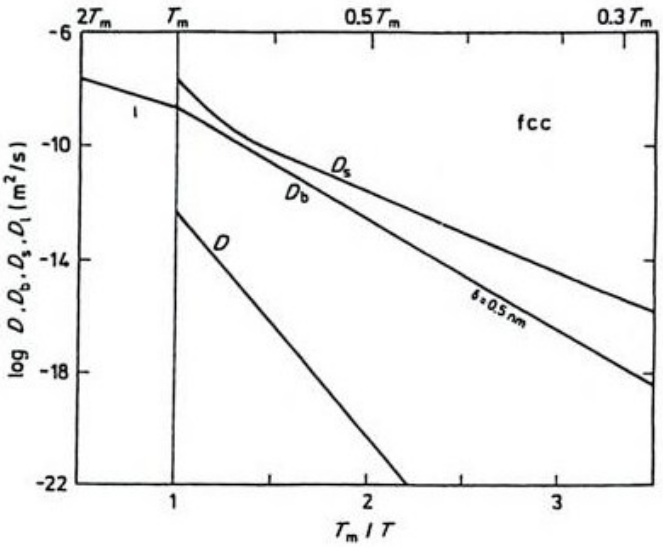

Figure 6.2: Self diffusion coefficients of FCC metals in the lattice (D), along grain boundaries (D_b), along the surface (D_s) and in the liquid phase (l). Image taken from [44]

For the case of germanides and silicides, a fairly limited amount of quantitative information on self-diffusivity is available in literature. For nickel diffusion in Ni_2Si, Ciccariello et al. [45] determined the activation energies for lattice and grain boundary diffusion as respectively 2.48 eV and 1.71 eV, and D_0 as 3.54 cm^2/s vs. 18.16 cm^2/s in the temperature range of 500-900°C, however, no information on the anisotropy of these coefficients is provided. This confirms that in this system and temperature range, grain boundary diffusion will be the most important mechanism in nickel redistribution.

In many cases, grain boundary diffusion will indeed be dominant, but this is certainly not always the case. For example, in the case of As diffusivity in Ni_2Si [46], the activation energy was found to be higher for grain boundary than for lattice diffusion. It is also important to note that even when grain boundary diffusion has a lower activation energy, the net effect on the diffusion still depends on on the D_0 coefficient: if this is orders of magnitude smaller for grain boundary than for lattice diffusion, one can still end up with a system where the effective diffusion is dominated by the lattice diffusion.

While this provides a qualitative idea of the importance of grain boundaries and texture for diffusion, to make practical use of this information, one would need quantitative information. This is problematic for 2 reasons. First of all, the measurement of grain boundary diffusion coefficients is complicated. It typically in-

volves radioactive tracer experiments and the measurement of resulting penetration profiles in the grain boundaries. To make things worse, the values for grain boundary diffusion obtained in this way cannot simply be used as a general grain boundary diffusion coefficient, because there is both an additional dependence on the type of grain boundary as well as the fact that the grain boundary diffusion coefficient can exhibit strong anisotropy. The large difference for grain boundary diffusion between large- and small-angle grain boundaries in metals [47, 48] (see figure 6.3), and the experiment by Hoffman [49] where for the grain boundary diffusion coefficients in small angle grain boundaries, a ratio of 15 could be found between the principal values of the grain boundary diffusion tensor illustrates this. In [50], a difference in nickel grain boundary diffusion in Ni_2Si was measured depending on the type of grain boundary, resulting in a factor 5 difference in grain boundary diffusion between small and high angle grain boundaries. These results demonstrate both the impact of the specific atomistic structure of the grain boundary and the large anisotropy for diffusion within one type of grain boundary.

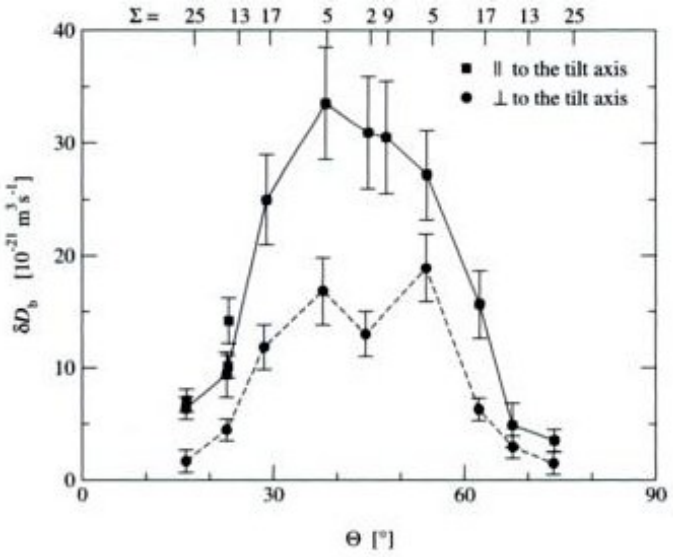

Figure 6.3: Self diffusion of silver metals in [001] symmetric tilt grain boundaries as a function of misorientation, at 771 K. Image taken from [48]

Secondly, even the limited amount of quantitative information regarding grain boundary diffusion in silicides and germanides is difficult to use, because a complete characterization of the microstructure during the whole solid state reaction needs to be available. As limited attention has been given to texture in silicides and germanides, this second aspect is not fulfilled either. While the averaged diffusion coefficients that are available for silicides and germanides have already provide

many insights into the growth of thin films, a complete understanding of the effect of microstructure and grain size on the different reaction steps will require more detailed information on the anisotropic material transport in these materials.

The importance of texture is also clear, more obviously, when considering the nucleation of a new phase. As the classical theory of nucleation is essentially a trade-off between volume effects (reduction due to the ΔG for the new phase) and interface effects (creation of new interface area with its associated energy), it is clear that the type of interface will affect this second contribution. There are many examples of epitaxial stabilization of phases in thin layers [51, 1, 52], as the low interface energy due to the epitaxial relation between the film and the substrate will prevent a new phase to nucleate if the gain in free energy between the old and the new phase is not sufficiently large. Strain effects can also play a role, due to the large anisotropy that some materials exhibit in their Young's modules and thermal expansion. The nucleation and growth of a new phase in an orientation that causes a large strain energy can then be significantly hindered.

Again, one of the main problems is the lack of quantitative information on interface energies and material properties. The interface energy is closely related to the chemical structure at the interface. In principle, one could try to calculate this using density functional theory, but the large number of possible orientations of the film grains with respect to the substrate, and the additional dependence of the interface energy on the habit plane, result in a large parameter space, which makes it currently not possible to predict low energy interfaces ab-initio. Concerning the material properties, the picture is less dramatic, as both the Young's modulus and the thermal expansion tensor are in principle accessible using experimental methods and theoretical calculations. An example of this is the experimental determination of the thermal expansion of NiSi [53, 54] and the calculation of its Young's modulus [55]. However, at the moment, no systematic report in literature of these properties for silicides and germanides is available.

In summary, one can identify two problems related to the microstructure, when trying to apply diffusion and nucleation theory to silicide and germanide formation: firstly, the limited availability of detailed material properties that describe the anisotropy for the different phases and their grain boundaries, and secondly the limited information on the microstructure itself. In this thesis, an attempt is made to resolve part of this second problem through the identification of the texture of a number of silicides and germanides and by rationalizing their occurrence. If possible, the connection to the phase formation will be made.

6.2.3 Texture of silicides

The interest in the texture of silicides is not new, but has been focused on the growth of epitaxial silicide films on single crystal silicon substrates, e.g. using molecular beam epitaxy. If one looks at literature, there has been a pre-occupation with the epitaxy of contacting materials, since it was assumed that the epitaxial interface between substrate and contact would lead to better electrical properties.

Epitaxy is expected when the silicide and the silicon substrate have a matching structure. In general, this means that there is a correspondence between the surface plane of the single crystal substrate and a specific crystal plane in the silicide lattice. A maximum lattice mismatch of 3 % between the silicide and silicon is considered as a rule-of-thumb for allowing epitaxy. Figure 6.4 shows an overview of different silicide phases, their lattice mismatch to Si (100), (110) and (111) substrates, and the unit cell area. Silicides with a low mismatch and small unit cell area will results in the best epitaxy. While a substantial list of silicides is shown in this figure, only the bottom left part will actually lead to epitaxial silicides when grown through a simple metal on silicon deposition and subsequent annealing. For the other silicides, more complicated techniques such as molecular beam epitaxy need to be used. Also, the majority of all silicide phases does not show up in figure 6.4: for those silicides, which have a larger mismatch, little regard has been given to their texture, or it has been implicitly assumed to be random.

This classification, of either epitaxial or random texture for silicides was found to be incomplete in the case of NiSi on Si(100) [2]. A new type of texture, axiotaxy, was shown to occur in these films. Since then, axiotaxy was reported in a number of other silicides as well, e.g. $CoSi_2$ on Si (100) [57], α-$FeSi_2$ [58], all using the same high resolution pole figure setup at the X20A beam line. This thesis is a continuation of this work, and aims to investigate this texture and relate it to the properties of the material.

6.2.4 Texture of germanides

The amount of research carried out on germanides is tiny when compared to that on silicides. As a result, even less information on the texture of the different germanide phases is available. On can find TEM results on the texture of Co_5Ge_7 on Ge (100)[59], of $CoGe_2$ on GaAs [60] using low resolution pole figures, however the low statistical reliability of these results and the quality of the measurements makes it risky to consider this information as a complete description of the texture in the germanide film. One recent article on the texture of germanides, i.c. NiGe, has been published and provides high resolution pole figures: it shows the complex texture, consisting of axiotaxy and epitaxy, of the NiGe phase on Ge (100) and Ge

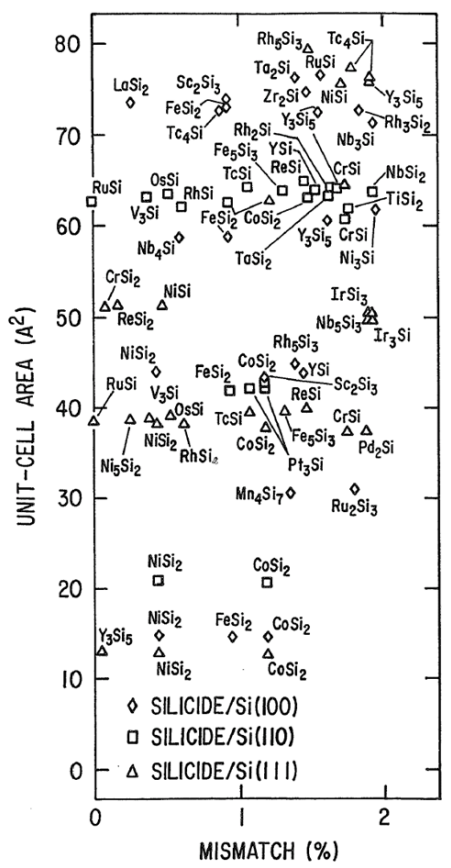

Figure 6.4: Overview of silicides that can be grown epitaxially on Si(100), Si(111) or Si(110), as a function of the lattice mismatch between the film and substrate, and the unit-cell-area of the matching area between film and substrate. Figure taken from [56]

(111) [61]. For the other germanide phases, the microstructural characterization is largely unexplored.

6.2.5 Observed textures in silicides and germanides

In figure 6.5, a series of pole figures collected on a wide variety of silicides and germanides films on different substrates, is shown. The complex textures, consisting of epitaxy, axiotaxy and fiber texture make it clear that a non-random texture is very common and the assumption of a random texture when no perfect epitaxy can be achieved, is often wrong.

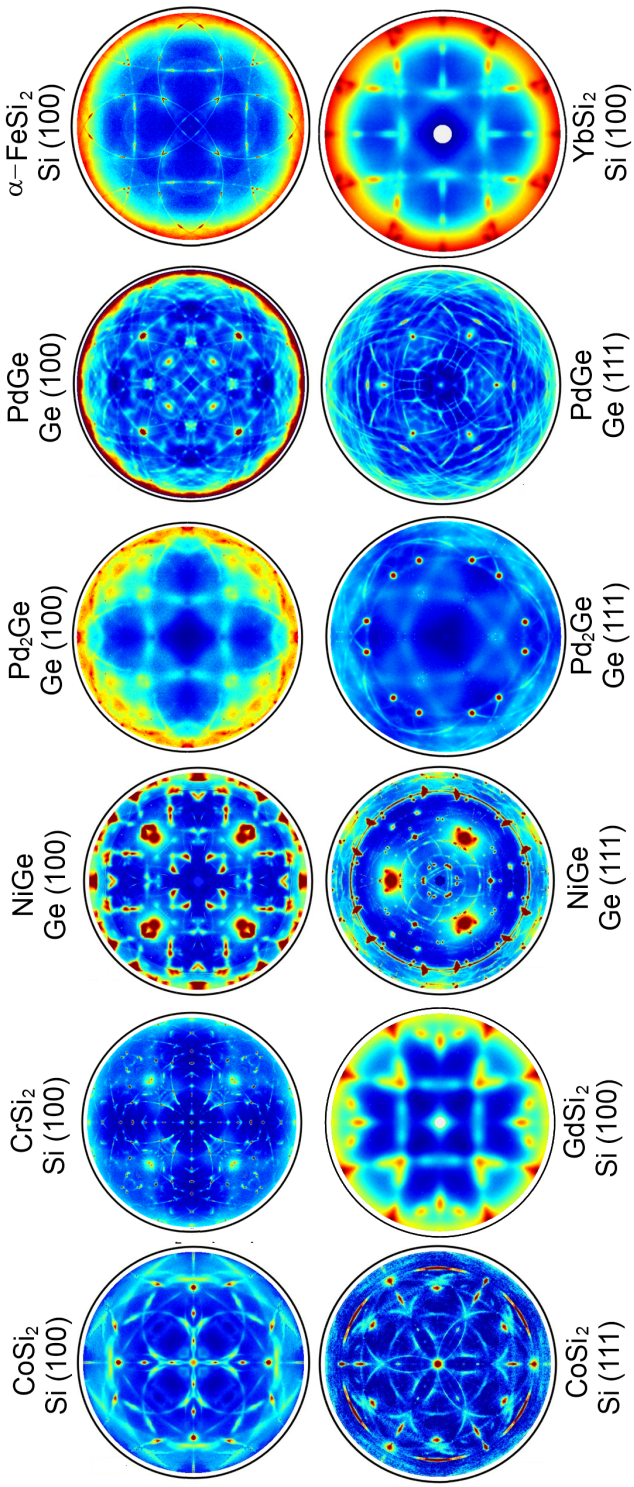

Figure 6.5: Pole figures for various silicides and germanides on different substrates. In many cases, a complex texture can be observed.

6.3 Conclusion

In this chapter, the importance of silicides and germanides for the micro-electronics industry was discussed. It was shown that the salicide technology results in the use of a solid-state reaction between a metal film and a semiconductor single crystal substrate. The problems related to the microstructure and texture, and their influence on diffusion and nucleation of new phases were discussed.

7

An EBSD study of the texture of NiSi on Si(100)

The reaction of thin nickel films with single crystal silicon substrates has received a lot of attention in literature. Many groups, using a variety of techniques such as Rutherford backscattering spectroscopy [62, 63], X-ray diffraction [64, 65], and especially transmission electron microscopy [66, 67, 68] have reported on the phase formation in this system. It became more or less accepted that the phase formation sequence of the thermally induced reaction of nickel with Si (100) consisted of pure nickel, followed by δ-Ni_2Si, then NiSi and finally $NiSi_2$, however this phase sequence failed to explain all of the reported observations on the Ni/Si(100) reaction, in particular some extra XRD peaks that show up at low temperature. In addition, little attention has been given to the texture of the different nickel-silicides, with the exception of the final $NiSi_2$ phase and its epitaxial orientation.

In this chapter, a short overview of the Ni/Si(100) reaction will be given, with the purpose of pointing out the importance of characterizing the texture of the different phases. Next, the qualitatively reported texture of NiSi will be described, and a quantitative EBSD study of this texture will be presented.

The results discussed in this chapter have been published in:

De Keyser K., Detavernier C., Van Meirhaeghe R.L., *Characterization of the texture of silicide films using electron backscattered diffraction* , Applied Physics Letters, 90(12), 121920 (2007)

7.1 An introduction to the Ni/Si system in thin films on Si (100)

If one studies X-ray diffraction data, both in-situ XRD describing the phase formation of Ni/Si(100), as well as θ-2θ scans or pole figure scans on the resulting NiSi film, one can observe two problems in the description of the Ni/Si(100) reaction. Firstly, at low temperatures, the observed XRD peaks do not match with the transient occurrence of only δ-Ni_2Si. An in-situ XRD spectrum is shown in figure 7.1, and one can notice a complex reaction taking place in the temperature window 250-350°C. Gaudet et al. [69] recently identified this reaction at relatively low temperatures as a combination of 3 phases, δ-Ni_2Si, θ-nickel-silicide and an additional currently unknown phase, given the preliminary designation X-phase, each occurring with strong epitaxial or fiber textures. Even though their compositions are all in the range of Ni_2Si to Ni_3Si_2 [70], their difference in crystal lattice and texture are important for the understanding of the Ni/Si(100) reaction. This makes it clear that even though a consensus was more or less reached on the phase formation, only part of the reaction was understood and this problem was only resolved due to the attention to the crystal structure (i.e. δ-Ni_2Si vs. θ-nickel-silicide) and texture (i.e. epitaxial phases) of the phases occurring during the reaction.

Secondly, if one studies the NiSi phase, which follows the metal-rich phases during the annealing, the abundance of XRD peaks visible in a θ-2θ scan might give the impression of little or no preferential orienation. However, a closer look at the intensities of the different NiSi Debye rings shown in figure 7.2, make it clear that NiSi does not have a random texture on Si(100): the difference with the uniform intensity of these rings when NiSi is formed from the reaction of a nickel film with an amorphous silicon layer is clear. This preferential orientation of NiSi on Si (100) was investigated and identified in [2] as axiotaxy.

From these results, it is clear that one should consider the texture of the different phases that occur in the Ni/Si(100) reaction, if one wants to work towards to complete understanding of this system. In this chapter, the texture of NiSi on Si(100) will be described, and results concerning the quantitative determination of the volume fractions of the different texture components will be presented.

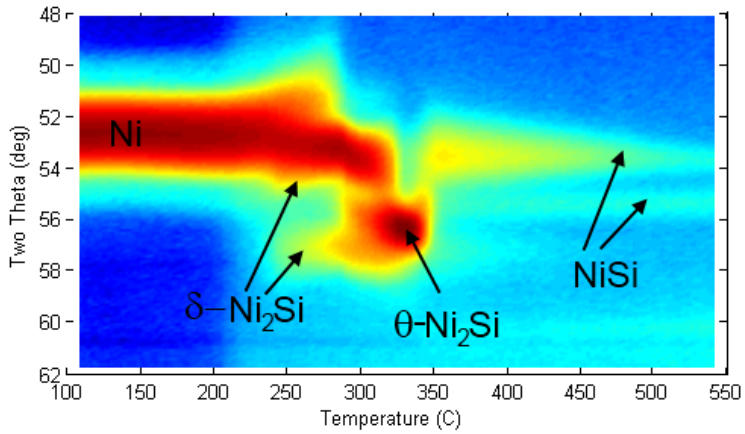

Figure 7.1: In-situ XRD (λ = 0.18 nm) on 10 nm Ni on Si (100) showing the XRD peaks as a function of temperature. Phase are identified following [69].

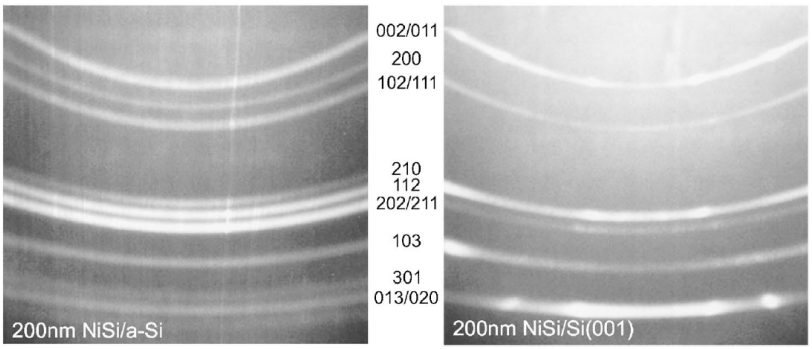

Figure 7.2: Photographic image of the Debeye rings produced by a NiSi film on amorphous silicon (left), exhibiting a random texture and thus a uniform intensity along the rings, and produced by a NiSi film formed by annealing a nickel film on Si(100) (right), where the variable intensity along the Debeye ring demonstrates the non-random texutre. (Image taken from [71])

7.2 The texture of NiSi on Si (100): axiotaxy

The texture of NiSi on Si(100) was systematicaly investigated using synchrotron pole figures in [2]. These pole figures and their analysis is shown in figure 7.3 and resulted in the identification of 4 major texture components:

- {202} axiotaxy: the preferential alignment of the NiSi {202} planes with

the Si $\{202\}$ planes due to the similar d-spacing (0.1921 nm vs. 0.19201 nm)

- $\{211\}$ axiotaxy: the preferential alignment of the NiSi $\{211\}$ planes with the Si $\{202\}$ planes due to the similar d-spacing (0.1919 nm vs. 0.19201 nm)
- $\{112\}$ axiotaxy: the preferential alignement of the NiSi $\{112\}$ planes with the Si $\{202\}$ planes due to the similar d-spacing (0.1978 nm vs. 0.19201 nm)
- $\{103\}$ axiotaxy: the preferential alignement of the NiSi $\{103\}$ planes with the Si $\{202\}$ planes due to the similar d-spacing (0.1778 nm vs. 0.19201 nm)
- Epitaxial component: NiSi $\{100\}$ // Si $\{010\}$ and NiSi $\{029\}$ // Si$\{001\}$

The origin of the axiotaxy texture is proposed to originate from a 1-dimensional matching at the interface. Indeed, if one draws the interface structure of the NiSi $\{202\}$ or $\{211\}$ planes, arriving at the interface (figure 7.4), one can notice that their d-spacing *projected* onto the interface plane (d_p), matches the projected d-spacing of the Si $\{202\}$ planes. This leads to the repeated matching of the NiSi and Si planes along a $<100>$-type direction within the interface plane. For the $\{103\}$ and $\{112\}$ axiotaxy, there is a difference in d-spacing with the Si $\{220\}$ planes of a couple of percent. This difference, which would destroy the 1D matching, is resolved by tilting the grain a couple of degrees: this results in the matching of the *projected* d-spacing, as can be witnessed in figure 7.4. This is indeed observed in the data, as the fiber axis corresponding to the $\{103\}$ and $\{112\}$ axiotaxy is no longer perfectly aligned with the Si $\{202\}$ poles, but is slightly tilted.

If the tilting of one set of planes can compensate for a difference in d-spacing, why does this not happen to different sets of planes, with even larger differences in d-spacing? The main argument here is that the tilting should be small. Indeed, if the tilting is small, a slight curvature of the interface will not disturb the matching. If the tilting is large however, then any deviation from a perfectly flat interface causes the destruction of the matching of the planes, as illustrated in figure 7.5. As the initial formation of a grain occurs through nucleation of a small nucleus in an area where the local composition has reached the required ratio, it is unlikely that the interface of the nucleus with the substrate will be perfectly flat.

In summary, axiotaxy in NiSi is caused by a matching of planes from the NiSi film to the Si substrate. These planes have a similar d-spacing, resulting in a matching at the interface in one direction. A slight difference in d-spacing can be accomodated by tilting, but this tilting has to be small to prevent interface roughness from destroying the matching.

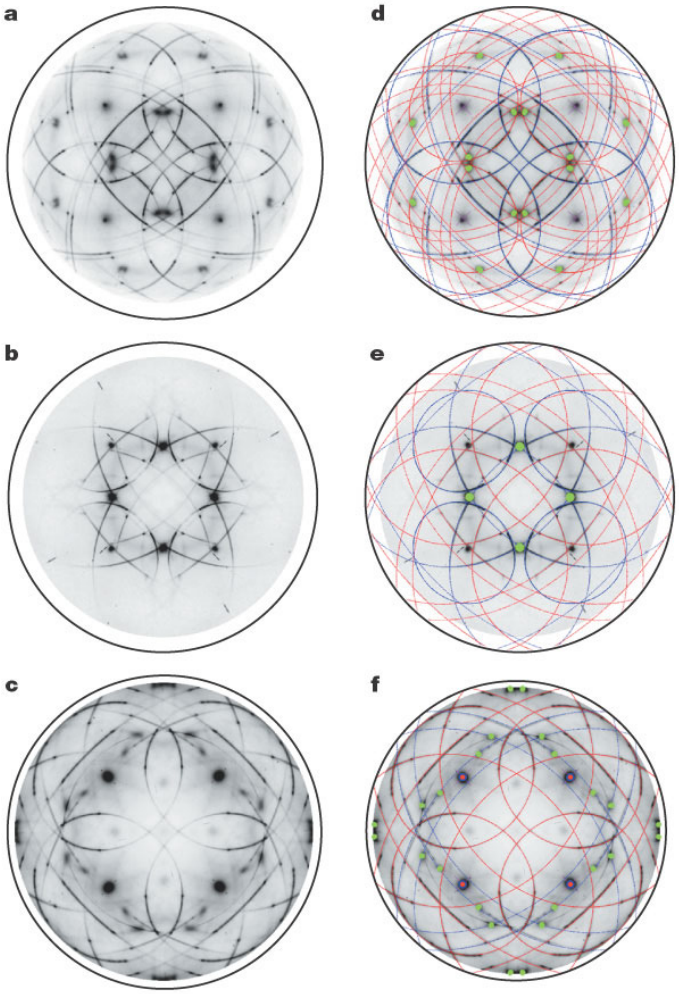

Figure 7.3: Pole figures recorded on a 60 nm NiSi film on Si (100), showing the (a) {112} pole figure, (b) {103} pole figure, (c) {202}+{211} pole figure, with the simulation of the axiotaxial and epitaxial texture components overlaid in (d), (e) and (f). (taken from [2]).

7.2.1 Transrotational structures

In addition to the occurrence of axiotaxy, a different microstructure in thin NiSi films on Si (100) has been reported. Alberti et al. [72, 73] observed transrotational structures, both in Ni_2Si and NiSi films. The structures correspond to large grains with many small subgrain boundaries, resulting in the observed bending of specific crystallographic planes. This bending can either be spherical or cylindrical. At

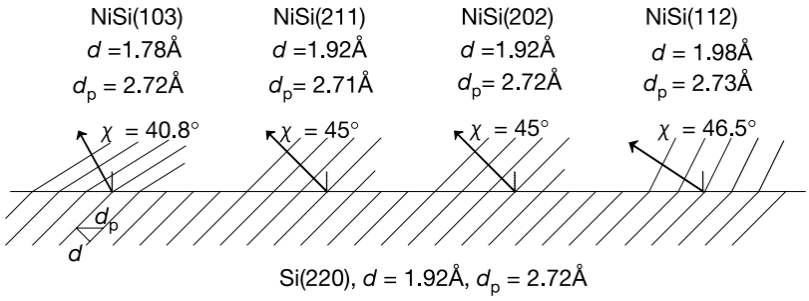

Figure 7.4: 1D matching of planes from NiSi and Si, leading to the observed axiotaxy. If the d-spacing of the NiSi plane is significantly different from that of the Si {202} plane, tilting of the NiSi grain is observed which results in a matching of the projected *d-spacing. Figure taken from [2]*

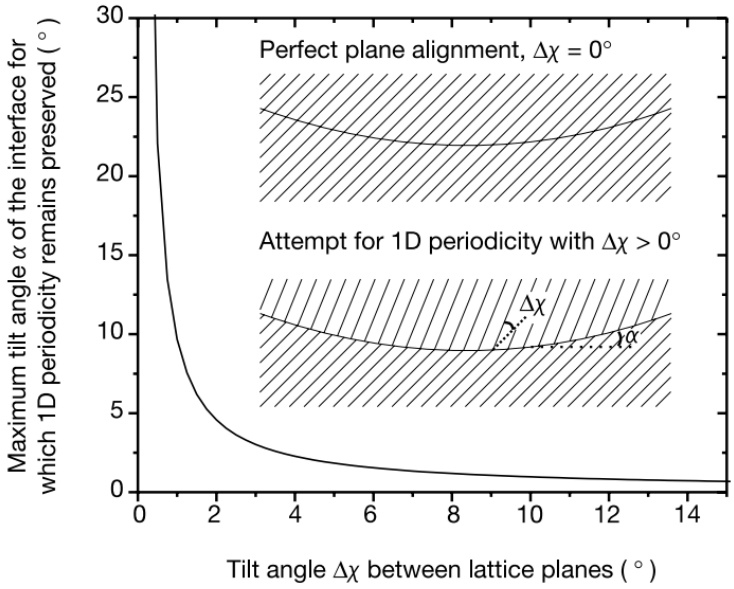

Figure 7.5: The effect of interface curvature on the 1D matching of axiotaxy. As the tilt angle increases, the maximum interface curvature becomes very small. Figure taken from [2].

the moment, it is unclear in which conditions either axiotaxy or transrotational structures will form. It might depend on the sample prepartion technniques, such as cleaning or deposition method, or on the way of annealing: in the case of samples

where transrotational structures were observed, isothermal anneals in vacuum were used, while axiotaxy is reported in samples using ramp anneals or rapid-thermal-anneals in nitrogen, helium or forming gas environments. It was reported that there is a critical Ni film thickness for the occurrence of transrotational NiSi [74], and another influence might come from the dopants in the silicon substrate. However as pointed out in [69], axiotaxy was observed in a wide range of experiments, including Si (100) substrates with different types and concentrations of dopants. Based on the amount of data available on the occurrence of axiotaxy, compared with the sporadic reports on transrotational structures, it is likely that axiotaxy is the *natural* microstructure, while a combination of specific sample preparation, metal thickness, annealing and dopant concentration will induce the formation of transrotational structures.

7.3 Quantitative texture determination using EBSD

In the scope of this thesis, it was the goal to corroborate the existence of axiotaxy, as only limited reports were available on this texture, all with data collected using the same technique (X-rays) as well as the same setup (X20A beam line). A second point of interest was the quantification of the importance of the different texture components to establish if axiotaxy is in fact the main texture component, or represents only a secondary effect. For both of these goals, EBSD measurements are ideal since it is a fundamentally different technique compared to X-ray diffraction, and volume fractions for the different texture components can be readily extracted from an EBSD data set.

7.3.1 Experimental

For the purpose of the EBSD measurements, films of 45, 30 and 12nm of Ni were sputter deposited onto HF-cleaned Si(100) substrates. After deposition, NiSi was formed by annealing in N_2 for 30 seconds at 550°C, resulting in NiSi films of 90, 60 and 24nm. The measurements were performed on the FEI Quanta 200F field emission SEM, using typical settings of 12.5 up to 20 kV acceleration voltage, 2nA-7nA beam current and a working distance of 12 mm. Special consideration was given to the long term stability of the microscope, as EBSD measurements can take multiple hours or even days. The orthorhombic unit cell of NiSi is nearly tetragonal, and this pseudo-symmetry makes a careful optimization of the pattern recognition parameters necessary. Carbon contamination can build up in significant quantities during the EBSD measurement, especially on NiSi, and ultimately blocks the backscattered electrons from reaching the detector. To remove this con-

tamination the samples were cleaned in a Ar/O_2 plasma. A test sample was measured before and after the plasma cleaning, showing no difference in texture information, only a faster deterioration of the pattern quality for the uncleaned sample. Analysis of the EBSD data was performed using the HKL Channel 5 software, combined with the GUSTAV software.

Two different types of measurements have been carried out: in a first measurement, EBSD data was collected in 420 000 individual measurement points, on a rectangular grid with a step size of 250 nm. Since the step size is as large or larger than the grain size, each data point is measured in a different grain. In this way, one can obtain texture information on a significant number of grains (10^5) in a reasonable measurement time. A second type of measurements uses a smaller step size, assuring that multiple data points are collected within each grain.

7.3.2 Identification of axiotaxy

From the EBSD measurements, pole figures were calculated and plotted on a log scale. These are shown in figure 7.6, where both the $\{103\}$ and the $\{202\}$+$\{211\}$ pole figures are shown for the 60 nm NiSi sample. If one compares them with the X-ray pole figures from figure 7.3, one can see that they are qualitatively identical, with the advantage that those calculated from the EBSD data do not suffer from substrate peak contamination as the EBSD signal originates from the top few nanometers of the sample.

The orientation densify function, and the Rodrigues-Frank space for the same data are shown in figure 7.7. The curved features in the ODF correspond to axiotaxy, and spots to epitaxy. The nature of the ODF makes it difficult to identify these features. On the other hand, the straight lines in Rodrigues-Frank space, and high intensity spots provide a much more clear representation of the texture.

On the 90 nm NiSi films, the results are identical and this confirmed that features on both the XRD and EBSD pole figures are identical. However, it was not possible to get EBSD patterns from the 24nm NiSi films annealed at 550°C, most likely due to the very small size of the grains.

7.3.3 Quantitative analysis of the texture

For the quantitative analysis, 4 axiotaxy components were considered, which will be indicated by specifying the plane normal ($\{211\}$, $\{202\}$, $\{103\}$ or $\{112\}$) which serves as fiber axis, and 1 epitaxial component. Because EBSD measures the complete orientation, one can simply walk through this list of data points and

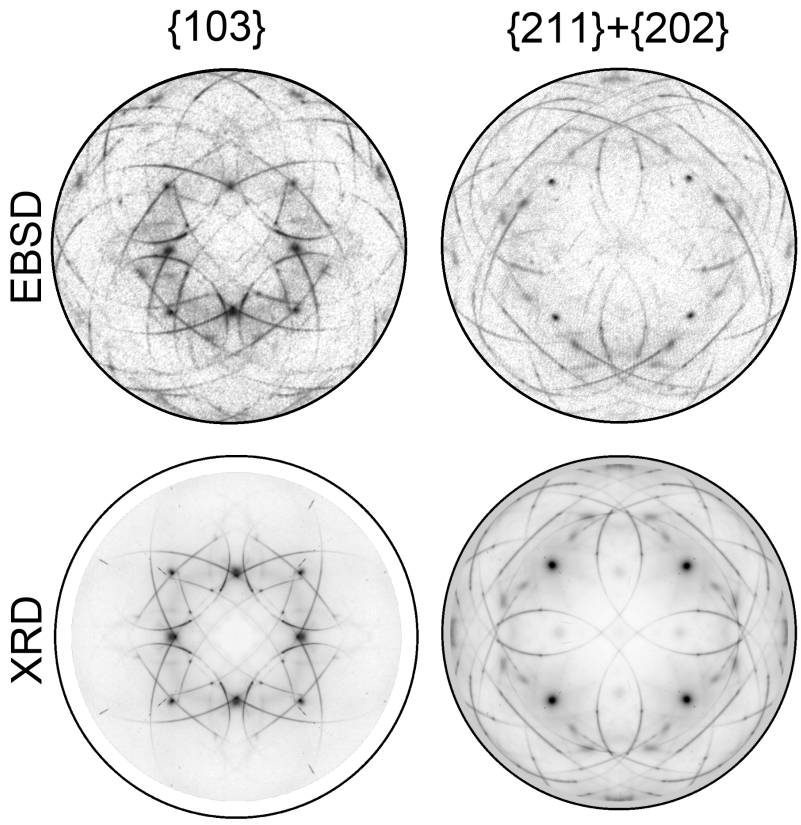

Figure 7.6: {103} and {202}+{211} pole figures, either recorded with XRD pole figures (Schulz method) or calculated from EBSD measurements on a 60 nm NiSi sample. The correspondence is clear, with the EBSD pole figures exhibiting more detail near the edges of the pole figure.

calculate the misorientation for each with respect to the texture component, taking into account the symmetry of the crystal lattice to obtain the disorientation. In the case of an epitaxial component, this is the minimum of all possible misorientation angles between the grain and the epitaxial orientation or a symmetrically equivalent orientation. As axiotaxy is defined as the fixed orientation of a specific plane, the misorientation is the minimal additional rotation a grain has to undergo, to make sure that in the resulting grain, this plane or a symmetrically equivalent one, has the specified orientation. From the disorientation for each combination of a data point and a texture component, the volume fractions for the various texture components are determined, as shown in table 7.1 for blanket films of 60 and 90 nm NiSi, where a maximum disorientation of 2° for axiotaxy components, and

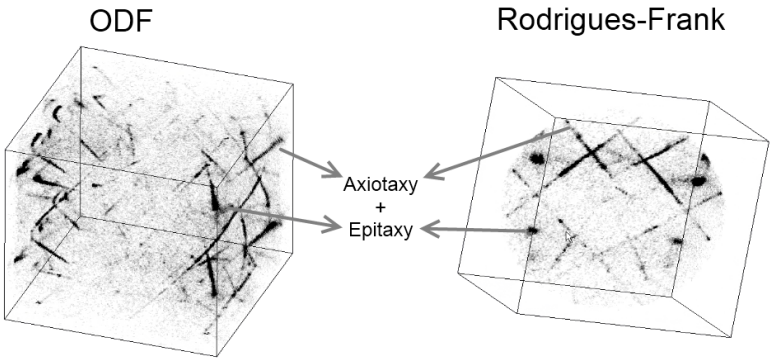

Figure 7.7: ODF and Rodrigues Frank visualization of the EBSD data with an epitaxial and axiotaxy texture component indicated.

Component	60 nm NiSi	90 nm NiSi (1)	90 nm NiSi (2)
211	19	16	15
202	17	17	15
103	5	4	4
112	3	2	2
epitaxy	3	2	2
total	45	41	38

Table 7.1: Volume fractions in % for a maximum misorientation of 2° for axiotaxy, and 3° for epitaxy

3° for epitaxy components is considered. The NiSi films are strongly textured, as almost 1 in 2 grains ($\approx 40\%$) belongs to one of the specified texture components. This also supports the division of the axiotaxy components into two groups, one with strong intensity ($\{211\}$ and $\{202\}$), and another with lower intensity ($\{103\}$ and $\{112\}$), corresponding to the better stability of the 1D periodic nature of the interface with respect to the curvature of the interface, for the $\{211\}$ and $\{202\}$ axiotaxy. The measurement on the 90 nm NiSi sample has been repeated using different settings for the SEM and the EBSD analysis software (last 2 columns of table 7.1): there is not a big impact on the volume fractions, suggesting that the error on the latter is of the order of a couple percent.

All of the axiotaxy features on the pole figures are sharply defined. One can quantify the variance within the various texture components by plotting the volume fractions as a function of the disorientation (figure 7.8). For all of the axiotaxy texture components, a peak in the fraction of grains can be seen at l° or less of disorientation, after which this fraction quickly falls off. This is especially clear for the strong axiotaxy components, $\{202\}$ and $\{211\}$: at around 2°, it has dropped

to less than half its peak value, which is the reason why a disorientation of 2° was chosen as the cut-off value in determining whether an orientation belongs to a specific axiotaxy texture component.

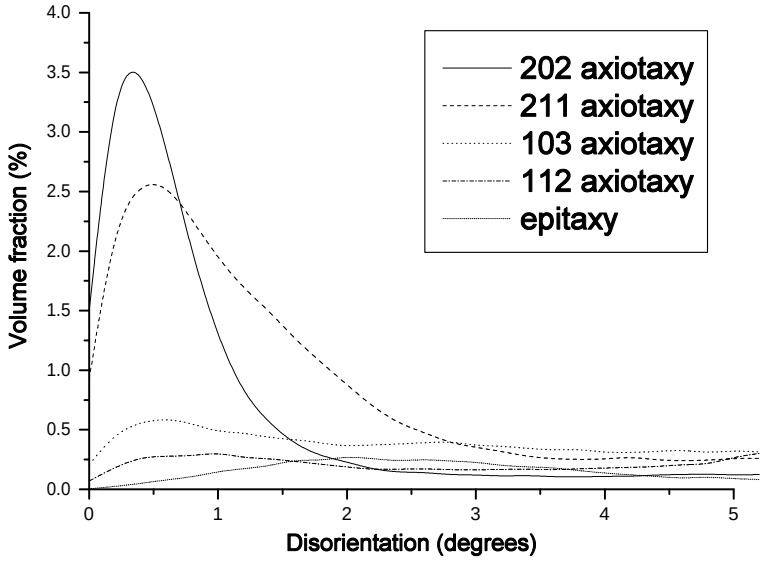

Figure 7.8: Volume fractions for a 60 nm NiSi film. One data point every 0.2° of misorientation.

For the epitaxial component, the peak value for the volume fraction occurs at 2°, and drops down a lot slower than for the axiotaxy. This is consistent with the observation that the epitaxial spots are quite broad on XRD pole figures. As a trade-off between accepting all the epitaxial data points, but not including too many randomly orientated points, a 3° cut-off value was selected.

These cut-off values can be compared to the intrinsic resolution of the measurement technique, which is limited by two factors. Firstly, the reported angular precision for EBSD when using a FEGSEM is about 1° [14], which could be reproduced by measuring a single crystal silicon wafer and calculating the misorientation between the successive data points. Secondly, the texture components are always defined in the reference frame of the single crystal substrate. However, EBSD measurements result in data in the reference frame of the microscope, which can be translated to the reference frame of the substrate if one knows how the sample was aligned inside the microscope. Based on a comparison between XRD pole figures, where the alignment of the sample can be done very precisely, and the

calculated EBSD pole figures, an estimate of the alignment of the sample in the microscope can be made with a precision of about 1°. Combining these two contributions, one can conclude that, for the axiotaxy components, the total error is about the same as the width of the peak, 2°. The spread on the orientation of the epitaxial component however, is larger, which indicates that the epitaxial grains have a few degrees of misorientation to one another.

7.3.4 Microstructure

A second type of measurements uses a smaller step size, assuring that multiple data points are collected within each grain. These EBSD measurements result in maps of grain orientation, showing the complete microstructure.

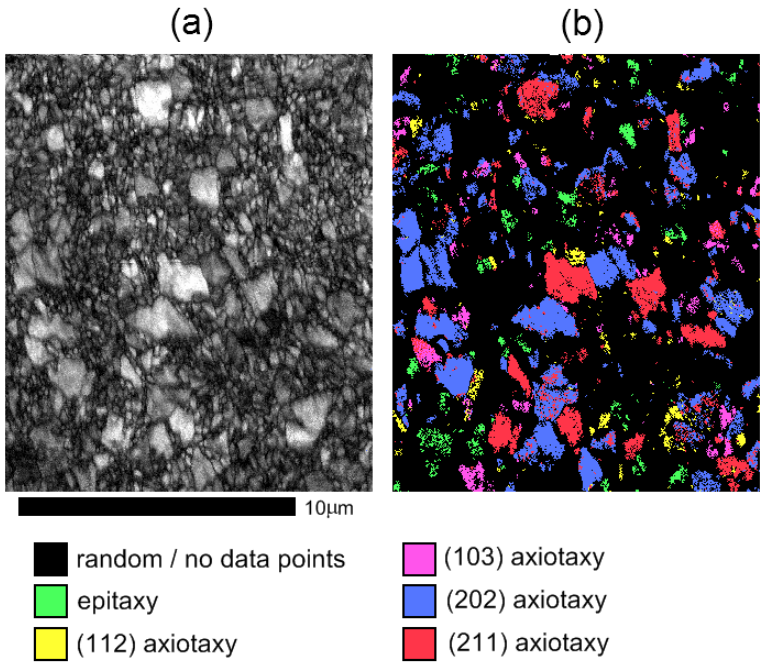

Figure 7.9: Map of a 90 nm NiSi film, showing band contrast (a) and texture components (b)

The left image in figure 7.9 is measured on the 90 nm NiSi sample with a step size of 40 nm and shows the band contrast, which is the measure for the quality of the Kikuchi pattern. Grain boundaries will typically result in worse contrast, and the band contrast map can therefore be used to get a qualitative idea of average grain size and morphology. The right image shows a false color image of the

location of grains that belong to different texture components. Again, a maximum disorientation of 2° (axiotaxy) or 3° (epitaxy) was used as the criterion to consider a grain as belonging to a certain texture component. From these maps, the spatial distribution of the texture components can be determined. The presented map clearly shows that almost all of the big grains belong to one of the axiotaxy texture components. These measurements show that the texture of NiSi also contains an important random fraction which consists mainly of very small grains. This suggests that the influence of interface energy on the nucleation is limited and that the origin of the axiotaxy texture is from a preferential growth of these axiotaxy nuclei. This can be caused either be a faster transport of material to the growing axiotaxy grains, or by strain effects, where the 1 dimensional matching of axiotaxy results in less strain during growth than in the case of randomly orientated grains.

A second conclusion can be drawn from the EBSD measurements: the rotational degree of freedom in orientation of the axiotaxy texture component is obtained through a different orientation of separate grains. This clearly distinguishes axiotaxy from transrotational structures, as the rotation in axiotaxy is *between* different grains, while the transrotation is *within* one grain.

7.4 Conclusions

In this chapter, the texture of NiSi on Si (100) substrates was discussed, and the importance of axiotaxy was established. It was shown the EBSD can be used to provide valuable information on the texture of silicides, making it possible to quantify the importance of texture components, get spatial and grain size information and relate this to specific texture components. Axiotaxy is confirmed as being the major texture component in NiSi films on Si(100) substrates, and a difference in grain size between axiotaxy and non-axiotaxy grains was observed.

8

Texture of $CoSi_2$ on Si (001), (111) and (110)

In view of the small lattice mismatch and similar crystallographic structure between $CoSi_2$ (cubic CaF_2 structure with $a = 5.36\mathring{A}$) and Si (cubic diamond structure with $a = 5.43\mathring{A}$), one expects that $CoSi_2$ will have a natural tendency to form epitaxially on Si substrates. However, it has proven surprisingly difficult to grow epitaxial $CoSi_2$ layers, especially on (001) oriented Si substrates [75, 76, 77, 78, 79, 80, 81, 82, 83, 84]. Bulle-Lieuwma et al. reported a detailed transmission electron microscopy study of $CoSi_2$/Si (001) interfaces [85], where it was observed that a variety of different alignments occur simultaneously. Each of these alignments can be considered as epitaxy by itself, but their combination results in the polycrystalline nature of the $CoSi_2$ on Si (001) film. In this chapter, the naturally occurring texture that is the result of a standard solid-state reaction between a Co film and three differently oriented Si substrates, i.e. Si (001), Si (111) and Si (110) will be discussed.

The results discussed in this chapter have been published in:

De Keyser K., Detavernier C., Jordan-Sweet J. and Lavoie C., *Texture of $CoSi_2$ films on Si(111), (110) and (001) substrates*, Thin Solid Films 519 (4), 1277-1284 (2010)

8.1 Experimental details

A 30 nm Co film was sputter deposited onto HF-cleaned Si(001), (110) and (111) substrates using an ultra-high-vacuum sputtering system. $CoSi_2$ was formed by a solid-state reaction between the Co film and the Si substrate, by annealing the sample for 30 seconds at 950°C in forming gas (N_2/H_2).

The samples were characterized using X-ray diffraction (XRD). Both θ-2θ scans, as well as pole figures using the Schulz method (point detector) were recorded, using an X-ray wavelength of $\lambda = 0.154$ nm. The pole figures were acquired in steps of 0.5° in χ and ϕ ($0 \leq \chi \leq 85°$ and $0 \leq \phi \leq 90°$ for Si(001) and Si(110), $0 \leq \phi \leq 120°$ for Si(111) substrates). The location of low-index substrate poles for the three types of substrates is indicated in figure 8.1. In view of the symmetry of the Si lattice, one only needs to measure $0 \leq \phi \leq 45°$ for Si(001), $0 \leq \phi \leq 90°$ for Si(110) and $0 \leq \phi \leq 60°$ for films on Si(111) substrates. It was decided to measure twice the necessary angular ϕ range for Si(111) and Si(001) substrates, to enable straightforward verification of the observed features in the pole figures. The complete pole figures were obtained by extending the measured data to the full range $0 \leq \phi \leq 360°$ by taking into account the symmetry of the Si substrate. The intensities are plotted using a logarithmic gray scale, where white corresponds to low intensity, and black to high.

8.2 Measurements

8.2.1 θ-2θ XRD scans

Standard $\theta/2\theta$ measurements for the three samples are shown in figure 8.2. The observation of many diffraction peaks in each of the three samples proves that the films are polycrystalline. Since the peak intensities strongly depend on the orientation of the substrate, and since the intensities in all three measurements are very different from what is expected for a $CoSi_2$ powder, one may conclude that the grains in the polycrystalline $CoSi_2$ films exhibit a high degree of preferential orientation, i.e. all three films are surely textured.

8.2.2 Pole figures for $CoSi_2$ on Si(111)

Pole figures were measured for the $CoSi_2\{111\}$ and $\{110\}$ planes (fig. 8.3). The features on these pole figures were used to identify the various texture components that are present in the film (table 8.1), using GUSTAV.

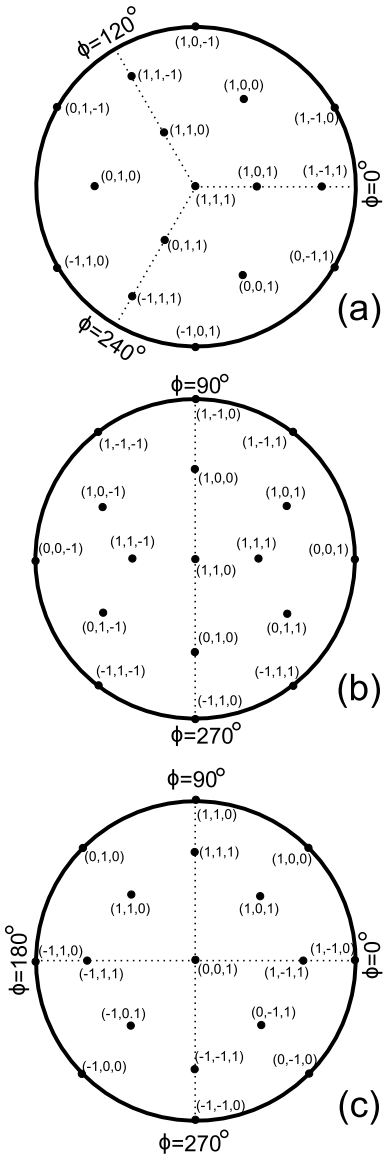

Figure 8.1: The location of low-index poles of the Si substrate for the sample alignments for (a) a Si(111) substrate, (b) a Si (110) substrate, (c) a Si (001) substrate

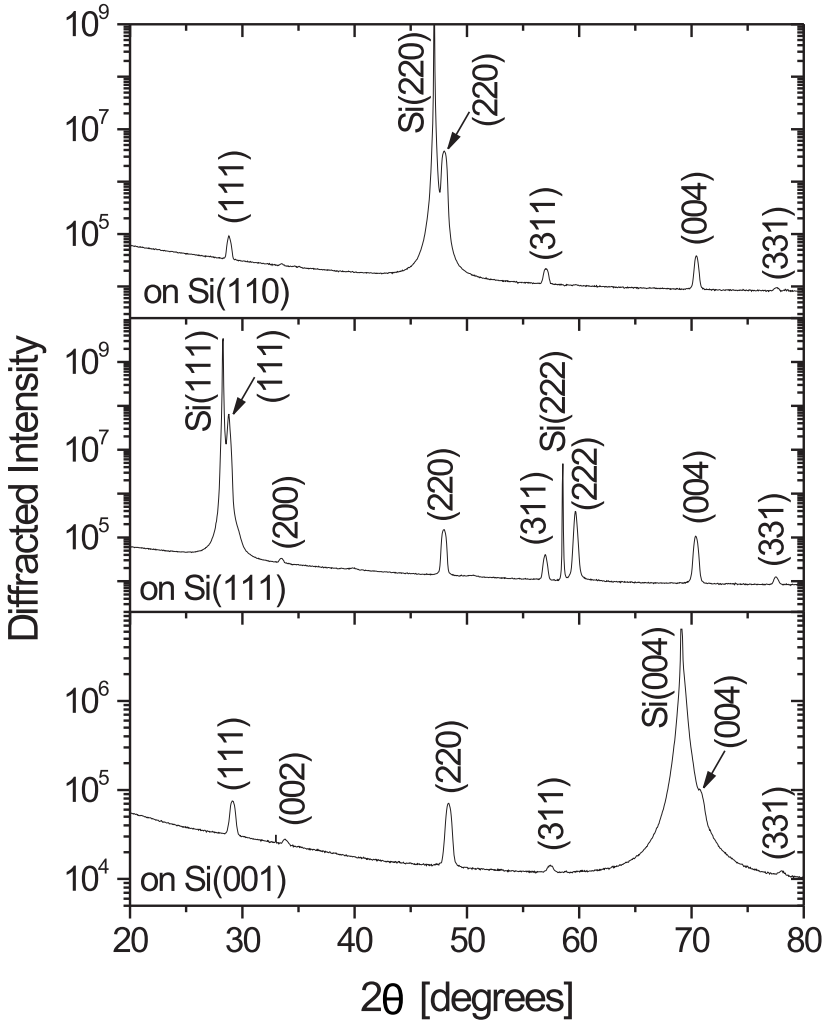

Figure 8.2: $\theta/2\theta$ XRD measurements for $CoSi_2$ films on Si(001), (111) and (110) substrates. The peaks are indexed according to cubic $CoSi_2$ (JCPDS 74-1371)

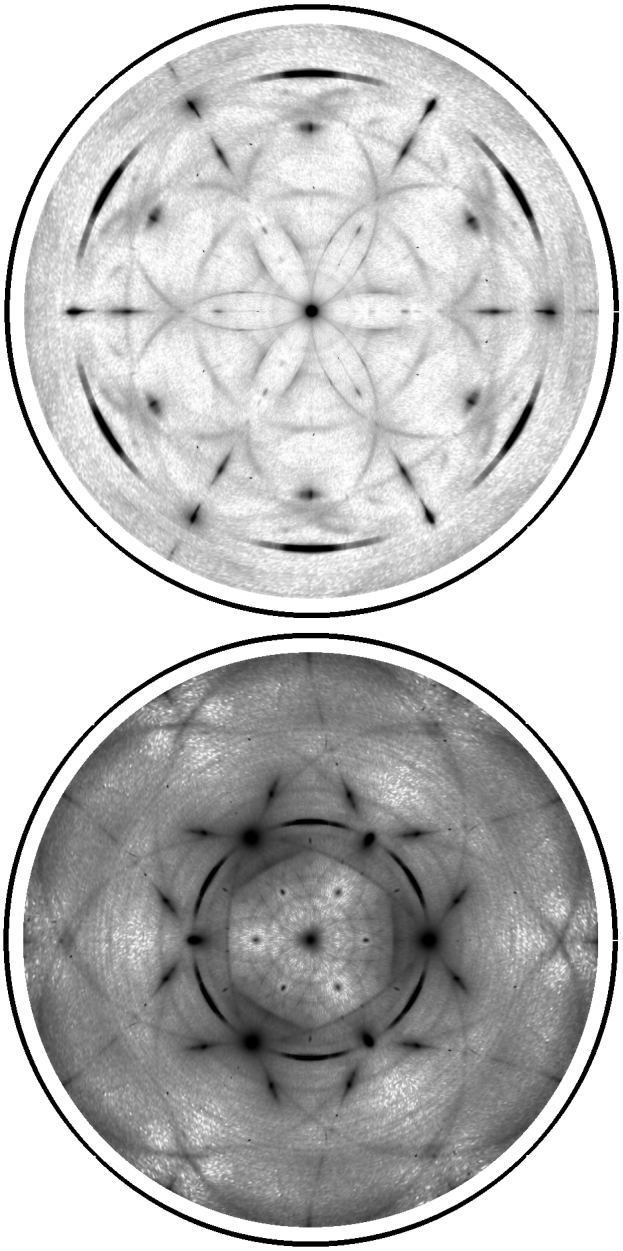

Figure 8.3: The $\{111\}$ (top) and $\{110\}$ (bottom) pole figures for a $CoSi_2$ film on Si(111).

Table 8.1

axiotaxy α_{111}	Fig. 8.4	an off-normal $CoSi_2$ (110) fiber texture with the fiber axis near $\chi = 35°$, $\phi = 0, 120, 240°$
axiotaxy β_{111}		an off-normal $CoSi_2$ (110) fiber texture with the fiber axis at $\chi = 90°$, $\phi = 30, 90, 150, 210, 270, 330°$
axiotaxy γ_{111}	Fig. 8.4	a twinned version of α_{111}, i.e. a $CoSi_2$ (110) fiber texture with the fiber axis near $\chi = 35°$, $\phi = 60, 180, 300°$
fiber I_{111}		a $CoSi_2$ (111) fiber texture with the fiber axis perpendicular to the surface (i.e. at $\chi = 0°$)
epitaxy A_{111}	Fig. 8.5(+)	with $CoSi_2$ (111) // Si(111) and $CoSi_2$ (110) // Si(110)
epitaxy B_{111}	Fig. 8.5(×)	a twinned version of A_{111} by rotating it over 180° around the Si[111] direction
epitaxy C_{111}	Fig. 8.5(○)	with $CoSi_2$ (001) // Si(111) and $CoSi_2$ $(1\bar{1}0)$ // Si$(\bar{1}10)$
epitaxy D_{111}	Fig. 8.5(□)	with $CoSi_2$ (111) // Si(111) and $CoSi_2$ $(11\bar{2})$//Si$(\bar{1}01)$
epitaxy E_{111}	Fig. 8.5(◇)	a twinned version of D_{111} by rotating it over 180° around the Si[111] direction

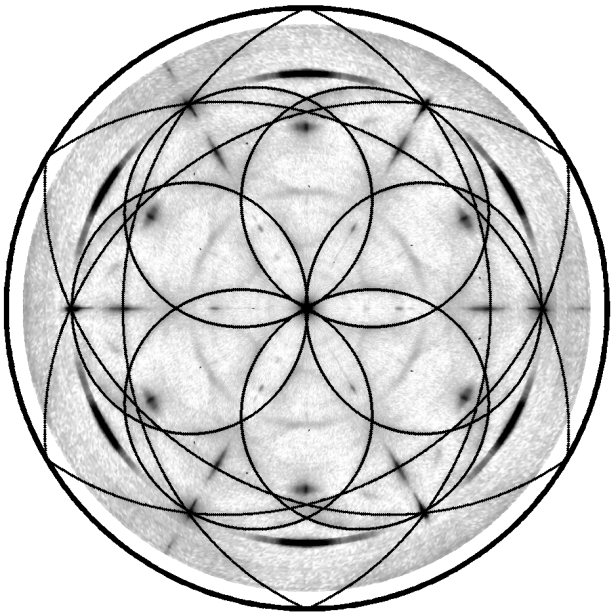

Figure 8.4: The (111) pole figure for a $CoSi_2$ film on Si(111), with the calculated patterns for α_{111} and γ_{111} type axiotaxy.

8.2.2.1 Axiotaxy

The patterns of lines on the pole figures are indicative of axiotaxy. They are caused by grains for which the $CoSi_2\{110\}$ plane is aligned parallel to $Si\{110\}$. Table 8.1 presents an overview of the different axiotaxy components that were observed in the $CoSi_2$ film on Si(111). Calculated patterns for the α_{111} and γ_{111} components are shown in figure 8.4, overlaid on top of the measured data. The α_{111} and β_{111} types of axiotaxy are both characterized by the preferred alignment of $CoSi_2\{110\}$ with $Si\{110\}$, i.e. with the fiber axes at either ($\chi = 35°$, $\phi = 0, 120, 240°$) or at ($\chi = 90°$, $\phi = 30, 90, 150, 210, 270, 330°$). A third type of axiotaxy is a twinned version of α_{111}, with the fiber axes rotated over 180° around the Si[111] direction.

8.2.2.2 Epitaxy

According to figure 8.5, the brightest spots on the pole figures are caused by five different types of epitaxial alignment, with either a $CoSi_2$ $\{111\}$ or $CoSi_2$ $\{100\}$ plane parallel to the Si (111) surface plane. The occurrence of different types of epitaxial components is somewhat surprising. Indeed, in view of the close lattice

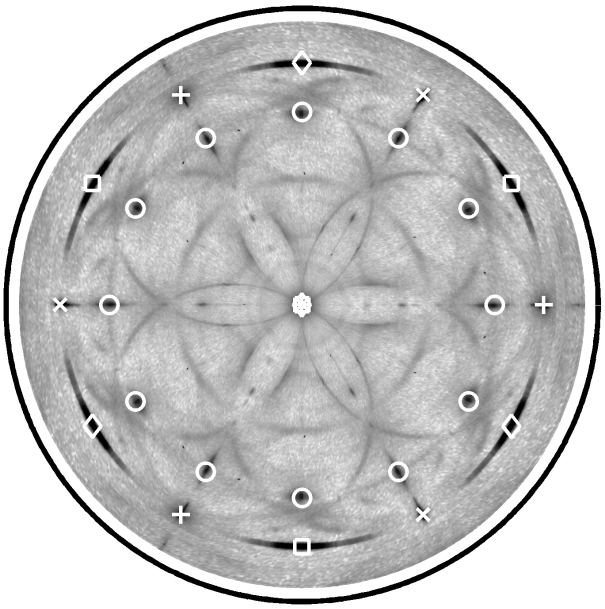

Figure 8.5: The (111) pole figure for a $CoSi_2$ film on Si (111), with the calculated locations for the epitaxial components from table 8.1 overlaid on top of the measurement. Poles labeled + refer to grains with type A_{111} epitaxy (with $CoSi_2$ (111) parallel to the surface), × indicates type B_{111} epitaxy (twin of type A_{111}), ○ refers to type C_{111} epitaxy (with $CoSi_2$ (100) parallel to the surface), □ and ◇ refer to types D_{111} and E_{111} (with $CoSi_2$ (111) parallel to the surface).

match and similar structure of $CoSi_2$ and Si, one could a priori expect a behavior similar to the growth of single crystal SiGe films on Si, which would only result in type A_{111} epitaxy (which is a simple continuation of the cubic substrate lattice into the film). The type B_{111} epitaxy has been studied extensively [75], and is a twinned version of type A_{111} (i.e. formed by a 180° rotation around the Si[111] direction).

Many of the intense spots that are indicative of the epitaxial components are located along the pattern of lines on the pole figure, suggesting that the different epitaxial components are somehow related to the axiotaxy, a topic which will be discussed further on.

8.2.3 Pole figures for $CoSi_2$ on Si (110)

As could be expected on the basis of the $\theta/2\theta$ measurement shown in figure 8.2, the $CoSi_2$ film on Si (110) is strongly textured. The pole figures are shown in figure 8.6. The different texture components are listed in table 8.2.

8.2.3.1 Axiotaxy

The patterns of lines observed in the pole figures (fig. 8.6) are caused by a variety of axiotaxial texture components, with either $CoSi_2\{110\}$//$Si\{110\}$ (for α_{110}, β_{110} and I_{110}), $CoSi_2\{111\}$//$Si\{111\}$ (for γ_{110}) and $CoSi_2\{112\}$//$Si\{112\}$ (for δ_{110}). In view of the large number of components and the relative complexity of the corresponding line patterns, not all calculated patterns are shown. Figure 8.7 shows the fitted patterns for the α_{110}, γ_{110} and I_{110} components overlaid on top of the measured $\{110\}$ pole figure.

8.2.3.2 Epitaxy

According to figure 8.8, the brightest spots on the pole figures are caused by different types of epitaxial alignment. Similarly as for the film on Si (111), it may be noted that most of the intense spots that are indicative of the epitaxial components are located along the pattern of lines on the pole figure. Further on, the relationship between the different epitaxial components and the axiotaxy will be discussed.

8.2.4 Pole figures for $CoSi_2$ on Si (001)

The $\{111\}$ and $\{110\}$ pole figures for $CoSi_2$ on Si (001) are presented in fig. 8.9 and the list of different texture components for the $CoSi_2$ film on Si (001) are listed in table 8.3.

In contrast to the cases where the substrate was Si (111) or Si (110), where little information regarding the texture of $CoSi_2$ was available in literature, $CoSi_2$ films on Si (001) substrates have already been studied in detail. The occurrence of axiotaxy in $CoSi_2$ on Si (001) has been reported in [57]. The observed axiotaxy components that are listed in table 8.3 correspond to those. The brightest spots along the lines on the pole figures are caused by four different types of epitaxial alignment that coexist within the same film : A_{001} with $CoSi_2$ (001) // Si (001), B_{001} with $CoSi_2$ (221) // Si (001), C_{001} with $CoSi_2$ (101) // Si (001) and D_{001} with $CoSi_2$ $(33\bar{5})$ // Si (001). The calculated locations of the poles for these epitaxial orientations are shown in figure 8.9. All four epitaxial components that are observed in the present

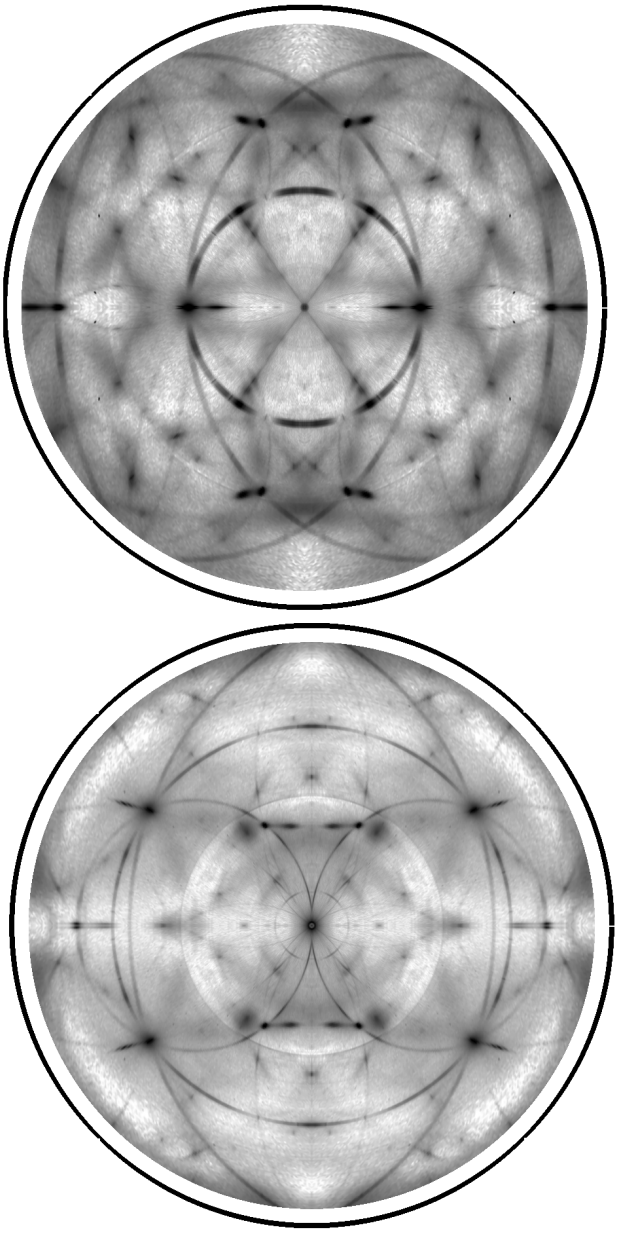

Figure 8.6: The $\{111\}$ (top) and $\{110\}$ (bottom) pole figures for a $CoSi_2$ film on Si (110).

Table 8.2

axiotaxy α_{110}	Fig. 8.7	an off-normal $CoSi_2$ (110) fiber texture with the fiber axis at $\chi = 90°$, $\phi = 90, 270°$
axiotaxy β_{110}		an off-normal $CoSi_2$ (110) fiber texture with the fiber axis at $\chi = 60°$, $\phi = 35, 145, 215, 325°$
axiotaxy γ_{110}	Fig. 8.7	an off-normal $CoSi_2$ (111) fiber texture with the fiber axis at $\chi = 35°$, $\phi = 0, 180°$
axiotaxy δ_{110}		a weak off-normal $CoSi_2$ (112) fiber texture with the fiber axis at $\chi = 90°$, $\phi = 35, 145, 215, 325°$
fiber I_{110}	Fig. 8.7	a $CoSi_2$ (110) fiber texture with the fiber axis perpendicular to the surface (i.e. at $\chi = 0°$)
epitaxy A_{110}	Fig. 8.8 ($\times$)	with $CoSi_2$ (110) // Si (110) and $CoSi_2$ ($1\bar{1}0$) // Si ($1\bar{1}0$)
epitaxy B_{110}	Fig. 8.8 ($\circ$)	with $CoSi_2$ (411) // Si (110) and $CoSi_2$ ($0\bar{1}1$) // Si ($1\bar{1}0$)
epitaxy C_{110}	Fig. 8.8 ($\square$)	with $CoSi_2$ ($3\bar{1}\bar{1}$) // Si (110) and $CoSi_2$ ($0\bar{1}1$) // Si ($1\bar{1}0$)
epitaxy D_{110}	Fig. 8.8 ($\diamond$)	with $CoSi_2$ ($10\bar{1}$) // Si (110) and $CoSi_2$ ($1\bar{2}1$) // Si ($1\bar{1}0$)
epitaxy E_{110}	Fig. 8.8 ($+$)	with $CoSi_2$ (111) // Si (111) and $CoSi_2$ ($\bar{1}\bar{1}2$) // Si ($21\bar{3}$)
epitaxy F_{110}	Fig. 8.8 ($\bullet$)	with $CoSi_2$ ($0\bar{1}1$) // Si (101) and $CoSi_2$ ($\bar{1}21$) // Si ($1\bar{1}\bar{2}$)
epitaxy G_{110}	Fig. 8.8 ($\star$)	with $CoSi_2$ (010) // Si (110) and $CoSi_2$ (001) // Si (001)

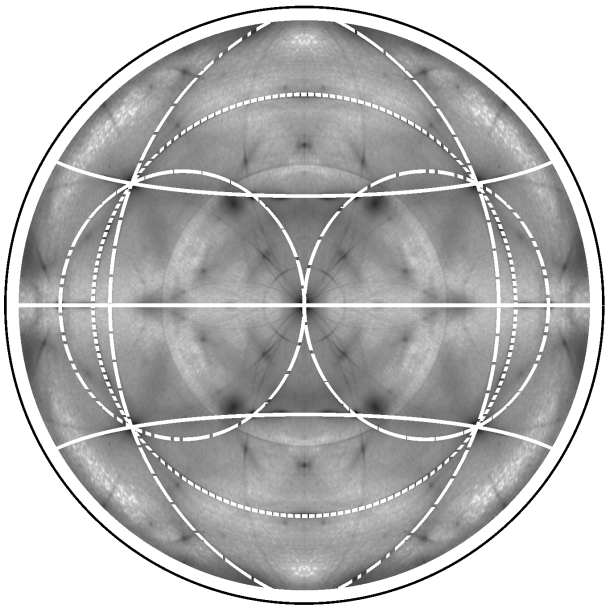

Figure 8.7: The (110) pole figure for a $CoSi_2$ film on Si (110) with the calculated pattern for the α_{110} (full line), γ_{110} (dash) and I_{110} (dotted) axiotaxy components overlaid on top of the measured data.

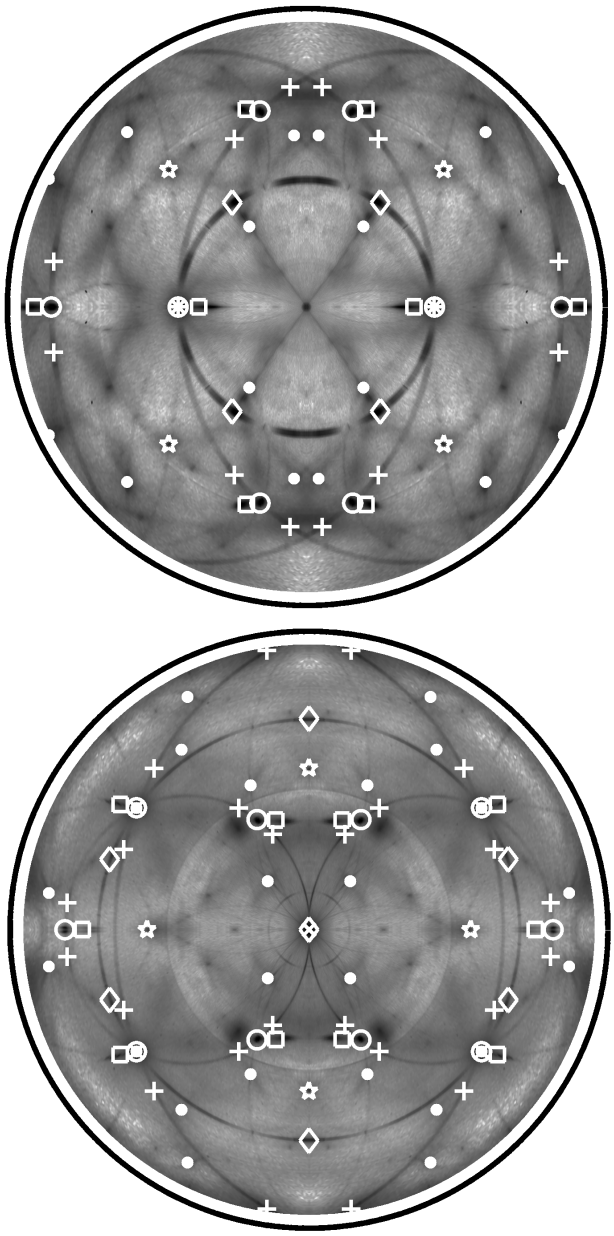

Figure 8.8: The (111) (top) and (110) (bottom) pole figures for the $CoSi_2$ film on Si (110), with the calculated locations for the epitaxial components from table 8.2 overlaid on top of the measurement. See table 8.2 for the definition of the symbols.

film have been previously reported in a detailed transmission electron microscopy study of the $CoSi_2$/Si (001) interface by Bulle-Lieuwma et al. [85].

8.3 Relation between the texture of $CoSi_2$ on Si (001), Si (111) and Si (110)

In the previous section, analysis of the pole figures allowed for the identification of the various texture components, and tables 8.1, 8.2 and 8.3 provide a crystallographic description of the preferred orientation in the three films. During the following discussion, an attempt will be made to rationalize why these particular grain orientations are selected, how these texture components relate to each other, and how the choice of substrate orientation affects the texture of the film.

8.3.1 Comparison of axiotaxial components for the three substrates

The line patterns on the pole figures are caused by grains for which lattice planes in film and substrate with similar d-spacings are aligned with each other. For instance, at the formation temperature of $CoSi_2$ (600°C [86], thermal expansion $CoSi_2$ = 14.2 ppm/K [87], thermal expansion Si = 2.6 ppm/K) the difference in d-spacing between $CoSi_2$ $\{110\}$ planes ($d = 1.920\mathring{A}$) and Si$\{110\}$ planes ($d = 1.924\mathring{A}$) is only 0.21%, and the alignment of these planes across the interface results in the creation of an interface structure which is periodic along a Si[100]-type direction in the plane of the interface. This axiotaxy results in a 1D periodicity within the plane of the interface, and axiotaxy can be considered as an intermediate case between the 2D periodicity characteristic of epitaxial alignment and the absence of periodicity for a random interface.

A cross-comparison of the different axiotaxy components that were observed for the three substrate orientations suggests that plane-alignment of $CoSi_2\{110\}$ with Si$\{110\}$ planes is strongly favored. A similar preference for alignment with Si$\{110\}$ planes has been previously observed for NiSi and α-$FeSi_2$ [2, 58]. While this apparent preference for alignment with Si$\{110\}$ is presently not fully understood, one possible explanation is related to the covalent bonding in the Si substrate. The bonds in Si are along $[111]$ directions, and two of the four bonds per atom are within a Si$\{110\}$ plane. None of the covalent bonds are within Si$\{100\}$ planes.

If plane alignment occurs with Si$\{110\}$ planes, the fiber axis is perpendicular to two of the four covalent bonds. Any rotation of the $CoSi_2$ grain around the fiber axis (which is oriented along a Si$[110]$ direction) will result in a deformation of

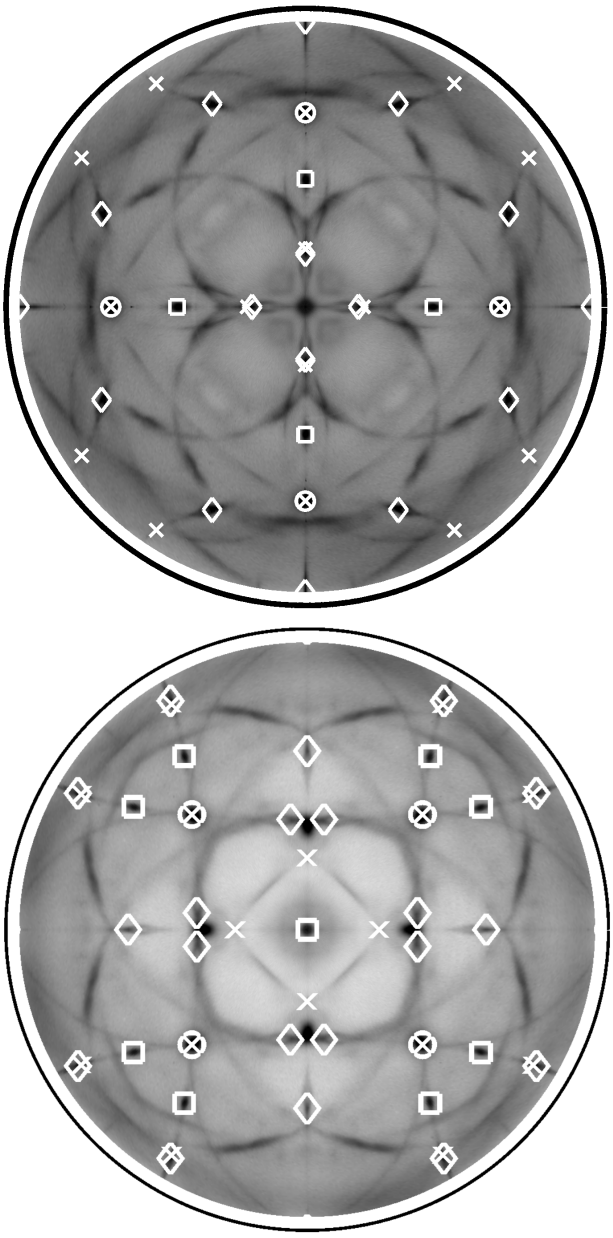

Figure 8.9: The (111) (top) and (110) (bottom) pole figures for the $CoSi_2$ film on Si (001), with the calculated locations for the epitaxial components from table 8.3 overlaid on top of the measurement. Poles labeled ∘ refer to grains with type A_{001} epitaxy (with $CoSi_2$ (001) parallel to the surface), × indicates type B_{001} epitaxy (with $CoSi_2$ (122) parallel to the surface), □ refers to type C_{001} epitaxy (with $CoSi_2$ (101) parallel to the surface) and ⋄ refers to type D_{001} epitaxy (with $CoSi_2$ (335) parallel to the surface).

Table 8.3

axiotaxy α_{001}	see [57]	off-normal $CoSi_2$ (110) fiber texture with the fiber axis at $\chi = 45°$, $\phi = 45, 135, 225, 315°$
axiotaxy β_{001}	see [57]	off-normal $CoSi_2$ (110) fiber texture with the fiber axis at $\chi = 90°$, $\phi = 0, 90, 180, 270°$
axiotaxy γ_{001}	see [57]	weak off-normal $CoSi_2$ (110) fiber texture with the fiber axis at $\chi = 30°$, $\phi = 0, 90, 180, 270°$
epitaxy A_{001}	Fig. 8.9 (○)	with $CoSi_2$ (001) // Si (001) and $CoSi_2$ (110) // Si (110)
epitaxy B_{001}	Fig. 8.9 (×)	with $CoSi_2$ $(1\bar{2}2)$ // Si (001) and $CoSi_2$ $(1\bar{1}0)$ // Si (101)
epitaxy C_{001}	Fig. 8.9 (□)	with $CoSi_2$ $(10\bar{1})$ // Si (001) and $CoSi_2$ (101) // Si $(1\bar{1}0)$
epitaxy D_{001}	Fig. 8.9 (◇)	with $CoSi_2$ $(5\bar{3}3)$ // Si (001) and $CoSi_2$ (011) // Si $(1\bar{1}0)$

the bonds for Si atoms located within the plane of the interface. The deformation of the Si bonds in this case actually resembles what happens when forming dimer-rows during the surface reconstruction of non-hydrogen terminated Si (001) substrates, suggesting that such deformation is energetically 'inexpensive'. For plane alignment with e.g. Si$\{100\}$ planes, there is no straightforward relationship between the direction of the fiber axes and the bonding directions for the Si atoms. Therefore, any rotation around such a fiber axis would imply severe deformation of the Si bonds.

Alternatively, in the edge-to-edge model [8], which is conceptually related to axiotaxy as it considers plane-to-plane matchings, the argument is made that atom rows that are close-packed will preferentially align. One can show that there is a relation between the structure factor of a plane and its packing [88], resulting in close-packed planes having the highest structure factors. If one lists the four planes with the highest structure factors, one gets in descending order for $CoSi_2$: $\{220\}$, $\{111\}$, $\{113\}$ and $\{224\}$, and for Si: $\{111\}$, $\{220\}$, $\{113\}$ and $\{224\}$. One can indeed observe that the axiotaxy texture components correspond to the alignment of $CoSi_2$ and Si planes from this selection, with the strongest components corresponding to the crystallographic planes with either the highest or second highest structure factors.

8.3.2 Relationship between axiotaxy and epitaxy

Both the location and shape of the epitaxy-related spots on the pole figures provide strong indications for a relationship between axiotaxial and epitaxial texture components. Indeed, the spots are often located along the pattern of lines on the pole figures, sometimes even at the intersection between two patterns of axiotaxy-related lines. This suggests that the epitaxial components are in fact special cases (subsets) of the axiotaxial components.

When placing a grain on a substrate, there are three degrees of freedom for orientation. Axiotaxy fixes the orientation of e.g. one of the $CoSi_2\{110\}$ planes parallel to a certain Si$\{110\}$ plane. Fixing the orientation for one plane in the grain provides a constraint which leaves a single degree of freedom (i.e. rotation around the fiber axis), creating one-dimensional features on the pole figures. The interfaces of all grains that belong to this axiotaxial component will be periodic along a certain low-index direction within the plane of the interface (1D periodicity). It can be expected that certain specific rotations around the fiber axis may result in the occurrence of periodicity along a second, independent direction within the plane of the interface, thus providing better matching across the interface and therefore resulting in a lower interface energy. This explains why the diffracted intensity is not homogeneously distributed along the axiotaxy-related lines on the pole figure:

certain angles for rotation around the off-normal fiber axes are preferred because they result in a higher degree of periodicity within the plane of the interface. The choice for the rotation angle around the off-normal fiber axis is actually defining a second constraint, which results in a situation with zero remaining degrees of freedom, i.e. the orientation of the grain is completely defined with respect to the single crystal substrate, and one obtains an epitaxial alignment. This explains why the epitaxial texture components can be located along the axiotaxy lines.

8.3.3 Relationships between the epitaxial components

At first sight, the epitaxial components listed in tables 8.1, 8.2 and 8.3 appear to be unrelated to each other. Traditionally, one considers these epitaxial components as the main texture components (as one is tempted on the basis of either a transmission electron microscopy study with a limited number of grains, or from a low resolution pole figure with limited signal to noise ratio [85]). In this interpretation, one emphasizes the 2D matching within the plane of the interface (i.e. plane-on-plane matching between the topmost lattice plane of the substrate and the lowest lattice plane in the silicide grain) as the main driving force for texture selection.

Alternatively, one can interpret the occurrence of the axiotaxy-related lines as an indication that the primary constraint on grain orientation concerns the preferred alignment of lattice planes across the interface (i.e. edge-to-edge matching of lattice planes that continue seemingly uninterrupted from the substrate into the film). In this view, the epitaxial components are special cases or subsets of axiotaxy, whereby the selection of a second constraint results in a 2D periodic interface. Apart from explaining the patterns of lines on the high-resolution pole figures, this approach has the additional advantage that it offers a unified view of the different, seemingly unrelated epitaxial components.

Indeed, table 8.4 shows that nearly all of the observed epitaxial components can in fact be considered as special cases or subsets of the axiotaxial texture components. One can distinguish two subcategories: epitaxial components for which axiotaxy occurs for two independent sets of $CoSi_2$ $\{110\}$-type planes within the same grain (a situation which will henceforth be referred to as 'double axiotaxy'), and epitaxial components for which the interface structure is periodic along one direction because of axiotaxy, while the periodicity along a second independent direction is not related to axiotaxy, but is a result of the specific properties of either the Si (001), (111) or (110) interface plane. This classification of the epitaxial components offers a way of predicting which components are transferable between substrate orientations. Since axiotaxy is a matching across the interface, the influence of the specific interface plane is only limited. Thus, the epitaxial components that are caused by double-axiotaxy are transferable between different

Table 8.4

Component	Type of $CoSi_2$ plane parallel to the surface	Classification of the epitaxial component
A_{111}	111	double axiotaxy (combination of α_{111} and β_{111})
B_{111}	111	twinned version of A_{111}
C_{111}	100	single axiotaxy β_{111} and $CoSi_2$ (100)-type plane parallel to the surface
D_{111}	111	subcategory of fiber I_{111}
E_{111}	111	twinned version of D_{111}
A_{110}	110	double axiotaxy (combination of α_{110} and β_{110})
B_{110}	114	double axiotaxy (combination of α_{110} and β_{110})
C_{110}	113	single axiotaxy α_{110} and $CoSi_2$ (113)-type plane parallel to the surface
D_{110}	101	subcategory of fiber I_{110}
E_{110}	high index	double axiotaxy (combination of γ_{110} and γ_{110})
F_{110}	high index	double axiotaxy (combination of β_{110} and δ_{110})
G_{110}	010	epitaxy
A_{001}	001	double axiotaxy (combination of α_{001} and β_{001})
B_{001}	122	double axiotaxy (combination of α_{001} and β_{001})
C_{001}	101	single axiotaxy β_{001} and $CoSi_2$ (101)-type plane parallel to the surface
D_{001}	335	single axiotaxy β_{001} and $CoSi_2$ (335)-type plane parallel to the surface
E_{001}	112	geometrically allowed double axiotaxy (combination of β_{001} and γ_{001}), reported in [85]

substrate orientations. For instance, types A_{001} and A_{111} are crystallographically identical, and the same is valid for B_{001} and D_{111}. However, the epitaxial components that are not related to double axiotaxy (e.g. C_{111}, C_{110} and C_{001}) depend on a particular substrate orientation. For example, it can be verified that transferring the C_{001} component to a Si (111) substrate would result in an orientation with the $CoSi_2\{105\}$ plane parallel to the Si (111) interface, a situation which is not observed experimentally.

8.3.4 Double axiotaxy

The case of double axiotaxy deserves some further discussion. One can think of the axiotaxial components as families or sets of grains which share a certain constraint on grain orientation (e.g. $CoSi_2$ (011)//Si (011)). The case of double axiotaxy should be considered as the intersection between two different sets of grains, i.e. it defines a subset of grains that fulfil both constrains. For instance, type A_{001} corresponds to a situation whereby $CoSi_2$ (011)//Si (011) and $CoSi_2$ (110)//Si (110), and therefore constitutes the intersection between α_{001} and β_{001}. When two independent types of axiotaxy are combined within the same grain, there are two independent directions within the plane of the interface along which a periodic interface structure is achieved. Since periodicity is achieved along two independent directions, the whole interface consists of a two-dimensional periodic structure, which leads to the interface "matching" well-known for epitaxial alignment.

Double axiotaxy can thus occur in films which have more than one axiotaxial texture component (either due to different types of planes that match, or due to symmetry), and each combination of any two of these axiotaxial texture components can in principle lead to a double axiotaxy. However, some combinations will not be geometrically possible due to the specific symmetry and size of the lattice. GUSTAV was used to determine which combinations of double-axiotaxy are geometrically allowed for the $CoSi_2$ case.

8.3.4.1 Double axiotaxy on Si (110)

For the Si (110) substrate, it was found that combinations of α_{110} and β_{110} can only result in type A_{110} and B_{110} epitaxy, with $CoSi_2$ $\{110\}$ or $\{114\}$ planes parallel to the Si (110) substrate.

8.3.4.2 Double axiotaxy on Si (001)

For the Si (001) substrate, it was found that combinations of type α_{001} and β_{001} axiotaxy can only result in types A_{001} or B_{001} epitaxy (i.e. with $CoSi_2$ $\{100\}$ or $\{221\}$ planes parallel to the Si (001) substrate). When also taking into account combinations with the weaker type γ_{001} axiotaxy, one finds two other possible epitaxial alignments with either a $CoSi_2$ (112) or (455)-type plane parallel to the surface. The (112)-type of epitaxial alignment has been observed by Bulle-Lieuwma et al. using transmission electron microscopy [85].

8.3.4.3 Double axiotaxy on Si (111)

A similar analysis for the Si (111) substrate showed that combinations of α_{111} and β_{111} can result in two types of epitaxy : A_{111} (with $CoSi_2$ $\{111\}$ parallel to the Si (111) interface), or an orientation with the $CoSi_2$ (115)-type plane parallel to the surface and interface of the film. While this type of alignment is geometrically allowed, it does not preferentially occur within the measured film. One could argue that the relatively high index nature of the surface plane for this type of orientation may explain why the A_{111}-type epitaxy (with the lower index $CoSi_2$ (111) plane parallel to the surface) is apparently favored.

8.3.5 Twinning

Apart from the apparent preference in the three films for the preferred alignment of $CoSi_2$ (110)-type planes with Si (110)-type planes in the substrate, one also observes a general tendency for twinning around the Si$[111]$ direction. For the axiotaxial components, it was previously mentioned that γ_{111} is a twinned version of α_{111}-axiotaxy. For the epitaxial components, twinning relationships exist between e.g. A_{111} and B_{111}, between A_{110} and B_{110}, and between A_{001}, B_{001} and D_{001} (as previously mentioned by Bulle-Lieuwma [85]).

8.4 Conclusions

We used x-ray diffraction to study the texture of about 100 nm thick $CoSi_2$ films that were formed by a solid state reaction on Si substrates. All measured pole figures consist of two different types of features : patterns of lines and bright spots. The patterns of lines are generated by axiotaxy, i.e. by the preferred alignment of lattice planes in film and substrate that share the same d-spacing. The bright spots are related to epitaxial alignment of grains in the film with the single crystal

substrate. The axiotaxial and epitaxial texture components were identified, and the different texture components were shown to be inter-related. Comparison of the different texture components observed on the three substrate orientations suggests a strong preference for the alignment of $CoSi_2$ (110)-type planes in the film with Si (110)-type planes in the substrate, and twinning around Si$[111]$ directions. These results show that the origin of most texture components is related to a matching of planes *across* the interface (i.e. axiotaxy), rather than a plane-on-plane matching *at* the interface.

9

Phase formation and texture of Co/Ge on Ge (100) and Ge (111)

Of all the germanides, only a fraction has the potential of being used as an electrical contact, as the electrical resistance of the germanide must be low, while at the same time it should exhibit a high thermal stability. A systematic overview of the phase sequence during reaction of germanium with a wide range of metals has been reported by Gaudet et al. [42] and resulted in a list of materials that fulfill these criteria: NiGe[61], PdGe and $CoGe_2$. In this chapter, the phase sequence during reaction of Co films on Ge (100) and Ge (111) substrates is investigated and the texture of the Co_5Ge_7 and $CoGe_2$ phases reported. The relation between texture and the formation temperature of $CoGe_2$ is pointed out.

The results discussed in this chapter have been published in:

De Keyser K., Van Meirhaeghe R.L., Detavernier C., Jordan-Sweet J., Lavoie C., *Texture of cobalt germanides on Ge(100) and Ge(111) and its influence on the formation temperature*, Journal of the Electrochemical Society 157 (4), H395 (2010)

9.1 Experimental details

Films of 30 nm of Co were sputter-deposited in ultra-high-vacuum conditions on HF cleaned, single crystal Ge (100) and (111) substrates. The samples were heated from 100 to 850°C, at a rate of 3°C/s in a high purity helium flow, during which the phase sequence was monitored using X-ray diffraction (XRD). These in-situ XRD experiments were performed at the X20C beam line at the National Synchrotron Light Source (NSLS) at Brookhaven National Laboratory (BNL) using monochromatic X-rays with a wavelength of 0.18 nm and a linear detector capable of recording a 2θ range of 14°. During a first run, the diffracted X-ray intensity was recorded in a 2θ range from 35° to 49° with an incident angle of 21°, and during a second run from 48° to 62° with an incident angle of 25.5°, resulting in a total 2θ range of 35° to 62°.

Quenches were made at 600°C and 725°C, on both substrates. At the X20A beam line at NSLS in BNL, high-resolution reflection pole figures and θ-2θ scans using synchrotron radiation and a point detector (Schulz method) were recorded (both using X-rays with a wavelength of 0.154 nm), to study texture and crystal phase. For the pole figures, a step size in χ (tilting of the sample) and ϕ (rotation of the sample about its normal) of 0.5° was used, and a 2θ range of roughly 1.5° is collected ($\pm 0.75°$ on the selected 2θ value). This relatively large 2θ collection range was used to collect as much information possible, including diffraction peaks that are shifted to different 2θ values, which can be caused by stress in the film. In some cases, this also results in multiple lattice planes with similar d-spacings, contributing to the diffracted intensity. The pole figures were analyzed using GUSTAV: the different texture components were identified and a rough estimate of their importance was based on the relative intensity in the pole figures. All of the pole figures are plotted on a logarithmic scale, allowing both weak and strong texture components to be visualized in a single figure, with white corresponding to a low intensity, and black to a high.

Electron backscatter diffraction (EBSD) measurements were carried out in a FEI Quanta 200F field emission gun scanning electron microscope (FEGSEM) using an Oxford Instruments/HKL Channel 5 EBSD system.

9.2 Measurements

9.2.1 In-situ XRD

The phase sequence during annealing was monitored using in-situ X-ray diffraction. Figure 9.1 shows the reaction of the Co film with a Ge (100) substrate, and

figure 9.2 with a Ge (111) substrate. The diffracted intensity is plotted as a function of both temperature (X-axis) and 2θ angle (Y-axis), on a gray scale with darker colors corresponding to higher intensities. Regions with high intensity indicate that at a certain temperature, a certain plane is in diffraction condition. These regions have been identified, and the best matching plane for any of the cobalt-germanide phases is indicated. This allows the temperature range to be divided in regions where different phases occur.

On Ge (100), four regions can be distinguished. At low temperatures (100-340°C), the as-deposited Co layer is visible, although with very low intensity, since the crystallinity of the layer will be low, due to the sputter deposition process at room temperature. Around 340°C, CoGe starts to form, making up the second region, which is transformed to Co_5Ge_7 in a narrow temperature range of 440-450°C. This Co_5Ge_7 phase appears to be stable in the range of 450-650°C (third region), and is finally converted to $CoGe_2$ (fourth region), which only disappears at 820 °C, its melting temperature.

On Ge (111), diffracted intensity is only visible in the temperature range of 680°C to 820°C, indicating the occurrence of $CoGe_2$. Below 680°C, no information is available from the in-situ XRD measurements.

Comparing the data on both substrates, one can conclude that there are two striking differences between the reaction of Co with Ge (100) on the one hand, and Ge (111) on the other. Firstly, the formation temperature of the $CoGe_2$ phase depends on the substrate orientation: on Ge (100), it forms at 650°C, while on Ge (111), the $CoGe_2$ XRD peaks only show up at 680°C. Secondly, the sequence of XRD peaks is dependent on the substrate orientation: on Ge(100), the XRD peaks allow the phase sequence to be identified as the previously reported [42] sequence of CoGe, Co_5Ge_7 and finally $CoGe_2$, while on Ge(111), prior to the formation of the $CoGe_2$ phase, almost no XRD peaks are visible, indicating that only amorphous or epitaxial crystalline phases precede the growth of $CoGe_2$ on Ge(111). From these results, it is clear that the phase formation sequence/temperature and the texture of the phases depend on the substrate orientation.

9.2.2 θ-2θ XRD scans

High resolution ex-situ $\theta - 2\theta$ scans were carried out on the quenches, both in the temperature window where the in-situ measurement indicated that $CoGe_2$ had formed (725°C), and at a temperature (600°C) before the formation of $CoGe_2$.

Figure 9.3 shows the θ-2θ XRD spectra of the samples quenched at 600°C. The peak positions indicate that the films consist of the Co_5Ge_7 phase, however, the number of visible XRD peaks and their relative intensity differ from the powder

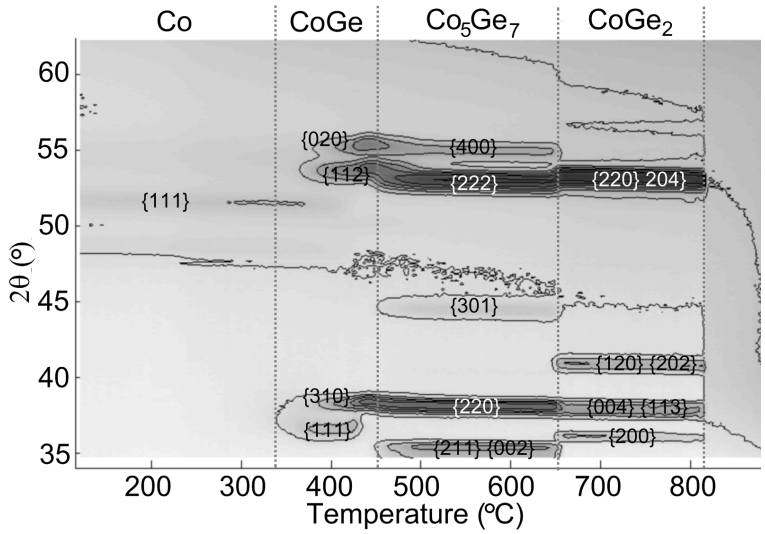

Figure 9.1: Diffracted X-ray intensity during in-situ XRD of 30 nm Co on Ge(100) during annealing at $3^{\circ}C/s$.

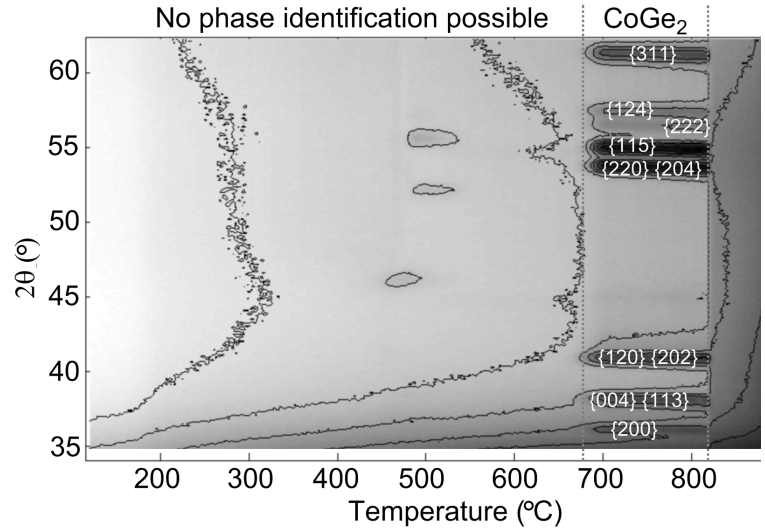

Figure 9.2: Diffracted X-ray intensity during in-situ XRD of 30 nm Co on Ge(111) during annealing at $3^{\circ}C/s$.

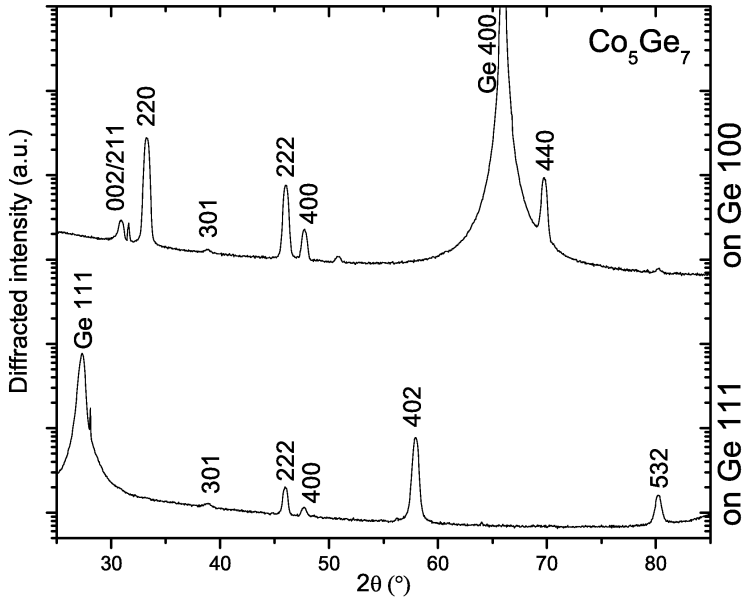

Figure 9.3: θ-2θ X-ray diffraction data recorded on the samples annealed to 600°C, on Ge (100) (top), and Ge (111) (bottom). The peaks can be attributed to Co_5Ge_7.

diffraction spectrum. The {222} diffraction peak has the largest structure factor, 3 times higher than any other. This clearly does not show in the measured spectrum, where other peaks have much higher intensity, and especially on the Ge(111) substrate, the high intensity of the {402} peak, which has a structure factor of only 1% of the {222} peak, indicates that the grains making up the film have a strong preferential orientation.

Figure 9.4 displays the XRD spectra for the samples annealed to 725°C. A variety of peaks is visible, which allows the phase to be identified as $CoGe_2$. On Ge (111), the XRD spectrum closely resembles that of a $CoGe_2$ powder, while on Ge (100), three peaks (i.e. {002}, {004}+{113} and {204}) have a high intensity, indicating some degree of preferential orientation.

9.2.3 XRD pole figures

Pole figures were recorded on the quenches to investigate the texture of the films. Since the pole figures describe the orientation of grains in the film with respect to the single crystal substrate, the pole figures are meaningless without a description of the reference frame, in this case the orientation of the Ge wafer: for pole figures recorded on (111) substrates, the samples were positioned so that the Ge poles are

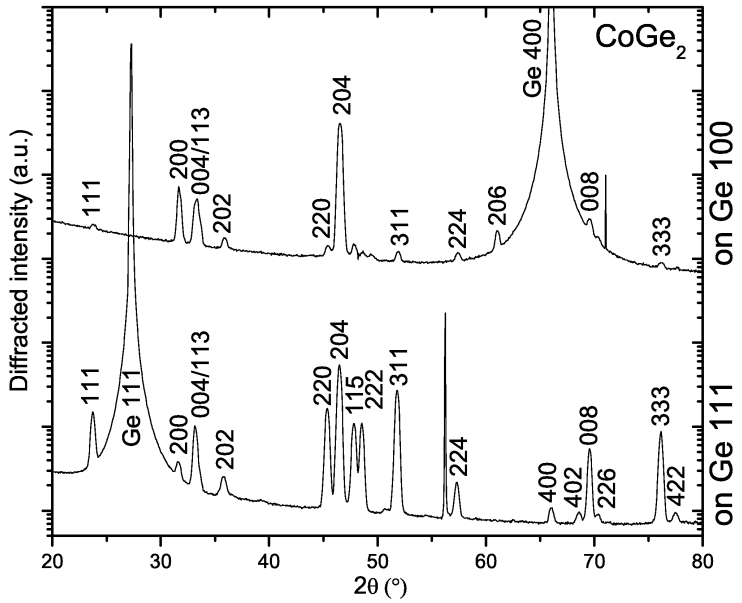

Figure 9.4: θ-2θ X-ray diffraction data recorded on the samples annealed to 725°C, on Ge (100) (top), and Ge (111) (bottom). The peaks can be attributed to $CoGe_2$.

at the χ, ϕ locations shown in figure 9.5a. For those with a (100) oriented substrate, their positions are shown in figure 9.5b.

On each of the samples, the analysis of the pole figures allowed for the identification of a series of texture components (epitaxy and axiotaxy). A summary is provided in table 9.1. The axiotaxy texture components are characterized as a matching of a plane of the film material, with a plane of the Ge substrate. The epitaxial orientations are described by a pair of matching planes of the film and the substrate. Simulations of these texture components are shown during the discussion of the pole figures, to allow for a comparison with the measurements. A legend, indicating the symbols (for epitaxy and substrate poles) and colors (epitaxy, substrate poles, as well as axiotaxy) used in these simulations, can be found in table 9.2.

9.2.3.1 Co on Ge (111)

Sample annealed to 600°C

A first pole figure was recorded at $2\theta = 30.74°$ (d-spacing of 2.906 $\mathring{A}$), corresponding to the Co_5Ge_7 $\{002\}$ plane. Since the $\{211\}$ plane is diffracting at a

Substrate	**Ge (111)**	
Temperature	600°C	725°C
Phases	Co_5Ge_7	Co_5Ge_7 + $CoGe_2$
Axiotaxy	None	None
Epitaxy	A_{111}: Co_5Ge_7 $(0\bar{2}1)$ // Ge (111) Co_5Ge_7 (100) // Ge $(01\bar{1})$	A_{111}: Co_5Ge_7 $(0\bar{2}1)$ // Ge (111) Co_5Ge_7 (100) // Ge $(01\bar{1})$
		J_{111}: $CoGe_2$ (102) // Ge (111) $CoGe_2$ (010) // Ge $(1\bar{2}1)$

Substrate	**Ge (100)**			
Temperature	600°C		725°C	
Phases	Co_5Ge_7		$CoGe_2$	
Axiotaxy	α:	Co_5Ge_7 $\{111\}$ // Ge (101)	γ:	$CoGe_2$ (012) // Ge (110)
	β:	Co_5Ge_7 $\{111\}$ // Ge $\{110\}$	δ:	$CoGe_2$ (115) // Ge (225)
			ϵ:	$CoGe_2$ (110) // Ge (101)
Epitaxy			E_{100}:	$CoGe_2$ (010) // Ge (001) $CoGe_2$ (100) // Ge (100)
	B_{100}:	Co_5Ge_7 $(13\bar{1})$ // Ge $(11\bar{2})$ Co_5Ge_7 (011) // Ge $(21\bar{1})$	F_{100}:	$CoGe_2$ (001) // Ge (001) $CoGe_2$ (100) // Ge (100)
	C_{100}:	Co_5Ge_7 $(0\bar{1}0)$ // Ge $(10\bar{1})$ Co_5Ge_7 $(\bar{1}\bar{1}1)$ // Ge (011)	G_{100}:	$CoGe_2$ (100) // Ge (001) $CoGe_2$ (001) // Ge (100)
	D_{100}:	Co_5Ge_7 $(\bar{2}10)$ // Ge $(1\bar{3}0)$ Co_5Ge_7 $(\bar{1}\bar{1}1)$ // Ge (101)	H_{100}:	$CoGe_2$ (102) // Ge (001) $CoGe_2$ (010) // Ge (110)
			I_{100}:	same as G_{100}, but 3° titled about Ge (100)

Table 9.1: Overview of the texture components and their crystallographic definition, on each of the samples.

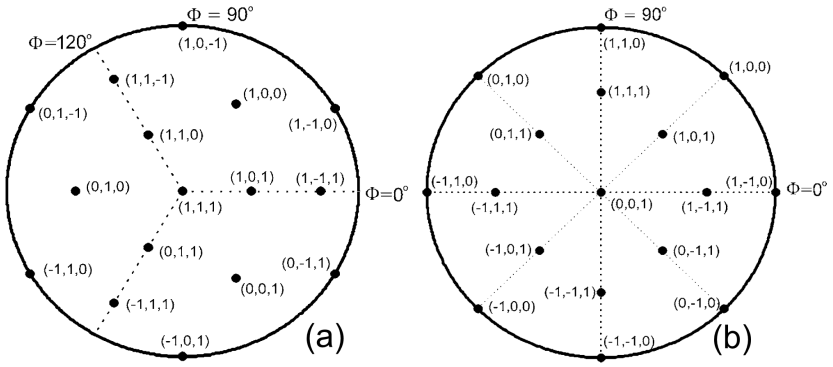

Figure 9.5: Location of the substrate poles in the pole figures for (a) Ge (111) and (b) Ge (100).

Epitaxial texture components

Texture component	Symbol	Color	Figure(s)
Epitaxy A_{111}	$\times$	red	9.6, 9.7
Epitaxy B_{100}	$+$	red	9.10, 9.11
Epitaxy C_{100}	$\Diamond$	black	
Epitaxy D_{100}	$\square$	blue	
Epitaxy E_{100}	$\circ$	cyan	9.12, 9.13
Epitaxy F_{100}	$\square$	green	
Epitaxy G_{100}	$+$	blue	
Epitaxy H_{100}	$\Diamond$	red	
Epitaxy I_{100}	$\triangle$	black	
Epitaxy J_{111}	$\square$	purple	9.8

Substrate

Texture component	Symbol	Color	Figure(s)
Ge substrate	$\star$	yellow	9.13

Axiotaxial texture components

Texture component	Color	Figure(s)
Axiotaxy α	yellow	9.10, 9.11
Axiotaxy β	green	
Axiotaxy γ	red	9.12, 9.13
Axiotaxy δ	black	
Axiotaxy ϵ	yellow	

Table 9.2: Colors and symbols used in the pole figure simulations of the different texture components.

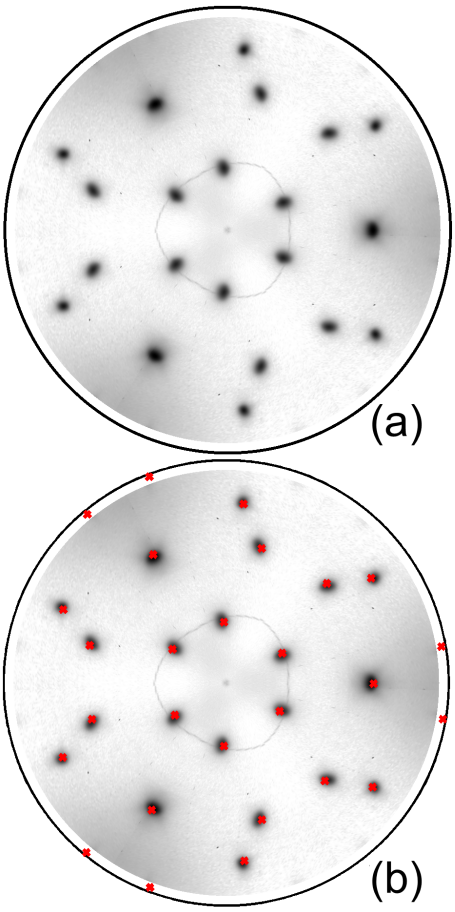

Figure 9.6: a: pole figure recorded on the quench at 600 °C on Ge(111), at 2θ=30.74° with the Co_5Ge_7 {002} and {211} planes in diffraction. b: simulation of the poles from the A_{111} epitaxy, overlaid on the measured data.

2θ value which is separated by only $0.4°$ from the value of the $\{002\}$ plane, the measured pole figure contains contributions from both $\{211\}$ and $\{002\}$ planes. The result of this measurement is shown in figure 9.6a and reveals a number of high intensity spots (ratio between the maximum and minimum diffracted X-ray intensity is 10000), indicating a strongly epitaxial film.

A second pole figure was recorded at $2\theta = 47.57°$ (d-spacing of 1.910 $\mathring{A}$), resulting in the Co_5Ge_7 $\{400\}$ plane being in diffraction. It is shown in figure 9.7a and confirms that the texture of the film is very strong, as evidenced by the limited number of spots on the pole figure, having a very high intensity. In this pole figure,

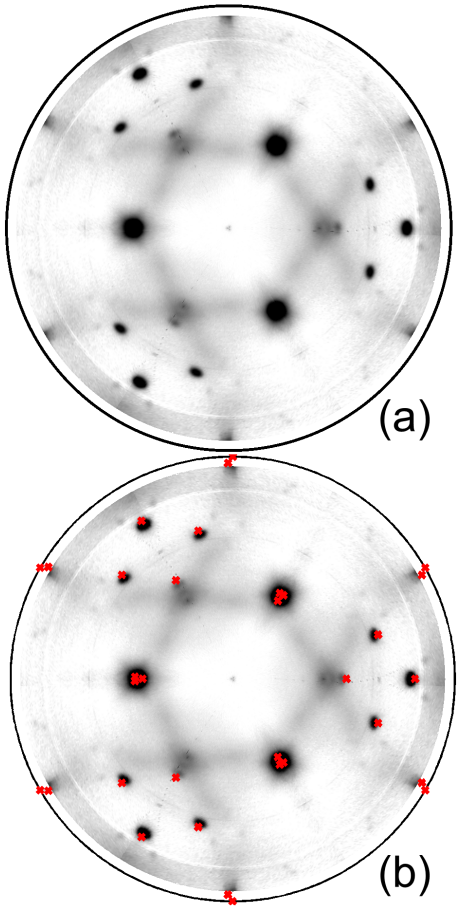

Figure 9.7: a: pole figure recorded on the quench at 600 °C on Ge(111), at 2θ=47.57° with the Co_5Ge_7 {400} planes in diffraction. Contributions from the Co_5Ge_7 {222} and Co_5Ge_7 {103} planes are showing up as well. b: simulation of the poles from the A_{111} epitaxy, overlaid on the measured data.

weak contributions from the {222} and {103} planes are picked up as well, even though the 2θ value at which they diffract should be just outside the detector range. It is likely that both the high intensity of the spots and the fact that stress in the film can shift the 2θ values results in these poles being visible in the pole figure.

Combining the data from both pole figures, one epitaxial orientation could be identified, and is labeled as A_{111} (see table 9.1 for details). Due to the threefold symmetry of the Ge(111) substrate, three orientational variants of this epitaxy can occur and are indeed observed. A simulation of the location of the epitaxial spots in the pole figures was made, and is displayed in figures 9.6b and 9.7b, overlaid

on the recorded pole figures. It shows that it can indeed account for all of the high intensity spots. There remain some very weak features in the background, which were not assignable to a specific texture component, but since the pole figures are plotted on a logarithmic scale, and these features still have a very low intensity, they represent only a tiny fraction of the texture.

In summary, one epitaxial Co_5Ge_7 orientation is formed after an anneal to $600°C$ of Co on Ge (111).

Sample annealed to 725°C

Based on the θ-2θ spectrum for this sample (figure 9.4), which was discussed in a previous section, one can expect the film to consist of randomly oriented $CoGe_2$. This should result in featureless pole figures.

A first pole figure, recorded at $2\theta = 46.33°$ (d-spacings of 1.958 $\mathring{A}$) has the $CoGe_2$ $\{204\}$ planes in diffraction and is shown in figure 9.8a. It displays a series of intense spots. While some of these spots originate from the Ge $\{220\}$ poles of the substrate, the others are caused by the film, which indicates the occurrence of an epitaxial phase and seems to conflict with the θ-2θ results of nearly random $CoGe_2$ texture.

The second pole figure (figure 9.9a), recorded at $2\theta = 51.66°$ (d-spacings of 1.768 $\mathring{A}$), with the $CoGe_2$ $\{311\}$ planes in diffraction, shows no features, except for the Ge $\{311\}$ substrate poles which are indicated in figure 9.9b. This indicates a largely random orientation of the $CoGe_2$ phase on Ge (111).

Comparing the data from both pole figures and the θ-2θ scan, there seems to be a discrepancy between the first pole figure, which suggests epitaxy, and the second pole figure and the θ-2θ results, both indicating random $CoGe_2$. However, an analysis of the locations of the spots on the first pole figure, which translate into angles between planes of the lattice of the film material, showed that these spots are incompatible with the $CoGe_2$ lattice and must be produced by a different phase. Taking into account the strong epitaxy of the preceding A_{111} Co_5Ge_7 epitaxy which was identified at 600°C, and the fact that the $\{222\}$ Co_5Ge_7 plane has a d-spacing of 1.979 $\mathring{A}$, which is very close to the 1.958 $\mathring{A}$ of the $CoGe_2$ $\{204\}$ plane for which the first pole figure is recorded, one can conclude that the spots in this pole figure can only be caused by some remaining epitaxial Co_5Ge_7 with the A_{111} orientation. This was confirmed by carrying out a simulation of the Co_5Ge_7 $\{222\}$ poles for epitaxy A_{111} and comparing this with the position of the spots in the pole figure. It is also consistent with the fact that in the second pole figure (with $CoGe_2$ $\{311\}$ in diffraction) no Co_5Ge_7 spots are observed: due to the fact that the only Co_5Ge_7 plane with similar d-spacing to $CoGe_2$ $\{311\}$ is the Co_5Ge_7 $\{411\}$ plane, which has a very low structure factor, so no traces of the remaining

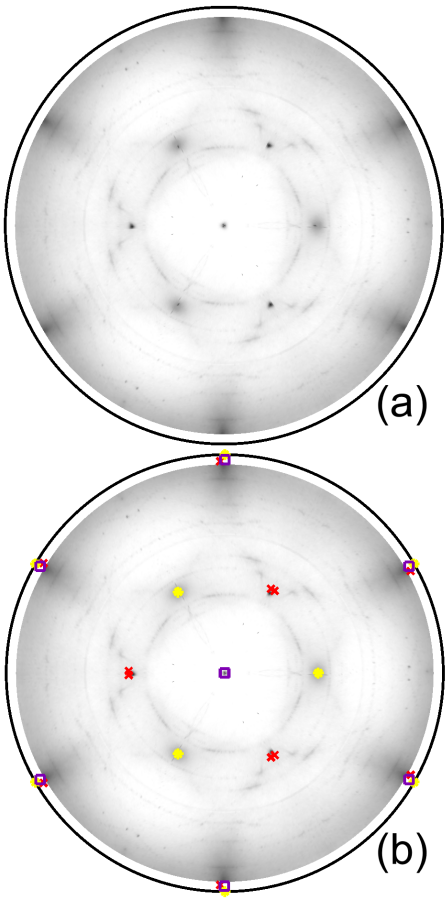

Figure 9.8: a: pole figure recorded on the quench at 725 °C on Ge(111), at 2θ=46.33° with the $CoGe_2$ {204} plane in diffraction. b: simulation of the poles from the J_{111} epitaxy ($CoGe_2$), the A_{111} epitaxy (Co_5Ge_7), and the Ge {220} substrate poles, overlaid on the measured data.

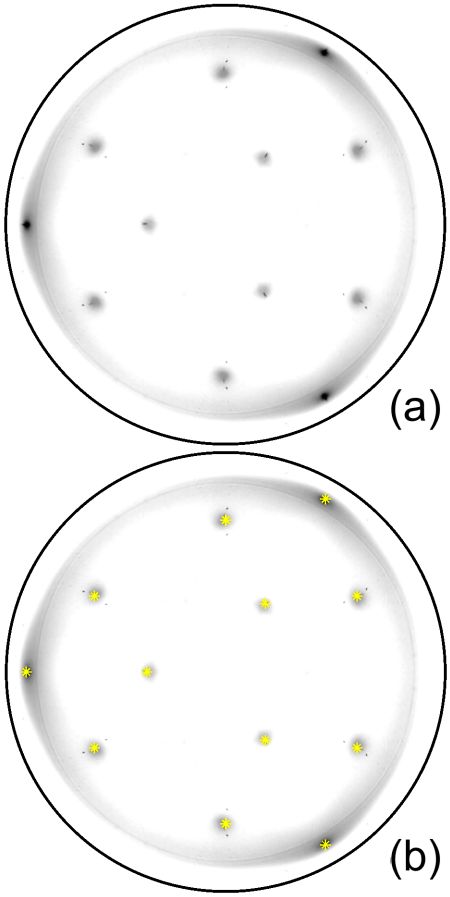

Figure 9.9: a: pole figure recorded on the quench at 725 °C on Ge(111), at 2θ=51.66° with the $CoGe_2$ {311} plane in diffraction. b: simulation of Ge {311} substrate poles on top of the measured data.

epitaxial Co_5Ge_7 grains are visible.

There remains one spot in the center of the first pole figure (figure 9.8a) which a combination of epitaxial Co_5Ge_7 and Ge $\{220\}$ poles cannot explain. It originates from a small amount of epitaxial $CoGe_2$ grains (epitaxy J_{111}). This epitaxy results in the grains having a $CoGe_2$ $\{204\}$ plane parallel to the Ge $\{111\}$ interface. Even though this epitaxy is very weak, the $CoGe_2$ $\{204\}$ spot in the center of the pole figure is still observed because all of the orientational variants of J_{111} have this plane parallel to the substrate and will contribute to the intensity of this single spot. The weak J_{111} epitaxy is not visible in the second pole figure (figure 9.9a), due to the fact that the $\{311\}$ poles of its variants do not coincide, no longer resulting in one spot with combined intensity, but in multiple spots all over the pole figure, each with such a low intensity that they are lost in the background.

In figure 9.8b, a simulation of the Co_5Ge_7 $\{222\}$ poles for epitaxy A_{111}, combined with the Ge $\{220\}$ substrate poles and $CoGe_2$ $\{204\}$ poles for the weak epitaxy J_{111} is shown. It produces a good agreement with the recorded pole figure of figure 9.8a. Figure 9.9b shows the simulation for the second pole figure, which only contains the Ge $\{311\}$ poles.

In summary, the reaction of Co on Ge(111) results in two phases at 725°C: $CoGe_2$ has grown on Ge (111) with a largely random texture and a fraction of the epitaxial Co_5Ge_7 that was found at 600°C, is still present. The phase formation during the reaction of Co with Ge (111) is thus not purely sequential, but Co_5Ge_7 and $CoGe_2$ are found to coexist in a temperature window of at least 45°C, as the in-situ XRD results (figure 9.2) show that on Ge (111), $CoGe_2$ starts forming at 680°C, but epitaxial Co_5Ge_7 is found up to a temperature of at least 725°C, the temperature of the quench the pole figures were collected on.

9.2.3.2 Co on Ge (100)

Sample annealed to 600°C

The recorded pole figures are shown in figure 9.10a (for $2\theta = 30.74°$ (d-spacing of 2.906 $\mathring{A}$), corresponding to the Co_5Ge_7 $\{002\}$ and $\{211\}$ planes) and 9.11a ($2\theta = 47.57°$ (d-spacing of 1.910 $\mathring{A}$), corresponding to Co_5Ge_7 $\{400\}$). They are complex, consisting of a large number of small spots, larger line shaped features and some broad regions of increased diffracted intensity. The texture was identified as a mixture of three different epitaxial orientations (B_{100}, C_{100} and D_{100}), in addition to two axiotaxy components (α and β). The crystallographic definitions of these texture components are given in table 9.1. The orientational variants, caused by the symmetry elements (four-fold [001] rotation axis, and two mirror planes) of the substrate are observed as well.

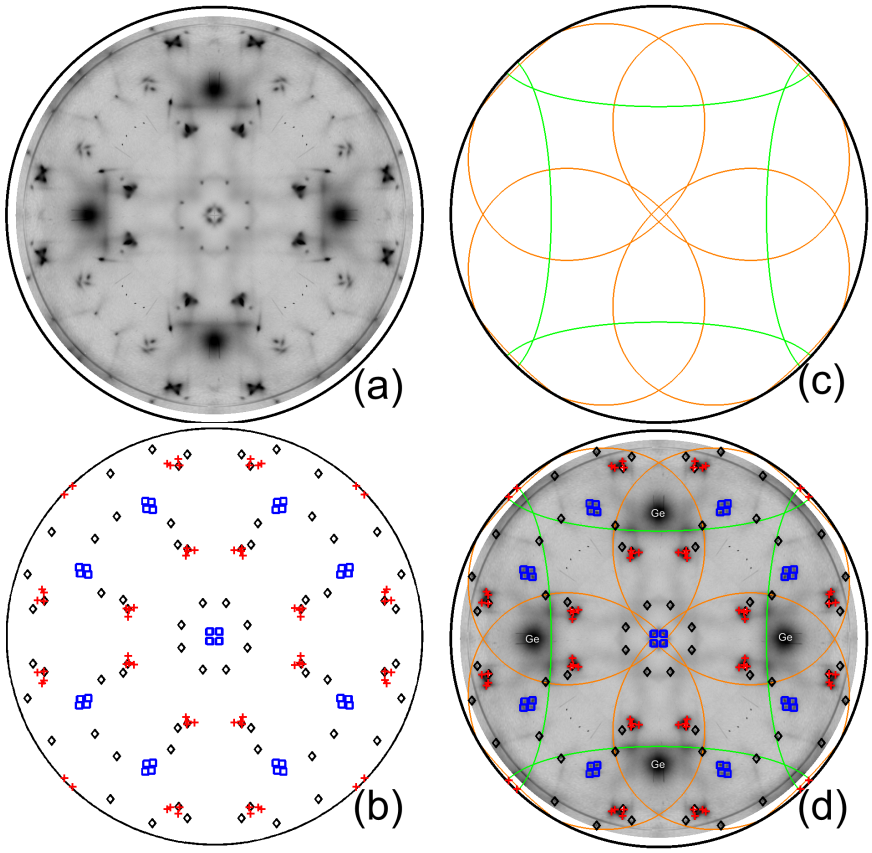

Figure 9.10: a: pole figure recorded on the quench at 600 °C on Ge(100), at 2θ=30.74° with the Co_5Ge_7 {002} and {211} planes in diffraction. b: simulation of the poles from the epitaxial orientations B_{100}, C_{100} and D_{100}. c: simulation of the axiotaxy texture components α and β. d: simulations overlaid on the measured data.

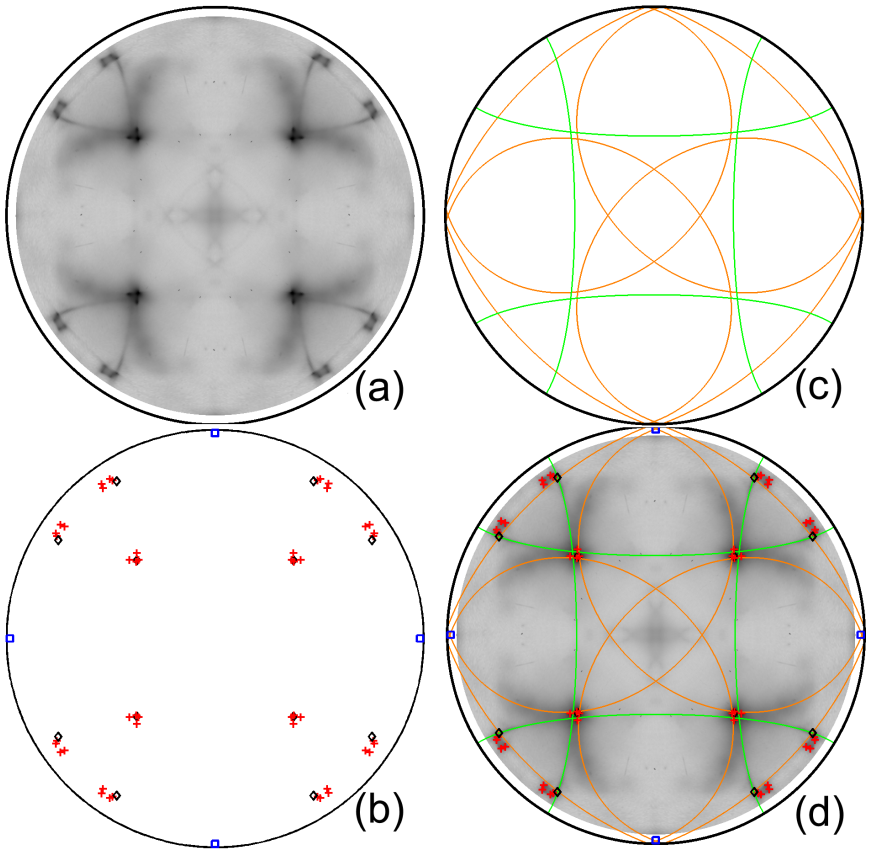

Figure 9.11: a: pole figure recorded on the quench at 600 °C on Ge(100), at 2θ=47.57° with the Co_5Ge_7 {400} planes in diffraction. b: simulation of the poles from the epitaxial orientations B_{100}, C_{100} and D_{100}. c: simulation of the axiotaxy texture components α and β. d: simulations overlaid on the measured data.

For the first pole figure, a simulation of the 3 epitaxial relationships is shown in figure 9.10b for the {002} and {211} poles. Figure 9.10c shows the location of the simulated axiotaxy patterns, but only for the {002} poles. Due to their limited intensity (the total diffracted intensity of an axiotaxy texture component is spread out along a line, while in the case of epitaxy, it is concentrated in a single point), the {211} contributions hardly show up in the pole figure. In figure 9.10d, all of the simulated texture components are superimposed on the measured pole figure, showing that they can indeed account for all of the observed features.

For the second pole figure (figure 9.11a), which was recorded at the 2θ value corresponding to the Co_5Ge_7 {400} poles, a first simulation of the identified epitaxial texture components for the {400} poles was carried out and it was found that

this could account for most of the observed spots. However some spots remained unexplained and were found to originate from $\{103\}$ poles of epitaxy B_{100}. A simulation combining the $\{400\}$ poles for epitaxy B_{100}, C_{100} and D_{100} and the $\{103\}$ poles for epitaxy B_{100} is shown in figure 9.11b, and does indeed correspond to all of the spots in the recorded pole figure.

While this fit agrees with the measured pole figure, it is rather surprising to detect the $\{103\}$ poles for epitaxy B_{100}: according to the Co_5Ge_7 powder-diffraction spectrum, the $\{103\}$ plane should diffract at a 2θ angle about 1° higher than the $\{400\}$ plane, which should put it out of the 2θ range of the detector. A compressive stress in the film could change the d-spacing of the $\{103\}$ planes, shifting the 2θ angle back within the detector range. This idea is supported by the fact that the $\{103\}$ poles are only observed for epitaxy B_{100}, and not for C_{100} or D_{100}. Since the $\{103\}$ planes in epitaxy B_{100} make an angle of 82° with the interface plane, which is much higher than for epitaxy C_{100} (62°) or D_{100} (17°), a compressive stress in the film will influence the d-spacing of the $\{103\}$ plane in epitaxy B_{100} the most.

In figure 9.11c, a simulation of the axiotaxy lines for the $\{400\}$ poles is provided, which explains the lines in the measured data. Both the epitaxy and axiotaxy simulations are overlaid on the measured data in figure 9.11d, showing an excellent agreement.

In summary, the reaction of Co with Ge (100) at 600°C results in the formation of Co_5Ge_7 with a complex texture consisting of 3 different epitaxial orientations and 2 axiotaxy components.

Samples annealed to 725°C

On the samples annealed to 725°C, two pole figures were collected. A first one is shown in figure 9.12a and was recorded at $2\theta = 46.33^\circ$, (d-spacings of 1.958 $\mathring{A}$) resulting in the $CoGe_2$ $\{204\}$ planes being in diffraction condition. The second one is shown in figure 9.13a, and was recorded at $2\theta = 51.66^\circ$ (d-spacings of 1.768 $\mathring{A}$), with the $CoGe_2$ $\{311\}$ planes diffracting.

In both pole figures, features are clearly visible, which confirms the non-random texture. The analysis of the spot locations allowed the identification of 5 preferential orientations of $CoGe_2$ grains (E_{100}, F_{100}, G_{100}, H_{100} and I_{100}). In addition to this, 3 $CoGe_2$ axiotaxy texture components were found (γ, δ and ϵ), 2 of which (δ and ϵ) have a very low intensity. Simulations of the epitaxial texture components are shown in figure 9.12b (for the first pole figure, $CoGe_2$ $\{204\}$) and 9.13b (for the second pole figure, $CoGe_2$ $\{311\}$, which also contains some contributions from the substrate, as the Ge $\{311\}$ poles are visible as well). Figures 9.12c and 9.13c show the axiotaxy simulations, while figure 9.12d and 9.13d provide an overlay

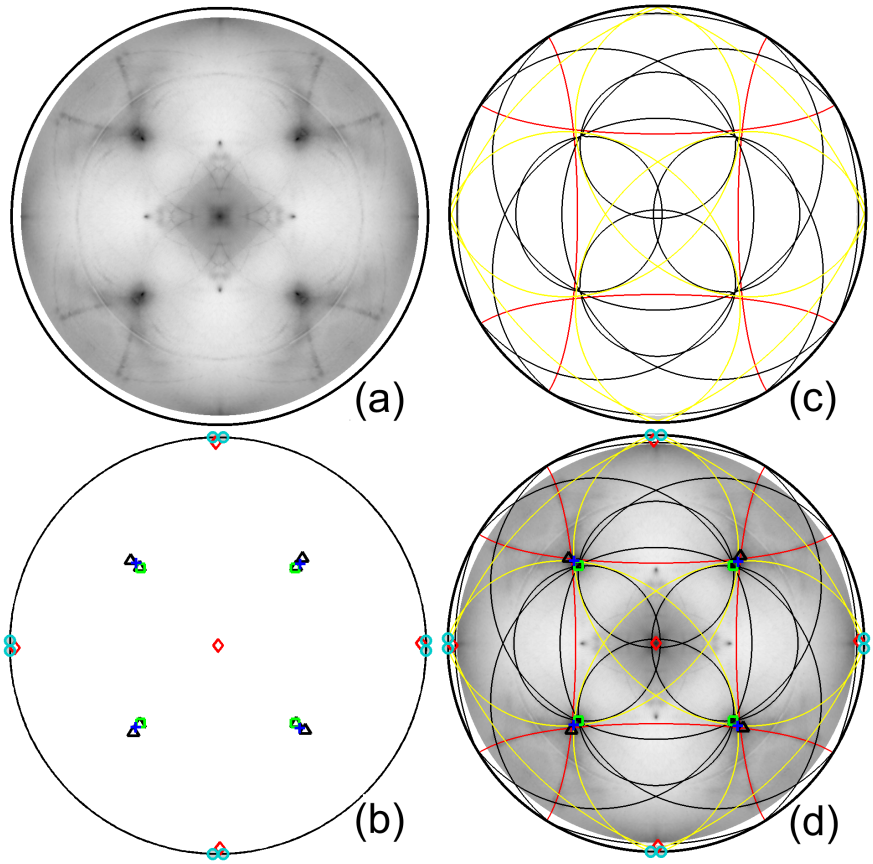

Figure 9.12: a: pole figure recorded on the quench at 725 °C on Ge(100), at 2θ=46.33° with the $CoGe_2$ {204} plane in diffraction. b: simulation of poles from the epitaxial orientations E_{100}, F_{100}, G_{100}, H_{100} and I_{100}. c: simulation of the axiotaxy texture components γ, δ, ϵ. d: simulations overlaid on the measured data.

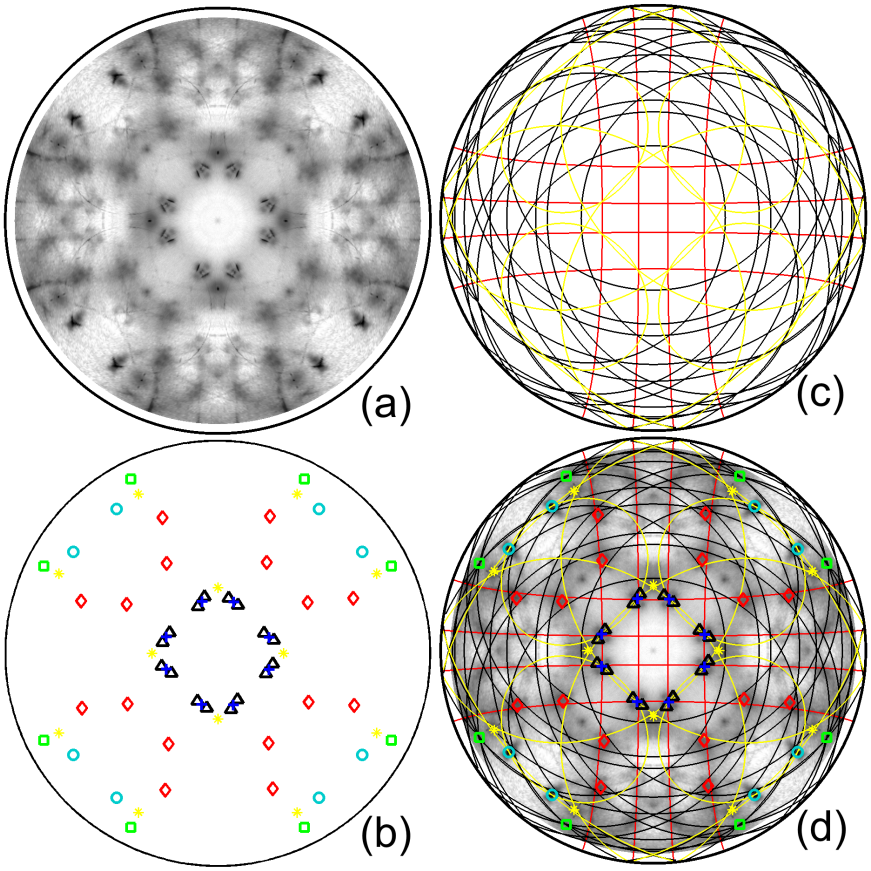

Figure 9.13: a: pole figure recorded on the quench at 725 °C on Ge(100), at 2θ=51.66° with the $CoGe_2$ {311} plane in diffraction. b: simulation of poles from the epitaxial orientations E_{100}, F_{100}, G_{100}, H_{100} and I_{100}. c: simulation of the axiotaxy texture components γ, δ, ϵ. d: simulations overlaid on the measured data.

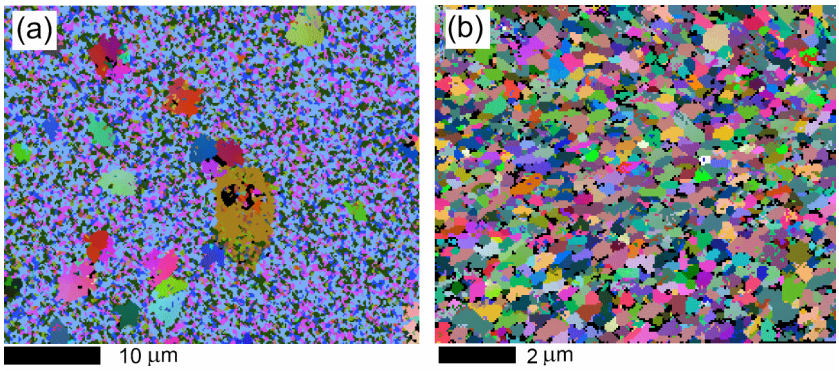

Figure 9.14: EBSD maps recorded on the films annealed to 600°C, both on (a) Ge (111) and on (b) Ge (100). On Ge (100), small grain with a variety of orientations are observed, whereas on Ge (111), an epitaxial background of Co_5Ge_7 is observed, containing isolated, differently orientated grains.

of the simulations on top of the measured data, showing a good match between simulation and measurement.

In summary, the reaction of Co with Ge (100) results in the formation of texture $CoGe_2$ at 725°C. This texture can be described as a combination of 5 epitaxial orientations and 3 axiotaxy texture components.

9.2.4 EBSD

EBSD measurements were carried out to determine grain size. They also provided information on the orientation of the grains, corroborating the XRD pole figure data.

Figure 9.14 shows EBSD maps recorded on the samples annealed to 600°C. After a preliminary scan to get an estimate of the grain size, an appropriate measurement grid was chosen for the film on Ge (100) (figure 9.14a, step size of 50 nm) and on Ge (111) (figure 9.14b, step size of 150 nm). The color code in these maps is euler coloring, showing different orientations of the grains, as different colors.

On Ge (100), a typical poly-crystalline thin film is visible, with an average grain size of 250 nm. The contrast with the microstructure of the same material on Ge (111) is big: figure 9.14b, which is shown on a much larger scale, shows a small number of large grains embedded in a background consisting of three different colors. Manual inspection of the EBSD patterns showed that this three-colored background is both caused by the different orientational variants, as well as due to the indexing software, which has difficulties to distinguish between the EBSD

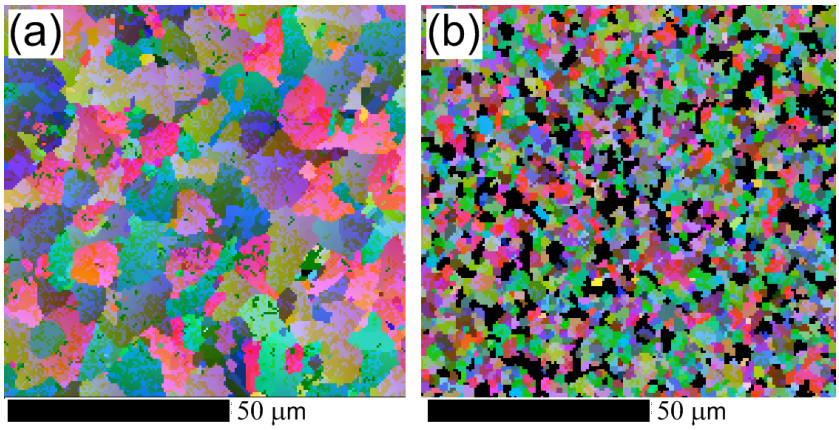

Figure 9.15: EBSD maps recorded on the films annealed to 725°C, both on (a) Ge (111) and on (b) Ge (100). A large difference in grain size is visible.

patterns of these variants, since their patterns are similar and the pattern quality was found to be rather poor. Manual inspection of the patterns showed that the epitaxial grains are at least 5 μm in size. The average grain size of Co_5Ge_7 on Ge(111) is therefore at least a factor 20 higher than on Ge(100), leading to a much lower density of grain boundaries in the Co_5Ge_7 on Ge (111) film, compared to Ge (100) substrates.

The samples annealed to 725°C were also investigated using EBSD. On Ge (111), they revealed huge grains of $CoGe_2$ (figure 9.15a) with an almost completely random orientation. On Ge (100), much smaller grains were found (figure 9.15b). This difference in grain size suggests that the conversion of Co_5Ge_7 to $CoGe_2$ is nucleation controlled: as the density of grain boundaries is much smaller in the Co_5Ge_7 film on Ge (111), less nucleation centers are available, leading to larger grains on Ge (111) since the nuclei can grow larger before encountering a competing $CoGe_2$ grain.

9.3 Discussion

The identified texture components were compared with literature on the oriented growth of cobalt germanides, both on Ge (100) and Ge (111) substrates.

9.3.1 Texture formation on Ge (100)

On Ge (100), Sun et al. [59] used transmission electron microcopy (TEM) to report on the epitaxial growth of Co_5Ge_7 in very thin films, with an orientation of $Co_5Ge_7 < 110 > (001)//Ge < 010 > (001)$. No grains with the exact same orientation could be found in the sample investigated here, but the grains belonging to epitaxy D_{100} (table 9.1) have a misorientation of just 3° (rotation about the Ge(100) plane normal) to the reported orientation. This 3° misorientation is likely the result of the increased thickness of the films compared to those of Sun et al.. As indicated in [59], the proposed epitaxy would require a large amount of strain, especially in thicker films, as the difference in d-spacing between the Ge (200) plane and that of the matching Co_5Ge_7 (110) plane is about 4.5%. The introduction of misfit dislocations to accommodate this mismatch has been shown to result in a tilting (typically of a few degrees) of the epitaxial grains[89, 90].

They also pointed out that, using TEM, one cannot exclude the existence of grains with a $Co_5Ge_7 < 100 > (110)//Ge < 100 > (001)$ orientation, which corresponds to the orientation that was labeled as epitaxy B_{100}. From the pole figures it is clear that this epitaxy does occur, and in a significant number of grains, as the diffracted intensity in the spots caused by epitaxy B_{100} and D_{100} is roughly equal. Epitaxy C_{100} was not reported in [59].

Concerning the texture of $CoGe_2$ on Ge (100), no information is available in literature.

9.3.2 Texture formation on Ge (111)

On Ge (111), the partial epitaxial growth of Co_5Ge_7 was reported [91], with a Co_5Ge_7 [011] // Ge [111] and Co_5Ge_7 (200) // Ge $(2\bar{2}0)$ orientation. This was found to correspond to epitaxy A_{111}. In the same work, two epitaxial orientations for $CoGe_2$ were reported as well, none of which correspond to the J_{111} orientation that was found both in the pole figures and the EBSD measurements. A simulation of the location of the poles corresponding to the previously reported orientations, indicated that these orientations do not occur in a significant amount in the films under investigation.

9.3.3 $CoGe_2$ formation temperature

A dependence of the formation temperature of $CoGe_2$ on the Ge substrate properties was reported in [92], where it was shown that the degree of substrate crystallinity influences the formation temperature of the germanide phases. In contrast,

in the current experiments, both samples have a single crystal substrate, so a different reason for the change in $CoGe_2$-formation temperature must exist.

As the Co_5Ge_7 grains grow almost completely epitaxially on Ge (111), the resulting film is stabilized, since the lower interface energy of the epitaxial grains (compared to randomly oriented grains), leads to a lower driving force for the conversion to $CoGe_2$. This change in the energy balance of the system will shift the formation of $CoGe_2$ to higher temperatures.

9.3.4 Sequential vs. simultaneous phase occurrence

The change from the sequential occurrence of Co_5Ge_7 and $CoGe_2$ on Ge (100), to the simultaneous existence of both phases on Ge (111), can also be explained by the microstructure of the Co_5Ge_7 phase. On Ge (100), the EBSD measurements revealed a typical microstructure for a polycrystalline film: small grains, leading to a high density of grain boundaries, and triple and quadruple points, ideal places for nucleation. In contrast, only large, isolated, grains in an epitaxial background are observed for the Co_5Ge_7 film on Ge (111). Since the rate of heterogeneous nucleation is heavily dependent on the amount and type of nucleation sites, it will be much lower on Ge (111). On Ge (100), all of the Co_5Ge_7 will be converted to $CoGe_2$ in a small time, and thus a small temperature window, leading to the observed sequential occurrence. On Ge (111), the nucleation rate is much lower, spreading the conversion to $CoGe_2$ over a much larger time (equivalent to a large temperature range for a ramp anneal) resulting in the observation of simultaneous occurrence.

9.4 Conclusions

A detailed analysis of the phase formation and texture of Co_5Ge_7 and $CoGe_2$, on Ge (100) and Ge (111) was carried out. Co_5Ge_7 was found to grow epitaxially on Ge (111), while on Ge (100), axiotaxy and a combination of 3 epitaxial orientations is observed. A large difference in grain size was observed, and these difference in microstructure were found to influence both the formation temperature and the grain size of the $CoGe_2$ phase: on Ge (100), all of the Co_5Ge_7 is converted to $CoGe_2$ at 650°C, which grows as a combination of epitaxy, axiotaxy, and randomly oriented grains. In contrast, on Ge (111) the microstructure of Co_5Ge_7 shifts the formation of randomly oriented $CoGe_2$ to higher temperatures, leading to the coexisting of both phases.

Part III

Impact of texture on technological properties

10

Thermal stability of NiSi and its relation to texture

The adoption of NiSi as the contacting material of choice, has enabled the continued downscaling, due to its ease of formation in narrow lines and limited silicon consumption. However the thermal stability of NiSi is problematic. In contrast to $CoSi_2$ and $TiSi_2$, the NiSi phase is not the end-phase of the metal-silicon reaction when there is a surplus of silicon ($NiSi_2$ is), which leads to the thermodynamical instability of NiSi, as in contact with the silicon substrate it can be converted to the higher resistive $NiSi_2$ phase, resulting in poor device performance. Secondly, thin NiSi films are morphologically unstable: they exhibit the problem of agglomeration, which is the tendency of thin films to break up into islands.

In this chapter, the thermal stability of NiSi will be investigated. A short overview of the literature regarding NiSi agglomeration is presented, and the main models regarding thin film agglomeration will be briefly discussed. Next, an investigation of the relation between texture and agglomeration for the case of NiSi on Si(100) is carried out.

The results discussed in this chapter have been published in:

De Keyser K., Detavernier C., Van Meirhaeghe R.L., Jordan-Sweet J., Lavoie C., *The texture of thin NiSi films and its effect on agglomeration*, Ceramic Transac-

tions, Volume 201, p. 3-10 (2008)

10.1 Agglomeration of NiSi

The agglomeration of NiSi on Si(100) leads to a huge increase in the resistivity of the contact, as the uniform, low-resistive contact is replaced by small islands of low resistivity (NiSi) embedded in a background of high resistive silicon. Figure 10.1 demonstrates this, by showing the sheet resistance of the NiSi contact as a function of annealing temperature. One can notice that it dramatically increases when annealing temperatures above 550°C are used. Top-view SEM images (figure 10.2) show the morphological evolution of the NiSi film: breakup and formation of NiSi islands (light) on the silicon background (dark) is clearly visible.

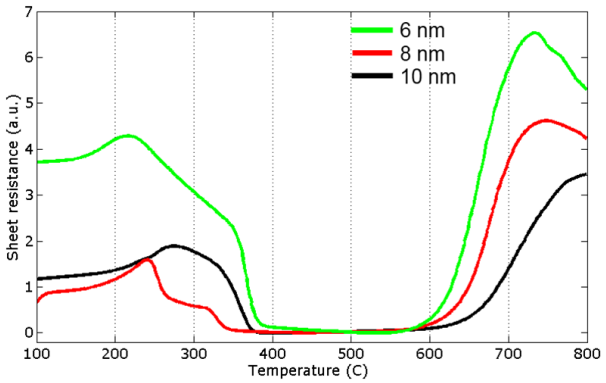

Figure 10.1: In-situ sheet resistance of thin Ni layers on SOI substrates, for 3 different layer thicknesses. Low resistive NiSi is formed around 380°C, but the resistance increases again when annealing to 550°C or higher.

It has been shown that depending on the thickness of the NiSi contact, either the thermodynamic or morphological instability presents the major problem. When the initial nickel layer thickness is less than 15 nm, which is the case for the most recent CMOS processes, it was shown [39] that the agglomeration of the layer occurs before the conversion to $NiSi_2$ has started, making methods of improving the morphological stability of NiSi crucial for the fabrication of reliable devices. The most common way to reach this goal is by alloying the nickel film with additional elements. In particular, the addition of Pt to the nickel layer results in both an increased thermodynamical stability [40] of the resulting NiSi contact (by shifting the nucleation of $NiSi_2$ to higher temperatures, as the solubility of Pt in this phase is very low), as well as increasing the morphological stability [93].

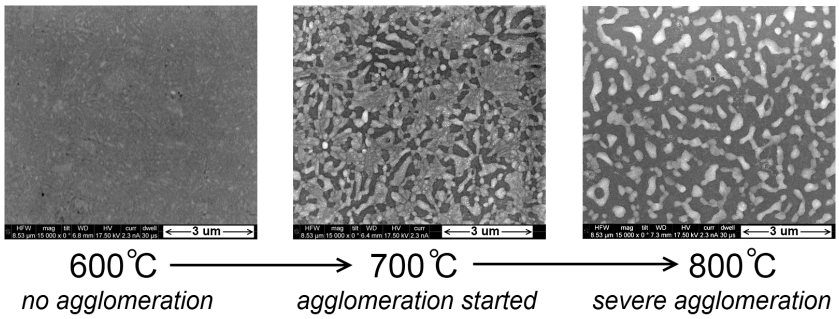

Figure 10.2: Top-view SEM images recorded on the 10 nm nickel film which has been annealed to either 600, 700 or 800 °C at 3° C/s. While the film annealed to 600 °C is continuous, the NiSi film has broken up due to agglomeration at 700 °C and is converted to isolated islands at 800 °C.

10.2 Atypical agglomeration of NiSi on Si (100)

While the usage of alloying elements in the nickel layer has sufficiently extended the morphological stability of NiSi to make it usable in CMOS technology, the fundamental understanding of the agglomeration mechanisms and how the alloying elements counteract these, is still fairly limited.

In general, agglomeration is described as a grain boundary grooving process, originating from the trade-off between the different free energy contributions in a multi-grained film: there is the bulk free energy of the phase that exists within the grain, the interface energy of the grain with the substrate, the surface energy of the grain, and the grain boundary energy where one grain meets another. If the grain boundary energy (per unit of area) is significantly higher that the interface or surface energy, transport of atoms from the grain boundary to the interface or surface will lower the total free energy and result in the grooving of the particular grain boundary (see figure 10.3). Agglomeration is thus caused by material transport, i.e. diffusion, which in itself is driven by the difference in energy between the grain boundary and the interface or surface. Based on this conclusion, it is clear that preventing material transport in the grain boundaries, or lowering the difference in energy between interface/surface and grain boundary will lead to an increased morphological stability.

In addition, if one considers a heavily agglomerated film, consisting of isolated grains, the smallest interface area for a given grain volume will be obtained when the shape of the interface is spherical. This means that once the grain grooving has resulted in the elimination of the grain boundary, the resulting isolated grain will obtain a spherical interface with the substrate.

Nolan et al [94] applied and extended this model to the case of polycrystalline thin films, and argued that because the curvature of the boundary of a small isolated grain will be larger than that of a larger grain, the grain size will also have its influence on agglomeration, with smaller, thicker grains being more stable. One problem with this model is that is essentially an equilibrium model: the shape of the interface is calculated by considering the equilibrium groove angle. The way and speed this equilibrium is reached is not considered, even though many thin films are in a non-equilibrium state, e.g. by quenching. This is certainly true for thin NiSi films on silicon substrates.

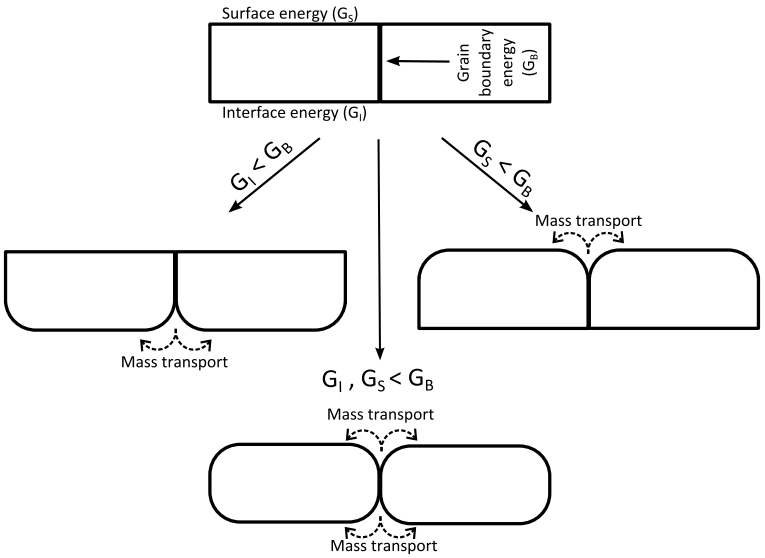

Figure 10.3: Origin of grain boundary grooving from a difference in free energy between surface, interface and grain boundary. Mass transport is driven by this difference, resulting in the grooving.

If one looks at a cross-section TEM image of the agglomeration of a NiSi film (figure 10.4), this indeed seems to confirm the grain boundary grooving: curved, isolated grains are visible which are consistent with the case where the interface energy is lower than the grain boundary energy.

When studying the agglomeration of NiSi, one observes an important dependence of the agglomeration on the orientation or type of the substrate, which is shown in figure 10.5, where the ex-situ sheet resistance of a 10 nm nickel film on poly-Si, Si (100), Si (111) and Si (110), is plotted as a function of the annealing temperature of the sample. A striking observation is that NiSi films of identical thickness will agglomerate at a lower temperature on Si (100) than on polycrystalline silicon. The possible impact on devices is illustrated in figure 10.6, where a test pattern

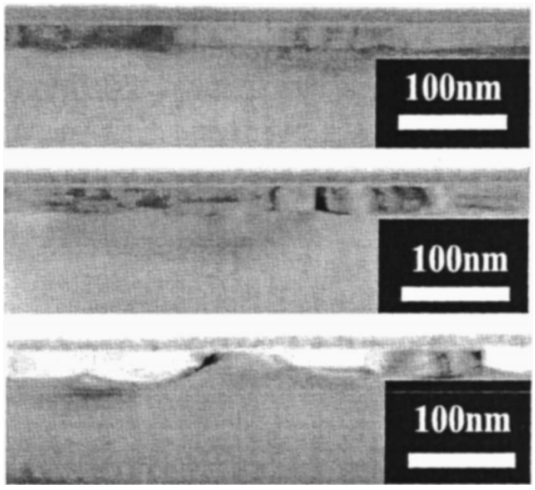

Figure 10.4: TEM cross section of the evolution in grain morphology for a NiSi film on a SOI substrate. A 10 nm Ni layer was heated for 80 s to 450, 500 and 550° C (taken from [39]). The agglomeration and curvature of the NiSi grains at 550 ° C indicates mass transport from the grain boundaries to the interface.

of NiSi lines for source/drain contacting on Si (100) and for gate contacting on poly-Si have been formed and exposed to a post-silicidation anneal. The contacts on single crystal Si (100) exhibit severe agglomeration, while those on poly-Si are still intact. This is unlike $TiSi_2$ or $CoSi_2$, where a single crystal substrate typically provides a more stable substrate as no grain growth or moving of grain boundaries can occur in the substrate.

Because the grain boundary grooving is driven by the interface energy, one can argue that the difference between the poly-Si and Si (100) substrates must be caused be a lower interface energy of NiSi on Si(100) when compared to poly-Si, which in the case of Si (100) results in a larger driving force for material transport from the grain boundary to the interface. If one extends this reasoning to epitaxial films, which have a very low interface energy due to the good atomic matching at the interface, this would however mean that epitaxial films should be the most prone to agglomeration. While this is also a result obtained from the Nolan model, this is not observed in experiments, as epitaxial films are typically much more stable.

The cause of this discrepancy lies in the fact that the grain boundary grooving model implicitly assumes that there is no influence of the interface shape on the interface energy, which is clearly not the case for epitaxial films where specific planes of the substrate and film match: any material transport from the grain boundary to the epitaxial interface results in the local disturbance of this matching and the generation of a high energy interface. Grain boundary grooving can there-

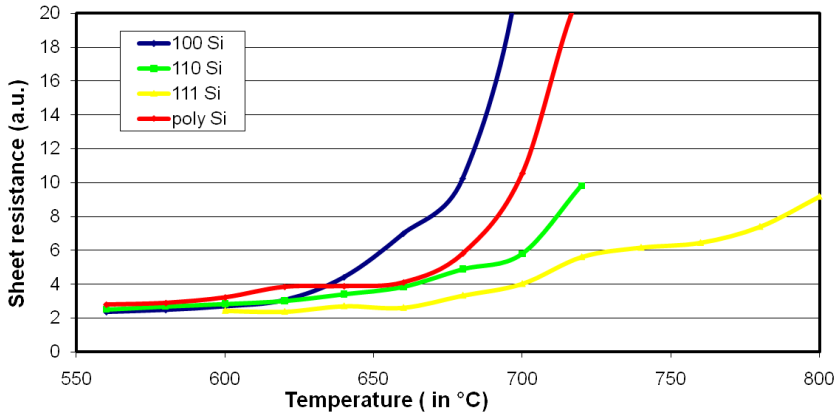

Figure 10.5: Sheet resistance measured on NiSi films obtained after rapid thermal annealing of 10 nm nickel films to different temperatures, deposited on different silicon substrates. The increase in resistivity is caused by agglomeration of the film, and this behavior is significantly dependent on the substrate orientation.

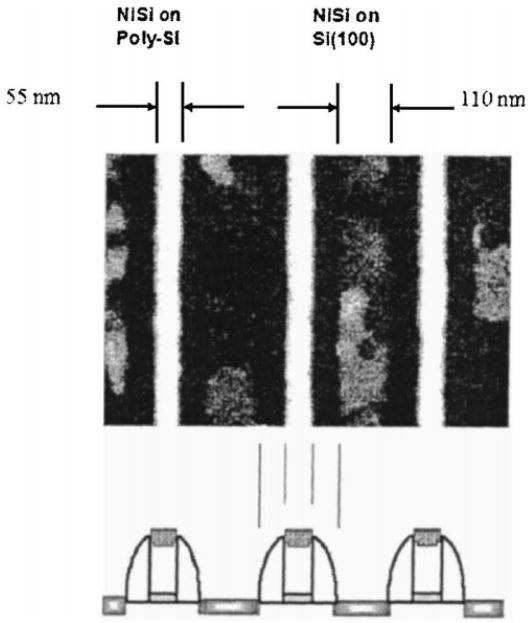

Figure 10.6: Top-view SEM picture of NiSi on SOI and on poly-Si, showing the difference in thermal stability. (from [39])

fore not occur. A similar argument can be made for a fiber texture, which is defined by a specific crystal plane that is aligned with the interface or surface. Therefore,

interface or surface curvature would also influence the interface or surface energy.

On the other hand, if the film is not epitaxial or fiber textured, but exhibits the axiotaxy texture, this problem does not exist: as axiotaxy is a matching across the interface which is not influenced by the shape of the interface, the change of the interface shape will in this case leave the interface energy value unchanged, as is shown in figure 10.7. This is consistent with the observed axiotaxy in NiSi on Si (100) and might be the reason for an extremely fast agglomeration when axiotaxy is present. In the case of a random texture, one can assume that the interface shape will also have little influence on the interface energy, and the grain boundary grooving model applies. However, due to the higher interface energy of a random interface compared to axiotaxy, agglomeration will occur more slowly when a random texture is observed than in the case of axiotaxy. This is consistent with the observed texture of NiSi on Si(100) (strong axiotaxy, poor stability), poly-Si (random texture, medium stability) [71] and Si(111) (strong epitaxy + weak axiotaxy, good stability) and the reported sheet resistance during annealing in figure 10.5. For NiSi on Si(110), the quantitative information on the texture provide in [71] is too limited to verify if it completely fits the model, however, the texture can be described as a combination of relatively weak axiotaxy, fiber and epitaxy, which would put it between NiSi on Si(100) and Si(111) in terms of thermal stability.

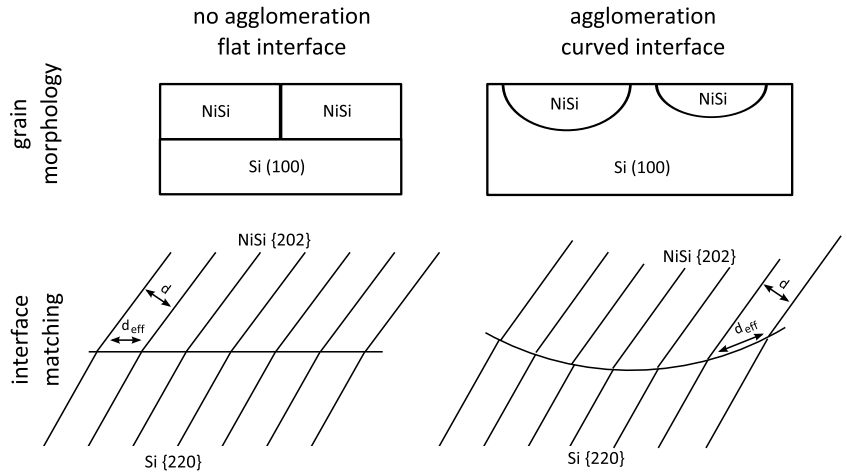

Figure 10.7: Example of grain morphology and interface matching for NiSi on Si (100). If axiotaxy is present, the interface structure is not influenced by the shape of the interface.

The effect of alloying elements on the agglomeration can be looked at from different perspectives: alloying elements might change the interface energy values, therefore changing the driving forces for agglomeration. This can either happen through a chemical effect, where the alloy element actively participates in the in-

terface formation between film and substrate, but might also be a crystallographic effect, where the periodic interface is destroyed or reinforced by the shrinking or extending of the crystal lattice of the film. In literature, the concept of grain boundary pinning is often used [95], where a mechanistic origin is given to the prevention of the agglomeration, as the slowly diffusing alloying atoms become concentrated in the grain boundaries and prevent further grain boundary diffusion. Here, the alloying element does not change the driving force for agglomeration, but slows it down by limiting grain boundary diffusion. This view however does not take the anisotropy of the interface energy into account. Considering only the diffusion speed as being the determining factor in agglomeration cannot explain the difference in agglomeration of NiSi on poly-Si vs. Si (100).

In summary, one obtains the following model for the agglomeration of NiSi on Si(100): as the film is heated, material transport occurs from the grain boundaries to the interface of the grain with the substrate, driven by the difference in free energy between the grain boundary and the interface. This process can only occur when the interface energy is relatively independent of the interface shape, and the transport will preferentially move towards the interface of the lowest free energy. This results in mass transport from grains with a random orientation (i.e. a high interface energy) towards the axiotaxy grains, which have a lower interface energy and obtain a curved interface with the Si (100) substrate.

Of course, this model is only valid in so far that it agrees with the experimental results. To investigate this, the texture evolution was studied, both during agglomeration, as well as during extended annealing of thicker films, where grain growth of grains with a low interface energy could occur. If the model is correct, one should see an increase in the volume of the grains that have the axiotaxy texture.

10.3 Experimental details

Ni films with a thickness of 10 and 30 nm were sputter deposited on HF cleaned Si (100) substrates, resulting in 20 and 60 nm NiSi films after annealing. The films consisting of 30 nm Ni received a 2nm Si cap.

In case of the 10 nm Ni samples, the goal is to investigate texture evolution during agglomeration. For this, the samples were ramp annealed at $3°C/s$ to either 500, 650, 700, 800 and 840°C, resulting in the formation of NiSi, after which the $\{112\}$ pole figure was recorded at the X20A beam line using a point detector (Schulz method). EBSD measurements could not be completed successfully due to the small grain size.

For the 30 nm Ni samples, grain growth was investigated during prolonged an-

nealings at a temperature below the typical formation temperature of $NiSi_2$. This should indicate whether there is preferential grain growth in the NiSi films. Both XRD pole figures using a point detector (Schulz method) and EBSD measurements in an FEI Quanta 200F FEGSEM were performed.

10.4 Texture evolution of 20nm NiSi films during agglomeration

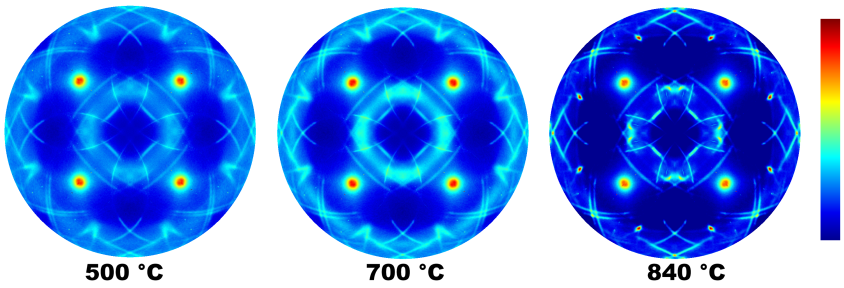

Figure 10.8: NiSi $\{112\}$ pole figures recorded on 20nm NiSi films after annealings at different temperature, showing the texture evolution. A decrease in the uniform intensity of the pole figure, caused by randomly oriented grains is observed, as well as an increase in intensity of the axiotaxy lines and epitaxy spots, when the temperature is increased.

Figure 10.8 shows the evolution of the texture of the film in a $\{112\}$ pole figure. All pole figures are plotted on the same logarithmic scale. From left to right (= increasing annealing temperature) one sees a clear evolution in the texture of the film. At 700 °C, the intensity in certain regions of the pole figures has significantly changed and the axiotaxy lines have increased in intensity. Further heating to 840 °C results in an increase of intensity in the epitaxial spots and a lower background signal. Since a $\{hkl\}$ type of axiotaxy reduces to a spot in an $\{hkl\}$ pole figure, the number of XRD counts in this spot is proportional to the volume of the grains having the axiotaxial orientation. One can therefore use the X-ray intensity in this spot to get an estimate of the importance of a specific axiotaxy texture component. However, for the $\{202\}$, $\{211\}$ and $\{112\}$ axiotaxy, the d-spacing of the NiSi planes is close to the one of the Si $\{220\}$ plane, making it impossible to isolate the XRD signal of NiSi from the Si $\{220\}$ signal, since they both result in spots at the same location in the pole figure. For NiSi $\{103\}$, this problem does not occur, and figure 10.9 shows the X-ray intensity, corrected for background, generated by the $\{103\}$ axiotaxy as a function of annealing temperature. On the same figure, the sheet resistance (at room temperature) of the resulting NiSi layer is plotted.

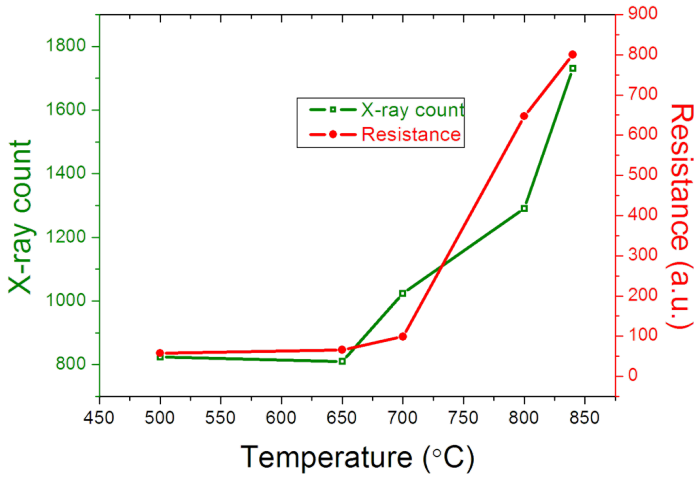

Figure 10.9: X-ray counts produced by the {103} NiSi axiotaxy in 20nm NiSi films annealed to different temperatures. This is correlated to the sheet resistance of the films, showing a clear correspondence between the increase in axiotaxy and the increase in sheet resistance due to agglomeration.

One can observe that the X-ray intensity stays constant up to 650°C, after which a sharp increase is visible. If one compares this to the resistance measurements, this can be correlated to the sharp increase in sheet resistance of the NiSi film as it starts to agglomerate.

Due to the experimental problems discussed above, no such quantitative data is available for the {202}, {211} or {112} axiotaxy components, but in the pole figures in figure 10.8, the qualitative trend of the increasing volume fractions of axiotaxy during agglomeration can be observed as well, indicating a correlation between axiotaxy and agglomeration.

10.5 Texture evolution of 60nm NiSi films during grain growth

Due to their increased thickness, agglomeration will occur much slower in a 60 nm NiSi film when compared to the 20 nm NiSi film. In fact, the layer will most likely convert to $NiSi_2$ before agglomerating, when heating to the higher temperatures ($> 700°C$) at which agglomeration occurs more rapidly. However, the initial stages of grain boundary grooving and grain growth of the grains with low inter-

Axiotaxy	550°C, 0h dwell time	550°C, 72h dwell time
{211}	9	11
{202}	10	12
{103}	3.5	5.5
{112}	1.5	1.5
Total axiotaxy	24	30

Table 10.1: Volume fractions of the axiotaxy texture components in % (with a maximum disorientation of 2°)

face energy can still occur below this temperature. To study this, a sample was first annealed to 550 °C to allow for NiSi formation. Part of the sample was then kept at 550°C for 72 hours to induce grain growth. On the samples, EBSD measurements were carried out by collecting 200000 data points, in both cases using identical settings for measurement and analysis parameters. Even though the resulting NiSi is thicker than in the previous section, the grain size is still in the range of 100-200 nm, making it impossible to collect reliable statistics on the grain size distribution (i.e. to follow its evolution during grain growth and possibly observe the typical bimodal size distribution associated with abnormal grain growth), since many individual measurement points would need to be collected in one single grain. Instead, the 200000 data points were collected using a step size of 250 nm between consecutive points, resulting in the sampling of 200000 different grains and excellent statistics of the volume fractions of the texture components. From this data, the volume fractions for each of the axiotaxy texture components were calculated and are shown in table 10.1. One can observe an increase in the volume fractions belonging to axiotaxy texture components during the 72h hour anneal. In total, the amount of axiotaxial grains has increased from 24% to 30%. One should notice that the values for the volume fractions of axiotaxy grains are lower than in the case discussed in chapter 7, table 7.1, which is likely caused by the use of a 2 nm Si cap in the samples investigated in this chapter, to prevent oxidation during the 72h anneal. The amorphous silicon on top of the nickel layer may promote the formation of nickel-silicides with a random texture. Since the interest here is in the texture evolution, these differences are of less importance.

XRD pole figures were recorded as well (figure 10.10). Plotted on the same scale, the increase of the axiotaxial and epitaxial components after a 72h anneal is clearly visible.

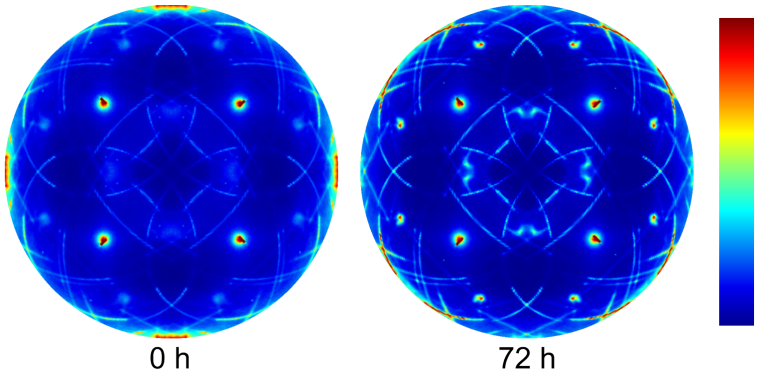

Figure 10.10: NiSi $\{112\}$ pole figures recorded on 60nm NiSi films after annealings at 550°C, and kept at this temperature for 0 or 72 hours. The intensity in the axiotaxy lines and the epitaxial spots has increased.

10.6 Conclusions

In this chapter, the agglomeration of NiSi was discussed and it was related to the grain boundary grooving model. It was pointed out that the dependence of the agglomeration on the substrate type and orientation is atypical and is likely related to the microstructure of the NiSi film. It was proposed that there exists a relation between axiotaxy and the speed of agglomeration, due to the fact that the axiotaxy interface structure is independent of the shape of the interface. This was corroborated by both the XRD and EBSD results on NiSi films, where an increase in the volume fraction of axiotaxy grains was observed during agglomeration in thin films and preferential growth of axiotaxy grains in thicker films.

11

θ-nickel-silicide and its influence on NiSi thermal stability

In this chapter, the relationship between the initial composition, phase formation and texture in thin films will be illustrated for the case of the Ni/Si system. The formation of the NiSi phase from the reaction of a pure metal film with the silicon substrate occurs through the formation of a series of intermediate phases, initially rich in nickel and becoming more and more silicon rich. Each phase transition in this sequence will occur through the driving force of the gain in free energy that can be accomplished by moving to a more silicon rich phase, but limited by both the nucleation of a new phase and/or the diffusion to reach the specific nickel/silicon ratio. If one intervenes artificially in this nickel/silicon ratio, by premixing the deposited nickel film with a certain fraction of silicon, one can expect to influence the phase selection during the solid state reaction. As phase formation, diffusion and texture can be closely related, this can have a profound impact on the formation of the different silicides phases, their texture and properties.

Van Bockstael et al. [96] reported a systematic overview of the effect of mixing a variable amount of silicon in the initial nickel layer on the initial phase selection. In this chapter, the case where 40% of silicon is mixed in the nickel film and where Si (100) and Si (111) substrates are used, will be investigated. The increase in thermal stability of NiSi formed from these layers will be related to the change in microstructure, and the effect of W and Pt on the phase sequence and texture in

the Ni/Si(40%) system will be related to the effects on the pure Ni/Si(100) system.

The results discussed in this chapter have been published in:

De Keyser K., Van Bockstael C., Detavernier C., Van Meirhaeghe R.L., Jordan-Sweet J., Lavoie C., *Epitaxial formation of a metastable hexagonal nickel-silicide*, Electrochemical and Solid-State Letters 11(9), H266 (2008)

Van Bockstael C., De Keyser K., Van Meirhaeghe R.L., Detavernier C., Jordan-Sweet J., Lavoie C., *Influence of a transient hexagonal phase on the microstructure and morphological stability of NiSi films*, Applied Physics Letters, 94(3), 033504 (2009)

11.1 Experimental details

Nickel and silicon were co-sputtered on standard RCA cleaned and HF dipped Si (100) and Si (111) wafers, at room temperature. The sputtering power and time for the nickel deposition were chosen so that the thickness of the nickel layer would correspond to 50 nm if no Si would have been co-sputtered. The sputtering power for the silicon was then chosen to result in a layer containing 40 percent silicon. The phase formation was monitored using in-situ XRD. Quenches were then made at 420°C, which were studied using Rutherford backscattering spectroscopy (RBS) to determine the composition, X-ray pole figures (Schulz method) to study the phase and texture, X-ray reflectivity to determine layer thickness and EBSD to determine microstructure and carry out phase identification.

11.2 Phase formation

The samples were studied using in-situ XRD at the X20C beam line using monochromatic X-rays with a wavelength of 0.18 nm, with an incidence angle of $\theta = 27°$ to the surface normal. While heating each sample from 100 °C to 700 °C at a rate of 3 °C/s in a high purity helium atmosphere, the diffracted X-ray intensity is recorded every 0.5 s, in a 2θ range from 48° to 61°. Figure 11.1 shows the results for the samples starting from the nickel layer containing 40% silicon (atomic percent). Three regions can be distinguished. In the first region, at temperatures below 370 °C for Si (100) or 360°C for Si (111), one sees a faint and broad peak at $2\theta = 53°$, caused by the as-deposited nickel-silicon layer. The poor crystallinity of this layer results in the weak and broad peak. In a second region, between 370 and 480°C (Si

(100)) or between 360 and 510°C (Si (111)), hardly any diffracted intensity is collected, hinting at either an epitaxial or amorphous phase being formed. At 480°C (Si (100)) or 510°C (Si (111)), the third region starts, where nickel monosilicide peaks are visible. On the Si (111) substrate, these peaks have very low intensity, once again hinting at either a strongly textured or a largely amorphous layer.

In figure 11.2, the traditional Ni/Si(100) and Ni/Si(111) phase formation is shown if no premixing of nickel and silicon is performed, using the same in-situ XRD setup. One can clearly see the important difference: the low-temperature range looks much simpler in the case of the Ni/Si premixed layer, when compared to the complex combination of different diffraction peaks that appear and disappear again in the same temperature window when pure Ni films are used. This is not surprising, as the changes in composition are much larger in the case of the reaction of pure Ni with the silicon substrate than when starting from a mixture that contains already 40% silicon. An important observation is that the premixing of 40% of silicon in the nickel layer does not simply result in "skipping" part of the phase formation sequence of the pure nickel case: the observed phase preceding the formation of NiSi is clearly different.

11.3 Formation of θ-nickel-silicide

The in-situ XRD results showed that the deposited Ni/Si mixture reacts around 400°C and forms a phase with a weak in-situ XRD signature. To study this phase, quenches were made at 420°C on both substrates. X-ray reflectivity measurements showed the thickness of the samples to be 100 nm after the anneal, and RBS measurements showed a slight increase in silicon content of the layer to about $44 \pm 2\%$ Si, uniformly distributed over the layer thickness. The crystallography of the resulting samples was analyzed using EBSD and XRD pole figures.

11.3.1 Phase identification using EBSD

EBSD can provide valuable information about silicides: it allows to distinguish between materials with different Laue groups, provides local crystal orientation information and grain sizes. Measurements were carried out on the samples quenched at 420°C, using an FEI Quanta 200F field emission gun scanning electron microscope, and an HKL Channel 5 system attached. The EBSD patterns were analyzed by comparing the measurements to simulated patterns of 5 different phases, which are reasonably close in Ni/Si composition to the results obtained by RBS: the hexagonal θ-nickel-silicide, ϵ-Ni_3Si_2 , δ-Ni_2Si, NiSi and $Ni_{31}Si_{12}$.

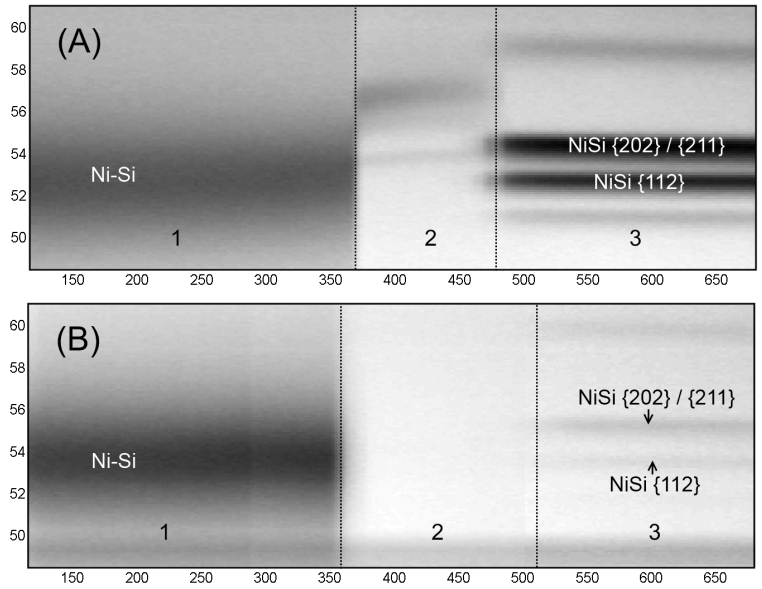

Figure 11.1: In-situ XRD measurement on Ni/Si premixed with 40% Si on Si (100) (subfigure A) and Si (111) (subfigure B) substrates

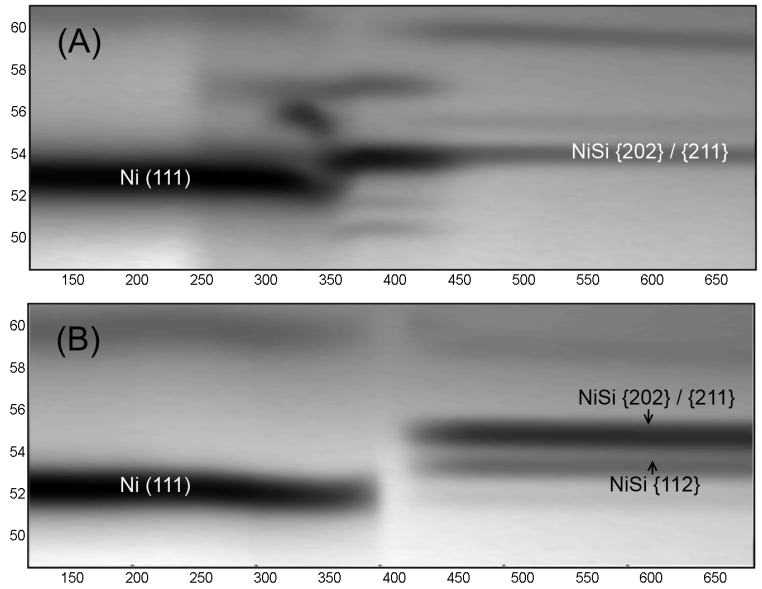

Figure 11.2: Reference in-situ XRD measurements of Ni on Si (100) (subfigure A) and Si (111) (subfigure B) substrates

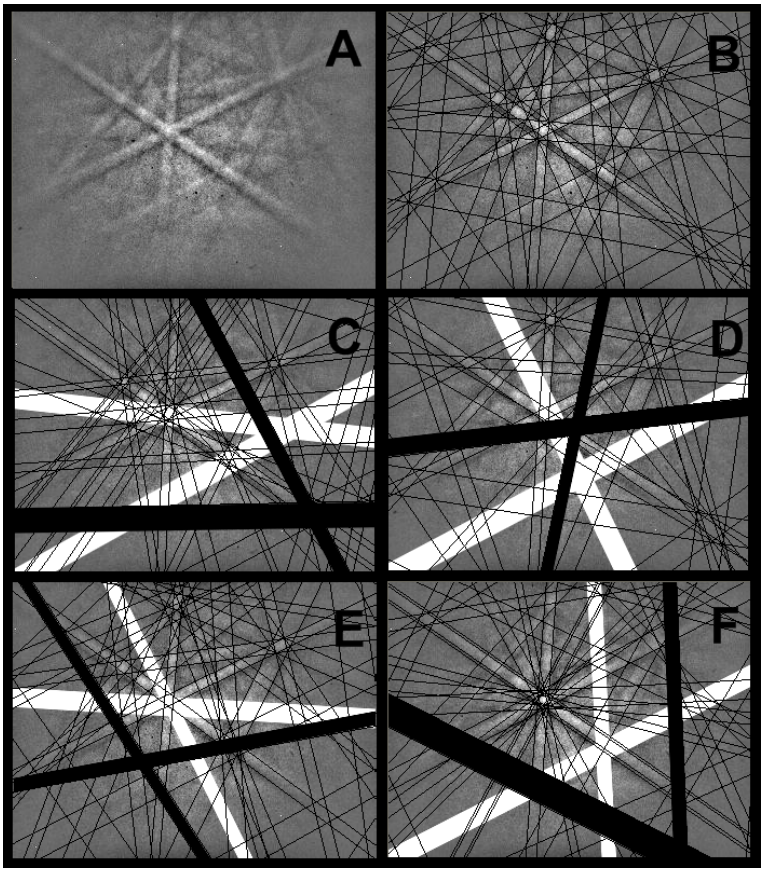

Figure 11.3: EBSD pattern (A) and best fit using θ-nickel-silicide (B), δ-Ni_2Si (C), ϵ-Ni_3Si_2 (D) $Ni_{31}Si_{12}$ (E) and NiSi (F). Missing bands are indicated in white, non-existing ones in black.

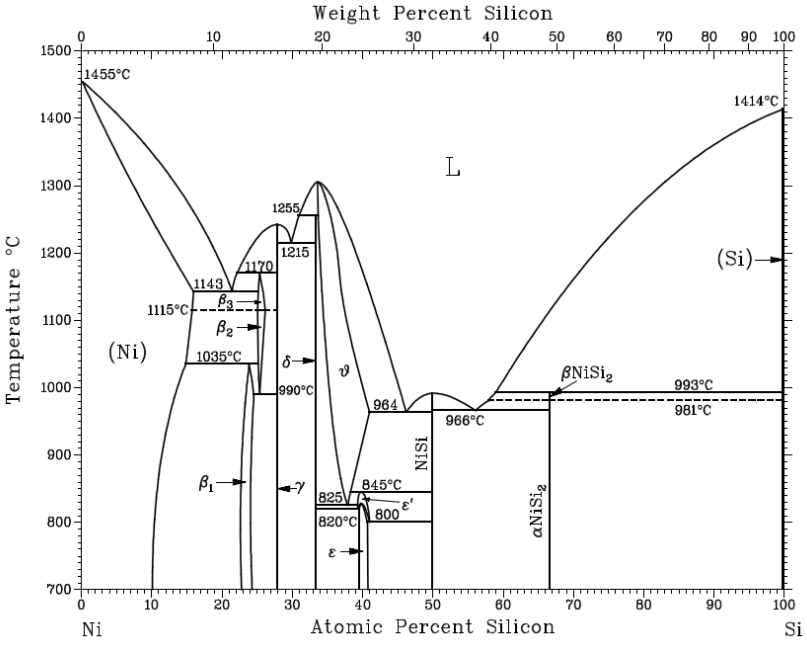

Figure 11.4: Phase diagram of Ni/Si (ASM International)

θ-nickel-silicide has a hexagonal lattice (space group P6$_3$/mmc), with variable composition. Typically, it has been reported containing 33% Si, resulting in lattice parameters a= 0.3805 nm and c=0.489 nm [97]. The unit cell has a series of sites that can be occupied by the nickel atoms. Depending on the occupation rate of these sites, the Si to Ni ratio can vary from 33% to 50%. In the phase diagram, θ-nickel-silicide is reported as only being thermodynamically stable at high temperatures (above 825°C) when it contains between 33% and 41% of silicon (see figure 11.4 for the phasediagram). However, these results apply to bulk materials. In thin films, the temperature and composition range might be different. Since θ-nickel-silicide is not a line phase, we prefer not to use the names θ-Ni_2Si or θ-Ni_3Si_2 as can be found in literature, as these can give the wrong impression of a fixed Ni-to-Si ratio.

The analysis of the EBSD patterns showed that a fit using the θ-nickel-silicide crystal structure is consistently much better than fits based on other phases. This has been shown for a typical EBSD pattern in figure 11.3, where subfigure A contains the recorded EBSD pattern. The fit for the θ-phase is shown in subfigure B. For each of the other phases (subfigures C-F), we show the best possible fit, however certain bands are missing, or bands are predicted that are not visible: a

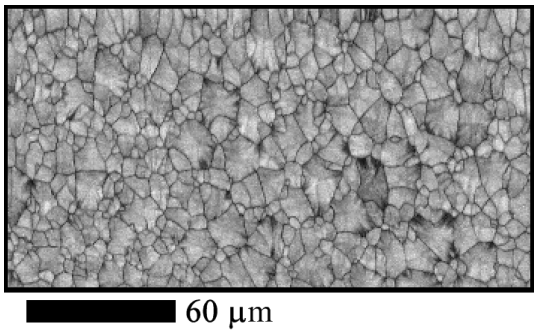

Figure 11.5: EBSD map collected on Ni/Si(40%) on Si(100) annleaed to 420°C, showing band contrast. The individual grains can be observed.

few missing bands were indicated in white on each of the fits, while predicted but not measured bands are indicated in black. Only for the θ-phase, a satisfactory -even excellent- fit could be produced, confirming that we are in fact dealing with a hexagonal phase which has a ratio of the lattice parameters c/a of 1.29. RBS showed a silicon content of about 44%, which is slightly larger than the reported composition range in the phase diagram. However, considering only a single RBS measurement on the θ-phase was carried out, and the error on the resulting concentration, it is currently impossible to tell whether the silicon concentration is significantly larger than what is reported in the phase diagram. Based on the crystallographic consideration expressed above, it is certainly possible for the θ-phase to contain more silicon.

The orientation information from EBSD showed that we have grown an epitaxial θ-nickel-silicide film. On Si (111), the basal $\{0001\}$ plane of the hexagonal θ-nickel-silicide phase is parallel to the Si (111) surface, and a $\{2\bar{1}\bar{1}0\}$ plane was found to be parallel to a Si $\{110\}$ plane. On Si (100), the matching planes are a $\{01\bar{1}1\}$ θ-plane parallel to a Si $\{100\}$ plane, and a $\{2\bar{1}\bar{1}0\}$ plane parallel to Si $\{110\}$. The grain size of the films was found to be around 10 μm on Si (100) (see figure 11.5). On Si (111), no grain boundaries could be found, leading to the conclusion that the film has huge grains, larger than 500 μm, the size of the measured area.

11.3.2 XRD pole figures

The identification of the θ-nickel-silicide phase and its epitaxial alignment using EBSD were corroborated by collecting multiple XRD pole figures. They are shown in figures 11.6 and 11.7. Multiple high intensity spots are visible, indicating the epitaxial texture of the film. Attempts to fit the spots on the pole figure with the

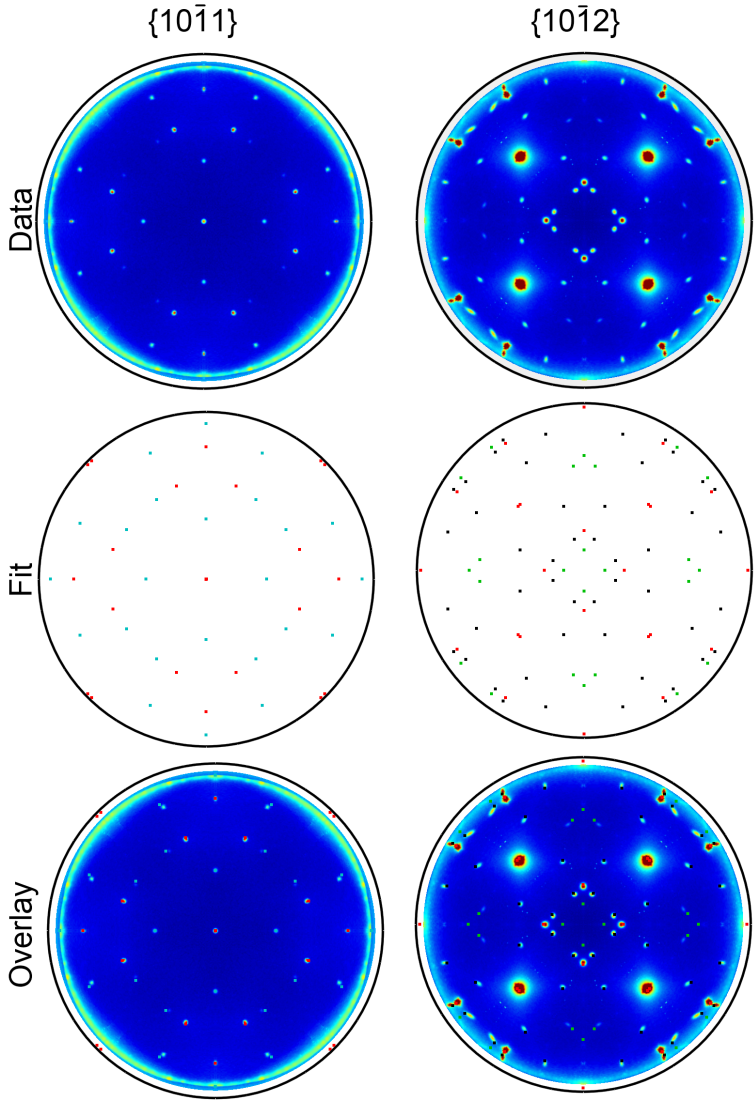

Figure 11.6: Pole figures on sample with nickel film and 40 atomic % silicon, Si(100) substrate, annealed at 420°C. A fit of the data is shown using the single epitaxial θ-nickel-silicide orientation. The spots belonging to either the $\{1011\}$ and $\{1012\}$ planes are shown in red. Black, green and cyan spots correspond to superstructure spots caused by resp. $\{\frac{1}{2}1\frac{\bar{3}}{2}\frac{3}{2}\}$, $\{0\frac{3}{2}\frac{\bar{3}}{2}1\}$ and $\{\frac{1}{2}0\frac{\bar{1}}{2}\frac{3}{2}\}$ planes.

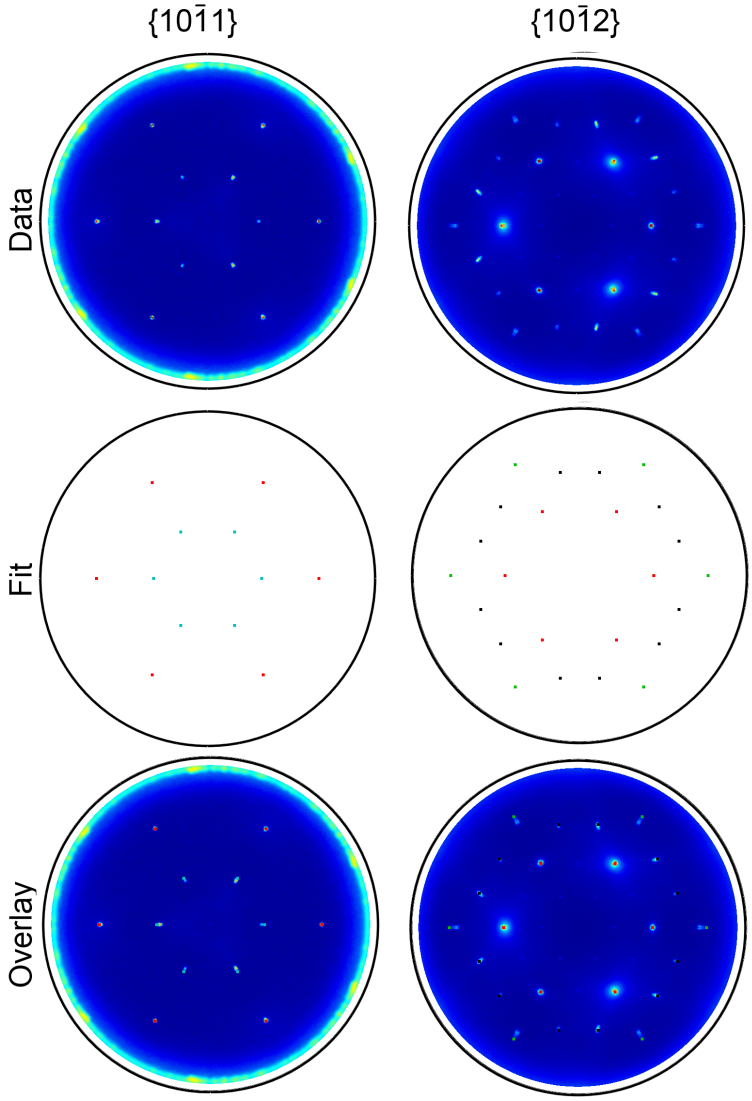

Figure 11.7: Pole figures on sample with nickel film and 40 atomic % silicon, Si(111) substrate, annealed at 420°C. A fit of the data is shown using the single epitaxial θ-nickel-silicide orientation. The spots belonging to either the {1011} and {1012} planes are shown in red. Black, green and cyan spots correspond to superstructure spots caused by resp. $\{\frac{1}{2}1\bar{\frac{3}{2}}\frac{3}{2}\}$, $\{0\frac{3}{2}\bar{\frac{3}{2}}1\}$ and $\{\frac{1}{2}0\bar{\frac{1}{2}}\frac{3}{2}\}$ planes.

different nickel silicide phases results in a good fit only when using the hexagonal θ-phase, and using the single epitaxial orientation identified using EBSD.

In addition to the high intensity spots, a large number of weaker spots can also be observed. It was found that these originate from superstructure planes, i.e. lattice planes with fractional indices when expressed in the θ-nickel-silicide unit cell. The most likely origin of the superstructure peaks is an ordering of vacancies within the θ-nickel-silicide unit cell, with a length scale twice the size of the unit cell. As the θ-nickel-silicide contains nickel sites with partial occupancy, these superstructure peaks can be caused by periodic occupancy/non-occupancy of these sites. This was also simulated in figures 11.6 and 11.7 and can indeed account for all of the weaker spots.

11.3.3 Origin of the formation of θ-nickel-silicide

The epitaxial formation of θ-nickel-silicide on a Si (111) substrate can be understood when comparing the position of the silicon atoms in the substrate and the film. Figure 11.8A shows the topmost layer of atoms of a Si (111) substrate. The hexagonal symmetry is visible: Si atoms are located at the vertices of the hexagons. Half of them (the white colored ones) are located slightly below the surface. The other half (the black ones), lay at the surface and have a dangling bond perpendicular to the Si (111) interface. These atoms have a distance of 3.84 Å, one to another. The silicon atoms in the $\{0001\}$ planes of the θ-nickel-silicide are located at the vertices of triangles, with a distance in between of 3.805 Å, which is shown in figure 11.8B. These layers will have a nearly perfect fit on the Si (111) surface atoms, saturating the dangling bonds and thus leading to a low energy interface.

On Si (100), there is no such obvious plane-on-plane match possible. However, close inspection of both orientation relations, on Si (100) and Si (111), reveals that they are in fact very similar: on Si (100), the $\{0001\}$ plane is almost parallel to the Si $\{111\}$ plane as well -there is only a small tilt of 1.1°- indicating that the epitaxial orientations on Si (111) and Si (100) are in fact strongly related. Figure 11.8C shows the Si (100) substrate. The Si $\{111\}$ planes are shown, arriving at the interface, as well as the $\{0001\}$ θ-planes. These are the same matching planes as in the case of the Si (111) substrate, and since the silicon atoms in these planes have identical spacing, dangling bonds at the interface will be saturated wherever they meet. To have a large fraction of the Si $\{111\}$ planes meet a $\{0001\}$ θ-plane, the spacing between the planes along the interface needs to be compatible. This is the reason for the small tilting of the $\{0001\}$ θ-planes in respect to the Si $\{111\}$ ones, as it leads to the shared periodicity along the interface, the same mechanism which was reported to lead to the one dimensional periodicity of axiotaxy. This results in about one in three of the Si $\{111\}$ planes meeting a $\{0001\}$ plane, which, while

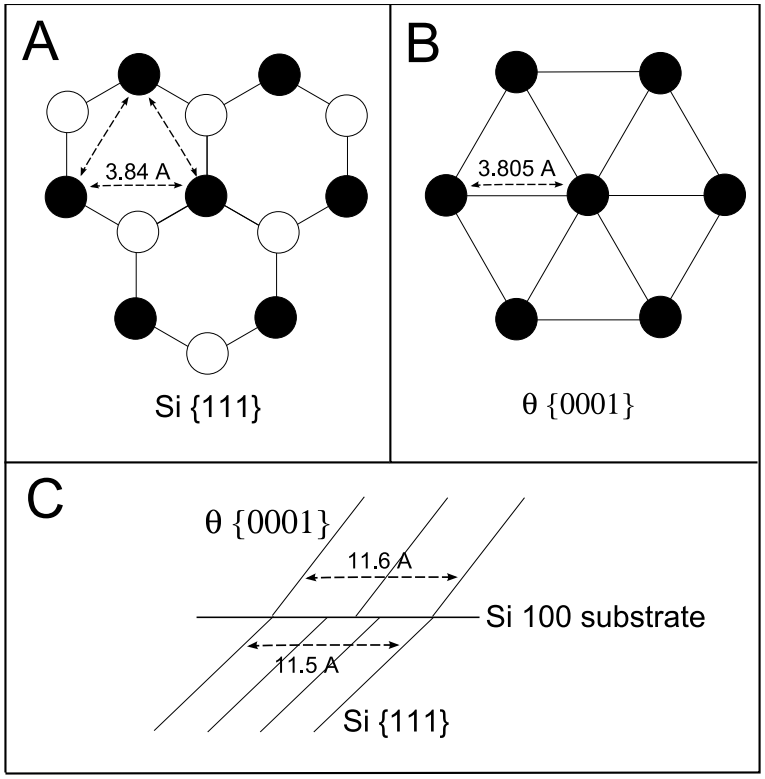

Figure 11.8: Silicon atoms at the Si (111) surface, black ones have a dangling bond (A). Silicon atoms in the basal plane of the θ-nickel-silicide phase (B). Plane matching of Si {111} planes and θ-{0001} planes at the interface of a Si (100) substrate (C)

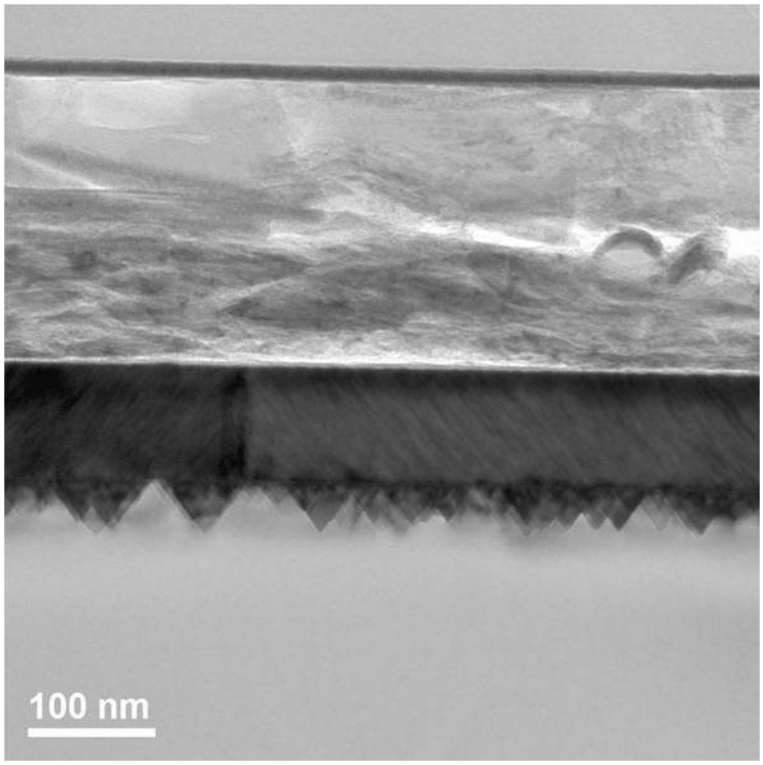

Figure 11.9: Cross section TEM of θ-nickel-silicide on Si (100). A large number of pyramids have been formed at the interface.

not as good as the match on a Si (111) substrate, still results in a lower energy interface than random orientation.

The matching of the basal $\{0001\}$ plane with the Si(111) plane also leads to the formation of pyramid structures at the interface, very similar to what can be observed for $NiSi_2$ on Si(100). A cross-section TEM image is shown in figure 11.9.

The different experimental characterization techniques all point toward an epitaxial layer of θ-nickel-silicide. However this phase is thermodynamically unstable: the lowest temperature at which θ-nickel-silicide can exist in thermodynamic equilibrium, is, according to the phase diagram, 825°C, at which point an eutectoid reaction takes place, transforming the θ-phase to a δ-Ni_2Si and ϵ-Ni_3Si_2 mixture. This is the case when the θ-phase contains 38% silicon. For higher concentrations of silicon, such as in our experiment, the θ-phase will reduce its silicon content by separating into NiSi and θ-nickel-silicde with a lower Si content, at temperatures even higher than 825°C. The existence of meta-stable layers such as CoSi[98] and

FeSi[99] has been reported before, but these layers were very thin, and grown using molecular beam epitaxy. The low interface energy was found to stabilize these epitaxial layers. For the nickel/silicon system, Gibson et al. reported [100] the existence of very thin (maximum 2 nm) layers of θ-nickel-silicide on Si (111) and their absence on Si (100) when depositing pure nickel on silicon, which suggests interface stabilization as well. While the epitaxial orientation of our films does seem to point into the direction of interface stabilization, its large thickness (100 nm) makes it unlikely that this is the sole determining factor.

All of the reactions leading up to the room temperature θ-phase take place at temperatures far below 825°C. As the θ-phase can grow in exactly the same composition as the amorphous mixture, only very limited diffusion, thus low temperature, is needed for congruent crystallization to occur. Since the rate of nucleation during crystallization generally depends exponentially on the supercooling, the crystallization will proceed easily due to the large supercooling at around 400°C. In addition, since almost no diffusion is necessary for grain growth due to the congruent crystallization, large grains will be formed, which agrees with the EBSD measurements. The expected subsequential eutectoid transformation that decomposes θ-nickel-silicide in either δ-Ni_2Si and Ni_3Si_2 or Ni_3Si_2 and NiSi, is a diffusive phase transformation, and being far below the eutectoid reaction temperature of 825°C, it is slowed down significantly due to the limited diffusion. In addition to this, the epitaxial orientation of the θ-phase also has an effect. It results in a low interface energy, which makes nucleation of the thermodynamically stable phases (δ-Ni_2Si, Ni_3Si_2 or NiSi) more difficult, further stabilizing the θ-phase.

The fact that the interface energy is only a secondary effect was confirmed by depositing identical mixtures of Ni/Si on polycrystalline silicon [96]. θ-nickel-silicide still formed and could be kept at room temperature after quenching, however, it is only very briefly stable, as it forms at $370°C$ and disappears again at $420°C$. The different stability range on Si (111), Si (100) (see figure 11.1) and polycrystalline silicon clearly demonstrates the effect of interface energy on the energy balance of the system. The fact that it still forms on polycrystalline silicon proves that interface stabilization in itself could not be responsible for the occurrence of θ-nickel-silicide, but it is the composition of the amorphous mixture that is the determining factor for the occurrence this phase.

From a technological point of view, the mixing of nickel and silicon in a 60/40 ratio makes little sense. It destroys the possibility of using the salicide process to form the contacts, which makes integration with current deep-submicron processes impossible. However, the Ni/Si mixture can serve as a model system for the thin amorphous layer that is created during deposition (e.g. sputter deposition) of nickel on silicon. The θ-nickel-silicide layer reported on Si(111) by Gibson [100], is likely related to this amorphous mixing layer. As the nickel layer gets

thinner, the intermixing layer will start to dominate the phase sequence. For this reason, the results discussed in this chapter are relevant for the phase formation of technological relevant layers. In chapter 13, these ultra-thin nickel films will be investigated in detail.

11.4 Influence on NiSi formation and thermal stability

The in-situ XRD results revealed the formation of NiSi when the Ni/Si(40%) sample was annealed to temperatures higher than 480°C on Si(100), or 510°C on Si(111). This NiSi is formed by the reaction of the epitaxial θ-nickel-silicide layer with the Si (100) substrate, and one can wonder what the effect of the epitaxial precursor θ-phase is on the microstructure of the NiSi film. For this, quenches were made at 700°C, and pole figures were recorded using the Schulz method. The NiSi $\{103\}$ pole figures are shown in figure 11.10, as well as pole figures recorded on reference samples obtained by quenching pure Ni films on both substrates.

The large difference in texture is clear: NiSi formed from the Ni/Si(40%) mixture exhibits strong peaks in the pole figure, indicating an epitaxial texture. On Si (100), the epitaxial relation could be identified as NiSi (011) // Si (001) and NiSi (100) // Si (100). On Si (111), NiSi was found to have NiSi (100) // Si (111) and NiSi (001) // Si ($1\bar{1}0$).

We have thus obtained a method of producing NiSi on Si(100) which does not exhibit the axiotaxy texture, without adding alloying elements. This provides an interesting test case for the ideas surrounding the relation between texture and agglomeration, as we can now isolate the effect of grain boundary pinning due to the high concentration of alloying elements in the grain boundaries, from the pure texture effects.

To study the thermal stability of the resulting NiSi, new samples were made, with a nickel thickness of 10 nm, still mixed with 40% Si, deposited on a SOI substrate to allow for in-situ sheet resistance measurements. No further experiments were made on Si (111), because NiSi agglomeration is much less of a problem on Si (111).

In-situ XRD (figure 11.11) showed an identical phase formation as in the thicker (50 nm) sample, and the same NiSi epitaxial texture was obtained as in the thicker films. This texture was confirmed with EBSD (figure 11.12), where large epitaxial grains were found, combined with smaller, randomly oriented NiSi grains.

If one compares the in-situ sheet resistance of both films as a function of temper-

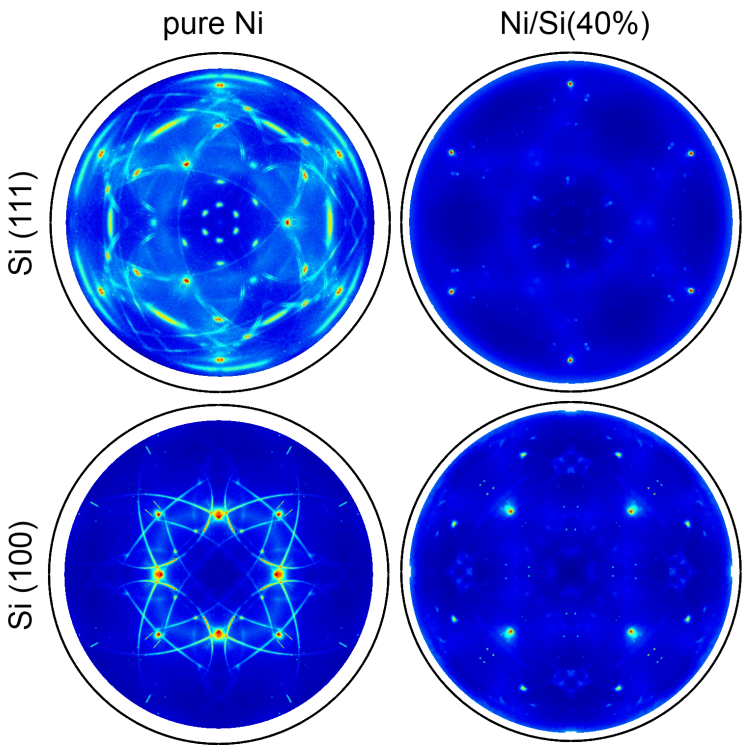

Figure 11.10: {103} pole figures recorded on 100 nm NiSi obtained after annealing either pure nickel, or nickel premixed with 40% silicon.

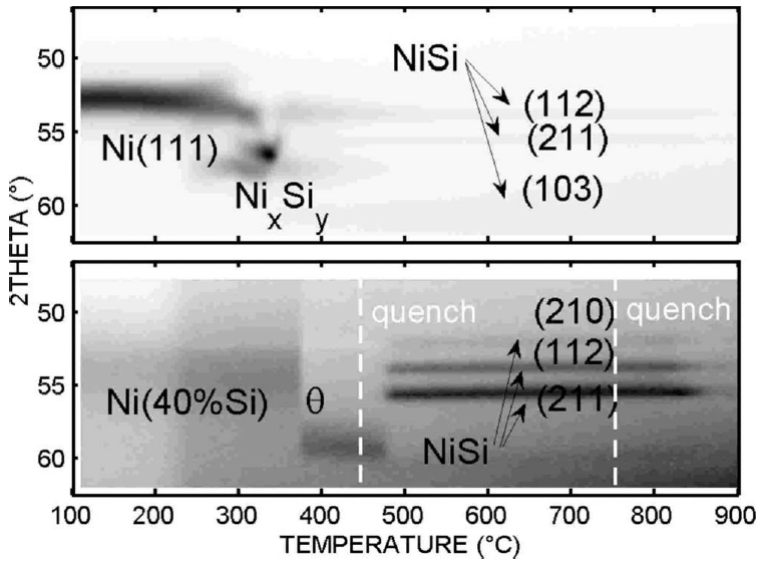

Figure 11.11: In-situ XRD measurement on 10 nm Ni on SOI (subfigure A) and on 10 nm Ni premixed with 40% Si on SOI (subfigure B)

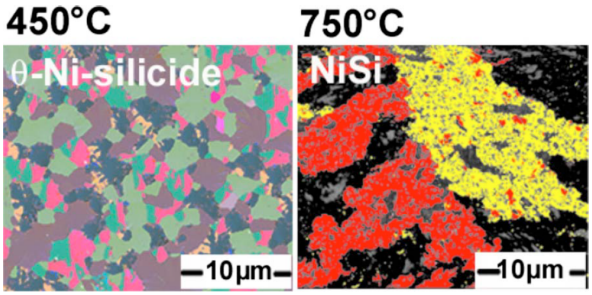

Figure 11.12: EBSD map recorded on a 10 nm nickel film on SOI, annealed to 450°C (formation of θ-nickel-silicide) and 750°C (formation of NiSi). The large yellow and red grains in the NiSi film have the epitaxial relation with the substrate. Small grains (gray) have a random orientation.

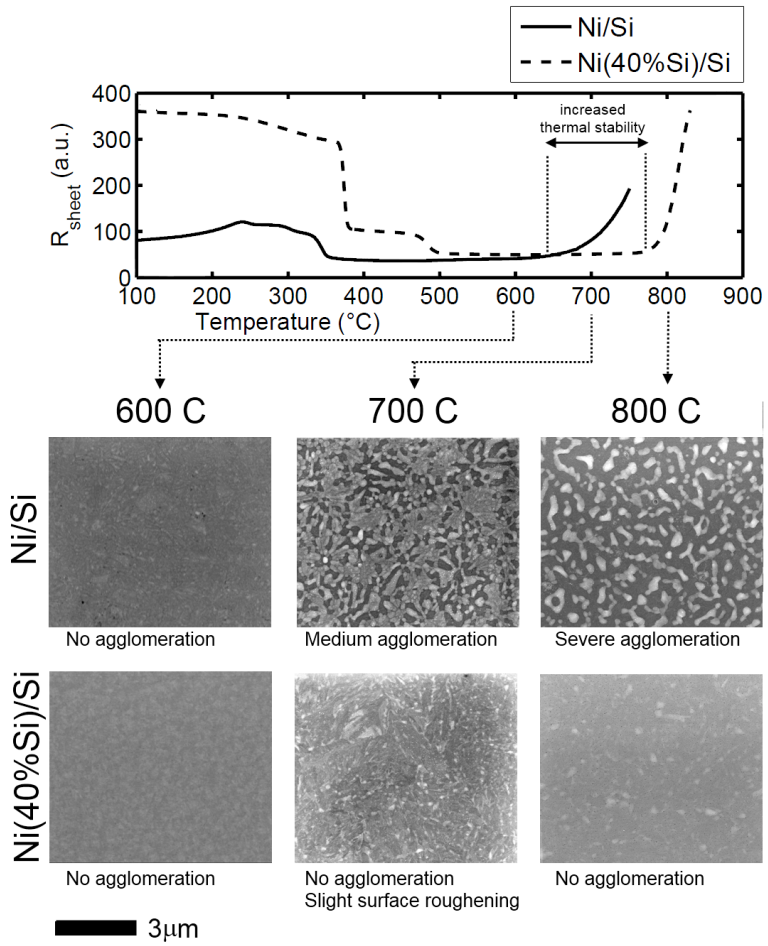

Figure 11.13: In-situ sheet resistance of 20 nm NiSi on SOI, obtained either through the use of a pure nickel film, or a premixed nickel/silicon (40%) film. Top-view SEM images on quenches show the degree of agglomeration.

ature, one observes a large difference in thermal stability (see figure 11.13), as the increase in resistance of the NiSi due to agglomeration is delayed to almost 800 °C when the nickel/silicon premixture is used, compared to the traditional pure nickel film on Si (100). The top-view SEM images corroborate this as only an increase in roughness is observed in the NiSi formed from the Ni/Si(40%) mixture, whereas the traditional NiSi shows severe agglomeration.

The increased thermal stability of the NiSi film formed from the premixed Ni/Si illustrates the importance of the microstructure (both grain size and texture) in

determining the agglomeration behavior of the film. It corroborates the proposed relation between axiotaxy and agglomeration (see chapter 10), as the Ni/Si(40%) system demonstrates that no additional elements such as Pt or W are necessary to improve the morphological stability. This indicates that at least part of the effect of alloying elements on the increased thermal stability of NiSi can be caused by the changes in microstructure induced by the introduction of these elements. In light of this, the observation that axiotaxy is suppressed in NiSi(Pt) [41] and NiSi(W) [101] could be the main cause for the improved morphological stability in these systems.

11.5 Effect of ternary elements on θ-nickel-silicide formation

11.5.1 Ternary elements as alloy or interlayer in the Ni/Si(100) system

Ternary elements are often introduced into the Ni/Si(100) reaction as a way to improve the properties of the NiSi contact. The best example of this is Pt addition to improve the thermal stability, but other elements such as W, Ti, Ta have also been investigated [102, 101, 103] and showed a clear improvement of the morphological stability.

11.5.1.1 W

In [101], the effect of alloying W in the Ni film was investigated, and the effect on the phase formation sequence was reported using in-situ XRD, the results of which are reproduced in figure 11.14b. It was suggested that in the temperature range of 300 to 400°C, where no diffracted X-ray intensity was recorded, only an amorphous phase might be present. However, no proof of this was presented. If one compares the reported Ni(W)/Si(100) in-situ XRD spectrum with that of the Ni/Si(40%) on Si (100) reaction, repeated in figure 11.14a, the similarity is clear, as 3 regions can be observed with similar X-ray peaks and intensity, except for a temperature shift of 70°C. This suggests that the W alloying might induce a similar change in phase sequence as the Ni/Si(40%) mixture.

To investigate which phases have formed in the 300 - 400°C temperature range, a sample was made by quenching the Ni(W 15%) film at 350°C. Pole figures were recorded using a linear detector (λ=0.154 nm) and diffracted intensity was only found in the region 45-48° (excluding the diffracted intensity caused by the silicon

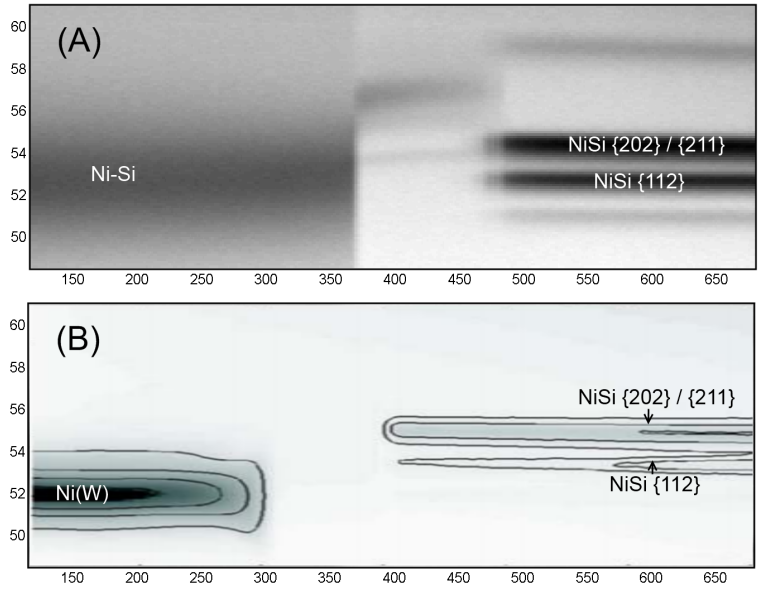

Figure 11.14: Phase formation sequence of (A) Ni/Si(40%) on Si (100) and (B) Ni(W) on Si (100) (data from [101]

substrate). Two pole figures show this diffracted intensity, which is concentrated in a number of spots (figure 11.15).

Identification of the exact 2θ values at which the peak intensity in these spots is the highest, is challenging, as their intensity remains largely unchanged in a range of 2°. This could be caused be a very small grain size in the material, as peak broadening is related to the grain size through the Scherrer equation, and makes phase identification impossible based on the pole figures.

One can however observe that the most intense spots coincide with the location of those caused by epitaxial θ-nickel-silicide on Si (100), if one compares with figure 11.14a, where the poles of the θ-nickel silicide $\{102\}$ plane are shown, which diffract at 2θ=46.2°. This is indeed within the range where diffracted intensity is observed for the Ni/W sample. However, the additional weaker peaks observed in the Ni/W sample and lack of diffraction outside the 2θ range of 45-48° exclude the possibility that this phase is exactly the same as the θ-phase.

No EBSD patterns could be collected on the sample, possibly due to the small grain size, or due to a random distribution of W within the film, which could destroy the diffraction pattern due to the additional random scattering of the backscattered electrons by the W atoms.

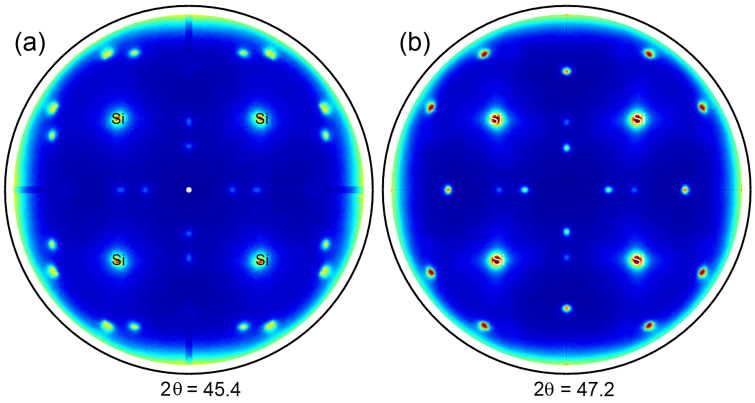

Figure 11.15: Pole figures recorded on a 30 nm Ni + 15% W film, annealed to 350°C, for (a) 2θ=45.4° and (b) 2θ=47.2°.

At the moment, no successful identification of the phase is possible using any of the in literature reported Ni/Si crystal structures. The most likely candidate, based on the limited amount of data available, would be a hexagonal, θ-like Ni/Si/W phase, having an epitaxial orientation identical to the one reported for θ-nickel-silicide on Si(100), and where the added W lowers the structure factors of the diffracting planes, resulting in only the $\{10\bar{1}2\}$ and $\{11\bar{2}0\}$ planes having a sufficiently high structure factor to produce measurable diffracted intensity. While this is largely speculative, a report by Ellner et al. [104] on Ni/Si mixtures in bulk showed that a large variety of related hexagonal Ni/Si crystal structures exists, each with distinctive but related diffraction patterns. In [104], this variety was caused by variations in the Ni/Si composition, resulting in changes in the c/a ratio of the hexagonal unit cell, the introduction of vacancies and inhomogeneous deformation of the crystal structure. The introduction of a small amount of W might lead to a similar effect and result in a θ-nickel-silicide related Ni/W/Si phase.

When the Ni/W layer is annealed to a temperature higher than 400°C, Ni(W)Si is formed. In [101], the texture of this Ni(W)Si was investigated using pole figure measurements. Comparing those results with the pole figures of NiSi formed from a Ni/Si(40%) layer, one can notice that they are very similar, as evidenced by the pole figures in figure 11.16: in both cases, NiSi exhibits the same largely epitaxial texture.

Both these observations seem to indicate a close connection between the effect of alloying W in the Ni film, or mixing Ni/Si(40%), as the X-ray diffraction results indicate a similar phase formation and texture.

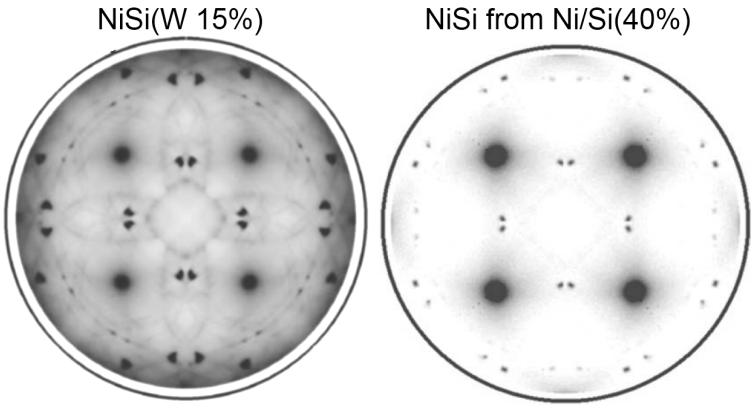

Figure 11.16: NiSi {112} pole figures recorded on NiSi formed either by alloying W in the Ni film, or by mixing the Ni film with 40% of Si. The high intensity spots (black) indicate a similar epitaxial texture in both films.

11.5.1.2 Pt

The effect of alloying a Ni film with Pt, both on the phase formation and the texture of NiSi on Si(100) has received a lot of attention. Demeulemeester et al. [105, 106] reported on the phase formation and redistribution of Pt during the reaction of Ni(Pt) on Si(100): it was shown that the addition of 7% of Pt to the Ni film suppresses the formation of the transient metal-rich nickel silicides (only pure Ni, δ-Ni_2Si, NiSi and $NiSi_2$ are observed) and also leads to the simultaneous growth of δ-Ni_2Si and NiSi. The addition of Pt was also reported to suppress axiotaxy in the NiSi phase [41], but the reported pole figures for the Ni(Pt)Si {112} plane show a different texture than in the case of NiSi originating from Ni/Si(40%) or Ni(W). Both the influence of Pt on the texture, as well as on the phase formation are thus different from the effect of alloying W or 40% Si. Pt does not induce the formation of a hexagonal Ni/Si phase - on the contrary, as it suppresses the formation of the θ-nickel-silicide phase which is briefly observed in the metal-rich phase sequence of pure Ni/Si(100) - and it does not produce the same epitaxial NiSi orientation as caused be the addition of W or the use of premixed Ni/Si(40%).

11.5.2 Effect of Pt and W on the Ni/Si(40%)/Si(100) system

The observed difference between W and Pt alloying in the nickel film, on the NiSi formation and texture, discussed in the previous section, suggests a fundamentally different effect of W and Pt on the metal-rich nickel-silicide phases, in particular on the θ- or θ-like nickel silicide, which W seems to promote while Pt prevents it for-

mation. The effect of W and Pt on the phase formation and texture of Ni/Si(40%) layers on Si(100) substrates will be investigated in this section, as a model system for the interaction of W and Pt with this θ-nickel-silicide phase that occurs during the metal-rich phase formation of the pure Ni/Si(100) reaction. While these results are preliminary, as only relatively small W and Pt fractions have been investigated, and additional characterization of the samples is required, the currently available results already provide new insights in the effect of W and Pt on the Ni/Si reaction on Si(100).

Samples were produced by co-sputtering Ni/W/Si(40%) and Ni/Pt/Si(40%) layers on RCA cleaned and HF dipped Si(100) substrates, with a nickel content corresponding to a 50 nm pure nickel layer. The W and Pt sputtering power was chosen to result in a 1, 2, 3 and 5% W/Pt to Ni ratio. On these sample, in-situ XRD was carried out (X20C, λ=0.18 nm) in the temperature range 100°C to 900°C, the results of which are displayed in figure 11.17.

11.5.2.1 Phase formation

In the case of W addition, the phase sequence remains qualitatively unchanged, when compared to the pure Ni/Si(40%) reference. There are 3 regions identifiable, starting with the as-deposited mixture, which is converted into a crystalline metal-rich phase at a temperature between 440 - 510°C, with higher temperatures corresponding to higher concentrations of W in the mixture. This phase is then converted to NiSi around 580 °C, with little influence of the W concentration on this temperature.

The influence of adding Pt to the Ni/Si mixture is different: only in the case of a very small amount of Pt (1%), one can observe 3 clearly distinct regions. If more Pt is added, the phase sequence can be best described as consisting of two regions, where the conversion from the mixture to a crystalline phase, identifiable as NiSi, is spread out over a temperature range of about 50°C.

11.5.2.2 Texture

For each Pt and W concentration, 2 quenches were made. In the case of W (all concentrations) and Pt (1%), a first quench was made in the metal-rich phase. For the other Pt concentrations, a quenching temperature was selected within the region of initial NiSi formation (380-440°C). A second quench was made at 700°C, a temperature at which in all of the samples, the film has been converted to NiSi. Pole figures were then collected using the linear detector setup (λ=0.154 nm) at the X20A beam line.

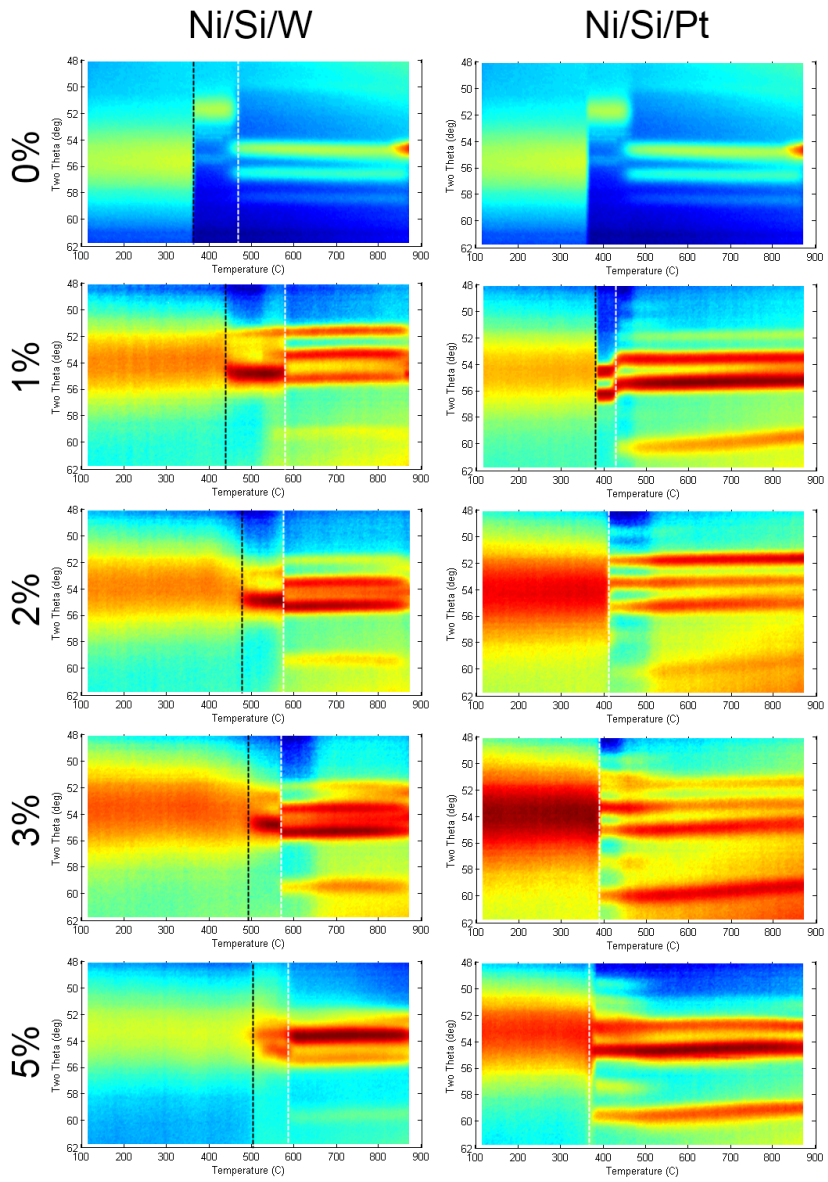

Figure 11.17: In-situ XRD of Ni/Si(40%)/W and Ni/Si(40%)/Pt on Si(100) at 3° C/s, with various W and Pt concentrations. The formation of a metal-rich nickel-silicide phase is indicated with a black striped line, the formation of NiSi by a white striped line.

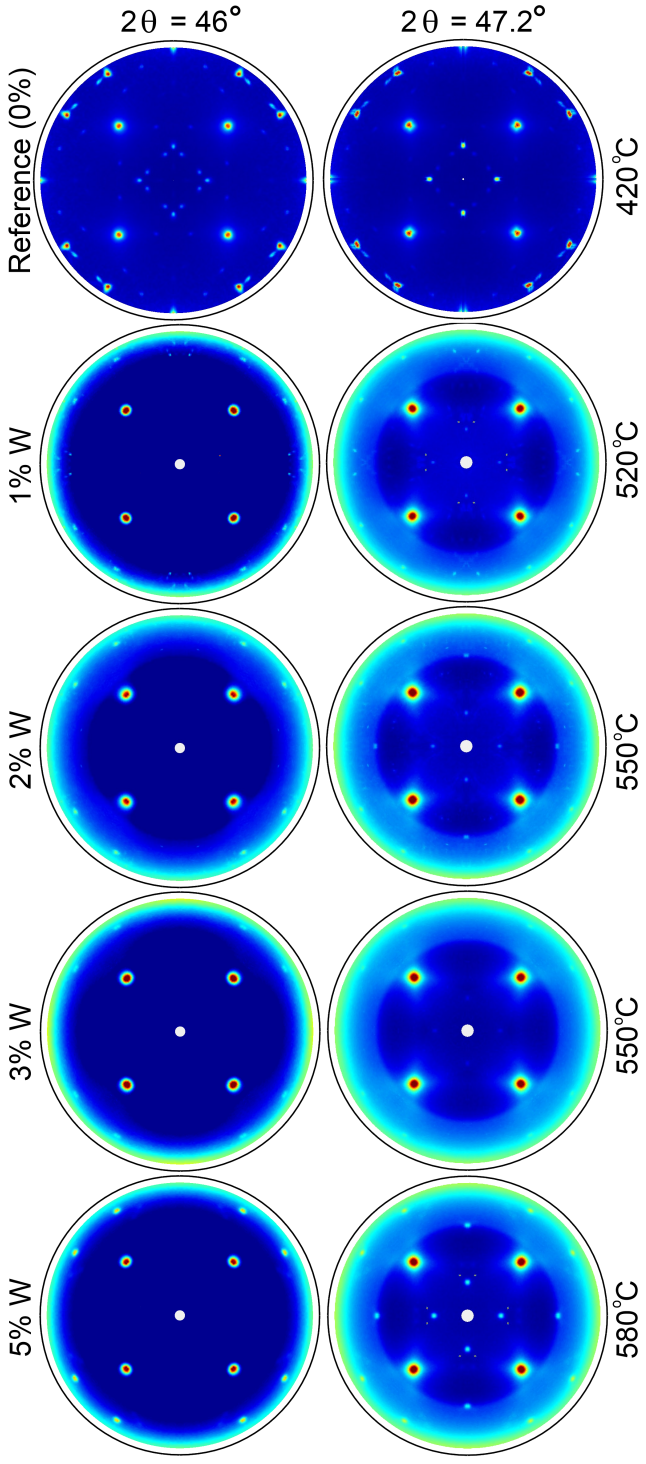

Figure 11.18: Pole figures showing the effect on the texture of the metal-rich phase of adding W to the Ni/Si(40%) system.

Figure 11.18 shows the effect of W on the formation of the metal-rich nickel-silicide phase from the Ni/Si(40%) mixture. At the top, reference pole figures are displayed for a sample which has no W added. In both pole figures, the most intense spots are 4 pairs along the outer edge of the pole figure. In addition, in the pole figure collected at 2θ=47.2°, four intense spots (at ϕ=0, 90, 180 and 270° and χ=20°) can also be observed, which are characteristic for the epitaxial θ-nickel-silicide phase on Si(100) (the other weaker spots are mainly related to a superstructure of vacancies within the θ-phase). The effect of adding W on these features is only limited, as it only causes intensity variations, but no significant changes in the position of the features nor does it introduce additional texture components. What is in fact remarkable is that the highest concentration of W (5%) leads to the most intense spots, which could indicate that a Ni/Si/W phase is actually forming, instead of just W being in solid solution in a Ni/Si phase. This would be consistent with the reported behaviour of the alloyed Ni+W/Si(100) in [101], where the phase formation discussed in section 11.5.1.1 was only observed if a sufficiently large amount of W (>5%) was alloyed in the deposited nickel films.

The texture of the NiSi obtained by annealing these Ni/W/Si(40%) samples to 700°C is shown in figure 11.19. In the case of 1% of W, a strong and complex texture of NiSi is found, which differs both from the axiotaxy of traditional NiSi on Si(100), as well as from the epitaxial NiSi formed from pure Ni/Si(40%) layers. Adding 2% of W results in an almost featureless pole figure, containing some very weak axiotaxy in the background. When 3 or 5% W was used, a completely random texture was observed, evidenced by the featureless pole figures.

At the moment, the origin of these textures, especially the random NiSi texture when 3 or 5% W was introduced, is unclear. If the epitaxial texture of NiSi, in the case it originates from Ni/Si(40%)/Si(100) or Ni+W/Si(100), is related to the epitaxy of the θ- or θ-like phase preceding it, one would also expect it to occur when Ni/W/Si(40%) is used, since a similar metal-rich phase and texture is observed. In the case of Ni/W on Si(100), it could be that the redistribution of W during the formation of the θ-like phase plays a crucial role in the subsequent texture selection during the nucleation of NiSi. To clarify the role of the location of W during the NiSi nucleation, in-situ RBS or atom probe tomography would be most useful.

The pole figures for the low-temperature (400-440°C) quenches made on Ni/Pt/Si(40%) samples are displayed in figure 11.20. In the case of 1 and 2% Pt, one can still observe the high intensity spots characteristic for the θ-like phase. However, in the case of 2% Pt, some additional features are visible as well. When 3 or 5% of Pt is added, NiSi is already observed at these temperatures, and exhibits the axiotaxy texture.

The texture of the NiSi obtained by annealing the Ni/Pt/Si(40%) samples to 700°C

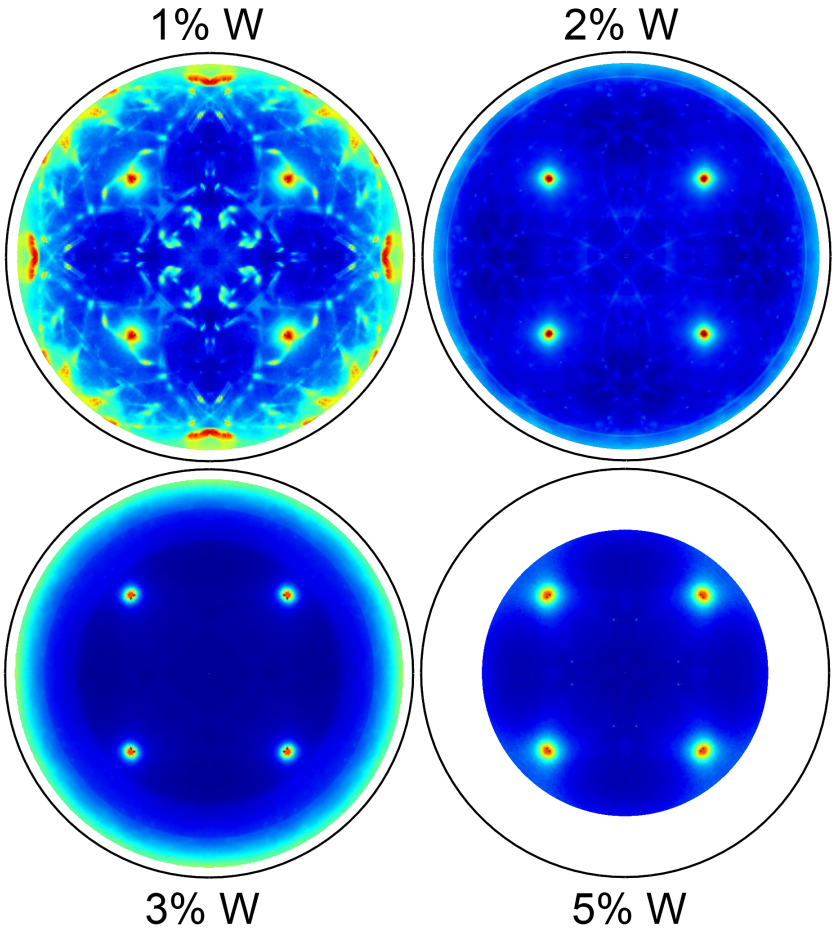

Figure 11.19: Pole figures showing the effect on the texture of the Ni(W)Si phase of adding W to the Ni/Si(40%) system. For the sample with 5%W, no complete pole figures have been recorded at the moment (only $\chi < 60^{\circ}$), but the lack of any features makes a random texture already clear.

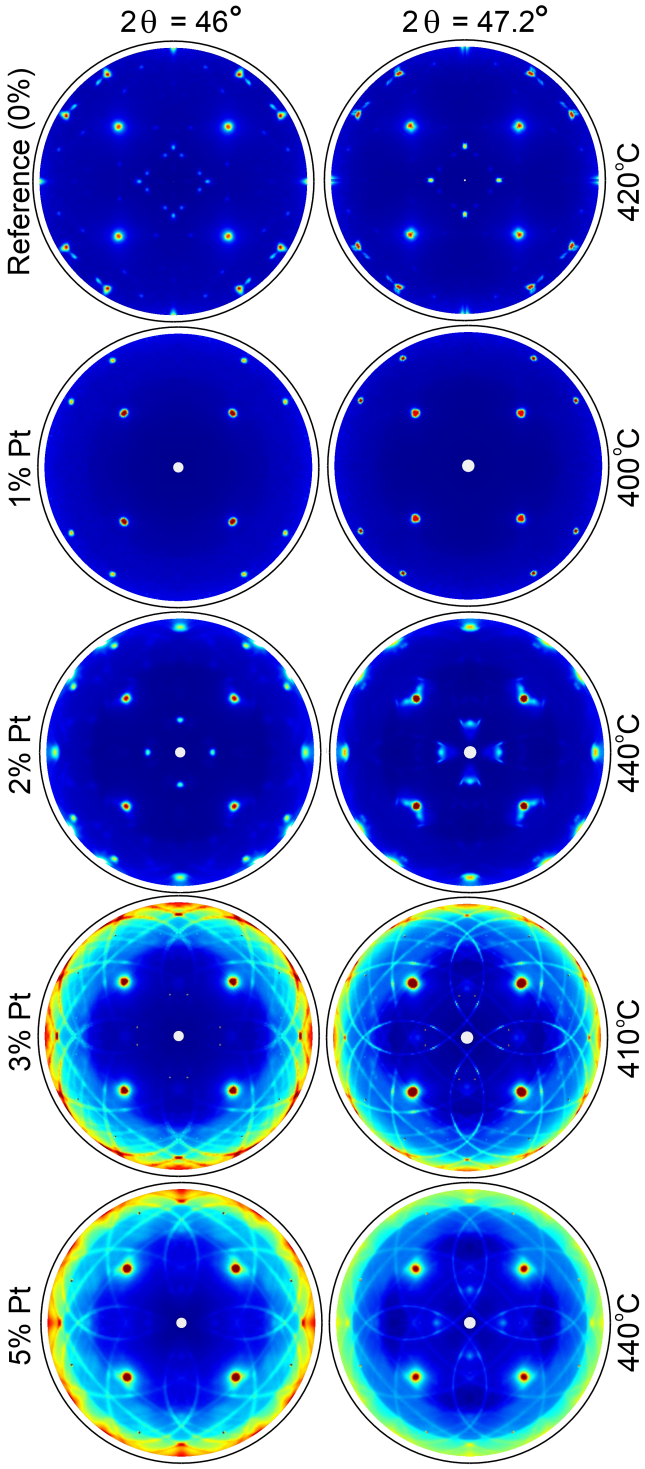

Figure 11.20: Pole figures showing the effect on the texture of the metal-rich phase of adding Pt to the Ni/Si(40%) system.

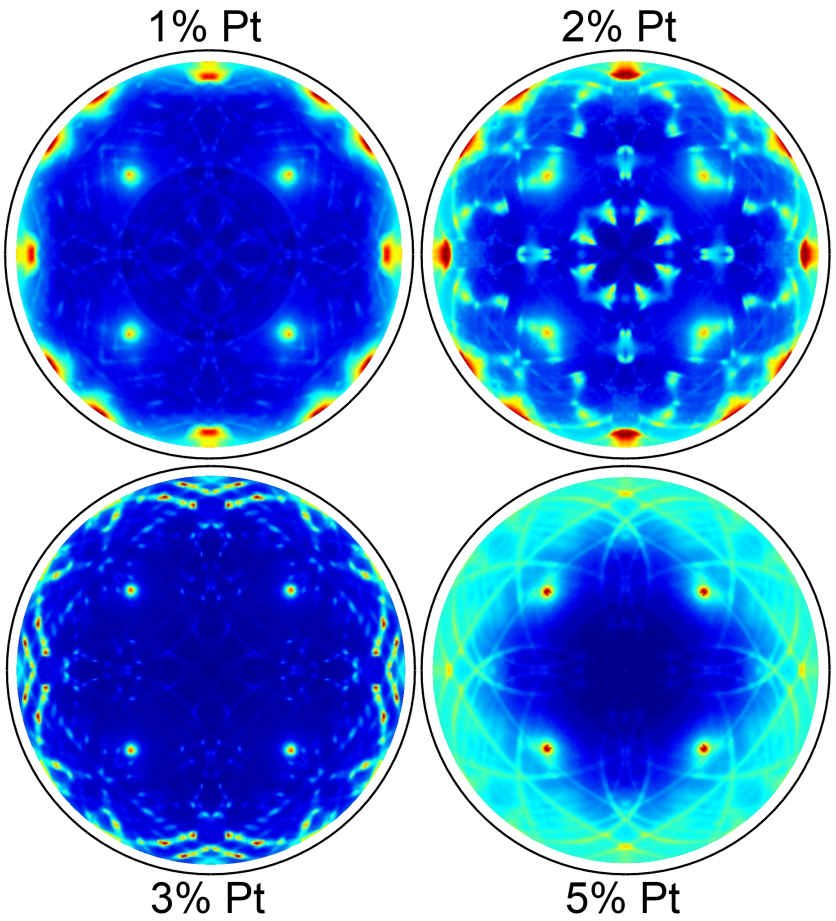

Figure 11.21: Pole figures showing the effect on the texture of the Ni(Pt)Si phase of adding Pt to the Ni/Si(40%) system.

is shown in figure 11.21. 1 and 2% Pt results in NiSi with a texture that consists of a limited number of high intensity spots, on a weak background of axiotaxy-like line patterns. As the Pt content is increased to 3%, the axiotaxy becomes stronger, but most intensity is concentrated in a limited number of high intensity spots along these axiotaxy lines. This must be caused by grain growth during the annealing, as the texture of the sample annealed at lower temperatures exhibited axiotaxy with uniform intensity along the lines. When 5% of Pt is added, NiSi exhibits a standard axiotaxy texure.

The return of NiSi to an axiotaxy texture as more Pt is added, is unexpected, as it was demonstrated [41] that the addition of Pt to pure Ni films on Si(100) results in the suppression of axiotaxy which is assumed to be caused by the incorporation of Pt in the NiSi grains, resulting in a change in d-spacing of the NiSi planes that match the Si $\{220\}$ planes. This is caused by the incorporation of a large amount of Pt into the NiSi seeds (i.e. larger than the average Pt concentration in the film), as Pt is distributed from the δ-Ni_2Si grains and grain boundaries to this seed layer. While this model can explain the observed texture and RBS results [106], recent atom-probe tomography results [107] indicate that the reality is probably even more complicated, as lateral non-uniformity in the Pt distribution of the NiSi seed layer is observed, which could not be resolved by RBS. It was found that only a limited amount of Pt is incorporated in the NiSi grains, while most of it sits in the NiSi grain boundaries and at the NiSi/Ni_2Si interface, and very little Pt is found at the NiSi/Si(100) interface. This would mean that the suppression of axiotaxy cannot be caused by a large change in the crystal lattice of the NiSi seed grains due to Pt incorporation within the NiSi grains, but might originate from a change in NiSi grain boundary energy or interface energy of the NiSi/Ni_2Si interface, which would start to dominate over the NiSi/Si(100) interface energy.

A further complication arises from a recent TEM investigation of the Pt distribution in δ-Ni_2Si and NiSi [108], where the Pt distribution in the NiSi phase is reported as having a grain-boundary-like structure, however not coinciding with the NiSi grain boundaries, but possibly with those of the preceding δ-Ni_2Si phase. In addition, the XRD peak shifts observed in Ni(Pt)Si [41] indicate that, in the end, a significant amount of Pt does end up within in the NiSi. Both of these results seem to conflict with the atom probe tomography measurements. While further research is needed to clarify this (e.g. additional Pt redistribution from the grain boundaries to the interior of the NiSi grains might happen at elevated temperatures), all of these results however have in common that the Pt concentration is non-uniform at the moment of NiSi nucleation. This contrasts with the Ni/Pt/Si(40%) samples, where the strongest effect of Pt is preventing the θ-phase from occurring. This eliminates the effect of this epitaxial phase on the NiSi texture, and results in the direct nucleation of NiSi from the as-deposited Ni/Pt/Si mixture. It is likely that

the concentration of Pt at the NiSi seeds is, at that moment, not sufficiently high to successfully prevent axiotaxy: no previous reaction step has occurred in the Ni/Pt/S(40%) samples prior to NiSi formation, so one can expect the Pt atoms to be more or less uniformly distributed over the layer.

The results described in this section, while preliminary, show a clear difference in the way Pt and W influence the formation of the θ-nickel-silicide, and allow to understand the effect of W and Pt on the formation of the metal-rich silicides from pure nickel films on Si(100): W, when added in sufficiently high concentrations, will stabilize a θ-like nickel-silicide phases, while Pt prevents its formation. It also illustrates that the effect of Pt on the texture selection is intimately connected to the non-uniform Pt distribution and that the distribution of the elements during the reaction, as well as the occurrence of the different phases needs to be well characterized if one wishes to understate a given solid-state reaction.

11.6 Conclusions

This chapter showed the effect of intervening in the phase formation of nickel-silicides in thin films, by premixing nickel and silicon before the solid-state reaction starts. It was shown that by adding 40% of silicon to the deposited nickel layer, the initial phase that grows becomes the metastable θ-nickel-silicide which grows epitaxially on Si (100) and Si (111). If this θ-nickel-silicide layer is allowed to react further with the silicon substrate, NiSi is formed, which exhibits a completely different microstructure when compared to the axiotaxy dominated texture of standard NiSi, i.e. formed from the reaction of pure Ni with Si. The increased thermal stability of NiSi formed from Ni/Si(40%) is related to this change in microstructure and it is pointed out that these results can be relevant for the understanding of the thermal stability of NiSi grown from nickel films alloyed with alloying elements such as Pt or W, as they either prevent or promote the formation of a θ-nickel-silicide-like phase.

12

The role of carbon in the stabilization of NiSi

A key drawback of NiSi is its poor thermal stability, which prevents NiSi from being used as a contact for high thermal budget applications. It is now well known that adding certain alloying elements, such as Pt [40] and W [101], may alleviate this problem in standard CMOS technology.

When compared with the CMOS process steps, the production steps of DRAM contain an additional high temperature anneal (e.g. 30 minutes at 750 ° C) which happens after the silicidation has occurred. Therefore, if one wants to use NiSi contacts in the DRAM periphery logic - to achieve a similar downscaling as in the current deep-submicron CMOS processes - the problem of the thermal stability of NiSi becomes even bigger than in the case of CMOS, as the use of Ni(Pt)Si can no longer prevent the thermal degradation of the contact.

Recently, it was shown that the addition of carbon to the substrate, either through implantation or through the use of epitaxial $Si_{1-x}C_x$ layers grown on Si(100), can further improve NiSi thermal stability. In these $Si_{1-x}C_x$ layers, a fraction of the silicon atoms is replaced by carbon atoms. Device performance and morphology of the NiSi(C) formed by depositing nickel films on these substrates were reported by Machkaoutsan et al. [109, 110]. It was found the the resulting NiSi(C) contacts exhibit a very high thermal stability, making it possible to survive the typical

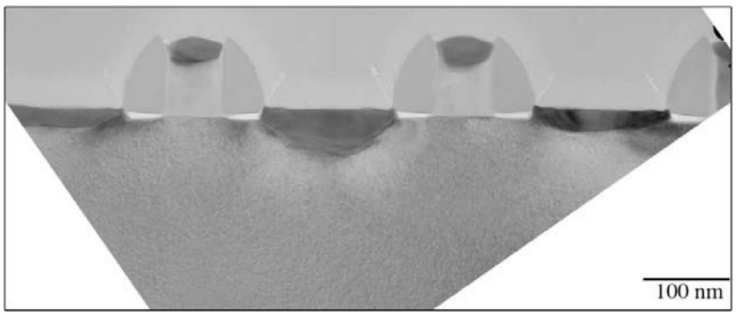

Figure 12.1: Cross-section TEM of NiSi(C) contacts after DRAM anneal (taken from [110])

DRAM anneals, as can bee seen in figure 12.1, where a cross section of the transistors shows the good NiSi(C) morphology.

In this chapter, the results are presented of the investigation of the influence of the $Si_{1-x}C_x$ epitaxial layer on the phase formation and texture of the NiSi(C) silicides as a function of the carbon content. In other silicides, e.g. $CoSi_2$, the presence of carbon has been shown to have a significant influence on phase formation and microstructure [111]. For NiSi, little information is available on the effect of carbon. The role of the initial location of the carbon on the phase formation and stabilization of the NiSi(C) contact is investigated, by comparing different methods of adding carbon: through the use of a $Si_{1-x}C_x$ layer, by alloying carbon in the nickel film or by adding an interlayer of pure carbon between the nickel film and the Si(100) substrate. It is investigated how this has an impact on the texture and thermal stability of the NiSi(C) phase.

The results discussed in this chapter have been published in:

De Keyser K., De Schutter B., Detavernier C., Machkaoutsan V., Bauer M., Thomas S.G., Jordan Sweet J., Lavoie C., *Phase formation and texture of nickel silicides on $Si_{1x}C_x$ epilayers*, Microelectronic Engineering 88 (2011), 536-540

12.1 Experimental details

The samples were fabricated by depositing 10 nm thick Ni layers using a Physical Vapor Deposition (PVD) tool on different substrates. For the $Si_{1-x}C_x$ samples, the substrates consist of a 40 nm thick $Si_{1-x}C_x$ epitaxial layer with either 1, 1.7, 2.2 and 2.5 atomic % C that were grown on Si(100) in an Epsilon reduced pressure

Chemical Vapor Deposition (CVD) single wafer epitaxial deposition tool manufactured by ASM. The samples containing an interlayer of carbon where produced by first depositing 0.6 nm or 1 nm of carbon on RCA cleaned and HF dipped Si(100) substrates, followed by a 10 nm Ni deposition. The third group of samples, consisting of nickel films alloyed with carbon, was made using co-deposition of nickel and carbon, resulting in the same total amount of nickel and carbon as in the interlayer case, but now distributed evenly over the whole nickel layer thickness.

Phase formation of the silicides was studied with in-situ X-ray diffraction (XRD) measurements that were carried out at the X20C beam line of the National Synchrotron Light Source. During these measurements the samples were annealed in a high purity He atmosphere at a rate of 3°C/s. The incoming X-ray beam had an incident angle of 22.5° to the sample surface. A linear detector was used, collecting a 2θ range between 48° and 62°, and using an X-ray wavelength of 0.18nm. For the texture evaluation, a series of quenches were made. Subsequently X-ray diffraction pole figures were measured, using a linear detector, collecting 640 pole figures in a range of 2θ=29.2° to 62.6° (with λ=0.154 nm), with a step size of 1° in χ (tilting of the sample) and ϕ (rotation of the sample). Sheet resistance was measured using a four-point probe. Top view scanning electron microscopy (SEM) images and EBSD maps were collected in an FEI Quanta 200F FEGSEM to study the morphology and microstructure of the films.

12.2 Reaction of Ni with $Si_{1-x}C_x$

Figure 12.2 shows an overview of the in-situ XRD results, showing the diffracted X-ray intensity on a color scale, with blue corresponding to low, and red to high values, as a function of both temperature (X-axis) and the 2θ value (Y-axis). As a reference, the reaction between Ni and Si (100) is shown in figure 12.2a. At room temperature, peaks characteristic for the as-deposited nickel film can be observed. This nickel film starts to react with the silicon at about 250-300°C to form a series of textured metal-rich nickel-silicides [69]. At a temperature of about 400°C the NiSi monosilicide phase is formed, of which only weak peaks are observed due to its axiotaxy texture. In contrast, Figure 12.2b shows the effect of the use of a $Si_{1-x}C_x$ epitaxial layer with 1% C. The formation of the nickel-rich phases is delayed to 330°C and the peak 2θ=56.3°, characteristic for a nickel-rich phase, is visible over a longer temperature range. The formation of the NiSi(C) monosilicide phase occurs at 500°C, about 100°C higher than in the reference Ni/Si(100) case. For the 2.5% C sample (figure 12.2c) the temperature range in which the metal-rich phases exist is similar to the 1% C case, however, the intensities of

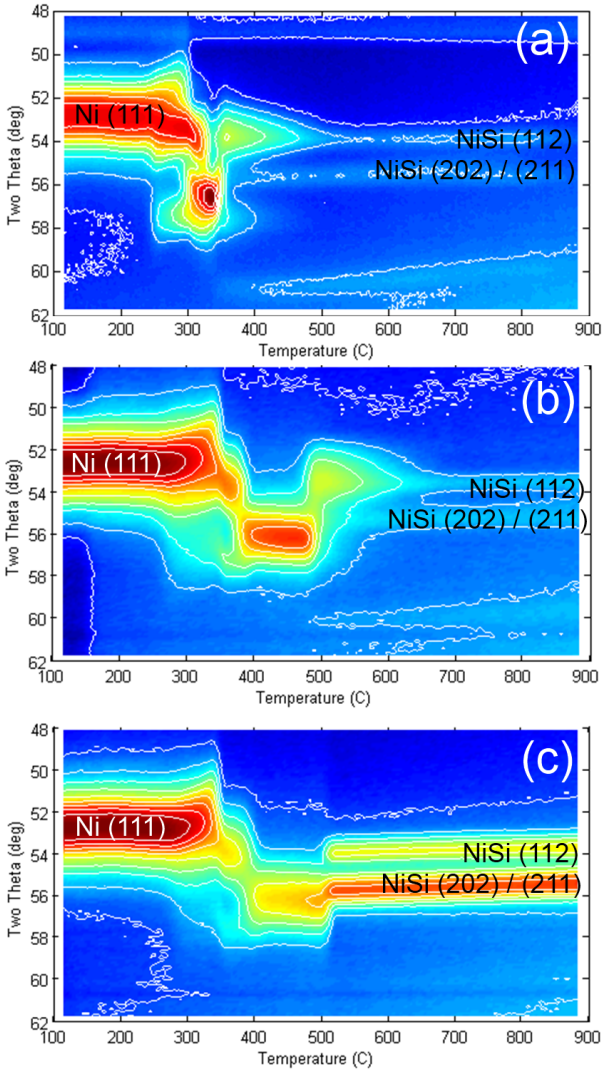

Figure 12.2: In-situ XRD of 10nm Ni on (a) Si(100), (b) $Si_{1-x}C_x$ (1%) and (c) $Si_{1-x}C_x$ (2.5%).

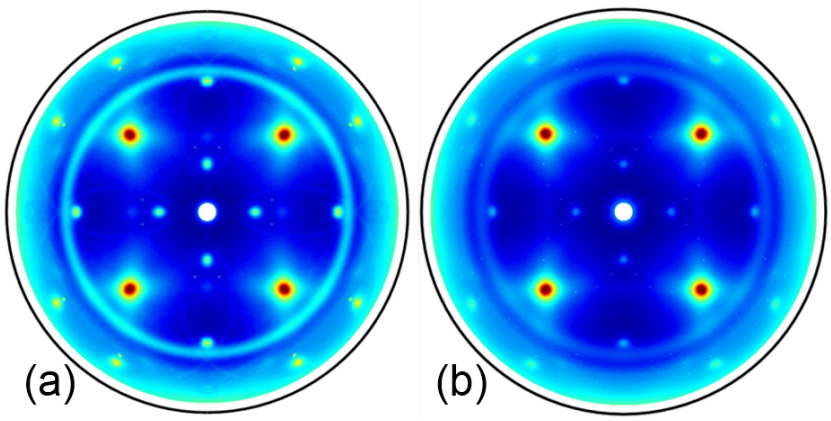

Figure 12.3: Pole figures for 2θ=47.3°±0.5°, recorded on (a) 10nm Ni on $Si_{1-x}C_x$ (1%), annealed to 470°C, and (b) 10nm Ni on $Si_{1-x}C_x$ (2.5%), annealed to 475°C, both plotted on the same logarithmic scale. The ring and spots on figure (a) are much more intense compared to (b).

the peaks originating from the metal-rich phase and monosilicide phase are very different in the case of 2.5% C, compared to those in the 0% and 1% C cases: a signficantly lower intensity is detected from the metal-rich phase and much higher intensity from the NiSi(C) phase.

To investigate the effect of the $Si_{1-x}C_x$ layer and its carbon concentration on the metal-rich phases, quenches were made at 470°C on the 1% C sample and at 475°C on the 2.5% C sample. Pole figures for 2θ=47.3°±0.5° measured on these samples are shown in figure 12.3. An identical color scale is used in both figures to be able to compare the relative occurrence of the phases. The result for the 1% $Si_{1-x}C_x$ layer (figure 12.3a) is identical to the case of pure Ni/Si(100) as reported in [69]. The high intensity spots (red) correspond to Si(100) poles from the substrate, and the other features originate from textured, metal-rich nickel-silicides. A circle of high intensity can be observed, which was recently attributed to the θ-nickel-silicide phase, growing with a fiber texture. In addition, a series of spots is visible as well, indicating an epitaxial phase. Currently, these spots have not been uniquely attributed to a specific nickel-silicide, but they have been reported in the pure Ni/Si reaction [69] as the transient X-phase, and are similar to what is observed in the case of ultra-thin nickel-silicide films on Si(100), which will be discussed in chapter 13. The pole figure recorded on the sample with the 2.5% $Si_{1-x}C_x$ layer is shown in figure 12.3b. The intensity of the features is significantly lower than in the 1% case. In particular, the fiber texture is much less pronounced, and the intensity of the epitaxial spots is lower as well. This indicates that the formation of the metal-rich phases is suppressed or results in these phases

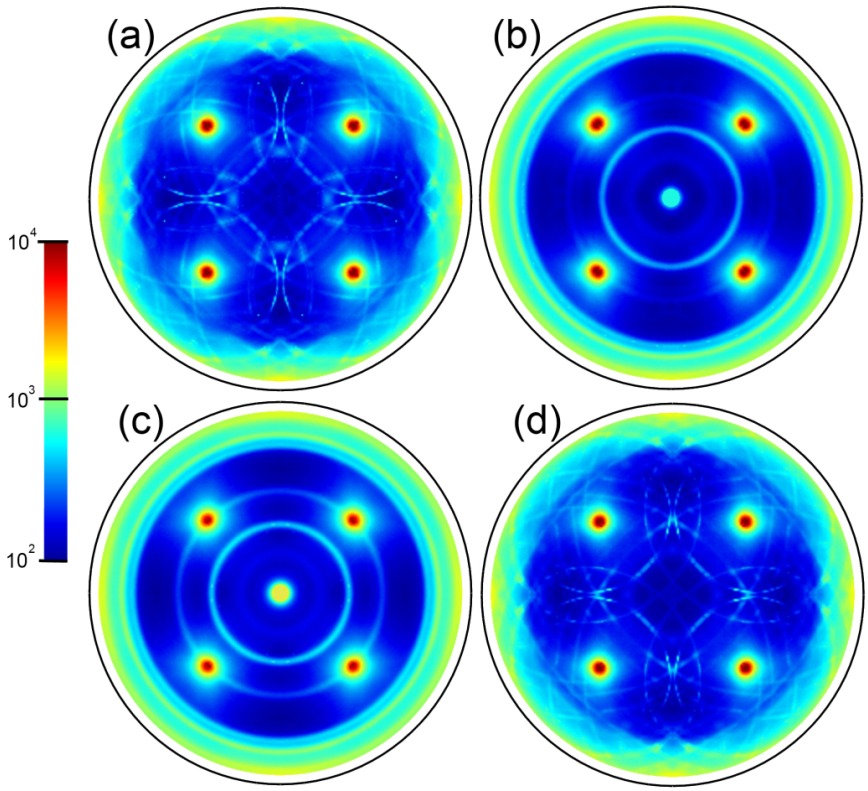

Figure 12.4: Pole figures for 2θ=45.8°±0.25°, showing the NiSiC {112} planes on an identical logarithmic scale. (a) NiSiC formed on $Si_{1-x}C_x$ (1%), (b) on $Si_{1-x}C_x$ (1.7%), (c) on $Si_{1-x}C_x$ (2.2%) and (d) on $Si_{1-x}C_x$ (2.2%) but with a pre-anneal, reducing the actual substitutional C concentration to 0.9%.

having a more random texture.

In order to simulate the thermal budget of a DRAM periphery logic flow, the samples with 1% C, 1.7% C and 2.2% C were silicided and subsequently given a post-silicidation anneal of 30 minutes at 750°C. The XRD pole figures for 2θ=45.8°± 0.25° (figure 12.4) show the diffracted intensity of the NiSi(C) {112} planes. For the sample with 1% C, the typical axiotaxy texture of NiSi on Si (100) is observed. The samples containing more carbon in the $Si_{1-x}C_x$ layer exhibit a completely different texture, i.e. a combination of NiSi(C) {202}, {211} and {112} fiber textures, evidenced by the concentric circles in the pole figure.

EBSD maps (figure 12.5) revealed large grains, much larger than what is typically observed in NiSi films on Si (100). This might indicate that the use of the $Si_{1-x}C_x$ layers lowers the nucleation rate of the NiSi(C) grains.

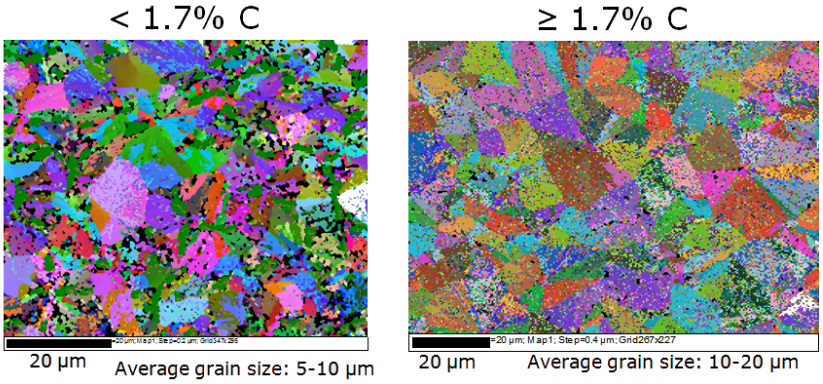

Figure 12.5: EBSD maps with Euler coloring showing the large grains of NiSi(C) on $Si_{1-x}C_x$ epilayers.

Until now, no distinction was made between the total amount of carbon and the fraction that is present in the $Si_{1-x}C_x$ layer as substitutional carbon. Indeed, it was shown before [109] that in the as-grown $Si_{1-x}C_x$ epilayers the total and substitutional C concentrations can be considered equal for the studied $Si_{1-x}C_x$ compositions. However, this leaves the question whether it is simply the occurrence of carbon in the layer that causes the change in texture, or if this is due to the change in lattice parameters of the $Si_{1-x}C_x$ layer. In order to decouple the effects of the total and substitutional carbon on the NiSi(C) monosilicide texture, a 2.2% C $Si_{1-x}C_x$ wafer was subjected to a spike anneal (He, 1050°C, 1.5 s) prior to Ni deposition. This anneal reduced the substitutional C concentration in the $Si_{1-x}C_x$ from 2.2 to 0.9 %, by precipitating part of the substitutional C into interstitial sites, thus partially relieving tensile strain induced in the $Si_{1-x}C_x$ epilayer. After Ni deposition, an identical silicidation and post-silicidation anneal as for the previously discussed samples was carried out, and a pole figure recorded on the resulting sample is shown in figure 12.4d. It no longer shows a fiber texture, as was the case for the sample without initial anneal of the wafer, but once again reveals the axiotaxy texture, which resembles the one shown in figure 12.4a for the 1% C sample.

12.3 Reaction of alloyed Ni/C and interlayer Ni/C on Si(100)

For a better understanding of the role of the location of the carbon on the phase formation and texture of the silicides, the comparison was made with samples having an interlayer of carbon between the nickel and the Si(100) substrate, and with

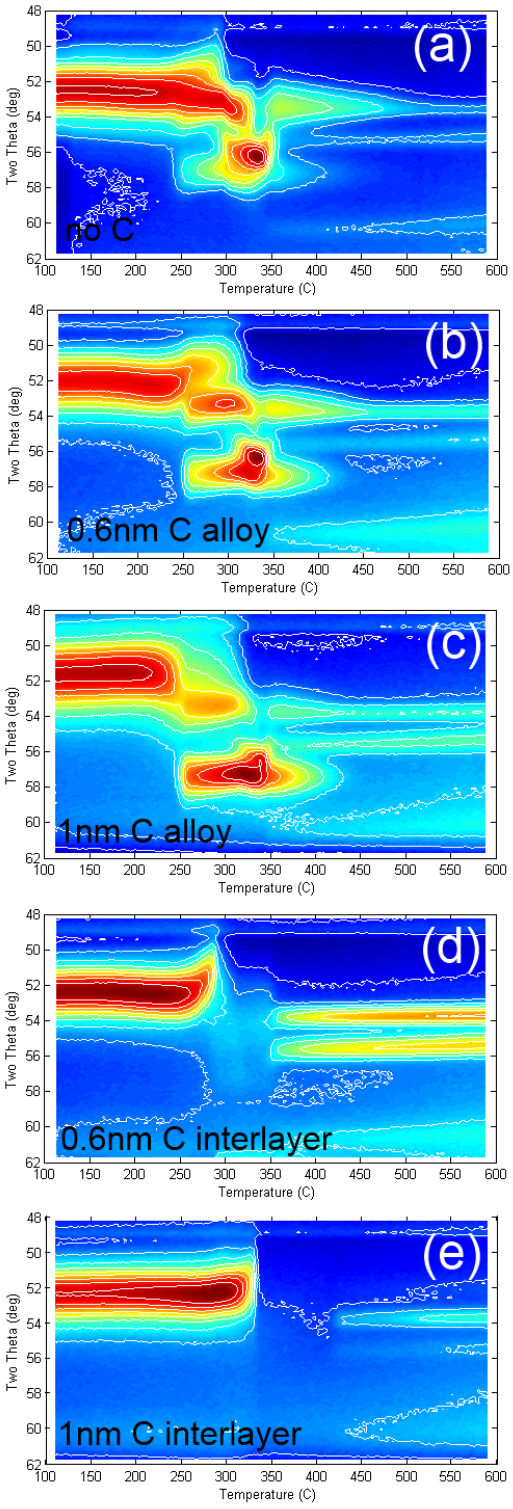

Figure 12.6: In-situ XRD of (a) 10 nm Ni on Si(100), (b) 10 nm Ni alloyed with 0.6 nm C on Si(100), (c) 10nm Ni alloyed with 1 nm C on Si(100), (d) 10 nm Ni on 0.6 nm C on Si(100), (e) 10 nm Ni on 1 nm C on Si(100)

	550 ° C 30 s	750 ° C 5 min	750 ° C 30 min
10 nm Ni	23.8	2463.7	
10 nm Ni + 0.6 nm C alloy	23.0	2547.1	
10 nm Ni + 0.6 nm C interlayer	18.0	62.3	
10 nm Ni + 1 nm C alloy	23.8	2723.7	
10 nm Ni + 1 nm C interlayer	36.8	40.4	41.4
10 nm Ni on $Si_{1-x}C_x$ (1%)	23.1		24.6
10 nm Ni on $Si_{1-x}C_x$ (2.2%)	22.4		22.8

Table 12.1: Sheet resistance ($\mu\Omega$.cm) of the NiSi layer after annealing at different temperatures / times

samples where the nickel layer is alloyed with carbon during deposition. As it is difficult to assess what the local carbon concentrations are during the reactions in the $Si_{1-x}C_x$ samples, it is impossible to obtain the exact same carbon concentration in the interlayer / alloy samples. For a first test, samples with a total carbon thickness of 0.6 nm and 1 nm were made, which should result in a C to Ni atomic ratio of about 5% and 10% (for the $Si_{1-x}C_x$, the atomic fraction of C to Si is between 0 and 2.5%, but this layer is 4 times thicker than the nickel layer).

The phase formation was studied using in-situ X-ray diffraction, up to a temperature of 600°C, and the results are shown in figure 12.6. It is clear that the use of C as an alloy in the Ni film has a very limited effect on the phase formation: only a slight change in the shape of the XRD peaks from the metal-rich phases (300°C to 350°C) is observed, while no effect on the NiSi(C) formation temperature is found. On the other hand, the use of the C interlayer has a more pronounced effect: in the temperature range where the metal-rich phases were previously observed, no XRD peaks are detected, indicating that only epitaxial or amorphous phases are formed. The use of the 1 nm interlayer also results in a shift of the formation of NiSi(C) to a higher temperature (420°C).

Pole figures were recorded on the resulting NiSi(C) films, and are shown in figure 12.7. It is clear that the addition of carbon as alloy or interlayer has only a limited effect on the texture: it can still be described as axiotaxy, but with increasing C content, the axiotaxy lines become less pronounced. In the case of the 1 nm interlayer, the texture of NiSi has changed the most, with isolated spots of higher intensity showing up.

The effect of the addition of carbon as alloy or interlayer on the thermal stability of the NiSi(C) film was also investigated. After the silicidation anneal (550°C, 30 s), the sheet resistance of the layer was measured ex-situ, to assess the resistance of the non-agglomerated NiSi(C) layer. Subsequently, the samples were heated to

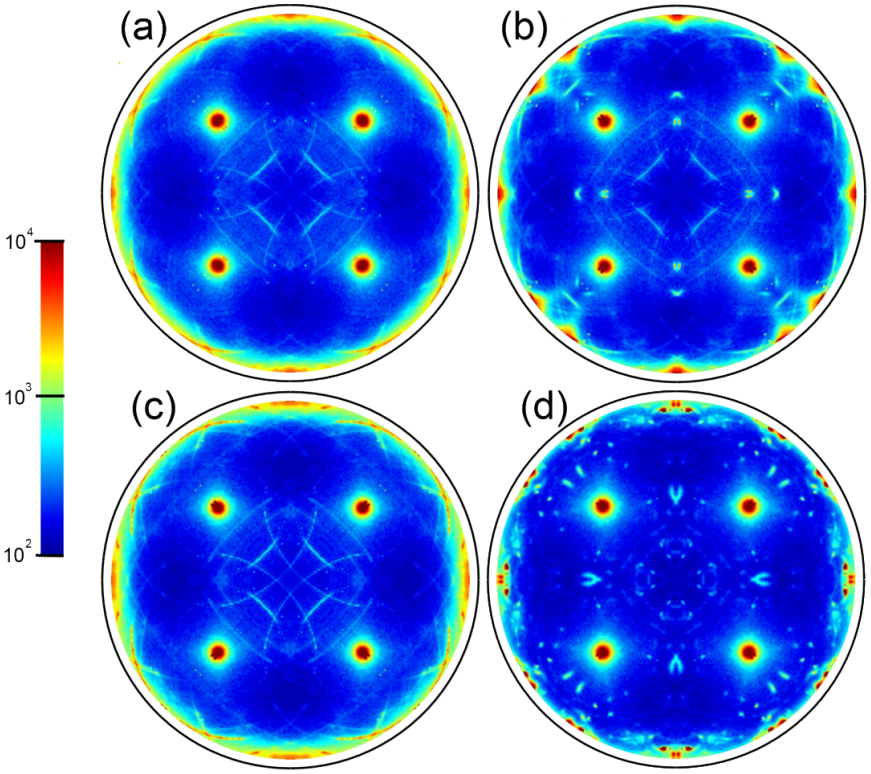

Figure 12.7: Pole figures for 2θ=45.8° ± 0.25°, showing the NiSiC {112} planes on an identical logarithmic scale. (a) NiSiC formed from 10 nm Ni alloyed with 0.6 nm C, (b) NiSiC formed from 10 nm Ni alloyed with 1 nm C, (c) NiSiC formed from 10 nm Ni on a 0.6 nm C interlayer, (d) NiSiC formed from 10 nm Ni on a 1 nm C interlayer.

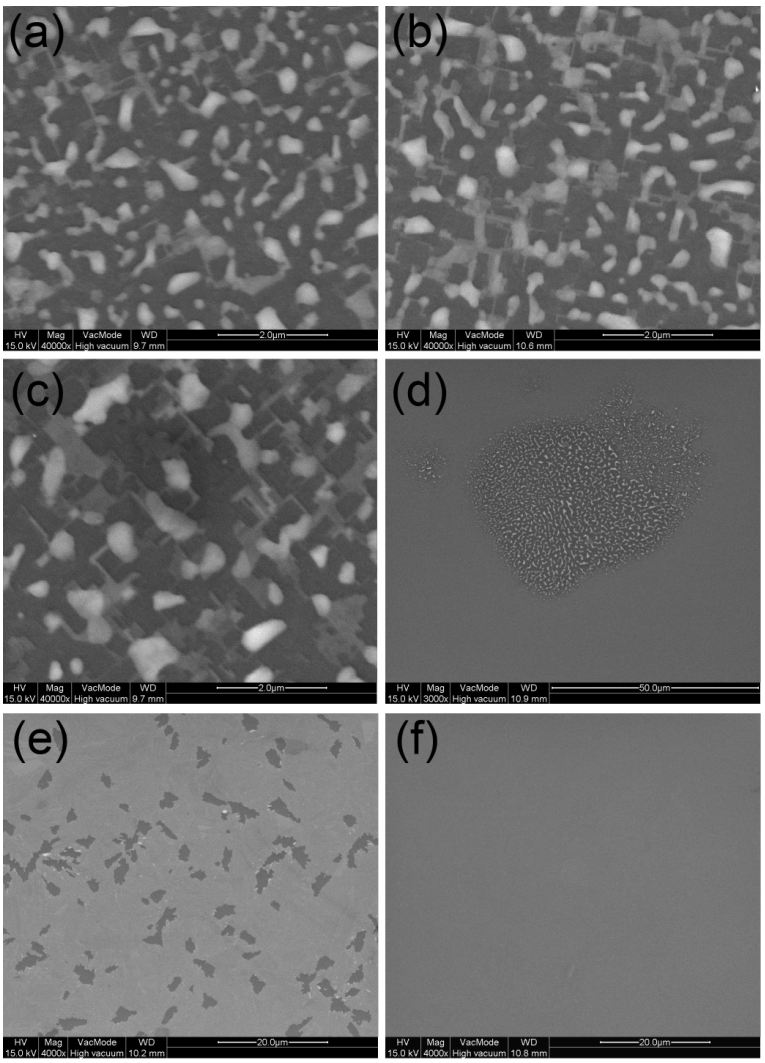

Figure 12.8: top view SEM images showing the morphology of the layers after a post-silicidation anneal. (a): 0.6 nm C alloyed in 10 nm Ni. (b): 1 nm C alloyed in 10 nm Ni. (c): 0.6 nm C as interlayer. (d): 1nm C as interlayer. (e): 10 nm Ni on $Si_{1-x}C_x$ (1%). (f): 10 nm Ni on $Si_{1-x}C_x$ (2.5%)

750°C for 5 minutes, after which the sheet resistance was measured and a top view SEM image was collected. Table 12.1 shows the sheet resistance measurements for the different samples. For both Ni/C alloyed samples, a 100x increase of the sheet resistance is observed, due to the complete agglomeration of the layer, which is clearly visible in the SEM images (figure 12.8a and figure 12.8b). The samples with the C interlayer were found to be more stable: while the resistance of the 0.6 nm C interlayer sample was already tripled after the 5 minute anneal due to moderate agglomeration (figure 12.8c), the 1 nm C interlayer sample did not show a significant increase in resistance. However, the SEM top view image (figure 12.8d) reveals that local agglomeration has occurred. Even though this has no significant effect on the sheet resistance of the total layer, it does prevent it from being used in devices due to the limited reliability. As a reference, top view SEM images of the $Si_{1-x}C_x$ samples with 1% and 2.2% carbon are shown as well, after an anneal of 30 min at 750°C (figure 12.8e and figure 12.8f), showing agglomeration in the 1% case, but no agglomeration in the 2.2% case, which is consistent with previously reported results [109].

12.4 Discussion

The results on the phase formation of the $Si_{1-x}C_x$ samples clearly show an influence of C on the phase formation of the Ni/Si reaction. Carbon was found to shift the transition to both the metal-rich and the NiSi(C) phase to higher temperatures, and adding more than 1% of C suppresses the axiotaxy texture of NiSi(C). This observation is consistent with the current model of the origin of axiotaxy, as being caused by a similarity in d-spacing between crystal planes of the substrate, (Si$\{220\}$), and those of the silicide film, (NiSi $\{202\}$, $\{211\}$, $\{103\}$ and $\{112\}$). The substitution of Si atoms with C in the substrate changes the d-spacing of the Si $\{220\}$ planes, and once this is sufficiently different from those of the matching NiSi d-spacing, axiotaxy can no longer occur and the texture changes to a fiber texture. This is clearly demonstrated by the fact that it is the amount of substitutional C that determines whether or not the axiotaxy constraint of d-spacing matching is fulfilled, as the cases where a 2.2% $Si_{1-x}C_x$ substrate is given a pre-anneal (reducing the substitutional C content below 1% C), and by the cases where C is alloyed or introduced as an interlayer, as they do not show the same suppression of the axiotaxy texture.

The study of the thermal stability of the samples demonstrates that the increase in stability cannot simply be explained by the occurrence of C in the NiSi(C) films: it is clear that the location of C during the reaction is important. This dependence of the thermal stability on the way carbon is added might be related to a different C

distribution after NiSi(C) formation. In addition, part of the increased stability will follow from the change in microstructure in the $Si_{1-x}C_x$ samples: a combination of large grains and a suppression of axiotaxy has been shown to significantly delay agglomeration (e.g. in the case of Pt addition [41]), but even when no additional elements are present this has been observed, as discussed in the formation of NiSi through the θ-nickel-silicide phase in chapter 11.

12.5 Conclusions

In summary, it was found that both the formation temperature, as well as the texture of the nickel-silicides formed during reaction of Ni with $Si_{1-x}C_x$, is influenced by the amount of carbon in the $Si_{1-x}C_x$ layer. In the monosilicide phase, the texture of NiSi(C) is determined by the amount of substitutional carbon present in the $Si_{1-x}C_x$ layer prior to Ni deposition. The thermal stability of NiSi(C) layers is shown to depend on the location of the C in the initial Ni/C/Si system. This is due to a difference in the resulting C distribution and in the microstructure of the resulting NiSi(C) film.

13

Ultra-thin nickel-silicides

The problem of NiSi agglomeration has been discussed in chapter 10. It was shown that the morphological stability of NiSi gets worse as the layer gets thinner, evidenced by figure 10.1, where the in-situ sheet resistance of thin NiSi films on SOI was shown for NiSi films formed from nickel layers with a thickness of 10, 8 and 6 nm. If one extrapolates the current downscaling trends, the NiSi contacts will have to become even thinner and one can expect the problem of agglomeration to become even bigger, making the use of nickel-silicides impossible. In this chapter, the problem of phase formation and thermal stability of these ultra-thin (< 6 nm) nickel-silicides is investigated.

The results discussed in this chapter have been published in:

De Keyser K., Van Bockstael C., Van Meirhaeghe R.L. Detavernier C., Verleysen E., Bender H., Vandervorst W., Jordan-Sweet J., Lavoie C., *Phase formation and thermal stability of ultra-thin nickel-silicides on Si(100)*, Applied Physics Letters 96 (17), 173503 (2010)

13.1 Experimental

Nickel films with a thickness of 2, 3.7, 4, 6, 8 and 10 nm were sputter deposited onto lightly p-doped ($\rho = 14 - 22\Omega$cm), RCA cleaned and HF dipped silicon-on-

insulator (SOI) substrates, with a top layer of 117 nm of Si (100). The deposition chamber was first evacuated to 10^{-4} Pa. During deposition, the samples were mounted on a rotating carousel to ensure a uniform deposition thickness. An argon pressure of 0.5 Pa and a sputtering power of 100 W were used, resulting in a deposition rate of 0.04 nm/s. After deposition, the samples were annealed in a high-purity He atmosphere, from 100°C to 850°C at a rate of 3°C/s. The sheet resistance (using a four point probe) was recorded in-situ during annealing.

Selected samples were further analyzed. 640 pole figures in a 2θ range of 29.2° to 62.6° were recorded, using a step size in ϕ (the rotation of the sample about its normal) and χ (the tilting of the sample) of 0.6°. Electron backscatter diffraction (EBSD) measurements were carried out using an HKL/Oxford Instruments Channel 5 system, mounted on an FEI Quanta 200F field emission gun scanning electron microscope, at 7.5 kV. High resolution transmission electron microscopy (HRTEM), nano-beam diffraction (NBD) and energy dispersive X-ray spectroscopy (EDS) measurements were carried out on a Tecnai F30 microscope.

13.2 Abnormal agglomeration behavior

Figure 13.1 shows the in-situ sheet resistance of nickel films with a thicknesses in the range 2-10 nm, on SOI substrtates. For the thickness range 6 - 10 nm, the observed behavior is identical to what has been described in chapter 10: a huge increase in the sheet resistance in the temperature range of 600-700°C occurs due to NiSi agglomeration. However, at a nickel film thickness of 3.7 nm or below, one can observe that this typical increase in sheet resistance associated with the NiSi agglomeration no longer occurs, indicating that the film remains relatively homogeneous.

This observation was corroborated with scanning electron microscopy (SEM) top-view images. The sample consisting of the 6 nm nickel film exhibits severe agglomeration when annealed to 650°C (figure 13.2a), while the SEM images recorded on the sample made by annealing a 3.7 nm nickel film to 650°C (figure 13.2b) and 850°C (figure 13.2c) reveal no signs of agglomeration.

13.3 Phase formation and texture

In chapter 10, the agglomeration of NiSi on Si (100) was related to the microstructure, indicating a connection between the axiotaxy texture of NiSi and fast agglomeration. The experiments carried out on the Ni(60%)/Si(40%) layers showed that the suppression of axiotaxy eliminates the agglomeration problem. There

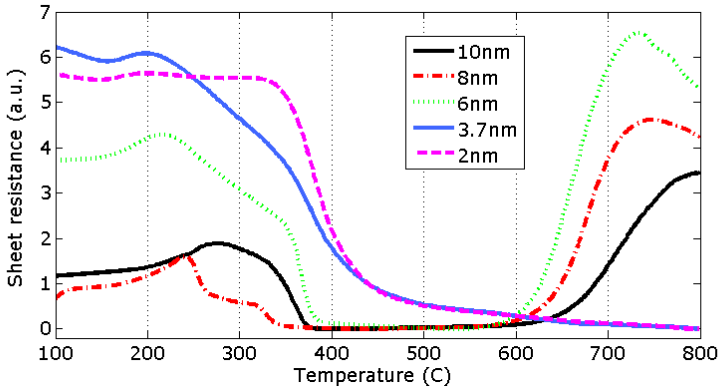

Figure 13.1: In-situ sheet resistance as a function of temperature and thickness for thin nickel films on SOI

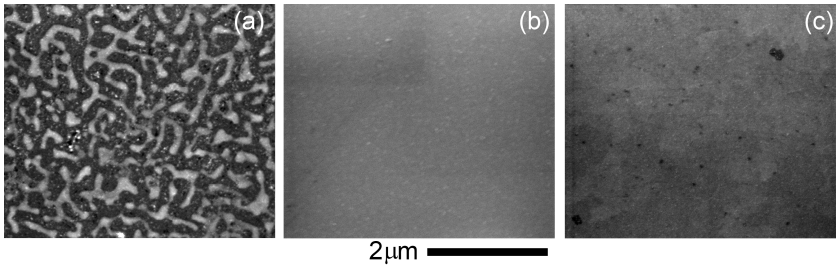

Figure 13.2: Top view SEM images of (a) a 6 nm film annealed to 650° C, showing severe agglomeration (b) a uniform 3.7 nm film annealed to 650° C and (c) a 3.7 nm film annealed to 850° C.

are therefore two likely origins of the increased stability of the ultra-thin nickel-slicides layers under investigation in this chapter: either a different (non-axiotaxy) microstructure occurs when the thickness of the nickel film drops below a certain threshold and/or a different phase (i.e. not NiSi) is formed, which exhibits an intrinsically higher thermal stability. These hypotheses were investigated by comparing the phase formation and texture of the 3.7 nm and 6 nm samples.

Due to the limited thickness of the nickel and silicide layers, in-situ XRD was not possible as the diffracted intensity was too low. Instead, quenches were made at various temperatures, which were then analyzed ex-situ.

Pole figures (λ=0.154 nm) were first recorded on the sample made by heating a 6 nm nickel film on SOI to 600°C at 3°C/s. They reveal the typical axiotaxy lines, at the 2θ values corresponding to NiSi. A selection of these pole figures is shown in the first row of figure 13.3.

Quenches at 350, 450, 600 and 850°C were made for the 3.7 nm film, and pole figures were recorded: axiotaxy lines are no longer visible, but instead a series of isolated spots appear, suggesting an epitaxial relationship between the film and the substrate (figure 13.3, rows 2-5). Only in the range of 2θ between 45° and 48°, diffracted X-rays are detected. These pole figures are shown in more detail in figure 13.4. At 350°C, a number of relatively intense spots is visible, which become weaker as the annealing temperature increases.

Due to the limited thickness of the film, the diffracted X-ray intensity is very low and the determination of the 2θ values has a large uncertainty. This makes it difficult to determine an exact 2θ value and hence determine the phase present. However, the fact that only a few spots are visible, at only a few 2θ values suggests that it is a high symmetry phase, probably hexagonal or cubic. In addition, the strongest poles coincide with the Si $\{115\}$ poles of the substrate, indicating a preferential alignment in the layer to these planes.

It is impossible to identify the phase based on these pole figures. In fact, none of the currently reported nickel-silicide phases can completely explain the observed spots without also giving rise to additional spots or diffraction peaks at other 2θ values, which are not observed.

The samples were also investigated using EBSD, which allows to discriminate between crystal phases with different symmetry (Laue group) or lattice parameters. No EBSD patterns could be recorded on the 6 nm sample, due to the small grain size of NiSi in these films, as pointed out in chapter 7.

EBSD patterns were also collected on various quenches of the 3.7 nm thick nickel films which are shown in figure 13.5. The as-deposited 3.7 nm Ni films showed no EBSD pattern (figure 13.5a), which confirms that the silicon substrate is covered,

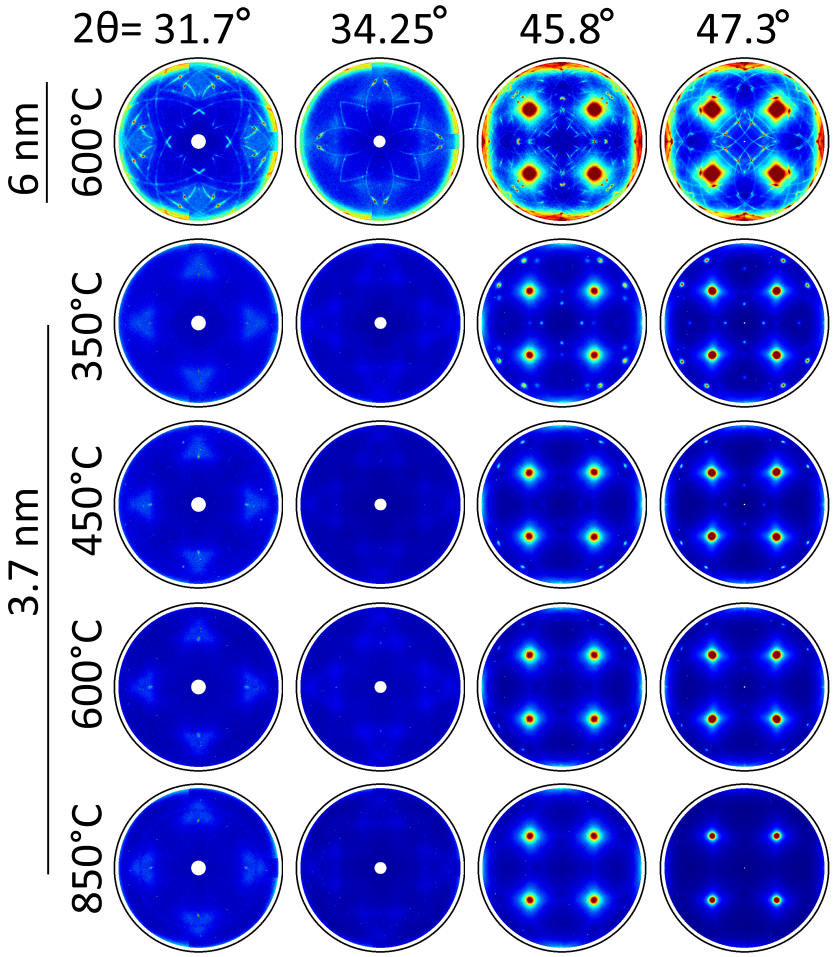

Figure 13.3: Overview of pole figures recorded on 3.7 nm and 6 nm nickel films on SOI, annealed to different temperatures.

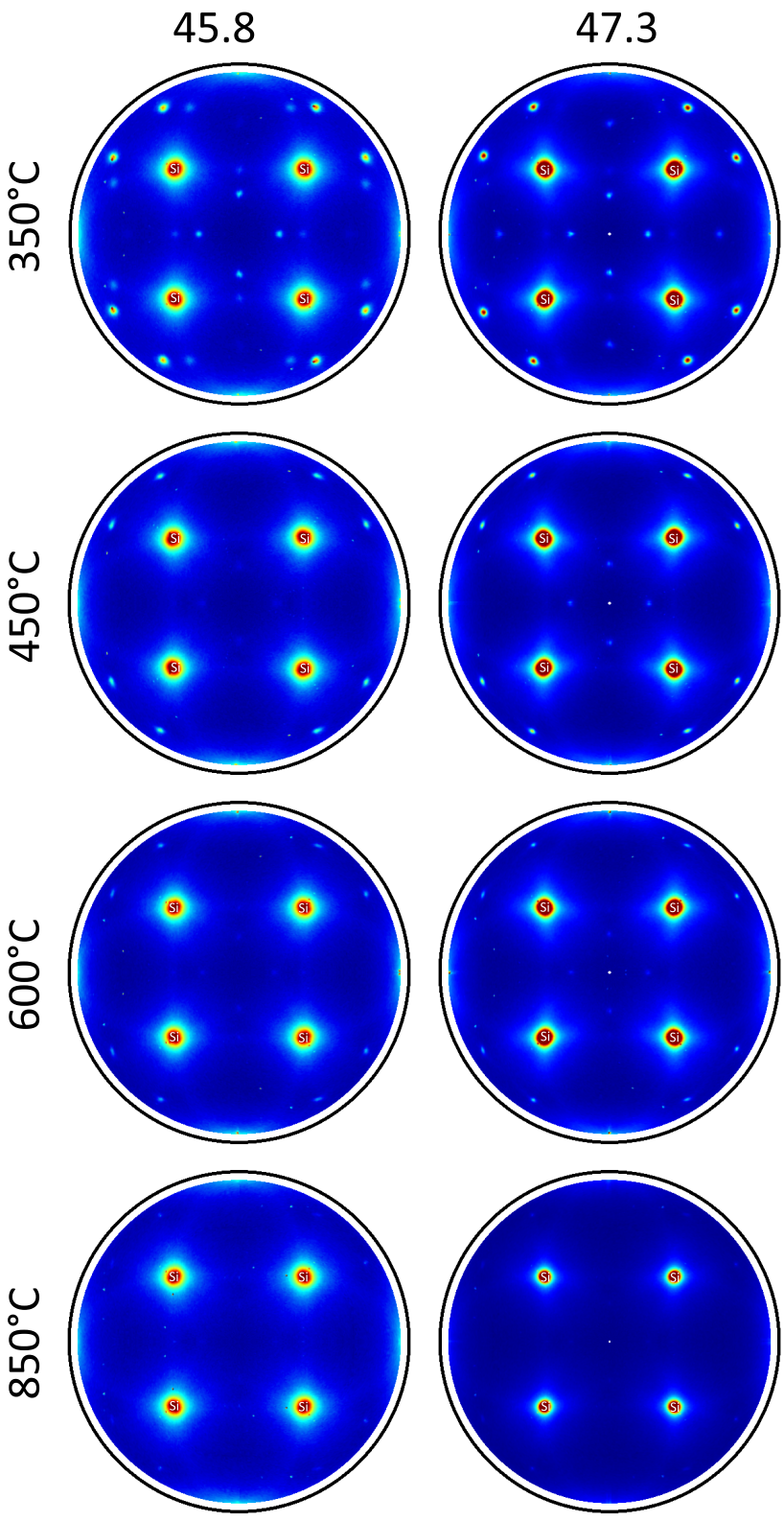

Figure 13.4: Pole figures recorded on 3.7 nm nickel films on SOI, annealed to different temperatures for the 2θ range where intensity is observed

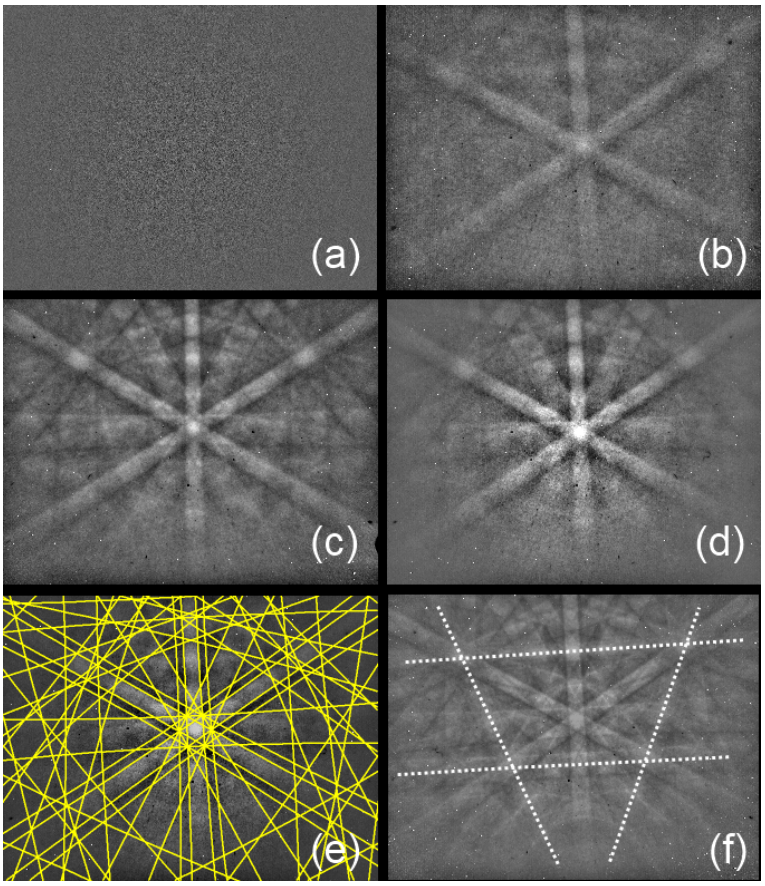

Figure 13.5: EBSD patterns recorded on a 3.7nm Ni film, as deposited (A), and after annealing to (B): 350° C, (C): 600° C and (D): 850° C. Sub figure E shows the simulated EBSD pattern for the θ-phase, while sub-figure F shows a cubic EBSD pattern, where the additional bands compared to the hexagonal pattern are indicated with arrows.

as one would observe the Si pattern if this were not the case. At 350°C (at which the resistance of the film has started to drop) a weak pattern appears showing a distinctive sixfold symmetry (figure 13.5b). At 600°C (figure 13.5c) and 850°C (figure 13.5d) the pattern has become more clear. Of the currently known nickel-silicides, the pattern was best fitted as a hexagonal phase, and the simulation when using the θ-nickel-silicide structure is shown in figure 13.5e. Fitting a cubic phase, like $NiSi_2$, also leads to a good agreement, however 3 fainter bands are missing in all of the EBSD patterns (indicated with dotted lines on a reference cubic pattern in figure 13.5f). The EBSD results therefore seem to suggest a hexagonal symmetry in the layer.

There exists an important discrepancy between the EBSD patterns and the XRD pole figures: while the EBSD patterns become more pronounced when the sample has been annealed to a higher temperature, the spots on the pole figures become weaker. There are three possible reasons for this. Firstly, as the crystallinity of the top-layer gets better during the annealing, the observed EBSD pattern can starts to contain a contribution of the underlying SOI substrate. Indeed, an EBSD pattern from Si (100) is almost identitical to the observed EBSD patterns and would in fact be indistinguishable from a perfect $NiSi_2$ EBSP. Secondly, there exists the possibility that the spots observed in the pole figures originate from defects (e.g. stacking faults) in an epitaxial film. The annealing process would then eliminate most of the defects, resulting in a decreasing intensity of the spots in the pole figures. At the same time, the decreasing defect concentration would result in EBSD patterns of increasing quality. Thirdly, there might occur a phase transition during the annealing, which converts the phase formed at 350°C into another phase of better epitaxial and crystalline quality, e.g. $NiSi_2$ or θ-nickel-silicide. Both these phases produce a very similar EBSD pattern, so that the conversion of the initial crystalline phase into one of these would look like an increase in EBSD pattern intensity and quality, even though a real phase transition has occurred.

The inconclusive results from the EBSD and XRD pole figures make it necessary to further characterize the samples. Cross section TEM images were recorded on the as-deposited 3.7 nm Ni films (figure 13.6a), and after anneals to 350°C (figure 13.6b) and 600°C (figure 13.6e). The as-deposited layer was found to be an amorphous mixture of Ni and Si, over the whole thickness range. This is due to the sputter deposition of the Ni, which causes the creation of an intermixed layer. EDS indicated a 47.2$\pm$0.4% Ni content. At the interface, a very thin crystalline layer with vertical planes of atoms (d-spacing of 0.19 nm) is already visible.

After the anneal to 350°C (figure 13.6b), the layer has become crystalline, with a flat interface. Its thickness has increased to 4.4 nm, and the layer (EDS) was now found to contain 52.8$\pm$0.4% Ni. The vertical planes, which match the Si $\{220\}$ planes, extend through the whole layer, and planes with an inclination of

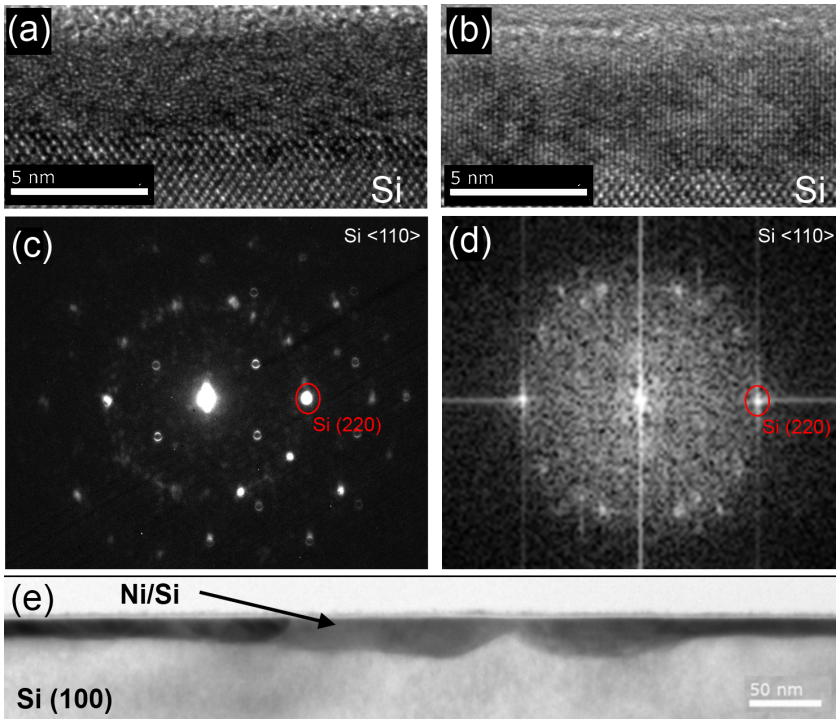

Figure 13.6: Cross section HRTEM images on (a) the as deposited 3.7 nm thick Ni layer and (b) after an anneal to 350°C. (c) shows the NBD image of the silicide at 350°C. In (d), the Fourier transform of picture (b) is shown, indicating the orientation of the atom layers in the silicide. After annealing to 600°C, the layer is no longer flat, and separate grains become visible (e)

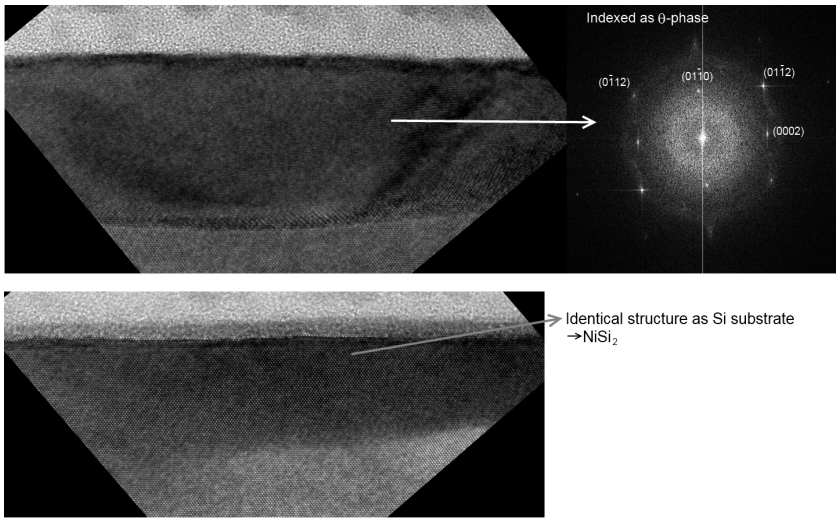

Figure 13.7: Cross section HRTEM images on 3.7 nm thick Ni layer after annealing to 600°C. Both θ-nickel-silicide and $NiSi_2$ was found.

20° to the interface have become visible (figure 13.6b and 13.6d). A nano-beam diffraction pattern was collected (figure 13.6c) and is in good agreement with the Fourier transform of the cross section (figure 13.6d). The d-spacing and inclination of these planes corresponds to the spots that are observed on the pole figures.

The analysis of the combined results of the EDS, TEM, EBSD and pole figure data showed that no single epitaxy of the currently know nickel-silicides can explain all of the data. This means that we are witnessing a new nickel-silicide phase and/or the layer is not purely epitaxial, but consists of small (a few nm) domains which share the alignment of a series of atomic planes, notably the vertical planes, and those with an inclination of 20° to the interface. This would result in all of these domains contributing to the diffraction pattern of the layer, as they will be averaged over the whole thickness of the TEM sample.

After an anneal to 600°C, the TEM cross section (figure 13.6e) shows that parts of the interface are no longer perfectly flat: in some places, the layer thickness has increased, and separate grains become visibl: both θ-nickel-silicide, and $NiSi_2$ grains have been formed (see figure 13.7). This confirms the hypothesis that the increase in EBSD pattern quality during annealing is being caused by a phase transition.

Combining the X-ray pole figures and TEM data, we can conclude that at a thickness of 3.7 nm or below, the as-deposited film is no longer pure Ni, but a mixture of Ni and Si. This changes the phase sequence, and results in the formation of

a currently unknown, epitaxy-like phase, which might consist of small domains which have some shared atomic planes. This shared periodicity is what is visible in the pole figures. The location of the spots on the pole figure at $\chi = 20°$ and their corresponding d-spacing (0.19 nm) are indeed consistent with the TEM diffraction results. During subsequent annealing, part of this layer is converted to θ-nickel-silicide and $NiSi_2$, keeping the sheet resistance low, but also resulting in a rougher interface. This presents a significant problem that must be overcome before these layers can be used in a device.

13.4 Discussion

The origin and exact structure of the epitaxy-like phase is at the moment unclear. A similar pole figure as those shown in figure 13.4 has been reported by Gaudet et al. in [69], where a thorough analysis of the phase formation and texture of the 10 nm Ni/Si(100) reaction at low temperatures was presented. The spots were identified as belonging to a transient phase in the Ni/Si(100) reaction and this phase was labelled as the X-phase, indicating the unknown crystal structure. The main difference with the ultra-thin samples investigated here is that in the 10 nm Ni/Si(100) reaction, the spots on the pole figure are only observed at low temperature (315 °C or less), as they disappear during the formation of the metal-rich nickel-silicides (δ-Ni_2Si and θ-Ni_2Si) and NiSi, as a result of nickel diffusion through this layer.

The results presented in this chapter seems to indicate that this X-phase occurs in all Ni/Si films and is a natural consequence of the sputter deposition process of the nickel film on the silicon substrate, which can be described as a two-step process: during the initial stages of the nickel deposition, an intermixed layer of Ni/Si is created which is relatively rich in silicon ($> 50\%$), and which is subsequently covered with pure nickel during the remaining part of the deposition. Upon annealing, this intermixed layer becomes crystalline as the X-phase is formed. If the intermixed layer is covered with pure nickel, the X-phase is unstable due to diffusion of nickel from the pure nickel layer to the intermixed layer, which increases the nickel content and ultimately results in the nucleation of one of the metal-rich nickel-silicides. On the other hand, if no such pure nickel film remains on top of the intermixed layer, as in the case of the 3.7 nm sample, the X-phase exhibits a much higher stability, as observed for the ultra-thin nickel films. This model essentially assumes that diffusion of nickel from the pure nickel layer to the intermixed layer occurs much faster than out-diffusion of nickel from the intermixed layer to the silicon substrate, an assumption for which there is currently no experimental proof.

In chapter 11, it was also shown that unexpected phases can occur in the Ni/Si sys-

tem, such as θ-nickel-silicide which crystallizes from a Ni(60%)/Si(40%) mixture. While this θ-phase in not a thermodynamically stable phase, it does occur due to the gain in free energy associated with the crystallization of the amorphous mixture, and remains metastable due to the lack of diffusion at these low temperatures, which prevent the nucleation of the thermodynamically stable phases. As the as-deposited layer of the 3.7 nm film is also a mixture of Ni and Si, a similar process might be occurring here. However, the exact phase that forms from this layer upon annealing can be different, as the Ni/Si ratio of the spontaneous intermixed layer in the ultra-thin films is different from the Ni(60%)/Si(40%) case we studied before (i.e. 47.2 % Ni vs. 60% Ni). Given the similarities between the EBSD patterns and pole figures of the X-phase and θ-nickel-silicide films, the X-phase is likely related to the θ-phase, i.e. a hexagonal phase with variable composition due to fractional occupation of nickel sites.

13.5 Ultra-thin nickel-platinum-silicides

Recently, the formation of ultra-thin Ni(Pt)-silicides has also received attention in literature. Zhang et al. [112] and Luo et al. [113] have reported on the formation of silicides from sub-10 nm Ni/Pt films, showing a similar epitaxial structure as in the ultra-thin nickel films discussed in this chapter, when the Ni(Pt) thickness is below a certain threshold. An interesting observation here is the dependence of the critical thickness of the metal layer on the Pt content: an increase in Pt concentration shifts this thickness to smaller values: from 4 nm when no Pt is used, to 2 nm in the case of 5% of Pt, to 1 nm when 10% Pt is used [112]. Luo et al. explained the Pt dependency of the critical thickness as being caused by the initial nucleation of either the δ-Ni_2Si or $NiSi_2$ phase. Pt addition will prevent the $NiSi_2$ phase from nucleating, resulting in δ-Ni_2Si formation, which is then converted to NiSi. A main problem with this explanation is that the experimental data shown in this chapter indicates that in the ultra-thin nickel-silicide layers, $NiSi_2$ is not directly formed from the intermixed layer, but instead that the X-phase is formed first, which makes it unlikely that it is the influence of Pt on the $NiSi_2$ formation that determines the critical thickness.

Two alternatives should be considered. Firstly, the deposition of Ni/Pt might reduce the thickness of the intermixed layer due to a different intermixing depth of Ni/Pt compared to pure Ni. This would in itself shift the critical thickness to lower values. Secondly, the Pt dependence of the critical thickness could be related to the influence of Pt on the free energy of the X-phase. If one accepts that the X-phase is related to the θ-phase, one can look back at the results in chapter 11, where the influence of Pt and W on the nucleation of θ-nickel-silicide was presented. It was

shown that Pt prevents θ-nickel-silicide formation in premixed Ni/Pt/Si layers, and it might have the same effect on the X-phase. If the X-phase cannot nucleate, an amorphous intermixed layer will remain, which during annealing will allow one of the other nickel-silicide phases, e.g. NiSi in which Pt is relatively soluble, to nucleate, returning to the traditional Ni/Si(100) reaction.

13.6 Conclusions

In conclusion, we found that there exists a specific thickness for sputter-deposited nickel films, which determines the phase sequence and the formation of the low resistive phase which is formed during a subsequent ramp anneal. Films with 3.7 nm of nickel or less form a low resistive phase consisting of an epitaxy-like phase. This layer exhibit a high thermal stability, and gets converted to $NiSi_2$ and θ-nickel silicide at higher temperatures, resulting in low electrical resistivity up to 800°C. The occurrence of this phase is likely caused by the interfacial intermixed layer, resulting from the sputter deposition.

14
Conclusions

Throughout this thesis, the importance of texture for thin film reactions on single crystal substrates has been pointed out.

It was shown that many different silicides and germanides exhibit a complex non-random texture:

- For NiSi on Si(100), the importance of the different texture components was quantified using EBSD. It was shown that axiotaxy represents the most important texture component and that the axiotaxy grains are larger than average. The one-dimensional rotational degree of freedom that defines axiotaxy was observed as not being caused by subgrain boundaries within one grain, but by a large amount of different grains that each have a well-defined orientation.
- The texture of $CoSi_2$ was reported on Si (100), (111) and (110), and weak axiotaxy was found in each of these systems. It was shown that the different epitaxial $CoSi_2$ orientations can be divided into two groups: double axiotaxy and plane-on-plane epitaxy. As axiotaxy is largely independent of the interface plane, this allowed to predict which epitaxial orientation are observed on all of the substrates, and which are unique to specific substrate orientations.
- The detailed study of texture in the Co/Ge system, on Ge (100) and Ge

(111) allowed to identify both axiotaxy and epitaxy. The strong epitaxy of Co_5Ge_7 on Ge (111) was found to be the cause of the coexistence of Co_5Ge_7 and $CoGe_2$ in a large temperature window on Ge (111).

The thermal stability of the Ni/Si system was studied in detail:

- The texture evolution during agglomeration was studied: it was shown that preferential grain growth occurs, as the fraction of axiotaxy grains increases during agglomeration. This indicates that the low interface energy of axiotaxy can provide a driving force for agglomeration.
- It was shown that by changing the initial Ni/Si ratio, one can obtain a metastable nickel-silicide phase: θ-nickel-silicide
- The effect of changing the phase sequence on the thermal stability of NiSi was shown to be related to a change in microstructure: axiotaxy was found to be suppressed, which was identified as being the cause of the increased thermal stability. This was related to the effect of W and Pt alloying elements which were found to either suppress of promote the occurrence of a θ-nickel-silicide-like phase.
- The effect of C on the Ni/Si(100) phase formation sequence and texture of the resulting NiSi was found to be strongly dependant on the initial location of the C. While mixing C in the Ni layer or depositing a C interlayer has only limited effect, using an epitaxial $Si_{1-x}C_x$ layer has a strong effect on the phase sequence and promotes the formation of NiSi with a fiber texture. Both these changes in NiSi texture and the occurrence of C in the NiSi film have an impact on the thermal stability, as $Si_{1-x}C_x$ layers make it possible to produce NiSi contacts that survive DRAM annealings.
- The effect of downscaling was investigated, and a critical nickel thickness of 3.7 nm was found below which the phase sequence and texture of the nickel-silicides changes dramatically. This was found to originate in the nickel/silicon intermixed layer at the interface.

List of publications

During the course of the research for this thesis, the following international publications were made:

1. *Phase formation and texture of nickel silicides on $Si_{1x}C_x$ epilayers*
   De Keyser K., De Schutter B., Detavernier C., Machkaoutsan V., Bauer M., Thomas S.G., Jordan Sweet J., Lavoie C.
   Microelectronic Engineering 88 (2011), 536-540

2. *Phase formation and thermal stability of ultra-thin nickel-silicides on Si(100)*
   De Keyser K., Van Bockstael C., Van Meirhaeghe R.L. Detavernier C., Verleysen E., Bender H., Vandervorst W., Jordan-Sweet J., Lavoie C.
   Applied Physics Letters 96 (17), 173503 (2010)

3. *Texture of $CoSi_2$ films on Si(111), (110) and (001) substrates*
   De Keyser K., Detavernier C., Jordan-Sweet J. and Lavoie C.
   Thin Solid Films 519 (4), 1277-1284 (2010)

4. *In situ study of the formation of silicide phases in amorphous Co-Si mixed layers*
   Van Bockstael C. De Keyser K., Demeulemeester J., Vantomme A., Van Meirhaeghe R.L., Detavernier C., Jordan-Sweet J.L., Lavoie C.
   Microelectronic Engineering 87 (3), 282-285 (2010)

5. *Texture of atomic layer deposited ruthenium*
   Musschoot J., Xie Q., Deduytsche D., De Keyser K., Longrie D., Haemers J., Van den Berghe S., Van Meirhaeghe R.L., DHaen J., Detavernier C.
   Microelectronic Engineering 87 (10), 1879-1883 (2010)

6. *The effect of sputtered W-based carbide diffusion barriers on the thermal stability and void formation in copper thin films*
   Xie Q., Jiang Y.L., De Keyser K., Detavernier C., Deduytsche D., Ru G.P., Qu X.P., Tu K.N.
   Microelectronic Engineering 87 (12), 2535-2539 (2010)

7. *Texture of cobalt germanides on Ge(100) and Ge(111) and its influence on the formation temperature*
   De Keyser K., Van Meirhaeghe R.L., Detavernier C., Jordan-Sweet J., Lavoie C.
   Journal of the Electrochemical Society 157 (4), H395 (2010)

8. *Influence of a transient hexagonal phase on the microstructure and morphological stability of NiSi films*
   Van Bockstael C., De Keyser K., Van Meirhaeghe R.L., Detavernier C., Jordan-Sweet J., Lavoie C.
   Applied Physics Letters, 94(3), 033504 (2009)

9. *The role of lattice mismatch and kinetics in texture development: $Co_{1-x}Ni_xSi_2$ thin films on Si(100)*
   Smeets D., Vantomme A., De Keyser K., Detavernier C., Lavoie C.
   Journal of Applied Physics 103(6), 063505 (2008)

10. *The texture of thin NiSi films and its effect on agglomeration*
    De Keyser K., Detavernier C., Van Meirhaeghe R.L., Jordan-Sweet J., Lavoie C.
    Ceramic Transactions, Volume 201, p. 3-10 (2008)

11. *Epitaxial formation of a metastable hexagonal nickel-silicide*
    De Keyser K., Van Bockstael C., Detavernier C., Van Meirhaeghe R.L., Jordan-Sweet J., Lavoie C.
    Electrochemical and Solid-State Letters 11(9), H266 (2008)

12. *Effect of Pt addition on growth stress and thermal stress of NiSi films*
    Van Bockstael C., De Keyser K., Deduytsche D., Van Meirhaeghe R.L., Detavernier C., Jordan-Sweet J., Lavoie C.
    Journal of Applied Physics, 104(5), 053510 (2008)

13. *Nucleation and diffusion during growth of ternary Co1-xNixSi2 thin films studied by complementary techniques in real time*
    Smeets D, Demeulemeester J., De Keyser K., Deduytsche D., Detavernier C., Comrie. C.M., Theron C.C., Lavoie C.,Vantomme A.
    Journal of Applied Physics, 104(9), 093533 (2008)

14. *Characterization of the texture of silicide films using electron backscattered diffraction*
    De Keyser K., Detavernier C., Van Meirhaeghe R.L.
    Applied Physics Letters, 90(12), 121920 (2007)

15. *Single crystal CaS : Eu and SrS : Eu luminescent particles obtained by solvothermal synthesis*
Van Haecke J.E., Smet P.F., De Keyser K., Poelman D.
Journal of the Electrochemical Society, 154(9), J278 (2007)

References

[1] R.T. Tung, J.M. Gibson, and J.M. Poate. Formation of ultrathin single-crystal silicide films on Si - surface and interfacial stabilization of Si-$NiSi_2$ epitaxial structures. *Physical Review Letters*, 50:429–432, 1983.

[2] C. Detavernier, A.S. Ozcan, J. Jordan-Sweet, E.A. Stach, J. Tersoff, F.M. Ross, and C. Lavoie. An off-normal fibre-like texture in thin films on single-crystal substrates. *Nature*, 426:641–645, 2003.

[3] V. Randle. *The Measurement of Grain Boundary Geometry*. Institute of Physics Publishing, 1993.

[4] Q. Liang and W.T. Reynolds. Determining interphase boundary orientations from near-coincidence sites. *Metallurgical and Materials Transactions A - Physical Metallurgy and Materials Science*, 29 (8):2059–2072, 1998.

[5] W. Bollmann. *Crystal Defects and Crystalline Interfaces*. Springer-Verlag, 1970.

[6] U. Dahmen. The role of the invariant line in the search for an optimum interphase boundary by O-lattice theory. *Scripta Metallurgica*, 15 (1):77–81, 1981.

[7] M.X. Zhang and P.M. Kelly. Crystallographic features of phase transformations in solids. *Progress in Materials Science*, 54 (8):1101 – 1170, 2009.

[8] M.X. Zhang and P.M. Kelly. Edge-to-edge matching and its applications: Part I. Application to the simple HCP/BCC system. *Acta Materialia*, 53 (4):1073– 1084, 2005.

[9] M. X. Zhang and P. M. Kelly. Application of edge-to-edge matching model to understand the in-plane texture of TiSi2 (C49) thin films on (001)(Si) surface. *Scripta Materialia*, 55:613–616, 2006.

[10] M.X. Zhang, P.M. Kelly, and C. Detavernier. Understanding of epitaxial alignment in NiSi thin films on a (001)(Si) surface using edge-to-edge

matching model. *Solid-Solid Phase Transformations in Inorganic Materials*, 1:145 – 151, 2005.

[11] P.M. Kelly and M.X. Zhang. Comments on edge-to-edge matching and the equivalence of the invariant line, Δg and Moire fringe approaches to the crystallographic features of precipitates. *Scripta Materialia*, 52 (7):679 – 682, 2005.

[12] A.J. Schwartz, M. Kumar, B.L. Adams, and D.P. Field, editors. *Electron Backscatter Diffraction in Materials Science*. Springer, 2009.

[13] F.J. Humphreys and I. Brough. High resolution electron backscatter diffraction with a field emission gun scanning electron microscope. *Journal of Microscopy - Oxford*, 195:6–9, 1999.

[14] F.J. Humphreys. Characterisation of fine-scale microstructures by electron backscatter diffraction. *Scripta Materialia*, 51:771–776, 2004.

[15] A.J. Wilkinson. A new method for determining small misorientations from electron back scatter diffraction patterns. *Scripta Materialia*, 44:2379–2385, 2001.

[16] D.J. Dingley. A comparison of diffraction techniques for the SEM. *Scanning Electron Microscopy*, 4:273–286, 1981.

[17] L.G. Schulz. A direct method of determining preferred orientation of a flat reflection sample using a geiger counter x-ray spectrometer. *Journal of Applied Physics*, 20:1030–1033, 1949.

[18] L.G. Schulz. Determination of preferred orientation in flat transmission samples using a geiger counter x-ray spectrometer. *Journal of Applied Physics*, 20:1033–1036, 1949.

[19] H.J. Bunge and C. Esling. Symmetries in texture analysis. *Acta Crystallographica A*, 41:59–67, 1985.

[20] S. Matthies and G.W. Vinel. On the reproduction of the orientation distribution function of texturized samples from reduced pole figures using the conception of a conditional ghost correction. *Physica Status Solidi B - Basic Research*, 112 (2):K111–K114, 1982.

[21] J.J. Heizmann and C. Laruelle. Simultaneous measurement of several x-ray pole figures. *Journal of Applied Crystallography*, 19:467–472, 1986.

[22] L. Wcislak, H.J. Bunge, and C.U. Nauergerhardt. X-ray diffraction texture analysis with a position-sensitive detector. *Zeitschrift fur Metallkunde*, 84 (7):479–493, 1993.

[23] L. Wcislak and C. Nauergerhardt. PSD-based Texture Investigations in Nonmetallic Materials. *Zeitschrift fur Metallkunde*, 85 (8):564–573, 1994.

[24] S. Gaudet, K. De Keyser, S. Lambert-Milot, J. Jordan-Sweet, C. Detavernier, C. Lavoie, and P. Desjardins. Three dimensional reciprocal space measurement by x-ray diffraction using linear and area detectors: Applications to texture and defects determination in oriented thin films and nanoprecipitates (submitted).

[25] S. Gaudet. http://code.google.com/p/xrd-texture/downloads/list.

[26] F. C. Frank. Orientation mapping. *Metallurgical Transactions A*, 19 (3):403–408, 1988.

[27] A. P. Sutton and Balluffi R. W. *Interfaces in Crystalline Materials*. Oxford Science Publications, 1995.

[28] Y.L. He and J.J. Jonas. Representation of orientation relationships in Rodrigues-Frank space for any two classes of lattice. *Journal of Applied Crystallography*, 40:559–569, 2007.

[29] L. Kestens, K. Verbeken, R Decocker, R. Petrov, P. Gobernado, and S.E. Offerman. The use of Rodrigues-Frank space for representing discrete misorientation distributions. *Materials Science Forum*, 495 - 497:157 – 166, 2005.

[30] J. Kruger and R. Westermann. Acceleration techniques for GPU-based volume rendering. In *IEEE Visualization 2003, Proceedings*, 2003.

[31] S.R. Hall. Space-group notation with an explicit origin. *Acta Crystallographica*, A37:517–525, 1981.

[32] T.A. Kircher and E.L. Courtright. Engineering limitations of $MoSi_2$ coatings. *Materials Science and Engineering A - Structural Materials Properties Microstructure and Processing*, 155:67–74, 1992.

[33] H.W. Grunling and R. Bauer. The role of silicon in corrosion-resistant high-temperature coatings. *Thin Solid Films*, 95:3–20, 1982.

[34] B.P. Bewlay, M.R. Jackson, J.C. Zhao, P.R. Subramanian, M.G. Mendiratta, and J.J. Lewandowski. Ultrahigh-temperature Nb-silicide-based composites. *MRS Bulletin*, 28:646–653, 2003.

[35] E. Gross, M. Riffel, and U. Stohrer. Thermoelectric generators made of $FeSi_2$ and HMS - fabrication and measurement. *Journal of Materials Research*, 10:34–40, 1995.

[36] J.L. Snelgrove, G.L. Hofman, M.K. Meyer, C.L. Trybus, and T.C. Wiencek. Development of very-high-density low-enriched-uranium fuels. *Nuclear Engineering and Design*, 178:119–126, 1997.

[37] L.J. Chen, editor. *Silicide Technology for Integrated Circuits*. The Institution of Electrical Engineers, 2004.

[38] S.L. Zhang and M. Ostling. Metal silicides in CMOS technology: past, present, and future trends. *Critical Reviews in Solid State and Materials Sciences*, 28:1–129, 2003.

[39] D. Deduytsche, C. Detavernier, R.L. Van Meirhaeghe, and C. Lavoie. High-temperature degradation of NiSi films: agglomeration versus NiSi2 nucleation. *Journal of Applied Physics*, 98:033526, 2005.

[40] D. Mangelinck, J.Y. Dai, J.S. Pan, and S.K. Lahiri. Enhancement of thermal stability of NiSi films on (100) Si and (111) Si by Pt addition. *Applied Physics Letters*, 75 (12):1736 – 1738, 1999.

[41] C. Detavernier and C. Lavoie. Influence of Pt addition on the texture of NiSi on Si(001). *Applied Physics Letters*, 84:3549–3551, 2004.

[42] S. Gaudet, C. Detavernier, A.J. Kellock, P. Desjardins, and C. Lavoie. Thin film reaction of transition metals with germanium. *Journal of Vacuum Science and Technology A*, 24 (3):474 – 485, 2006.

[43] J.C. Fisher. Calculation of diffusion penetration curves for surface and grain boundary diffusion. *Journal of Applied Physics*, 22:74–77, 1951.

[44] P. Heitjans and J. Krger, editors. *Diffusion in condensed matter: methods, materials, models*. Springer, 2005.

[45] J.C. Ciccariello, S. Poize, and P. Gas. Lattice and grain-boundary self-diffusion In Ni_2Si - comparison with thin-film formation. *Journal of Applied Physics*, 67:3315–3322, 1990.

[46] I. Blum, A. Portavoce, D. Mangelinck, R. Daineche, K. Hoummada, J. L. Labar, V. Carron, and J. Bernardini. Measurement of As diffusivity in Ni2Si thin films. *Microelectronic Engineering*, 87:263–266, 2010.

[47] A. Brokman, P.D. Bristowe, and Balluffi R. W. Computer simulation study of the structure of vacancies in grain boundaries. *Journal of Applied Physics*, 52 (10):6116, 1981.

[48] J. Sommer, C. Herzig, S. Mayer, and W. Gust. Grain boundary self-diffusion in silver bicrystals. *Defects and Diffusion Forum*, 66-69:843–848, 1989.

[49] R.E. Hoffmann. Anisotropy of grain boundary self-diffusion. *Acta Metallurgica*, 4:97–98, 1956.

[50] P.M. Jardim, W. Acchar, and W. Losch. Grain boundary reactive diffusion during Ni_2Si formation in thin films and its dependence on the grain boundary angle. *Applied Surface Science*, 137:163–169, 1999.

[51] G.A. Prinz. Stabilization of BCC Co via epitaxial-growth on GaAs. *Physical Review Letters*, 54:1051–1054, 1985.

[52] A. Madan, I.W. Kim, S.C. Cheng, P. Yashar, V.P. Dravid, and S.A. Barnett. Stabilization of cubic AlN in epitaxial AlN/TiN superlattices. *Physical Review Letters*, 78:1743–1746, 1997.

[53] D.F. Wilson and O.B. Cavin. Thermal-expansion behavior of NiSi/$NiSi_2$. *Scripta Metallurgica et Materialia*, 26 (1):85–88, 1992.

[54] C. Detavernier, C. Lavoie, and d'Heurle F.M. Thermal expansion of the isostructural PtSi and NiSi: Negative expansion coefficient in NiSi and stress effects in thin films. *Journal of Applied Physics*, 93 (5):2510–2515, 2003.

[55] D. Connetable and O. Thomas. First-principles study of the structural, electronic, vibrational, and elastic properties of orthorhombic NiSi. *Physical Review B*, 79 (9):094101, 2009.

[56] K. Maex and M. Van Rossum, editors. *Properties of Metal Silicides*. INSPEC, The Institution of Electrical Engineers, 1995.

[57] A.S. Özcan, K.F. Ludwig, C. Detavernier, C. Lavoie, and J.L. Jordan-Sweet. Axiotaxy of $CoSi_2$ thin films on Si(100) substrates and the effects of Ti alloying. *Journal of Applied Physics*, 95 (12):8376 – 8381, 2004.

[58] C. Detavernier, C. Lavoie, J.L. Jordan-Sweet, and A.S. Özcan. Texture of tetragonal α-$FeSi_2$ films on Si(001). *Physical Review B*, 69 (17):174106, 2004.

[59] H.P. Sun, Y.B. Chen, X.Q. Pan, D.Z. Chi, R. Nath, and Y.L. Foo. Formation and evolution of epitaxial Co_5Ge_7 film on Ge(001) surface by solid-state reaction in an in situ ultrahigh-vacuum transmission electron microscope. *Applied Physics Letters*, 87 (21):211909, 2005.

[60] K.E. Mello, S.P. Murarka, T.M. Lu, and S.L. Lee. Texture analysis of $CoGe_2$ alloy films grown heteroepitaxially on GaAs(100) using partially ionized beam deposition. *Journal of Applied Physics*, 81:7261–7267, 1997.

[61] S. Gaudet, C. Detavernier, C. Lavoie, and P. Desjardins. Reaction of thin Ni films with Ge: Phase formation and texture. *Journal of Applied Physics*, 100 (3):034306, 2006.

[62] M. Tinani, A. Mueller, Y. Gao, E.A. Irene, Y.Z. Hu, and S.P. Tay. In situ real-time studies of nickel silicide phase formation. *Journal of Vacuum Science and Technology B*, 19:376–383, 2001.

[63] J. Demeulemeester, D. Smeets, N.P. Barradas, A. Vieira, C.M. Comrie, K. Temst, and A. Vantomme. Artificial neural networks for instantaneous analysis of real-time Rutherford backscattering spectra. *Nuclear Instruments & Methods in Physics Research, Section B (Beam Interactions with Materials and Atoms)*, 268(10):1676–1681, 15 May 2010.

[64] F. Dheurle, C.S. Petersson, J.E.E. Baglin, S.J. Laplaca, and C.Y. Wong. Formation of thin-films of NiSi - metastable structure, diffusion mechanisms in intermetallic compounds. *Journal of Applied Physics*, 55:4208–4218, 1984.

[65] C. Lavoie, C. Coia, F.M. d'Heurle, C. Detavernier, C. Cabral, P. Desjardins, and A.J. Kellock. Reactive diffusion in the Ni-Si system: phase sequence and formation of metal-rich phases. In *Diffusion in Materials: DIMAT 2004, Pts 1 And 2*, 2005.

[66] H. Foll, P.S. Ho, and K.N. Tu. Transmission electron-microscopy of the formation of Nickel Silicides. *Philosophical Magazine A-Physics Of Condensed Matter Structure Defects And Mechanical Properties*, 45:31–47, 1982.

[67] H. Vonkanel. Growth and characterization of epitaxial Ni-silicide and Co-silicide. *Materials Science Reports*, 8:193–269, 1992.

[68] V. Teodorescu, L. Nistor, H. Bender, A. Steegen, A. Lauwers, K. Maex, and J. Van Landuyt. In situ transmission electron microscopy study of Ni silicide phases formed on (001) Si active lines. *Journal of Applied Physics*, 90:167–174, 2001.

[69] S. Gaudet, C. Coia, P. Desjardins, and C. Lavoie. Metastable phase formation during the reaction of Ni films with Si(001): the role of texture inheritance. *Journal of Applied Physics*, 107:093515, 2010.

[70] K. Hoummada, I. Blum, D. Mangelinck, and A. Portavoce. Composition measurement of the Ni-silicide transient phase by atom probe tomography. *Applied Physics Letters*, 96:261904, 2010.

[71] C. Detavernier, J. Jordan-Sweet, and C. Lavoie. Texture of NiSi films on Si(001), (111), and (110) substrates. *Journal of Applied Physics*, 103, 2008.

[72] A. Alberti, C. Bongiorno, B. Cafra, G. Mannino, E. Rimini, T. Metzger, C. Mocuta, T. Kammler, and T. Feudel. Pseudoepitaxial transrotational structures in 14 nm-thick NiSi layers on [001] silicon. *Acta Crystallographica Section B - Structural Science*, 61:486–491, 2005.

[73] A. Alberti, C. Spinella, A. La Magna, and E. Rimini. Nucleation and growth of NiSi from Ni_2Si transrotational domains. *Applied Physics Letters*, 90:053507, 2007.

[74] A. Alberti, C. Bongiorno, E. Rimini, and M.G. Grimaldi. Critical nickel thickness to form silicide transrotational structures on (001) silicon. *Applied Physics Letters*, 89:102105, 2006.

[75] S.M. Yalisove, R.T. Tung, and Loretto D. Epitaxial orientation and morphology of thin $CoSi_2$ films grown on Si(100) - effects of growth-parameters. *Journal of Vacuum Science and Technology A - Vacuum Surfaces and Films*, &:1472, 1989.

[76] M.L.A. Dass, D.B. Fraser, and C.S. Wei. Growth of epitaxial $CoSi_2$ on (100)Si. *Applied Physics Letters*, 58 (12):1308–1310, 1991.

[77] S. Mantl and H.L. Bay. New method for epitaxial heterostructure layer growth. *Applied Physics Letters*, 61 (3):267 – 269, 1992.

[78] R.T. Tung. Oxide mediated epitaxy of $CoSi_2$ on silicon. *Applied Physics Letters*, 68 (24):3461 – 3463, 1996.

[79] C. Detavernier, R.L. Van Meirhaeghe, R. Cardon, R.A. Donaton, and K. Maex. $CoSi_2$ formation in the presence of interfacial silicon oxide. *Applied Physics Letters*, 74 (20):2930 – 2932, 1999.

[80] A. Vantomme, S. Degroote, J. Dekoster, G. Langouche, and R. Pretorius. Concentration-controlled phase selection of silicide formation during reactive deposition. *Applied Physics Letters*, 74 (21):3137 – 3139, 1999.

[81] M. Falke, B. Gebhardt, G. Beddies, S. Teichert, and H.J. Hinneberg. The growth of an intermediate CoSi phase during the formation of epitaxial $CoSi_2$ by solid phase reaction. *Thin Solid Films*, 336:201 – 204, 1998.

[82] M. Falke, B. Gebhardt, G. Beddies, S. Teichert, and H.J. Hinneberg. Epitaxial $CoSi_2$ by solid phase reaction of Co/Ti and Co/Hf bilayers on Si(001). *Microelectronic Engineering*, 55:171 – 175, 2001.

[83] C. Detavernier, R.L. Van Meirhaeghe, K. Maex, W. Vandervorst, B. Brijs, and F. Cardon. Influence of Ti on $CoSi_2$ nucleation. *Applied Physics Letters*, 77:3170 – 3172, 2000.

[84] C. Detavernier, R.L. Van Meirhaeghe, F. Cardon, K. Maex, H. Bender, B. Brijs, and W. Vandervorst. Formation of epitaxial $CoSi_2$ by a Cr or Mo interlayer: Comparison with a Ti interlayer. *Journal of Applied Physics*, 89 (4):2146 – 2150, 2001.

[85] C.W.T. Bulle-Lieuwma, A.H. van Ommen, J. Hornstra, and Aussems C.N.A.M. Observation and analysis of epitaxial-growth of $CoSi_2$ on (100) Si. *Journal of Applied Physics*, 71 (5):2211 – 2224, 1992.

[86] C. Lavoie, C. Cabral, F.M. d'Heurle, J.L. Jordan-Sweet, and J.M.E. Harper. Effects of alloying elements on cobalt silicide formation. *Journal of Electronic Materials*, 31:597–609, 2002.

[87] D. Smeets, G. Vanhoyland, J. D'Haen, and A. Vantomme. On the thermal expansion coefficient of CoS_2 and $NiSi_2$. *Journal of Physics D: Applied Physics*, 42:235402, 2009.

[88] P.M. Kelly, H.P. Ren, D. Qiu, and M.X. Zhang. Identifying close-packed planes in complex crystal structures. *Acta Materialia*, 58 (8):3091–3095, 2010.

[89] A. Yamada, P.J. Fons, R. Hunger, K. Iwata, K. Matsubara, and S. Niki. Static analysis of off-axis crystal film growth onto a lattice-mismatched substrate. *Applied Physics Letters*, 79 (5):608 – 610, 2001.

[90] H. Ehsani, I. Bhat, R.J. Gutmann, G. Charache, and Freeman M. Role of relative tilt on the structural properties of GaInSb epitaxial layers grown on (001) GaSb substrates. *Journal of Applied Physics*, 86 (2):835 – 840, 1999.

[91] Y.F. Hsieh, L.J. Chen, E.D. Marshall, and S.S. Lau. Partial epitaxial-growth of cobalt germanides on (111) Ge. *Applied Physics Letters*, 51 (20):1588 – 1590, 1987.

[92] K. Opsomer, D. Deduytsche, C. Detavernier, R.L. Van Meirhaeghe, A. Lauwers, K. Maex, and C. Lavoie. Influence of Ge substrate crystallinity on Co germanide formation in solid-state reactions. *Applied Physics Letters*, 90 (3):031906, 2007.

[93] C. Lavoie, C. Detavernier, C. Cabral, Jr., F. M. d'Heurle, A. J. Kellock, J. Jordan-Sweet, and J. M. E. Harper. Effects of additive elements on the phase formation and morphological stability of nickel monosilicide films. *Microelectronic Engineering*, 83:2042–2054, 2006.

[94] T.P. Nolan, R. Sinclair, and R. Beyers. Modeling of agglomeration in polycrystalline thin-films - application to $TiSi_2$ on a silicon substrate. *Journal of Applied Physics*, 71:720–724, 1992.

[95] M. Bouville, C. Dongzhi, and D.J. Srolovitz. Grain-boundary grooving and agglomeration of alloy thin films with a slow-diffusing species. *Physical Review Letters*, 98(8):085503, 23 February 2007.

[96] C. Van Bockstael, C. Detavernier, R.L. Van Meirhaeghe, J.L. Jordan-Sweet, and C. Lavoie. In situ study of the formation of silicide phases in amorphous Ni-Si mixed layers. *Journal of Applied Physics*, 106:064515, 2009.

[97] K. Toman. The structure of Ni_2Si. *Acta Crystallographica*, 5, 1952.

[98] H. Vonkanel, C. Schwarz, S. Goncalvesconto, E. Muller, L. Miglio, F. Tavazza, and G. Malegori. New epitaxially stabilized CoSi phase with the CsCl structure. *Physical Review Letters*, 74:1163–1166, 1995.

[99] H. Vonkanel, K.A. Mader, E. Muller, N. Onda, and H. Sirringhaus. Structural and electronic-properties of metastable epitaxial $FeSi_{1+x}$ films on Si(111). *Physical Review B*, 45:13807–13810, 1992.

[100] J.M. Gibson and J.L. Batstone. Insitu transmission electron-microscopy of $NiSi_2$ formation by molecular-beam epitaxy. *Surface Science*, 208:317–350, 1989.

[101] D. Deduytsche, C. Detavernier, R.L. Van Meirhaeghe, J.L. Jordan-Sweet, and C. Lavoie. Formation and morphological stability of NiSi in the presence of W, Ti, and Ta alloying elements. *Journal of Applied Physics*, 101 (4):044508, 2007.

[102] W. Huang, L.C. Zhang, H.Y. Gao, Y.Z.and Jin, B.J. Ning, and G.Q. Zhang. Effect of a thin W interlayer on the thermal stability and electrical characteristics of NiSi film. *Journal of Vacuum Science and Technology B*, 23:2304–2308, 2005.

[103] M.J. Kim, H.J. Choi, D.H. Ko, J.H. Ku, S. Choi, K. Fujihara, and C.W. Yang. High thermal stability of Ni monosilicide from Ni-Ta alloy films on Si(100). *Electrochemical and Solid-State Letters*, 6:G122–G125, 2003.

[104] M. Ellner, S. Heinrich, M.K. Bhargava, and K. Schubert. Einige strukturelle untersuchungen in der mischung $NiSi_N$. *Journal of Less Common Metals*, 66:163–173, 1979.

[105] J. Demeulemeester, D. Smeets, C. Van Bockstael, C. Detavernier, C. M. Comrie, N. P. Barradas, A. Vieira, and A. Vantomme. Pt redistribution during Ni(Pt) silicide formation. *Applied Physics Letters*, 93:261912, 2008.

[106] J. Demeulemeester, D. Smeets, C.M. Comrie, C. Van Bockstael, W. Knaepen, C. Detavernier, K. Temst, and A. Vantomme. The influence

of Pt redistribution on $Ni_{1-x}Pt_xSi$ growth properties. *Journal of Applied Physics*, 108:043505, 2010.

[107] D. Mangelinck, K. Hoummada, A. Portavoce, C. Perrin, R. Daineche, M. Descoins, D. J. Larson, and P. H. Clifton. Three-dimensional composition mapping of NiSi phase distribution and Pt diffusion via grain boundaries in Ni_2Si. *Scripta Materialia*, 62:568–571, 2010.

[108] M. Tsuchiaki and A. Nishiyama. Leakage reduction by thermal annealing of NiPtSi silicided junctions and anomalous grain-incompatible Pt network. *Japanese Journal of Applied Physics*, 49:04DA01, 2010.

[109] N. Machkaoutsan, S. Mertens, M. Bauer, A. Lauwers, K. Verheyden, K. Vanormelingen, P. Verheyen, R. Loo, M. Caymax, S. Jakschik, D. Theodore, P. Absil, S. G. Thomas, and E. H. A. Granneman. Improved thermal stability of Ni-silicides on Si : C epitaxial layers. *Microelectronic Engineering*, 84:2542–2546, 2007.

[110] V. Machkaoutsan, P. Verheyen, M. Bauer, Y. Zhang, S. Koelling, A. Franquet, K. Vanormelingen, R. Loo, C. S. Kim, A. Lauwers, N. Horiguchi, C. Kerner, T. Hoffmann, E. Granneman, W. Vandervorst, P. Absil, and S. G. Thomas. Electrical demonstration of thermally stable Ni silicides on $Si_{1-x}C_x$ epitaxial layers. *Microelectronic Engineering*, 87:306–310, 2010.

[111] C. Detavernier, R.L. Van Meirhaeghe, H. Bender, O. Richard, B. Brijs, and K. Maex. $CoSi_2$ formation in the presence of carbon. *Journal of Applied Physics*, 92:1207–1211, 2002.

[112] Z. Zhang, S.L. Zhang, B. Yang, Y. Zhu, S.M. Rossnagel, S. Gaudet, A.J. Kellock, J. Jordan-Sweet, and C. Lavoie. Morphological stability and specific resistivity of sub-10 nm silicide films of $Ni_{1-x}Ptx$ on Si substrate. *Applied Physics Letters*, 96:071915, 2010.

[113] J. Luo, Z. Qiu, C. Zha, Z. Zhang, D. Wu, J. Lu, J. Akerman, M. Ostling, L. Hultman, and S.L. Zhang. Surface-energy triggered phase formation and epitaxy in nanometer-thick $Ni_{1-x}Pt_x$ silicide films. *Applied Physics Letters*, 96:031911, 2010.